To the Graduate Council:

I am submitting herewith a dissertation written by Thomas Andrew Canada entitled "Optical Sensors for the Determination of Strong Base and Acid in Harsh Organic and Saline Environments." I have examined the final paper copy of this dissertation for form and content and recommend that it be accepted in partial fulfillment of the requirements for the degree of Doctor of Philosophy, with a major in Chemistry.

Ziling (Ben) Xue, Major Professor

We have read this dissertation
and recommend its acceptance:

James Q. Chambers

Jamie L. Adcock

Charles F. Moore

Accepted for the Council:

Vice Provost and
Dean of Graduate Studies

Optical Sensors for the Determination of Strong Base and Acid in Harsh Organic and Saline Environments

A Dissertation

Presented for the

Doctor of Philosophy

Degree

The University of Tennessee, Knoxville

Thomas Andrew Canada

August 2002

IN MEMORY

This dissertation is in loving memory of my

"older brother," Christopher Thomas Canada.

ACKNOWLEDGEMENTS

First and foremost, I would like to acknowledge my parents, Thomas and Geraldine Canada, my brother, Tommy, and my wife, Carrie for all the support and encouragement through the years. They have been an integral part of my life. I owe a special appreciation for my advisor, Prof. Ziling (Ben) Xue for his steady, intellectual guidance, and support through my further development as a scientist. I would also like to thank the members of my defense committee, Professors Jamie Adcock, James Chambers, and Charles Moore for taking time to critique this dissertation.

A special thanks goes to Dr. David Beach, head of the Advanced Inorganic Materials Group, Chemical Sciences Division at Oak Ridge National Laboratory for his much appreciated assistance evaluating the surface features of the films by SEM and film thickness studies.

I would like to thank Bill Gurley and Johnny Jones of the electronics shop for training me to use certain software programs, as well as providing insightful computing advice. Thanks go to Arthur Pratt in the glass shop for help in cutting the sensor glass micro slides. I will miss my friendships and frequent, casual conversations with these gentlemen.

I am also grateful for all the friendships that I have established over my four-year stay at the University of Tennessee. I will remember all the sports conversations and friendships including, but not limited to, the following: The "Arkansas Boys", Bryan Fagan and Terry Yost, for going to the University of

Kentucky (UK) football games in Lexington with me, Dr. Eric Eastwood, Charles O'Brien, Mike Arlen, Kevin Rice, Scott Fontana, Steve Wargacki, Nathan Crawford, Chris Kolesnik, and Dewayne Wilson for frequent visits; Dr. Tianniu (Rick) Chen and the many conversations we had about Kentucky basketball; Dr. Mark Burleigh and his witty observations; and Kentucky native, Greg Duncan for being a loyal Kentucky fan and going to UK basketball games with me.

I am grateful to Dr. Leonardo Allain and Karn Sorasaenee for their early work on the sensor projects. It was their hard work that laid the foundation. I would also like to acknowledge Drs. Hu (Frank) Cai and Hee-Jung Im for insightful advice. Thanks to Dr. Yvette Yang for sharing office space with me and providing friendly conversation.

I am appreciative of Professor John Selegue at the University of Kentucky for "jumpstarting" my career in inorganic chemistry during my undergraduate tenure.

The research described in this dissertations was financially supported by the Measurement and Control Engineering Center (MCEC) at the UT College of Engineering and its member companies (3M, ABB, Amoco, Ciba Specialty Chemicals, Coates Consulting, Dow Corning, DuPont, Eastman Chemical, Elf Aquitaine, Equistar Chemicals, ExxonMobile, Goodyear, Hercules, Imperial Chemical Industries, Kaiser Optical, Lubrizol, Oak Ridge National Laboratory, Solutia, and Union Carbide). American Holographic is also recognized for the donation of the Rainbow Meter spectrometer used for collecting visible spectra. I would also like to acknowledge the following research grants and institutions for

their financial support: Dupont Young Professor Award, Camille Dreyfus Teacher-Scholar Award, and the University of Tennessee at Knoxville.

ABSTRACT

This dissertation focuses on the development of optical acid and base sensors and their uses in ternary systems. Chapter 1 provides an overview of the dissertation. Background on topics related to the optical sensors is discussed including: measurement of *p*H (mild and harsh conditions), optical *p*H sensing (aqueous and ternary systems), basic sol-gel processing, and a summary of instruments used in this research.

Chapter 2 involves the use of optical acid and base sensors in concentrated NaOH-ROH-H_2O (R = Me, Et, i-Pr) mixed solvent systems, in which a novel linear relationship is observed between $(\partial A/\partial C_{alcohol})$ and C_{base} for high pK_a indicators encapsulated in sol-gel ($Zr_xSi_yO_{2(x+y)}$)-organic polymer composites. This relationship leads to a dual transducer approach to give C_{base} and $C_{alcohol}$ with high accuracy and precision. In addition, the selection of indicators with high pK_as, large dynamic spectral ranges, and chemical stability to OH^- attack and oxidation is presented.

Chapter 3 involves the evaluation of sensor performance by analysis of response times, hysteresis effects, and durability in NaOH-ROH-H_2O ternary solutions (R = Me, Et, and i-Pr). It has been found that the film morphology (porosity, surface area, and thickness) directly determines the performance of the sensor and ultimately controls the sensor kinetics and magnitude of hysteresis effects. We also studied the Si-O-Zr bonding characteristics of our sensor materials to understand their stability to OH^- attack, and explored the mixed

metal oxide bonding rationale for the enhancement in the durability. Chemical and physical properties of our sensor films were investigated by solid-state ^{29}Si NMR, reflectance FT-IR, XPS, BET, SEM, and profilometry to gain an insight into the chemistry of the sensor films.

Chapter 4 involves the continuation of previous work in our group on a dual-transducer approach for acid determination in HCl-salt-H_2O ternary systems. Previously a dual-transducer approach was development for a system containing one salt ($CaCl_2$) demonstrated for *one* acid concentration (5 M). In the current work, we studied a broad scope in order to use this approach to estimate C_{acid} at 2-9 M in LiCl-HCl, $CaCl_2$-HCl, and $AlCl_3$-HCl solutions (0-2 M).

A cocktail sensor approach is evaluated in Chapter 5. A cocktail sensor essentially consists of two or more indicators immobilized upon the same sensing support. The use of high and low pK_a dyes and their associated optical spectra are evaluated. The influences of sensor film composition on chemical equilibria and pK_a of the indicators encapsulated in the film were investigated.

A method to deconvolute the absorbance of a cocktail sensor containing two indicators was developed and used to predict C_{HCl} and C_{salt} in HCl-salt-H_2O ternary solutions. Errors in C_{HCl} and C_{salt} predictions were evaluated.

TABLE OF CONTENTS

Chapter **Page**

1 Introduction.....1

1.1 Measurement of *p*H in *Mild* Conditions.....1

1.2 Measurement of *p*H in *Extreme* Conditions.....2

1.3 Optical *p*H Sensing.....5

1.3.1 Optical Sensors for Highly Alkaline Aqueous Media.....9

1.3.2 Optical Sensors for Highly Alkaline Ternary (NaOH-ROH-H_2O) Media.....11

1.3.3 Optical Sensors for Highly Acidic Aqueous Media.....11

1.3.4 Optical Sensors for Highly Acidic Ternary (HCl-Salt-H_2O) media.....12

1.4 Basic Sol-Gel Process.....13

1.4.1 History of Sol-Gel Chemistry.....13

1.4.2 Sol-Gel Processing.....14

1.4.3 Immobilization Methods.....19

1.4.4 Developments and Applications of Sol-Gel Sensors.....21

1.4.5 Preparation of the Sensor Substrate and Spin Coating Techniques.....21

1.5 Characterization of Sol-Gel Sensor Materials Used in the Current Study.....22

1.5.1 SEM.....24

1.5.2 Profilometry.....25

1.5.3 BET.....25

1.5.4 Infrared Spectroscopy.....26

1.5.5 ^{29}Si Solid-State NMR.....27

1.5.6 XPS (ESCA).....28

1.6 Overview of This Dissertation.....29

2 High-Basicity Determination in Mixed Water Alcohol Solutions by a Dual Optical Sensor Approach.....32

2.1 Introduction.....32

2.2 Experimental.....34

2.2.1 Preparation of the Sol-Gel Composite Sensors.....35

2.2.1-a Sensors **TY1-3**.....35

2.2.1-b Sensor **TY4**.....36

2.2.1-c Sensors **AY1-3**.....36

2.2.1-d Sensors **AY4**.....37

2.2.2 Curing of the Sensors.....37

2.2.3 Conditioning.....37

2.3 Results and Discussion.....37

2.3.1 Alkalinity in NaOH-H_2O-Organic Solvent Ternary Systems.....37

2.3.2 Dual Optical Transducer Approach.....43

2.3.3 Error Analysis.....62

2.3.4 Indicator Selection.....68

2.3.5 Impact of Sol-Gel Environment on Indicator Equilibria...69

2.4 Concluding Remarks.....75

3 Characterization of the Materials of the Optical Sensor for Highly Alkaline Solutions and the Sensor Performance Evaluation.....76

3.1 Introduction.....76

3.2 Experimental Section.....81

3.2.1 Preparation of the Sol-Gel Bulks.....82

3.2.1-a ZrO_2 (Powder **4**).....82

3.2.1-b SiO_2 (Powder **5**).....82

3.2.1-c $Zr_{0.66}Si_1O_{3.32}$ (Powder **6**).....83

3.2.1-d $Zr_xSi_yO_{2(x+y)}$ (Powders **7-9**).....83

3.2.1-e $Zr_{0.66}Si_1O_{3.32}$-Nafion (Powder **10**).....83

3.2.1-f $Zr_{0.66}Si_1O_{3.32}$-Nafion-AY (Powder **11**).....84

3.2.1-g $Zr_{0.66}Si_1O_{3.32}$-Nafion-TY (Powder **12**).....84

3.2.2 Instrument.....84

3.2.2-a Scanning Electron Microscopy (SEM).....84

3.2.2-b Profilometer.....85

3.2.2-c BET Measurement.....85

3.2.2-d X-ray Photoelectron Spectroscopy (XPS).....86

3.2.2-e ^{29}Si Solid-State NMR.....87

3.2.2-f FT-IR.....87

3.2.3 Sensor Data Collection.....88

3.2.3-a Hystersis, Kinetic, and Durability Data Collection.....88

3.2.3-b Kinetics and Hystersis Experiments.....88

3.2.3-c Durability Experiments.....88

3.3 Results and Discussion.....89

3.3.1 Physical Characterization of Sensor Films.....89

3.3.2 Chemical Characterization of Sensor Films.....91

3.3.2-a X-Ray Photoelectron Spectroscopy 91

3.3.2-b FT-IR.....105

3.3.2-c ^{29}Si Solid-State NMR.....112

3.3.3 Sensor Performance.....119

3.3.3-a Kinetic and Hysteresis Studies of Optical Sensors in NaOH-ROH-H_2O (R = Me, Et, and i-Pr) Ternary Media.....119

3.3.3-b Durability Studies of Optical Sensors in NaOH-ROH-H_2O Media.....137

3.4 Concluding Remarks.....141

4 High-Acidity Determination in Salt-Containing Acids by Optical Sensors. The Scope of a New Dual-Transducer Approach.....142

4.1 Introduction.....142

4.2 Experimental Section.....146

4.2.1 Preparation of Sensors **BCG1-3**.....147

4.2.2 Preparation of Sensors **BCP1-3**.....148

4.2.3 Preparation of Sensors **NR1-3**.....148

4.2.4 Sensor Conditioning.....148

4.2.5 Measurement Procedure.....149

4.2.6 Characterization.....149

4.3 Results and Discussion.....149

4.3.1 Salt Selection.....149

4.3.2 Characterization of the Sensor Materials.....150

4.3.3 The Salt-Effect and Dual Optical Transducer Approach.....152

4.3.4 Scope of the New Dual-Sensor Approach and Error Analysis.....169

4.4 Concluding Remarks.....183

5 Single Optical Sensors Containing Multiple Transducers - Cocktail Sensors.....185

5.1 Introduction.....185

5.2 Experimental Section.....188

5.2.1 Preparation of Sensors.....190

5.2.1-a Sensor **TY9**.....190

5.2.1-b Sensor **AY9**.....190

5.2.1-c Sensor **AYTY1**.....191

5.2.1-d Sensor **BCP4**.....191

5.2.1-e Sensor **BCG4**.....191

5.2.1-f Sensor **FG1**.....191

5.2.1-g Sensor **NR4**.....192

5.2.1-h Sensors **BCPBCG1**.....192

5.2.1-i Sensors **BCGFG1** and **BCPFG1**.....192

5.2.1-j Sensor **NRBCP1**.....192

5.2.1-k Sensors **NRFG1** and **NRBCG1**.....193

5.2.2 Curing of the Sensors.....193

5.2.3 Conditioning of the Sensors.....193

5.3 Results and Discussion.....194

5.3.1 Studies of Dissolved and Encapsulated Acid Indicators in Highly Acidic Solutions 194

5.3.1-a Bromocresol Purple Dissolved in Highly Acidic Solutions.....194

5.3.1-b Bromocresol Purple Encapsulated in a Sol-Gel Solid and Tested in Highly Acidic Solutions.....199

5.3.1-c Bromocresol Green Dissolved in Highly Acidic Solutions.....199

5.3.1-d Bromocresol Green Encapsulated in a Sol-Gel Solid and Tested in Highly Acidic Solutions.....202

5.3.1-e Neutral Red.....207

5.3.1-f Fast Green FCF.....212

5.3.2 Spectral Deconvolution of Cocktail Sensors.....215

5.3.3 Salt Study Using a Cocktail Sensor.....222

5.4 Concluding Remarks.....230

References.....231

Appendices.....244

Appendix A.....245

Appendix B.....250

Appendix C.....252

Appendix D.....256

Vita.....257

LIST OF TABLES

Table **Page**

2.1 Results of the Dual Sensor Approach for NaOH-MeOH-H_2O Solutions Using Sensors **TY1** and **AY1**.....65

2.2 Results of the Dual Sensor Approach for NaOH-EtOH-H_2O Solutions Using Sensors **TY2** and **AY2**.....66

2.3 Results of the Dual Sensor Approach for NaOH-i-PrOH-H_2O Solutions Using Sensors **TY3** and **AY3**.....67

2.4 Thermodynamic Dissociation Constants for Thiazole Yellow GGM (Sensors **TY3** and **TY4**) and Alizarin Yellow R (Sensors **AY3** and **AY4**) in ($Zr_{0.66}Si_1O_{3.32}$) and ($Zr_{0.66}Si_1O_{3.32}$)-Nafion Composite.....72

3.1 BET Results of the Bulk Samples.....90

3.2 Relative XPS Peak Designations.....99

3.3 XPS Peaks of Powders.....101

3.4 Kinetic Data Based Upon the Time in Seconds to Reach 90% of the Analytical Signal.....121

4.1 BET Results of the Bulk Samples.....151

4.2 Comparisons for the HCl-LiCl-H_2O Solutions.....180

4.3 Comparisons for the HCl-$CaCl_2$-H_2O Solutions.....181

4.4 Comparisons for the HCl-$AlCl_3$-H_2O Solutions.....182

5.1 Molar Extinction Coefficients (ε) of Fast Green FCF, Bromocresol

Purple, and Bromocresol Green as Determined Optically in Solution.....200

LIST OF FIGURES

Figure **Page**

1.1 Schematic representation of the glass and calomel electrodes for *p*H meters.....3

1.2 A schematic of the optical flow system.....7

1.3 A schematic of the optical flow cell.....8

1.4 A summary of the basic sol-gel reactions.....15

1.5 A representation of the spin coating process.....23

2.1 Possible structures of (a) the stable $OH(H_2O)_3^-$ species in solution and (b) the "Solvent-bridged" ion pairs.....38

2.2 Relationship between density and NaOH concentration in aqueous systems.....41

2.3 C_{NaOH} inaccuracies using Sensors (a) **TY1** and (b) **AY1** in NaOH-MeOH-H_2O ternary solutions without correction.....44

2.4 C_{NaOH} inaccuracies using Sensors (a) **TY2** and (b) **AY2** in NaOH-EtOH-H_2O solutions without correction.....45

2.5 C_{NaOH} inaccuracies using Sensors (a) **TY3** and (b) **AY3** in NaOH-i-PrOH-H_2O solutions without correction.....46

2.6 Ternary phase diagrams.....47

2.7 Responses of Sensors (a) **TY1** and (b) **AY1** in NaOH-MeOH-H_2O solutions.....49

2.8 Responses of Sensors (a) **TY2** and (b) **AY2** in NaOH-EtOH-H_2O solutions.....50

2.9 Responses of Sensors (a) **TY3** and (b) **AY3** in NaOH-i-PrOH-H_2O solutions.....51

2.10 Calibration plots of A vs. C_{NaOH} for Sensors (a) **TY1**, (b) **TY2**, and (c) **TY3** in alcohol-free, aqueous solutions.....52

2.11 Calibration plots of A vs. C_{NaOH} for Sensors (a) **AY1**, (b) **AY2**, and (c) **AY3** in alcohol-free, aqueous solutions.....53

2.12 Calibration plots of A vs. C_{MeOH} for Sensors (a) **TY1** and (b) **AY1** in NaOH-MeOH-H_2O solutions.....55

2.13 Calibration plots of A vs. C_{EtOH} for Sensors (a) **TY2** and (b) **AY2** in NaOH-EtOH-H_2O solutions.....56

2.14 Calibration plots of A vs. $C_{i\text{-}PrOH}$ for Sensors (a) **TY3** and (b) **AY3** in NaOH-i-PrOH-H_2O solutions.....57

2.15 C_{NaOH} vs. $(\partial A/\partial C_{MeOH})_{C_{NaOH}}$ plots for Sensors (a) **TY1** and (b) **AY1**.....58

2.16 C_{NaOH} vs. $(\partial A/\partial C_{EtOH})_{C_{NaOH}}$ plots for Sensors (a) **TY2** and (b) **AY2**.....59

2.17 C_{NaOH} vs. $(\partial A/\partial C_{i\text{-}PrOH})_{C_{NaOH}}$ plots for Sensors (a) **TY3** and (b) **AY3**.....60

2.18 Errors in C_{NaOH} *after* corrections using Sensors **TY1-3** and **AY1-3**: (a) NaOH-MeOH-H_2O, (b) NaOH-EtOH-H_2O, (c) NaOH-i-PrOH-H_2O.....63

2.19 Sample plots of actual $C_{alcohol}$ vs. predicted $C_{alcohol}$ in NaOH-

ROH-H_2O ternary solutions: (a) 0.50 M NaOH (ROH = MeOH), (b) 1.28 M NaOH (ROH = EtOH), (c) 0.050 M NaOH (ROH = i-PrOH).....64

2.20 Equilibria involving the protonated and deprotonated forms of (a) Thiazole Yellow GGM and (b) Alizarin Yellow R.....70

2.21 Distribution curves for the first ionization of Sensor **TY2** doped in a ($Zr_xSi_yO_{2(x+y)}$)-Nafion sol-gel matrix.....73

2.22 Transmittance spectra of a typical (a) Thiazole Yellow sensor and (b) Alizarin Yellow sensor in a ($Zr_xSi_yO_{2(x+y)}$)-Nafion support.....74

3.1 Two representations of the structure of zircon $ZrSiO_4$ consisting of independent tetrahedra SiO_2 and distorted ZrO_8 cubes.....78

3.2 An example of a typical spectrum recorded by a profilometer.....92

3.3 SEM images of Sensor **AY1** at (a) 100x magnification and (b) 1000x magnification.....93

3.4 SEM images of Sensor **AY1** at (a) 10000x magnification and (b) 30000x magnification.....94

3.5 The XPS spectra of Powders (a) **1** and (b) **5**.....96

3.6 The XPS spectra of Powders (a) **3** and (b) **4**.....97

3.7 The XPS spectra of Powders (a) **2** and (b) **6**.....98

3.8 Si (2*p*) photoelectron peaks of Powders (a) **1** and **2**, and (b) **5** and **6**.....103

3.9 Zr (3*d* 5/2) photoelectron peaks of Powders (a) **2** and **3**, and (b) **4** and **6**.....104

3.10 O (1*s*) photoelectron peaks of Powders (a) **1-3**, and (b) **4-6**.....106

3.11 The reflectance FT-IR spectra of (a) sol-gel SiO_2 Powder **5** and (b) sol-gel ZrO_2 Powder **4**.....107

3.12 The reflectance FT-IR spectra of (a) Powder **9** ($Zr_{0.10}Si_1O_{2.20}$) and (b) Powder **8** ($Zr_{0.20}Si_1O_{2.40}$).....109

3.13 The reflectance FT-IR spectra of (a) Powder **7** ($Zr_{0.40}Si_1O_{2.80}$) and (b) Powder **6** ($Zr_{0.66}Si_1O_{3.32}$).....110

3.14 Solid-state ^{29}Si NMR spectrum of sol-gel SiO_2 Powder **5**.....114

3.15 Solid-state ^{29}Si NMR spectra of (a) Powder **8** ($Zr_{0.20}Si_1O_{2.40}$), (b) Powder **7** ($Zr_{0.40}Si_1O_{2.80}$), and (c) Powder **6** ($Zr_{0.66}Si_1O_{3.32}$).....115

3.16 Comparisons of solid-state ^{29}Si NMR chemical shifts vs Zr:Si ratios for Powders **6-9**.....117

3.17 Solid-state ^{29}Si NMR spectra of (a) Powder **1** (SiO_2) and (b) zircon Powder **2** ($ZrSiO_4$).....118

3.18 Sensor response kinetics during the positive concentration gradient in aqueous NaOH solutions for Sensors (a) **TY5** and (b) **AY5**.....122

3.19 Sensor response kinetics during the positive NaOH concentration gradient in 50% v/v MeOH-H_2O solutions for Sensors (a) **TY5** and (b) **AY5**.....123

3.20 Sensor response kinetics during the positive NaOH concentration gradient in 50% v/v EtOH-H_2O solutions for Sensors (a) **TY5** and (b) **AY5**.....124

3.21 Sensor response kinetics during the positive NaOH concentration gradient in 50% v/v i-PrOH-H_2O solutions for Sensors (a) **TY5** and (b) **AY5**.....125

3.22 Three basic zones of hydroxide diffusion.....128

3.23 The logarithm of the buffer power per liter of water (B_W'/c) as a function of *p*H in the alkaline region.....129

3.24 Sensor response kinetics during the negative NaOH concentration gradient in *aqueous* solutions for Sensors (a) **TY5** and (b) **AY5**.....131

3.25 Hysteresis profile for Sensors (a) **TY5** and (b) **AY5** in aqueous NaOH solutions.....133

3.26 Hysteresis profile for Sensors (a) **TY5** and (b) **AY5** in NaOH-MeOH-H_2O 50% v/v solutions.....134

3.27 Hysteresis profile for Sensors (a) **TY5** and (b) **AY5** in NaOH-EtOH-H_2O 50% v/v solutions.....135

3.28 Hysteresis profile for Sensors (a) **TY5** and (b) **AY5** in NaOH-i-PrOH-H_2O 50% v/v solutions.....136

3.29 Durability of Sensors (a) **TY6** and (b) **AY6** in 2.00 M NaOH-MeOH-H_2O 50% (v/v) solutions.....138

3.30 Durability of Sensors (a) **TY7** and (b) **AY7** in 2.00 M NaOH-EtOH-H_2O 50% (v/v) solutions.....139

3.31 Durability of Sensors (a) **TY8** and (b) **AY8** in 0.50 M NaOH-i-PrOH-H_2O 50% (v/v) solutions.....140

4.1 Acid and alkaline error for selected glass electrodes at 25

°C.....145

4.2 Sensors (a) **BCG1**, (b) **BCP1**, and (c) **NR1** in HCl-LiCl-H_2O solutions.....153

4.3 Sensors (a) **BCP2** and (b) **NR2** in HCl-$CaCl_2$-H_2O solutions.....154

4.4 Sensors (a) **BCG3**, (b) **NR3**, and (c) **BCP3** in HCl-$AlCl_3$-H_2O solutions.....155

4.5 Sensors (a) **BCG1**, (b) **BCP1**, and (c) **NR1** in HCl-LiCl-H_2O solutions.....156

4.6 Sensors (a) **BCP2** and (b) **NR2** in HCl-$CaCl_2$-H_2O solutions.....157

4.7 Sensors (a) **BCG3**, (b) **NR3**, and (c) **BCP3** in HCl-$AlCl_3$-H_2O solutions.....158

4.8 Calibration plots for Sensors (a) **BCG1**, (b) **BCP1**, and (c) **NR1** in salt-free HCl solutions.....160

4.9 Calibration plots for Sensors (a) **BCP2** and (b) **NR2** in salt-free HCl solutions.....161

4.10 Calibration plots for Sensors (a) **BCG3**, (b) **BCP3**, and (c) **NR3** in salt-free HCl solutions.....162

4.11 Plot of $\left(dA^o/dC_{acid}\right)_{C_{salt}=0}$ vs. $\left(\partial A/\partial C_{salt}\right)_{C_{acid}}$ in HCl-LiCl-H_2O solutions: Sensors (a) **BCG1**, (b) **BCP1**, (c) **NR1** (unit: $mol^{-1}.L$).....163

4.12 Plot of $\left(dA^o/dC_{acid}\right)_{C_{salt}=0}$ vs. $\left(\partial A/\partial C_{salt}\right)_{C_{acid}}$ in HCl-$CaCl_2$-H_2O

solutions: Sensors (a) **BCP2** (b) **NR2**, (unit: $mol^{-1}.L$).....164

4.13 Plots of $\left(dA^{0}/dC_{acid}\right)_{C_{salt}=0}$ vs. $\left(\partial A/\partial C_{salt}\right)_{C_{acid}}$ in HCl-$AlCl_3$-H_2O solutions: Sensors (a) **BCG3**, (b) **BCP3**, (c) **NR3** (unit: $mol^{-1}.L$).....165

4.14 Typical representation of the plots of computed (C_{salt}, C_{acid}) pairs for given *A* readings from Sensors **BCP1** and **BCG1** in a HCl-LiCl-H_2O solution.....170

4.15 Errors in C_{HCl} measurement in HCl-LiCl-H_2O solutions using sensors (a) **BCP1**, (b) **BCG1**, (c) **NR1** without correction.....171

4.16 Errors in C_{HCl} in HCl-$CaCl_2$-H_2O solutions using Sensors (a) **BCP2** And (b) **NR2** before correction.....172

4.17 Errors in C_{HCl} in HCl-$AlCl_3$-H_2O solutions using Sensors (a) **NR3** and (b) **BCP3** *before* correction.....173

4.18 Errors in C_{HCl} after corrections were made for the presence of LiCl in HCl-LiCl-H_2O solutions using combinations of Sensors **BCP1**, **BCG1**, and **NR1**.....174

4.19 Errors in C_{HCl} after corrections were made for the presence of $CaCl_2$ in HCl-$CaCl_2$-H_2O solutions using Sensors **BCP2** and **NR2**.....175

4.20 Errors in C_{HCl} after corrections were made for the presence of AlCl3 in HCl-$AlCl_3$-H_2O solutions using Sensors **BCP3** and **NR3**.....176

4.21 Validation plots of predicted vs. actual C_{salt} ($g.L^{-1}$) in HCl-LiCl-H_2O

solutions.....177

4.22 Validation plots of predicted vs. actual C_{salt} ($g.L^{-1}$) in HCl-$CaCl_2$-H_2O solutions.....178

4.23 Validation plots of predicted vs. actual C_{salt} ($g.L^{-1}$) in HCl-$AlCl_3$-H_2O solutions.....179

5.1 The acid-base equilibrium of (a) Bromocresol Purple and (b) Bromocresol Green.....195

5.2 The optical spectrum of Sensor **BCP4** in aqueous HCl solutions.....196

5.3 Determination of K_{a_1} for Bromocresol Purple in solution by (a) Method 1 and (b) Method 2.....198

5.4 Distribution curves for the first ionization of Sensor **BCP4** encapsulated in a sol-gel matrix.....201

5.5 The optical spectrum of Sensor **BCG4** in aqueous HCl solutions.....203

5.6 Distribution curves for the first ionization of Sensor **BCG4**. 204

5.7 Distribution curves for the first ionization of a CTAB free-BCG Sensor **BCG5**.....206

5.8 The acid-base equilibrium of NR.....208

5.9 Typical spectra of Sensor **NR4** in HCl solutions.....209

5.10 Distribution curves for the first ionization of Sensor **NR4**. 211

5.11 The acid-base equilibrium of FG.....213

5.12 The optical spectrum of Sensor **FG1** in aqueous HCl solution.....214

5.13 Distribution curves for the first ionization of Sensor **FG1** encapsulated in a sol-gel matrix.....216

5.14 The optical spectrum of Sensor **BCPBCG1** in aqueous HCl solutions.....218

5.15 The optical spectrum of Sensor **BCPFG1** in aqueous HCl solutions.....219

5.16 The optical spectrum of Sensor **BCGFG1** in aqueous HCl solutions.....220

5.17 Deconvoluted plots of A vs. C_{HCl} at (a) 534 nm and (b) 564 nm for each transducing component using the cocktail Sensor **BCPBCG1**.....223

5.18 Deconvoluted spectra for (a) BCP and (b) BCG in cocktail Sensor **BCPBCG1** in HCl-$CaCl_2$-H_2O solutions.....225

5.19 Plot of $\left(dA^0/dC_{acid}\right)_{C_{salt}=0}$ vs. $\left(\partial A/\partial C_{salt}\right)_{C_{acid}}$ in HCl-$CaCl_2$-H_2O solutions for (a) BCP and (b) BCG in the cocktail Sensor **BCPBCG1**.....226

5.20 Comparison of errors in C_{acid} measurements before and after the corrections for (a) 5.00, (b) 7.00, and (c) 9.00 M HCl in HCl-$CaCl_2$-H_2O solutions.....228

5.21 C_{salt} predictions via the dual-transducer approach; (a) BCP and (b) BCG components of Sensor **BCPBCG1**.....229

NOMENCLATURE AND ABBREVIATIONS

A	absorbance
A_T	absorbance total
a	activity
AY	Alizarin Yellow
Å	angstrom
BCG	Bromocresol Green
BCP	Bromocresol Purple
BET	Brunauer-Emmett-Teller
c	speed of light
cm^3	cubic centimeter
C_{acid}	concentration of acid
C_{base}	concentration of base
$C_{alcohol}$	concentration of alcohol
C_{salt}	concentration of salt
C_W	concentration of water
CCD	charged coupled device
CTAB	cetyl trimethyl ammonium bromide
d	density
DFT-LDA	density functional theory in the local density approximation
DMF	dimethylformamide

E_b	binding energy
eV	electron volt
ESCA	electron spectroscopy for chemical analysis
EtOH	ethanol
FG	Fast Green FCF
f	force constant
FIA	flow injection analysis
FT-IR	Fourier transform-infrared
g	gram
*H_*	Hammett acidity function
i-PrOH	iso-propanol
IR	infrared
l	angular mementum
ln	natural logarithm
M	molar
MAS	magic angle spinning
MeOH	methanol
MHz	mega-Hertz
MICSPOMS	metal island coated swelling polymer over a mirror system
mm	millimeter
MW	molecular weight
ε	molar absorptivity coefficient (extinction coefficient)

n	hydration number
n-BuOH	normal butanol
NIRS	near infrared spectroscopy
nm	nanometer
NR	Neutral Red
ppm	parts per million
Q	designation for the number of –OSi groups
R^2	correlation factor
RPM	revolutions per minute
s	second
SEM	scanning electron microscopy
SSNMR	solid-state nuclear magnetic resonance
TEOS	tetramethyl orthosilicate, $Si(OMe)_4$
TMOS	tetraethyl orthosilicate, $Si(OEt)_4$
TY	Thiazole Yellow
V	correction term
v	frequency
v/v%	percentage of solute volume divided by solution volume
λ	wavelength
XPS	X-ray photoelectron spectroscopy
γ	activity coefficient
μs	microsecond
∂	partial derivative

CHAPTER 1

Introduction

1.1 Measurement of *p*H in *Mild* Conditions

There exist a variety of techniques for the determination of *p*H between 2 and 12: determination that is based upon conductive polymers, micron-submicron fiber-optic sensors, sensors based upon imaging fibers, nanosphere sensors, or microparticle sensors, to name a few.[1] However, electrochemical sensors are the most accurate and reliable amongst these techniques. Advantages of electrochemical sensors include:[2] (a) high sensitivity; (b) large dynamic range; (c) compactness; (d) small power requirements; (e) good performance in electrolyte sensing; (f) activity measurements instead of concentration. Some disadvantages are:[2] (a) drifts caused by liquid-liquid-junction potentials and sensor component leaching; (b) sensitivities due to electric fields, small surface potentials, and light; (c) very poor performance at extreme *p*H (*p*H <2 or >12); (d) remote sensing difficulties; (e) limited specificity.

The H^+ ion activity of a solution is usually reported in terms of its *p*H. However, the activity of a single ion cannot be determined, and thus *p*H meters are calibrated with buffer solutions for which the *p*H has already been determined by using extended Debye-Huckel theory.[3] The *p*H can be measured using a calomel electrode that is connected to a hydrogen electrode through a salt

bridge.[4]

Usually, *p*H is measured by a glass electrode. A glass electrode consists of a reversible calomel or Ag-AgCl electrode in a solution of constant *p*H. This setup is enclosed inside a thin membrane that is inside a special glass (Figure 1.1). The reversible electrode is immersed in a solution to be studied along with a reference calomel electrode.[4]

The potential of a glass electrode varies with the activity of the H^+ ions in the same fashion as the hydrogen electrode (0.0591 V/*p*H unit at 25 ^oC). An electronic voltmeter is used to measure the potential of the cell because of the high resistivity of the glass membrane. A typical pH meter has a standard deviation of ± 0.01 *p*H units.[4]

1.2 Measurement of *p*H in *Extreme* Conditions

Electrochemical sensors are based upon a direct relationship with the analyte activity. Optical sensors are based upon functions between absorbance and analyte concentration and optical parameters.[5] However, in more concentrated solutions ($[H^+]$ or $[OH^-] > 0.01$ M), optical sensors are far more accurate than electrochemical sensors.[5] In these more concentrated systems, electrochemical sensors experience a substantial error. There are several sources contributing to the error: (a) A *p*H electrode has a non-linear response to H^+ concentrations since the activity of the solution changes at a faster rate than the concentration in strongly acidic or alkaline media. Below *p*H 1 or above *p*H 13, solutions appear to be more "acidic" or "basic" than their concentrations

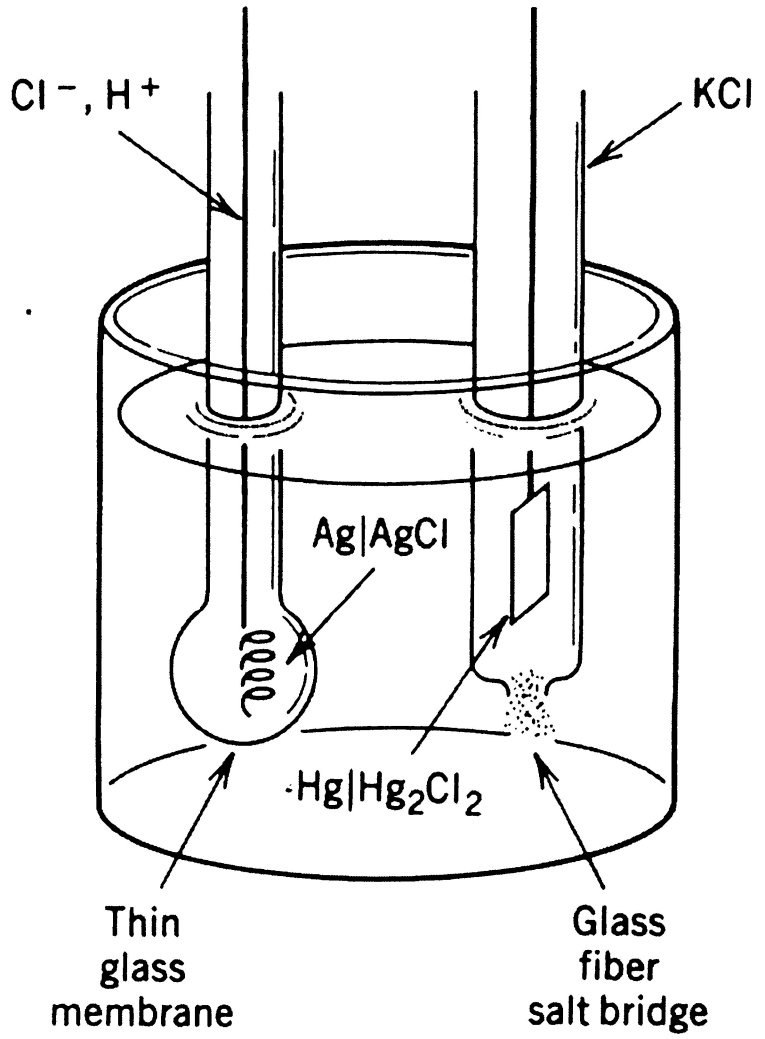

Figure 1.1. Schematic representation of the glass and calomel electrodes for *p*H meters. (Adapted from Alberty, R. A.; Silbey, R. J. *Physical Chemistry*; John Wiley & Sons: New York, 1997, p 245.)

would suggest. This effect results in large positive errors at low or high *p*H. (b) A *alkalinity* or *acidity error* also occurs in highly alkaline or acidic solutions.[6] The *alkalinity error* can be correlated to the activity of Na^+ ions becoming large when compared to the activity of H^+ ions. This results in a negative error (the measured *p*H value is lower than the true value) because the electrode is experiencing a partial response to the Na^+ ions as the *p*H is changing. The response of the electrode is falling below the ideal hydrogen electrode response.[6] In the case of the *acidity error* at low *p*H, a resultant positive error is observed by *p*H probes.[6] (c) Silicate-based glass electrode dissolves in the highly alkaline solution. The positive charge on silicon atoms in SiO_2 makes it susceptible to attack by nucleophilic OH^-, thus forming the salt of the glass.[7] This process not only erodes the glass electrode, but also alters the exchange equilibrium between the H^+ ions on the glass surface and the cations in the solution.[8] Large errors thus occur with electrochemical sensors at high *p*H.

There are several other methods available for measuring *p*H in concentrated strong alkaline solutions besides electrochemical techniques. These methods include near infrared spectroscopy (NIRS), flow injection analysis (FIA), on-line titration, and measurement of refractive index or density. All of these methods have certain limitations. NIRS suffers from severe spectral overlap and low resolution. FIA requires extensive sampling of solutions. On-line titrations are costly, time-consuming, complex, and do not allow for continuous monitoring of a system. Measurements of refractive index and density are only accurate for clean caustic solutions at a constant temperature.[9]

1.3 Optical *p*H Sensing

Optical sensors are known to have several advantages according to Wolfbeis:[2] (a) They generally do not require a reference cell; (b) They may be miniaturized through the used of fiber-optics, and designed for remote sensing; (c) Multiple analysis for different analyte detection may be designed with optical sensors; (d) non-destructive measurements; (e) fiber optics can transmit much more information than electrical leads. Some general disadvantages according to Wolfbeis include:[2] (a) ambient light interferences; (b) leaching of transducer for transducer-doped sensors; (c) limited dynamic range in some cases; (d) background absorptions, fluorescence, and Raman scattering; (e) commercial accessories of the optical system are not optimal yet; (f) in indicator phase sensors of *p*H and electrolytes, it is the concentration of the dye that is measured rather than the analyte itself.

A chemical sensor is a device that can periodically and reversibly give information about the environment. Mechanical, electrochemical, and optical sensors are the most common. For example, a *p*H electrode is an electrochemical sensor. An ideal sensor should have direct contact with a sample and record a reading within a few seconds. Continuous sensing of chemical analytes is more efficient than off-line sampling. Therefore, there is a need for "real-time" analysis.[10]

Optical sensors and electrochemical sensors make up the two largest classes of chemical sensors used today. Speed of information acquisition is becoming very important today in process control. Optical sensors open new

avenues of sensing capabilities by using conduits such as fibers, waveguides, mid-range IR, integrated optics, quantum cascade lasers, and new non-linear optical elements.[11] Optical sensors have vast potential in biomedical and environmental fields.

Optical sensors consist of several distinct components: light source, a monochromator, a light coupler, a fiber or fiber bundle, an analyte sensing coating, a transducer, a filter if necessary, an optical detection unit, an amplifier, a data acquisition or processing unit, and a data output or a computer.[10] Figures 1.2 and 1.3 give schematics of the optical sensor system and flow cell, respectively, used in the current research.[12] The visible spectra were recorded using a single array portable spectrometer (Rainbow Meter System) by American Holographic Inc. (Fitchburg, MA 01420). The dual-beam spectrometer was composed of a single diode array of 128 channels. The spectrometer consisted of an opto-electronic device and a standard RS-232 host interface box. The light source was a xenon flash lamp (EG&G LS-1102-5 Flash-Pac). The maximum output of energy was 360 mJ per flash at a maximum flash rate of 55 Hz. Bifurcated fiber-optic bundles were used to transmit the light. Indicator purity was considered appropriate by thin layer chromatography. The transducer is composed of encapsulated *p*H indicators within SiO_2 (for acid sensors) or a $(Zr_xSi_yO_{2(x+y)})$-polymer composite.

The optical sensing here is based upon the Beer-Lambert Law: the absorption of light is directly proportional to the concentration of the absorbing species.[13] Departures from the Beer-Lambert Law occur at high concentrations

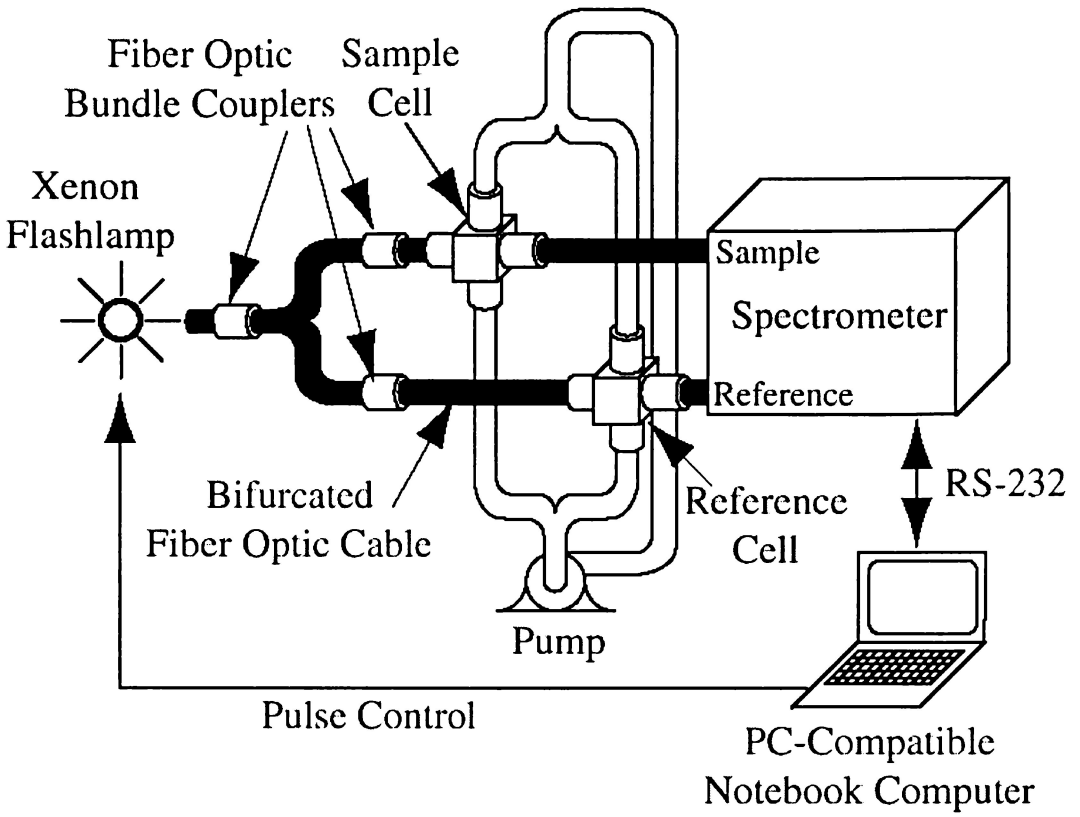

Figure 1.2. A schematic of the optical flow system.

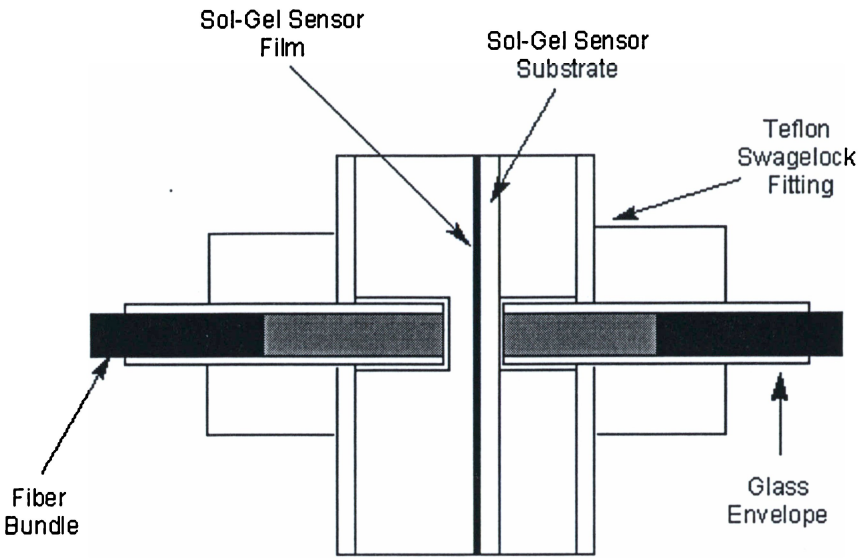

Figure 1.3. A schematic of the optical flow cell.

(>0.01 M) because the average distances between ions in the absorbing species is small. Hypochromic (decrease in absorption intensity) and hyperchromic (increase in absorption intensity) effects in the absorbing species are often observed as a consequence.[13]

The absorbance of the organic indicator molecules encapsulated in the sensor films gives the optical sensor signal. Usually acidic and basic forms of the indicator are in equilibrium. The analyte changes the equilibrium, and thus the change is observed in the visible spectroscopy. In other words, the analyte concentration is inferred indirectly from the chemical changes in the organic indicator molecules.

1.3.1 Optical Sensors for Highly Alkaline Aqueous Media. Due to the corrosive nature of concentrated hydroxide (*p*H > 11), there exists a need for accurate, reliable sensors. Today, few sensors are available that can measure the concentration of NaOH between 0.1 to 10 M without limitations. Avnir and coworkers[14] first reported using sensors composed of encapsulated *p*H indicators into sol-gel glass for *p*H sensing. The *p*H sensors developed by Avnir were for less stringent alkaline media.[14]

Optical base sensors have been reported based upon immobilization of *p*H indicators on cellulose thins film, which are attached to a polyester support. However, these types of sensors are limited to *p*H 13.[15] There have been other cellulose based sensors, but all suffer degradation in strong alkali media.[16] Conductivity sensors that are durable in strong alkali media have been

constructed but are often nonselective.[17]

Recently, our group[18,19] developed optical base sensors for basicity determination in highly alkaline solutions. These sensors are based on encapsulation of a *p*H sensitive dye into mixed ($Zr_xSi_yO_{2(x+y)}$)-polymer composite thin film by standard sol-gel procedures.[19] Although SiO_2 is susceptible to nucleophilic attach by OH^- anions, the mixed oxide ($Zr_xSi_yO_{2(x+y)}$) sol-gels were found stable at high *p*H, as observed in other cases.[7] Although the hydration of ZrO_2 is energetically favorable, the predominance of ZrO^{2+}, Zr^{4+}, and $HZrO_3^-$ only occurs below *p*H 0 or above *p*H 17, thus limiting the possibility of nucleophilic attack.[7]

Other factors such as indicator selection and composite support were explored and found important in forming a durable sensor that was fast and reproducible.[19] Alizarin Yellow, Thiazole Yellow GGM, Calcion, Arsenazo III, Azoviolet, and Chromotrope 2B were selected for their stablility and response in concentrated alkaline solution.[19] The presence of polymers such as Nafion™ and PSMMA in the ($Zr_xSi_yO_{2(x+y)}$)-polymer composite thin films were found to increase the physical integrity of the films.[19]

These studies dealt with hydroxide determination in 0.1-11 M aqueous alkaline media.[19] Investigation of these sensors in organic solvents was not performed.[19] Increasing the base concentration in aqueous systems is one method to give strongly basic media. Another method is to prepare alkaline solutions in mixed organic-water media.[20]

1.3.2 Optical Sensors for Highly Alkaline Ternary ($NaOH$-ROH-H_2O) Media.

Ternary NaOH-organic-H_2O systems are widely used.[21] The presence of an organic solvent such as alcohol significantly changes the ionic strength of the solution, and thus alkalinity. The activity of water is progressively reduced as a solvent of a lower dielectric constant replaces the water at fixed hydroxide concentration. The activity of OH^- rapidly increases as the organic solvent replaces H_2O.[22] Determination of alkalinity in such ternary systems by optical sol-gel sensors, to our knowledge, has not been addressed. This is the topic of Chapter 2 in this dissertation.

1.3.3 Optical Sensors for Highly Acidic Aqueous Media. Concentrated acids such as HCl, HNO_3, and H_2SO_4 are consumed in large volumes in global chemical manufacture.[23] Classical off-line titrations continue to be the method of choice for concentrated acid determination, despite their limitations such as being labor intensive, time-consuming, expensive, and non-continuous.[24] Some current alternative methods include: pre-dilution flow injection analysis (FIA), optical sensors based on organic polymers and polymers doped with indicators, and sensors with ion exchange membranes.[25-29]

Recently in our group,[12,18,30] optical acid sol-gel sensors for the determination of concentrated strong acid were developed. The sensors were based upon indicator molecules doped within a porous SiO_2 substrate. This approach was found to be fast, highly sensitive, fully reversible, and durable in concentrated strong acids.

1.3.4 Optical Sensors for Highly Acidic Ternary (HCl-Salt-H_2O) Media.

Concentrated acids such as HCl are often used in the presence of other chemicals such as salts. Salts contribute to the total ionic strength of the acid system.[4] The ionic strength contributions of inorganic salts can produce significant errors if not taken into account.[18,31,32] It has been long proposed that salts remove water from the bulk system via solvation, thus reducing the activity of the water.[33]

Some current studies based upon the contribution of a salt to optical sensor response in acidic media include: a dual *p*H fluorescent indicator system used to study pK_a and ionic strength,[34] a method based upon covalent immobilization of dyes onto porous glass substrates with distinct surface chemistries in order to evaluate *p*H and ionic strength,[35] a sensor array using a multi-coated sensor surface integrated with a CCD (charge coupled device) used to examine *p*H and other cationic species,[36] and ionic strength measurements based on an optical reflection interference filter.[37]

Recently in our group,[18] a dual-transducer approach based upon a novel linear relationship was established in order to obtain both C_{acid} and C_{salt} in salt-containing concentrated strong acids. This study involved only one salt, $CaCl_2$, at one C_{acid}, 5 M. We have extended this approach to cover LiCl, $CaCl_2$ and $AlCl_3$ at multiple acid concentrations (e.g., 2 to 9 M). This is the topic of Chapter 4 of this dissertation.

1.4 Basic Sol-Gel Process

1.4.1 History of Sol-Gel Chemistry. The interest in sol-gel chemistry began as early as the mid-1800's by Ebelman and Graham's studies of silica glass. They observed that SiO_2 was produced by the acid catalyzed reaction of tetraethyl orthosilicate $Si(OEt)_4$ (TEOS). As sol-gel drying time was ca. one year to prevent fracturing of the sol-gel, little interest was focused on this new area of chemistry.[38] In the 1930's interest in sol-gel science resurged. By the late 1930's, the widely accepted network structure of the silica gels was that of a polymeric skeleton of silicic acid enclosing a continuous liquid phase.[39]

By the 1950's and 1960's, Roy and coworkers envisioned an enormous potential for sol-gel science in the years to come. Roy was able to synthesize a variety of novel homogenous ceramic oxide composites involving Al, Si, Ti, Zr, and other metals. This was achieved by using a standard sol-gel method.[40] However, an understanding of the mechanisms of reactions and gelation was not well established at the time. More sophisticated work was conducted in the nuclear fuel industry that was not published until a later time. The goal of the research in this industry was to prepare small spheres or radioactive oxides. These spheres could then be packed into fuel cells for nuclear reactors.[39] The advantages of the new technique would eliminate dangerous dust and allow for the formation of spheres. Dispersing aqueous sol into hydrophobic organic solutions thus producing droplets that subsequently gelled to form the spheres.

The ceramics industry began to show more interest in sol-gel science by early 1970s. At the time, several ceramic companies produced ceramic fibers

from organosilicon precursors.[39] However, the most noted advances in sol-gel chemistry was accomplished by Yoldas, Yamane and coworkers.[39] They were able to create sol-gel monoliths by carefully drying the gels. The appeal of forming solid structures at room temperature was an attractive appeal to many scientists around the world. Sol-gel technology precedes the science in many regards. It was only in the last twenty years that researchers were able to more fully understand the chemistry behind homogenous multicomponent ceramics derived from alkoxide precursors.[39]

1.4.2 Sol-Gel Processing. The production of a sol-gel can be envisioned through five basic steps: mixing, casting, gelation, aging, and drying.[41] Sol-gel glass offers many advantages in sensing applications: compatibility with many chemical reagents, stability (mechanical, photochemical, chemical, and thermal), optical transparency, low temperature reactions under mild conditions, long shelf life of products (through encapsulation techniques), and various geometric forms of casting.[42]

An alkoxide precursor, in an appropriate solvent needed for homogenization, is hydrolyzed by mixing with water. The newly formed tetrahedral silanol molecules interact through condensation reactions that ultimately result in a cross-linked inorganic matrix. Figure 1.4 illustrates the bimolecular nucleophilic displacement reactions (S_N2) and condensation reactions in standard sol-gel production. The rate of hydrolysis and condensation is dependent upon several variables that will be discussed later.

Hydrolysis

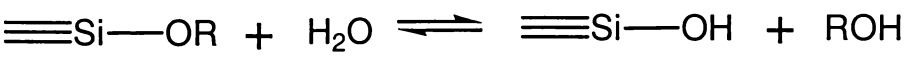

Condensation

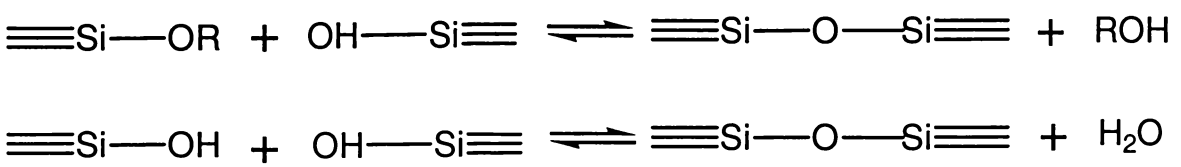

Figure 1.4. A summary of the basic sol-gel reactions.

The alcohol and water that are produced remain in the pores of the network. When enough Si-O-Si bonds are formed, a colloidal particle or sol is produced. The relative size of the sol is *p*H dependent.

Due to the relatively low reactivity of silicon alkoxide precursors, a catalyst is often employed to enhance the hydrolysis rate. In an acidic medium, protonation of the alkoxide ligand results in a partial positive charge on the ligand. The central Si atom then withdraws electron density from the ligand, which renders the Si atom for nucleophilic attack by H_2O. Alcohol then leaves the Si atom. After regeneration of the acid, a Si-OH group is left behind. In base-catalyzed hydrolysis, the central Si atom undergoes a direct nucleophilic attack by OH^-. Si-OH groups and RO^- anions are then produced.[39]

Condensation is the second phase of the sol-gel reaction. The condensation step is two-fold, and involves silanol-ester and silanol-silanol condensation. The extent of hydrolysis of the alkoxide precursors dictates which type of condensation occurs predominately.[39] If hydrolysis is complete, a OH^- group reacts with another OH^- group of a different precursor molecule. In the case of incomplete hydrolysis, a OH^- group reacts with an alkoxide group of a different precursor molecule. In both cases Si-O-Si linkages are formed. As the interconnection of the sol increases, the viscosity and density also increases. In the sol-gel processes, the formation of inorganic particles is much different than the formation of organic polymers. The latter evolves by first forming dimers, trimers, and/or linear chains that eventually form a gel state. Inorganic particles are formed through the aggregation of small colloids or simply by the addition of

low molecular weight polymers to larger ones.[43]

As mentioned earlier, the rate of hydrolysis and condensation is dependent upon many variables but are mostly influenced by *p*H and the moles of water/moles of alkoxide (*R*-ratio).[39]

At high *p*H both hydrolysis and condensation reactions of the Si species are accelerated. A continuous source of Si species of low molecular weight induces particle ripening due to the increased dissolution of the silica particles. Under these conditions, deprotonation and surface charges are increased, which in turn postpones aggregation and gelation. High *p*H thus yields gels that are composed of large building blocks with an increased void fraction and specific-area.[43]

At low *p*H silica particle dissolution is minimum. Gelation is obstructed by the positively charged protonated surface. Acid catalysis increases hydrolysis and condensation rates. Polycondensation yields dense, low surface-area gels.[43]

Large *R*-ratios increase the rate of hydrolysis and decreases the rate of aggregation. The porosity and specific surface area are thus enhanced. When the *R*-ratio approaches four [the stoichiometric ratio of $H_2O/Si(OR)_4$], however, the rate of condensation controls the polymerization. At this stage the rate of hydrolysis is slowed and ripening becomes minimum.[43] A *R*-ratio of about two is generally needed for complete hydrolysis.[44] Low *R*-ratios tend to produce chain-like structures that have a large excess of organic residue. The organic residue originate from the unhydrolyzed alkoxy groups.[43]

Combined, the *p*H and *R*-value of a sol-gel system can drastically determine the physical nature of the final gel. At high *p*H and high *R*-values, the rates of the condensation reactions are accelerated relative to the hydrolysis reaction rate. This environment produces loose gels with large average pore diameters.[44] At low *p*H and low *R*-values, the hydrolysis reaction is accelerated relative to the condensation reaction rates. Since the hydrolysis concludes at an earlier stage, condensation between silanol groups can take place to give a densely compacted, entangled matrix of linear chains. The resulting sol-gel is dense with small pores.[44]

Other factors such as the amount of solvent, addition of cross-linking agent, pressure, addition of surfactants, size of alkoxide precursor, and temperature, to a lesser degree, may influence the final product.[43] Excess solvent tends to decrease aggregation thus increasing porosity. A surfactant can reduce surface tension, increase the specific surface area, function in fracture prevention, and stabilize the smaller particles. Bulkier alkoxide groups tend to slow reaction rates. Cross-linking agents can increase the specific area of gels. High temperature increases solubility of silicon oligomers, porosity, and specific surface area.[43]

Emphasis has been placed on mixing and gelation but other key steps are important in sol-gel preparation. Castings to form, e.g., a film, monolith, powders, or fibers are methods to create the shape of a sol-gel product. The type of casting that is implemented drastically affects variables such as diffusion time and capacity. After the gel is formed in a specific geometry, aging and

drying are performed. During the aging process, the gel is placed in a liquid and allowed to sit for several days. Aging ensures complete polycondensation and increases the strength of the gel. Upon complete polycondensation, gels are more crack-resistant. During drying, the gel is removed from the liquid and allowed to aerate. Upon drying, solvents such as water and alcohol are removed from the inner channels of the gel. If special care is not taken during the drying process, gels can suffer monumental cracking due to the large capillary stresses that are produced. Addition of surfactants, which decrease the liquid surface energy, can minimize cracking. The last step in the sol-gel process is dehydration, which involves the removal of surface silanol groups. After dehydration, a chemically stable, ultraporous solid should remain, and is ready for analytical evaluation.[41]

1.4.3 Immobilization Methods. Adsorption, grafting through covalent attachment, and encapsulation are the three most common techniques used for immobilization of sensing agents onto solid substrates to give sensors. Each technique has distinct advantages and disadvantages. In general, a good immobilization technique should obey the following: (a) be simple and fast; (b) be nonspecific to the type of reagent being immobilized; (c) produce stable products (minimum or no leaching); and (d) allow immobilized reagents to retain their initial chemical activities.[42,45]

The adsorption method is the simplest to use. This method utilizes a support that is coated with a sensing agent. The sensing agent adsorbs onto the

substrate. This method may have leaching problems produced by the sensing agent leaking out of the support. The net result is short life-time and lack of reproducibility as a sensor.[42]

In the grafting process, reagents are strongly anchored to a substrate through covalent bonds. Hydroxyl groups located on the periphery of the silica substrate provide sites for such covalent attachment. Products tend to be very stable (long shelf life) and reproducible as a sensor. However, the grafting process may be tedious and time consuming due to chemical reaction specificities.[42,45] In some cases, sensing response kinetics is increased due to a reduction in the degree of freedom of the molecules arising from the formation of bonds.[42,45]

Encapsulation, the method in the current work to prepare optical sensors, involves physical entrapment of a reagent (in our case, organic, *p*H sensitive indicator molecules) inside a porous silica substrate. This method is simple and non-discriminative. The sensors thus prepared in the current work give fast and reproducible responses.[42] However, leaching of the encapsulated reagent is unavoidable, and porosity control is thus important to minimize the leaching. In this case, the sol-gel sensors need to be conditioned to remove any reagent molecules that were not fully entrapped before their use as sensors. Encapsulation is the more recent technique.[42] Avnir[46] and Sadik[47] are amongst several researchers actively studying doped sol-gel *p*H sensors.

1.4.4 Developments and Applications of Sol-Gel Sensors. There have been many applications of sol-gel based sensors in environment, medicine, and industry. Environmental waste monitoring is a very important application of sol-gel sensors.[42] There have been several examples of sol-gel sensors designed for waste monitoring. Focus has been on the development of sensors to measure and monitor concentrations of metal ions such as Sr^{2+}, Cu^{2+}, Fe^{2+}, Al^{3+}, Co^{2+}, Ni^{2+}, Pb^{2+}, Zn^{2+}, and Cd^{2+}, radioactive waste, and *p*H in groundwater and soil.[1,14,42,48-52]

Intracellar *p*H measurement studies have been conducted using submicron, and nanosphere optical sol-gel derived sensors. For example, imaging fiber-optic *p*H sensors were used to yield images of the fibroblast cells in mice and to explore fertilization of sea urchin eggs.[42,53-57]

In the medical field, continuous monitoring and testing of *p*H, glucose, proteins, enzymes, O_2, and CO_2 are very important. There was much interest since the 1990's in fiber-optic sensors for such applications.[10,42,58-61]

Monitoring industrial processes is of importance. In particular, the measurement of acidity and alkalinity is of intense current interest, as discussed earlier. Monitoring of NH_3, CO, NO and CO_2 by gaseous sol-gel sensors has been actively studied as well.[42,61-63]

1.4.5 Preparation of the Sensor Substrate and Spin Coating Techniques. A microscope slide (Fisher Scientific) was either coated first before being cut into 25 mm x 12 mm (to match the Teflon cell size in the spectrometer[12]) platforms or

was cut first and then coated. No noticeable difference in the sensor performance was observed. The slide was then roughened by carborandum, an abrasive, to break Si-O-Si bonds and placed in a concentrated KOH-i-PrOH bath to insure Maximum surface bond breakage. The glass slide was then washed vigorously with distilled water and placed in 1 M HCl for about 30 min to insure maximum Si-OH formation on the surface of the slide. Finally the slide was washed sequentially and thoroughly with water, scrubbed with a micro soap solution, water, hexane, water, i-PrOH, water, and distilled water at high flow. The slide was then air dried under a high air flow and left to the open air for 1 to 2 days.

The glass slide could then be fastened to a spin coater. The solution was then dripped onto the roughened surface of the glass slide and spun at a given RPM-setting, depending upon the viscosity of the sol solution (Figure 1.5). The spin coater consisted of a computer fan that was fastened to a solid support. A variable voltage supply was used to adjust the amount of current that was to be delivered to the spin coater. The blades of the computer fan were trimmed to the core to minimize air convection. A strobe light was used to calibrate the spin coater to match the voltage setting to the corresponding RPM.

The sensor films were subsequently cured and conditioned before use.

1.5 Characterization of Sol-Gel Sensor Materials Used in the Current Study

The following instrumental techniques were used: scanning electron microscopy (SEM), profilometry, Brunauer-Emmett-Teller (BET) gas adsorption

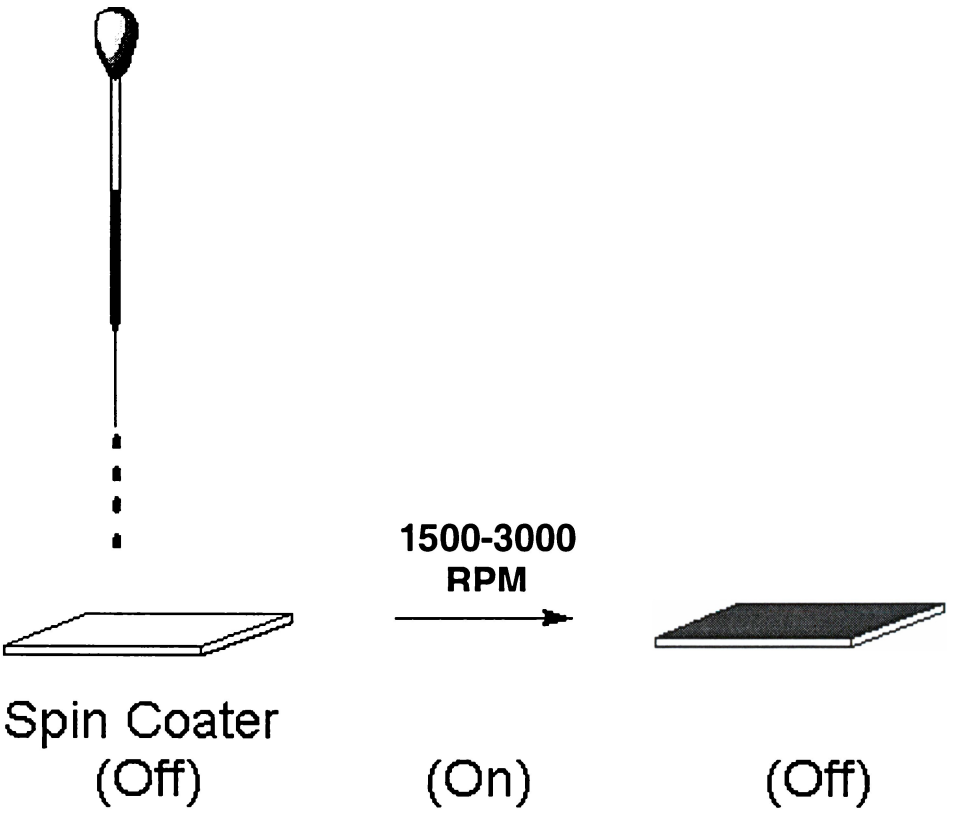

Figure 1.5. A representation of the spin coating process.

analysis, infrared spectroscopy (IR), ^{29}Si solid-state nuclear magnetic resonance spectroscopy (SSNMR), and X-ray photoelectron spectroscopy [XPS, also known as Electron Spectroscopy for Chemical Analysis (ESCA)]. The features of these techniques and their uses in the current study are summarized.

1.5.1 SEM. Electrons from a field emission cathode or thermionic are accelerated between a cathode and anode producing an electron beam (probe). A series of lenses are used to increase or decrease the diameter and current of the electron probe. Changing excitations in the first condenser lenses and the aperture-limiting diaphragm can vary electron-probe current, aperture, and size. High resolution is achieved by using an aperture of an order of ten milliradians. The depth of focus is increased by slightly lowering the aperture.[64]

A deflection coil scans the electron probe across the specimen in synchronism with the electron beam produced from a separate cathode-ray tube. The image results from the modulation of the cathode-ray tube intensity by one of the signals recorded. Either increasing or decreasing the scan-coil current controls magnification while keeping the image size on the cathode-ray tube constant.[64] In general, the reflection of electrons from the surface of a sample produces the image. The ratio of the final image display and the field scanned on the specimen results in the magnification. For example, if an electron probe scans an area of 1 mm^2 and the display screen reads 100 mm^2, the magnification is 100x. A typical SEM has a working range of 20 to 100,000x.[65]

SEM allows a wide variety of specimens examined through electron-

specimen interactions to furnish qualitative and quantitative data. Straightforward sample preparations, excellent contrast, and large depth of focus contribute to the widespread success of SEM. SEM is capable of producing high-resolution images at high magnification.

1.5.2 Profilometry. Profilometry is a simple technique that merely involves passing a diamond stylus over the surface of a specimen. The stylus is attached to an arm that rotates about a flexure pivot, which enables smooth and stable scanning across a surface. All aberrations are recorded by a detector and plotted. There are two baselines, film surface and substrate surface, separated by a step. The step represents the film thickness based upon the difference in the two averaged baselines. Surface profilers have the ability to measure micro-roughness up to a 1 Å resolution and thickness ranging from 100 Å to 0.3 mm.

1.5.3 BET. The total pore volume can be calculated by a series of BET equations based upon the amount of N_2 vapor that is adsorbed by a sample.[66] Furthermore, the average pore size can be estimated based upon the pore volume. The pore size distribution is determined by the pore size with respect to disbursement of pore volume. In other words, the pore size distribution indicates the range of pore sizes that make up the bulk pore volume. A sharp peak in a plot of pore volume vs average pore diameter indicates a narrow pore size distribution, and suggests that the sample is relatively uniform in regards to pore sizes. Pores have been categorized based on their average diameters: >20 Å

(microporous), 20 to 300 Å (mesoporous), and >300 Å (macroporous).[67]

Another important feature to be obtained through BET measurements is an isotherm plot. By definition an isotherm plot is the total volume adsorbed verses the relative pressure. There are six distinct types of isotherm plots (*types I-VI*). Isotherm plots are used to classify samples based upon porosity, surface area, and other surface features. Usually microporous, mesoporous, and macroporous adsorbents display *type I*, *IV*, and *II* isotherms, respectively.[68]

1.5.4 IR Spectroscopy. IR spectroscopy is based upon the vibrations of molecules. Nearly every compound has its characteristic IR spectrum. Therefore, an IR spectrum is an excellent means of "fingerprinting" a compound. Experimental spectra can be compared to reference spectra. IR spectra provide an excellent means of determining purity.

Molecular vibrational energy is the result of infrared radiation in the range of 10,000 to 100 cm^{-1}. Vibrational spectra appear as bands not lines even though the energy absorbed is quantized. The bands are the result of accompanying rotational energy changes. Vibrational and rotational bands between 4000 to 400 cm^{-1} are often used. The wavelength of absorption depends primarily upon three factors: relative masses of the atoms, force constants of the bonds, and geometric arrangement of the atoms through the Hooke's law. There are two basic types of vibrations, stretching and bending. Bending includes rocking, twisting, and torsion changes.[69]

1.5.5 ^{29}Si Solid-State NMR. The development of NMR techniques for solids has been much slower than for fluids. The immobility of molecules in the solid state has been the major obstacle in the slow development of SSNMR. Unlike fluids, dipolar couplings in solids are not averaged to zero by molecular tumbling. If not corrected broad spectra are obtained. Chemical shifts are also substantially affected. The chemical shift of a nucleus depends on the orientation of the molecule. In solids, molecular tumbling does not average out chemical shift anisotropy. Finally, it is difficult to gain a spectrum with a good signal to noise ratio because of long T_1 relaxation times. The immobility of the nucleus in the solid state is the inherent factor in all three cases.[70]

There are special techniques available to minimize the effects of immobile nuclei. Chemical anisotropy can be averaged out by a technique known as magic angle spinning (MAS). If a sample is rotated rapidly at an angle of 54.7 degrees to the magnetic field, the line broadening due to chemical shift anisotropy is eliminated. For nuclei such as ^{13}C and ^{29}Si, fast rotation can remove line broadening. In the cases of heavier elements, rotations fast enough to remove line broadening are unattainable. In these situations, each single resonance line is replaced by a central line and equally spaced spinning side bands.[70]

If the rotation rate due to MAS is greater than the corresponding line widths, averaging of dipolar couplings to zero mimics fluid molecular tumbling. In practice some dipolar coupling will remain due to its high frequency (usually greater than 50 kHz).[70]

Long T_1 relaxation time still remains an inherently associated problem in SSNMR. However, this problem can be overcome for dilute nuclei with a ½ spin by a technique know as cross-polarization. Cross-polarization is used to transfer magnetization from rich spin nuclei such as ^{1}H to dilute spin nuclei such as ^{13}C. The net result is an intensity gain in the insensitive nuclei which otherwise may not have been resolved from the baseline.[70]

If cross-polarization and MAS are used in communion, highly resolved spectra of solid compounds can be achieved. These spectra may be very helpful in the evaluation of bonding patterns.

1.5.6 XPS (ESCA). XPS is a widely used analytical technique for the investigation of chemical compositions in solid or gas samples. Solid samples are more prevalent. To perform XPS analysis, a solid surface is irradiated with monoenergetic soft X-ray or ultraviolet radiation under vacuum. The energy of the emitted electrons is measured, which reflects the bonding energy of these electrons in the sample. If the X-ray or ultraviolet radiation energy is greater than the difference between the initial electronic energy level and any higher level, the atom ejects one or more electrons. The velocities of individual electrons are determined by the differences in the initial electronic energy states and the energy of the X-ray or ultraviolet radiation used to irradiate the sample. The ejection of electrons by this type of process is known as the photoelectron effect.[71]

The bonding energies of each element are unique. In XPS, only the top

few atomic layers can be evaluated due to the small mean free path of the electrons. Peak location or separation can be used to give qualitative identification of elements in the sample, and peak integration may give quantitative information of these elements in the sample. Other spectral contours can be examined as well. A comprehensive listing of previously determined spectra of several different compounds is provided by Wagner and coworkers.[72]

A basic XPS spectrometer consists of a source of electromagnetic radiation (ultraviolet or X-ray), an electron energy analyzer, a sample holder or chamber, a high vacuum ion pump (to prevent air ionization), a detector, and a recorder. The most diverse component is the electron energy analyzer. Electrostatic and magnetic types are the two designs. In either case, the electron path in the analyzer must be shielded from the earth magnetic field. Most commercial instruments use electrostatic analyzers because they are easily shielded and are more compact than the magnetic protocols.[71]

1.6. Overview of This Dissertation

The main objectives of this dissertation are to develop dual-sensor approaches for accurate basicity and acidity determination in NaOH-alcohol-H_2O and HCl-salt-H_2O ternary systems. Cocktail sensors were explored as a means of doping more than one indicator in sol-gel thin films as a possible new approach for sensors in these ternary systems. Indicator selection (e.g., pK_a evaluation in these doped systems) and physical characteristics of the sensors were carefully evaluated. In addition, sol-gel ($Zr_xSi_yO_{2(x+y)}$)-Nafion composite

materials that are used in the current studies for basicity determination in highly alkaline solutions were extensively characterized. We are interested in an understanding as to why such mixed oxide-polymer composites are resistant to OH^- attack.

Novel dual-sensor approaches in NaOH-alcohol-H_2O ternary systems are reported in Chapter 2. If the organic solvent effects are not taken into consideration, large errors in basicity determination are observed. A novel relationship is established.

Hysteresis, reproducibility, and kinetics of our base sensors in aqueous, as well as, in NaOH-alcohol-H_2O ternary systems are evaluated and compared in Chapter 3. The effects of concentrations of alcohol and NaOH on sensor response are evaluated. In addition, ($Zr_xSi_yO_{2(x+y)}$)-Nafion composite materials used as our base sensor matrixes are fully characterized. Characterization of the sensor surface including porosity, surface area, and film thickness by BET, profilometry, and SEM is reported in Chapter 3.

In Chapter 4, a dual sensor approach for HCl-salt-H_2O is reported. The studies here follow earlier work in our group[18,19] which developed and confirmed such a dual-sensor approach for one salt ($CaCl_2$) at one C_{acid} (5 M) in HCl-$CaCl_2$-H_2O systems.[19] Chapter 4 reports an improved model for the dual-sensor approach, and demonstrates that such an approach significantly reduces errors in acidity determination. In the current work an extended range of C_{acid} (ca. 2 to 9 M) with LiCl, $CaCl_2$, and $AlCl_3$ (ca. 0 to 2 M) is probed to extend the scope of the approach and to investigate the impact of C_{salt} on the errors in C_{acid}

predictions in HCl-salt-H_2O systems.

Chapter 5 explores the cocktail sensor approach to encapsulate more than one indicator into sol-gel matrices as possible new sensors for ternary systems. The influences of sensor film composition on chemical equilibria and pK_a of the indicators encapsulated in the film were investigated.

CHAPTER 2

High-Basicity Determination in Mixed Water Alcohol Solutions by a Dual Optical Sensor Approach

2.1 Introduction

Optical sensors and their uses in multi-component systems are of intense current interest.[34-37,73-75] In the multi-component systems, the activity of the analyte and sensor response are often affected by change in ionic strength. For optical sensors that are based on indicator equilibria involving the analyte as their transducing mechanism, this effect is particularly significant. The concentrations of both the analyte and other chemicals affect ionic strength, and the sensor response to concentration of the analyte is thus often indistinguishable from those of other chemicals. An accurate measurement of each component in these multi-component systems is actively studied. Several approaches have been developed to correct ionic strength in optical sensing for the *p*H region and solutions of low-to-medium ionic strength.[34-37,73-77] We recently reported a dual-transducer approach to measure acid concentrations (2 to 9 M HCl) in salt-containing, concentrated strong acids such as MCl_x-HCl (M = Li, Ca, Al) solutions.[31] This approach was shown to reduce the error in C_{acid} from, e.g., 60% to <4%, and is based on optical sensors containing indicators doped in silica sol-gel thin films.[76,77]

Caustic soda (NaOH) is amongst the largest volume chemicals manufactured in the world.[21,23] Over a half of NaOH is primarily used for chemical production, *p*H control, neutralization, off-gas scrubbing, and catalysis,[23] and the other half of NaOH is used in paper and pulp, cleaning products, soap and detergents, petroleum, cellulosics and textiles industries.[21] In many such applications, NaOH is used in the presence of other chemicals or in aqueous-organic mixed solvents. For example, streamlines in the pulp bleaching processes, which bleach more than 50 million tons of pulp annually in the world, often consist of hydroxide, water, and alcohol.[21] During the process of cellulose digestion using kraft liquors, NaOH is often used in water-alcohol mixtures as well.[21] Basicity measurement and control are important for these processes. There exists, to our knowledge, no standard procedure to accurately measure C_{base} and $C_{alcohol}$ simultaneously in these NaOH-water-alcohol ternary systems.

We recently reported an optical base sensor system for the determination of *aqueous* concentrated strong bases ($[OH^-]$ = 1 to 10 M).[19] Individual sensors consist of a ($Zr_xSi_yO_{2(x+y)}$)-organic polymer composite and a doped high pK_a indicator, and show fast response (<5 sec), small hysteresis, and good durability (for at least one month). In the use of such sensors for NaOH determination in mixed aqueous organic solvents, we found that the ionic strength change by the organic solvent was a considerable source of analytical error that had to be addressed to give accurate concentrations of the base. This prompted us to develop a new approach to measure the concentrations of the base and the organic solvent in the mixed solvent systems. We focused on NaOH in mixed

water alcohol solutions, as they are amongst the most common alkaline ternary systems in industry.[21,23]

In the current work in NaOH-ROH-H_2O (R = Me, Et, i-Pr) mixed solvent systems, a novel linear relationship was observed between $(\partial A/\partial C_{alcohol})$ and C_{base} for high pK_a indicators encapsulated in sol-gel ($Zr_xSi_yO_{2(x+y)}$)-organic polymer composites. This relationship led to a dual transducer approach to give C_{base} and $C_{alcohol}$ with high accuracy and precision. A decomposition algorithm that is based on a combination of two different sensors is used in this dual transducer approach. These two sensors have distinct ionic strength dependencies, and the signal array is decomposed to give the base and alcohol concentrations. This novel linear relationship between $(\partial A/\partial C_{alcohol})$ and C_{base} and the dual transducer approach based on this relationship are reported here. In addition, the selection of indicators with high pK_as, a large dynamic spectral range, and chemical stability to OH^- attack and oxidation is presented.

2.2 Experimental

Visible spectra were recorded using a visible spectrometer described in Section 1.1.3.[12] Repetition scans were recorded and averaged to minimize the drift error in the instrument. Alcoholic solutions were prepared by volumetric dilution (v/v%). Hydroxide is known to adsorb a small amount of carbon dioxide from the atmosphere; therefore solutions were prepared by gravimetric dilution before each trial to ensure maximum accuracy. Hydroxide solutions were titrated with standard HCl to the phenolphthalein end point to verify their concentrations.

EtOH used for the sol-gel sensor preparation was dried by the standard procedures.[78] Thiazole Yellow GGM (TY, 40% dye content, Eastman), Alizarin Yellow R (AY, 80% dye content, Eastman), $Si(OMe)_4$ (99+%, Aldrich), $Zr(O\text{-}n\text{-}Bu)_4$ (80% wt. in 1-n-BuOH, Aldrich), Nafion (5% Nafion in an alcoholic mixture containing 5% w/w water, Aldrich), $HCONMe_2$ (DMF, 99.9+%, Aldrich), MeOH (99.9%, Fisher), EtOH (absolute, AAPER) used for making NaOH-EtOH-H_2O ternary solutions, i-PrOH (99.9%, Aldrich), HCl standard (0.25 N, LabChem. Inc.), and NaOH (99.99%, Fisher) were used as received. Data Analysis was conducted by the following programs: Matlab™ (The Math Works, Inc., 3 Apple Hill Drive, Natick, MA 01760-2098; http://mathworks.com), Sigma Plot™ (SPSS Inc., 233 Wacker Drive, 11th floor, Chicago, IL 60606-6307; http://www.spss.com), and Maple™ (Waterloo Maple Inc., 57 Erb Street, W. Waterloo, Ontario, Canada N2L 6C2; http://www.maplesoft.com). The substrates were coated with the sensor films before cutting into smaller pieces.

An improved procedure for the preparation of Thiazole Yellow GGM sensors is described here.[19] The preparation of a new optical sensor containing Alizarin Yellow R is reported.

2.2.1 Preparation of the Sol-Gel Composite Sensors

(a) Sensors TY1-3. A solution containing H_2O (10 μL), 1.00 M HCl (5 μL), DMF (125 μL), and Thiazole Yellow GGM (27.5 mg) was stirred at room temperature in a closed vial for 3-5 min to insure maximum solubility. Nafion (170 mg) was added by pipet and stirred for ca. 1 min. Dry MeOH (150 μL) and $Si(OMe)_4$ (200

μL) were then added to the stirring solution. The vial was kept closed and stirred for 10 min in order for pre-hydrolysis to occur. While stirring vigorously, Zr(O-n-Bu)$_4$ (325 μL) was added, and the vial was immediately resealed to prevent precipitation of ZrO_2, as Zr(O-n-Bu)$_4$ is very air-sensitive. The solution was vigorously stirred at room temperature for 2 min. The solution was then immediately spin-coated (3000 RPM) onto individual glass substrates for ca. 1 min following the technique listed in Section 1.4.5. After ca. 4 to 5 min, additional sensors were prepared from the residual sol, and the substrates were spun at 3000 RPM for 1 min due to increased viscosity of the sol.

(b) Sensor TY4. The same procedure as described for Sensors **TY1-3** was followed for the preparation of Sensor **TY4** except that no Nafion was used. Spin-coating was conducted at 3000 RPM for approximately 1 min.

(c) Sensors AY1-3. A solution containing H_2O (5 μL), 1.00 M HCl (10 μL), DMF (150 μL), and Alizarin Yellow R (16.0 mg) were stirred at room temperature in a closed vial for 3 to 5 min. Nafion (160 mg) was added and stirred for ca. 1 min. Dry EtOH (150 μL) and Si(OMe)$_4$ (200 μL) were then added to the stirring solution. The vial was kept close and stirred for 10 min. While stirring vigorously, Zr(O-n-Bu)$_4$ (325 μL) was added, and the vial was immediately resealed. The solution was vigorously stirred at room temperature for 3 h. The solution was then spin-coated at 1800 RPM onto individual glass substrates for 1 min. After ca. 4 to 5 min, additional sensors were prepared from the residual sol, and the substrates were spun at 3000 RPM for 1 min due to increased viscosity of the sol.

(d) Sensors AY4. The same procedure as described for Sensors **AY1-3** was followed for the preparation of Sensor **AY4** except that no Nafion was used. Spin-coating was conducted at 1800 RPM for approximately 1 min.

2.2.2 Curing of the Sensors. The sensors were cured for 3 days in the air at room temperature, and then placed in an oven at 45 °C for 5 days. Nafion in the sensors was found to degrade if the sensors were left in the oven for over 5 days.

2.2.3 Conditioning. The cured sensors were placed in water for 2 days, and in 3 M NaOH for 1 day, and finally in distilled water for 1 day. This procedure was performed at room temperature in air. When no appreciable leaching of dye was observed spectrometrically, each sensor was ready for testing.

2.3 Results and Discussion

2.3.1 Alkalinity in NaOH-Organic Solvent-H_2O Ternary Systems. Alkalinity of a solution is determined by both the concentration of the base and the solvent(s).[20] In an aqueous solution, replacing water with another solvent of a lower dielectric constant at fixed OH^- concentration increases the OH^- activity and reduces the water activity.

Three structures of OH^- ions have been suggested in aqueous solutions (Figure 2.1).[79] Raman[80] and IR[81] spectroscopic studies and thermodynamic ionic entropy data show that the stable $OH(H_2O)_3^-$ ions predominate when an

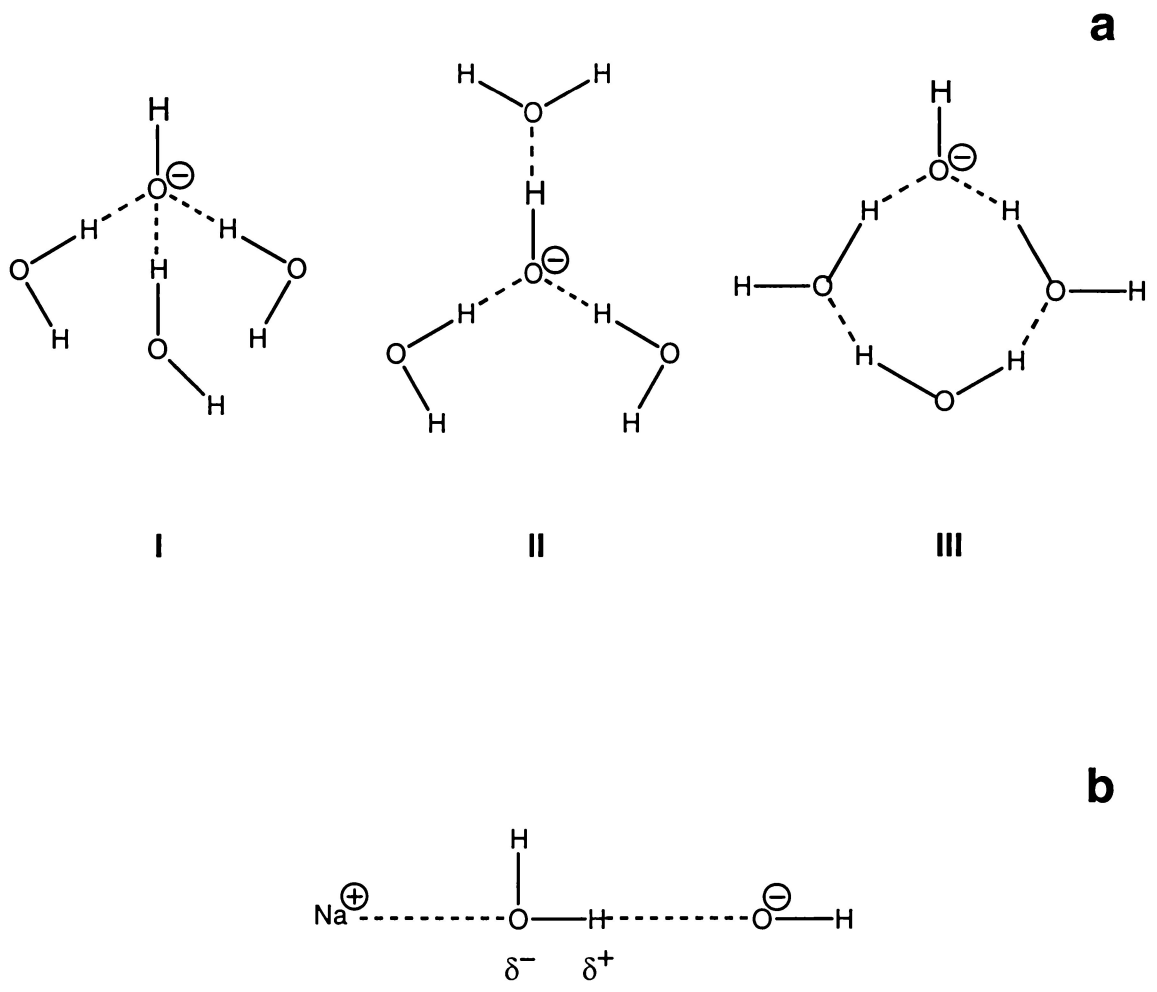

Figure 2.1. Possible structures of (a) the stable $OH(H_2O)_3^-$ species in solution and (b) the "Solvent-bridged" ion pairs. (Adapted from Bowden, K. *Chem. Rev.* 1966, *66*, 119.)

adequate amount of H_2O is present.[79] Water bridging stabilizes the OH^- ions in solution, and requires an adequate amount of the polar solvent in the process. Strong ^1H NMR chemical shifts of OH^- species in concentrated MOH (M = alkali metal) solutions (>0.1 M) or low water concentrations suggest that "solvent-bridged" ion pairs exist in these solutions (Figure 2.1).[79,82,83] In such cases, the oxygen of the water molecule is attached to the cation and the hydrogen to the hydroxide.

In dilute aqueous NaOH solutions ($[OH^-] < 0.1$ M), the traditional *p*H scale is adequate to reflect alkalinity. In such systems, the activity term approaches unity, i.e., a_{OH^-} approximately equals its concentration $[OH^-]$. Solutions with *p*H > 13 become "non-ideal" media, and the traditional *p*H scale cannot adequately reflect alkalinity in these solutions. The Hammett acidity function in Eq. 2.1 was introduced for these highly alkaline media.[3,20,79] In the relationship in Eq. 2.1, a weakly acidic indicator was used to address severe deviations due to the non-linearity between $[OH^-]$ and activity a_{OH^-} in concentrated alkaline solutions.[3]

$$H_- = pK_w + \log C_{OH^-} - \log a_w + \log (\gamma_{HInd}\gamma_{OH^-}/\gamma_{Ind^-}) \qquad \text{(Eq. 2.1)}$$

The activity coefficient term in Eq. 2.1 makes an important contribution to the H_- value.[3] Individual activity coefficients cannot be directly determined experimentally. Yagil and Anbar modified Eq. 2.1 to give Eq. 2.2 for H_- calculation.[82]

$$H_ = pK_w + \log C_{OH^-} - (n + 1) \log C_w \quad \text{(Eq. 2.2)}$$

The term, C_w, is the concentration of "free water," and is defined to be the amount of water that is not bound to OH^- in hydration. C_w ($mol.L^{-1}$) can be determined from Eq. 2.3, where d ($g.L^{-1}$) is the density of the aqueous NaOH solution (Figure 2.2), MW is the molecular weight of NaOH, and C_{OH^-} is the molar concentration of NaOH.[82] The hydroxide hydration number, n, is taken to be 3. The assumption is that the two different forms of indicator are equally hydrated.[82] $H_$ values determined by this method agree well with the experimental results by Schwarzenbach and Sulzberger up to 7 M NaOH concentrations.[84] It is important to note that in Eq. 2.3, that the equilibrium constants and observed rate constants are usually computed on the assumption that in dilute solution the concentration of water is unity instead of 55.5.[82] Therefore water concentrations are normalized via dividing by 55.5.[82] Yagil and Anbar, in these equations, provided a detailed discussion for determining $H_$.[82]

$$C_w = d - 0.001 (MW + 18.0\, n) C_{OH^-} \quad \text{(Eq. 2.3)}$$

Eqs. 2.2-2.3 were used in the current studies for the determination of pK_as of TY and AY encapsulated in our sensor sensors, which is discussed below.

$H_$ was found to strongly depend upon the solvent.[79] For instance, $H_$ was found to equal 12.66, 14.57, and 16.95 for *non-aqueous* MeOH, EtOH, and

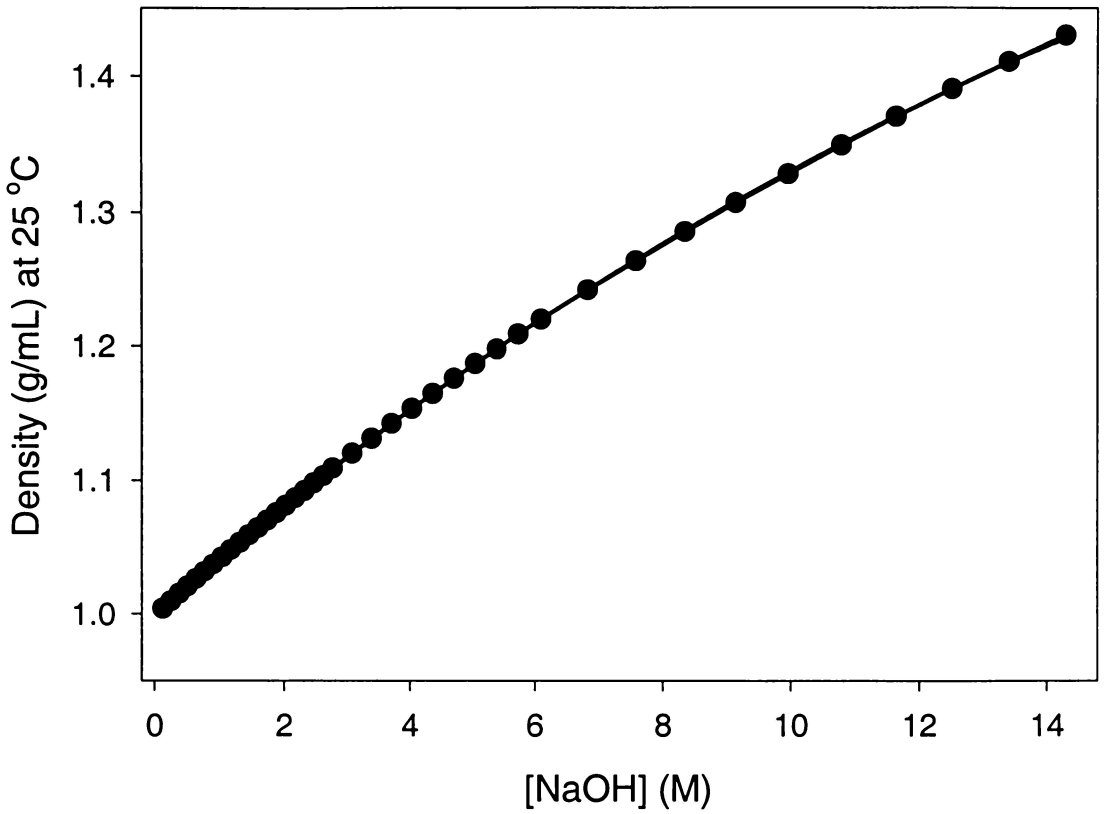

Figure 2.2. Relationship between density and NaOH concentration in aqueous systems. The curve was fitted by a 2nd degree quadratic equation. (Adapted from Lide, D. R., Ed., 74 ed.; CRC Press, Inc.: Boca Raton, 1975-76, p. D-218.)

i-PrOH solutions of 0.10 M NaOH, respectively.[79] The solvent dielectric constants at 25 °C for MeOH, EtOH, and i-PrOH are 32.6, 24.3, and 18.3, respectively.[79,85] In other words, at a constant concentration of NaOH, the OH^- activity is greater in a protic solvent of a lower dielectric constant.[79] Solvents of low dielectric constants are generally nonpolar hydrocarbons that are poor at solvating ions because of the diminished ability to hydrogen bond, thus leading to higher OH^- activity.[86] *H_* values in various *non-aqueous* alcoholic NaOH solutions were reviewed by Bowden.[79]

In a NaOH aqueous-organic *mixed solvent* system, the basicity of such a ternary system appears to be a function of the autoprotolysis constant and the proton affinity of the organic solvent.[79] Insufficient organic solvate molecules or solvate molecules of a lower dielectric constant than water can both contribute to the generation of fewer hydrated hydroxide ions.[79,87] Two factors that affect the OH^- activity have been considered in these NaOH-H_2O-organic solvent ternary systems.[79] First, solvation effects involving "good hydrogen bonders" lower hydroxide activity. If solvents of low dielectric constants and poor hydrogen bond acceptors such as i-PrOH are present, the concentration of non-solvated hydroxide occur is elevated.[79] In some cases the added solvent can compete with hydroxide for hydrogen bonding, therefore removing water from the solution that would normally hydrogen bond to hydroxide.[79] The second factor is the reduction in the number of solvent molecules in mixed H_2O-organic solvents. In dilute aqueous hydroxide solutions, there are adequate water molecules to readily solvate OH^- ions. However, when an organic solvent replaces water, a

deficiency in solvate molecules may arise. For example, an equal volume of EtOH contains fewer moles of the solvent than that of water. Therefore, there exist fewer available solvating molecules in mixed H_2O-organic solvents, thereby increasing the OH^- activity.[87]

The effect of the organic solvent on alkalinity in NaOH-organic-H_2O systems is also shown in acidity function $H_$. Eq. 2.2 indicates that, as the C_{water} is reduced (while increasing $C_{alcohol}$) at constant C_{OH^-}, the $H_$ inherently increases.[79] For example, $H_$ incrementally rises from 11.74 to 15.71 when i-PrOH concentration increases from 0 to 100% at a constant 0.005 M NaOH.[79] In the base sensors studied here, an increase in A was observed when C_{base} or $C_{alcohol}$ are increased in mixed aqueous-alcohol solutions. If no correction for organic solvent is performed in mixed aqueous-organic solvent systems, we found that measurements in C_{base} by our optical sensors gave errors as large as 99.4%. As an example, Figures 2.3-2.5 show errors in C_{base} measurements by Sensors **TY1-3** and **AY1-3** in NaOH-EtOH-H_2O solutions.

2.3.2 Dual Optical Transducer Approach. We have chosen NaOH-ROH-H_2O (R = Me, Et, i-Pr) ternary systems to demonstrate our dual optical transducer approach to accurately measure C_{base} and $C_{alcohol}$. The solubility of NaOH and water in the alcohol is an important criterion in choosing these media. MeOH and water are miscible, and the solubility of NaOH in MeOH is high (23.9 g/100 mL or ~6 M).[88] Ternary phase diagrams of NaOH-EtOH-H_2O and NaOH-i-PrOH-H_2O solutions have been reported (Figure 2.6).[89,90]

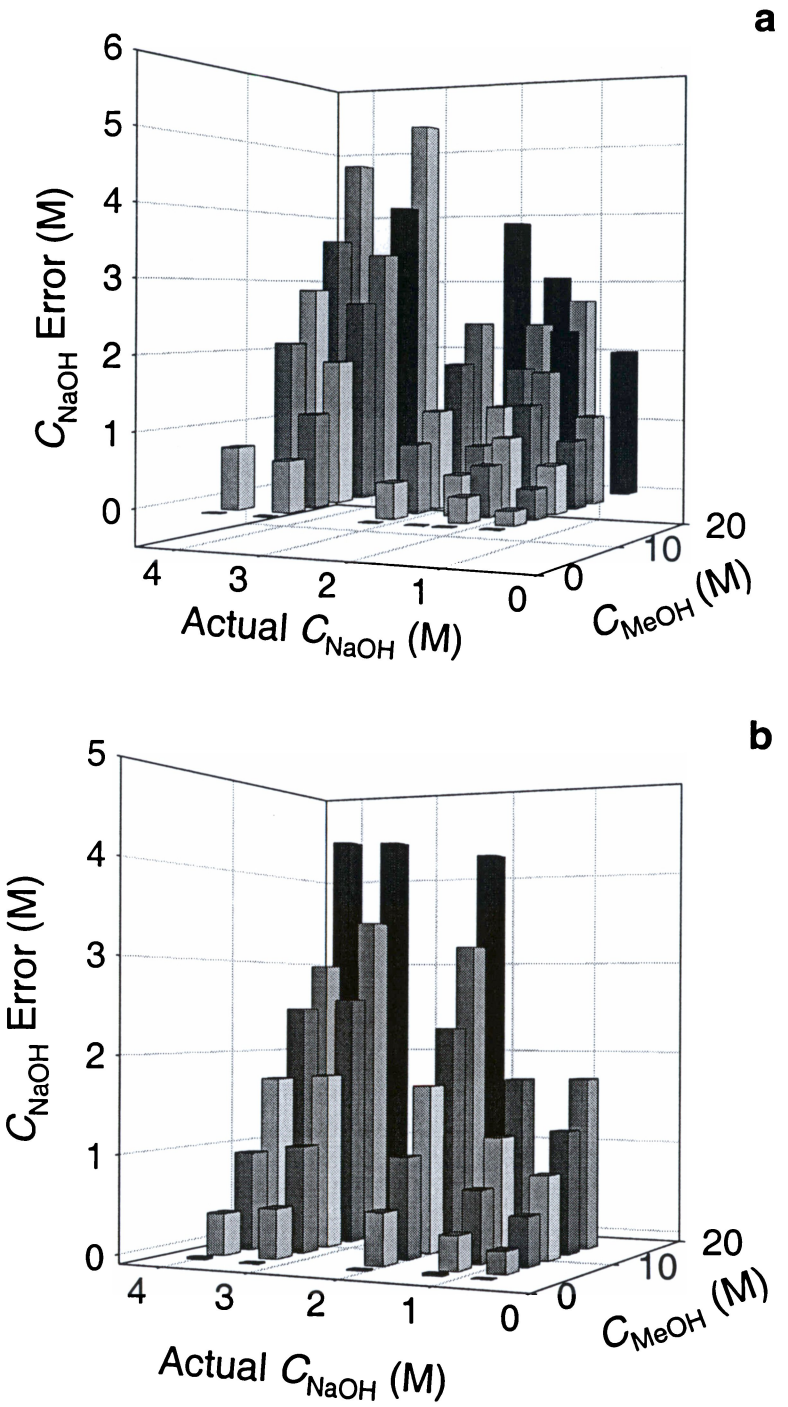

Figure 2.3. C_{NaOH} inaccuracies using Sensors (a) **TY1** and (b) **AY1** in NaOH-MeOH-H_2O ternary solutions without correction.

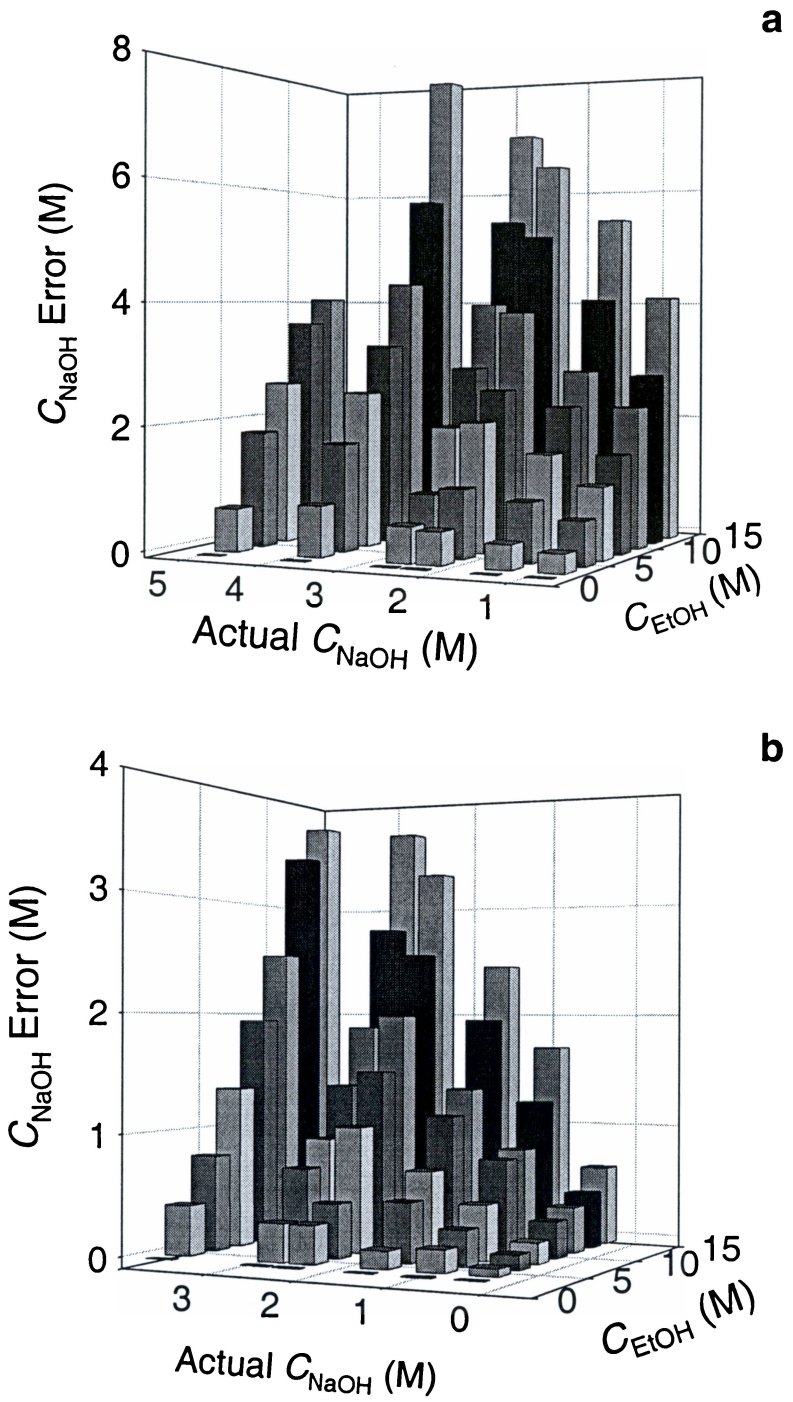

Figure 2.4. C_{NaOH} inaccuracies using Sensors (a) **TY2** and (b) **AY2** in NaOH-EtOH-H_2O solutions without correction.

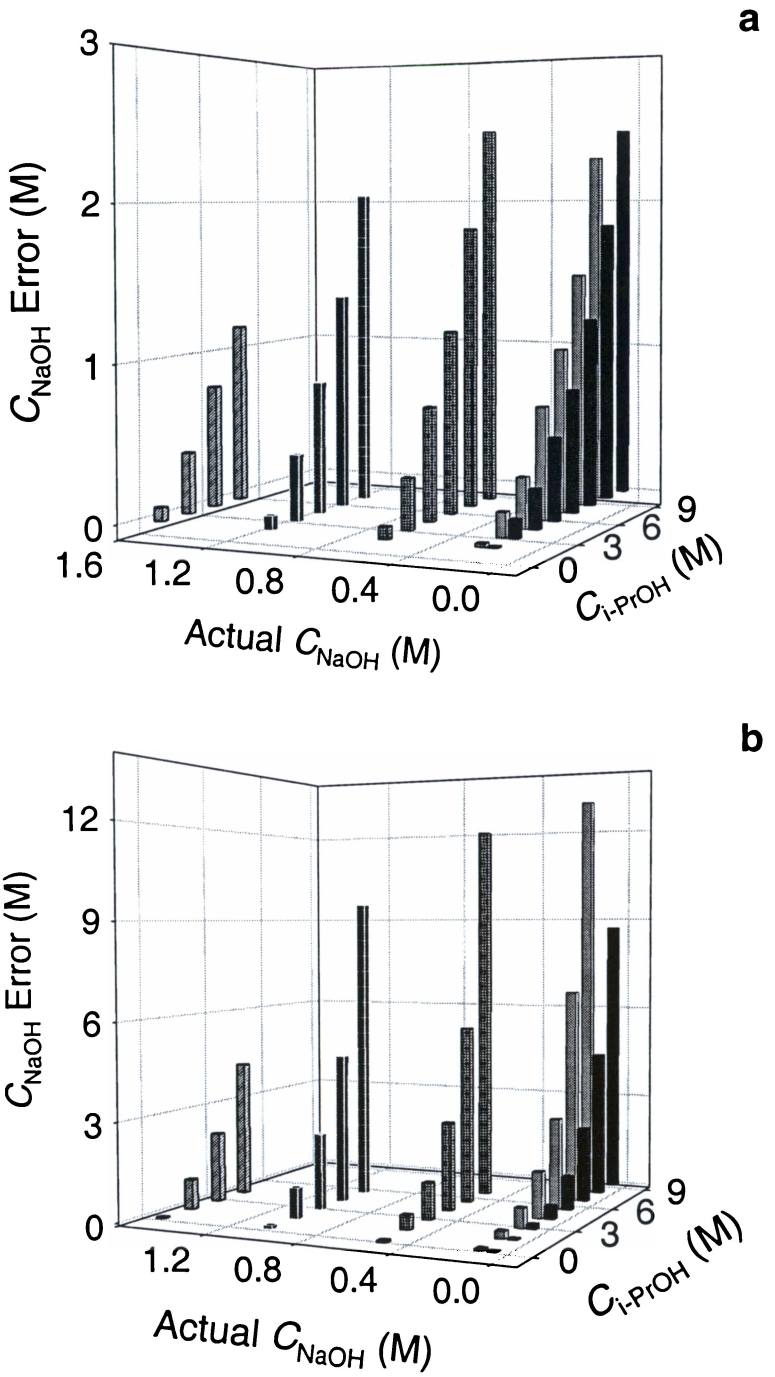

Figure 2.5. C_{NaOH} inaccuracies using Sensors (a) **TY3** and (b) **AY3** in NaOH-i-PrOH-H_2O solutions without correction.

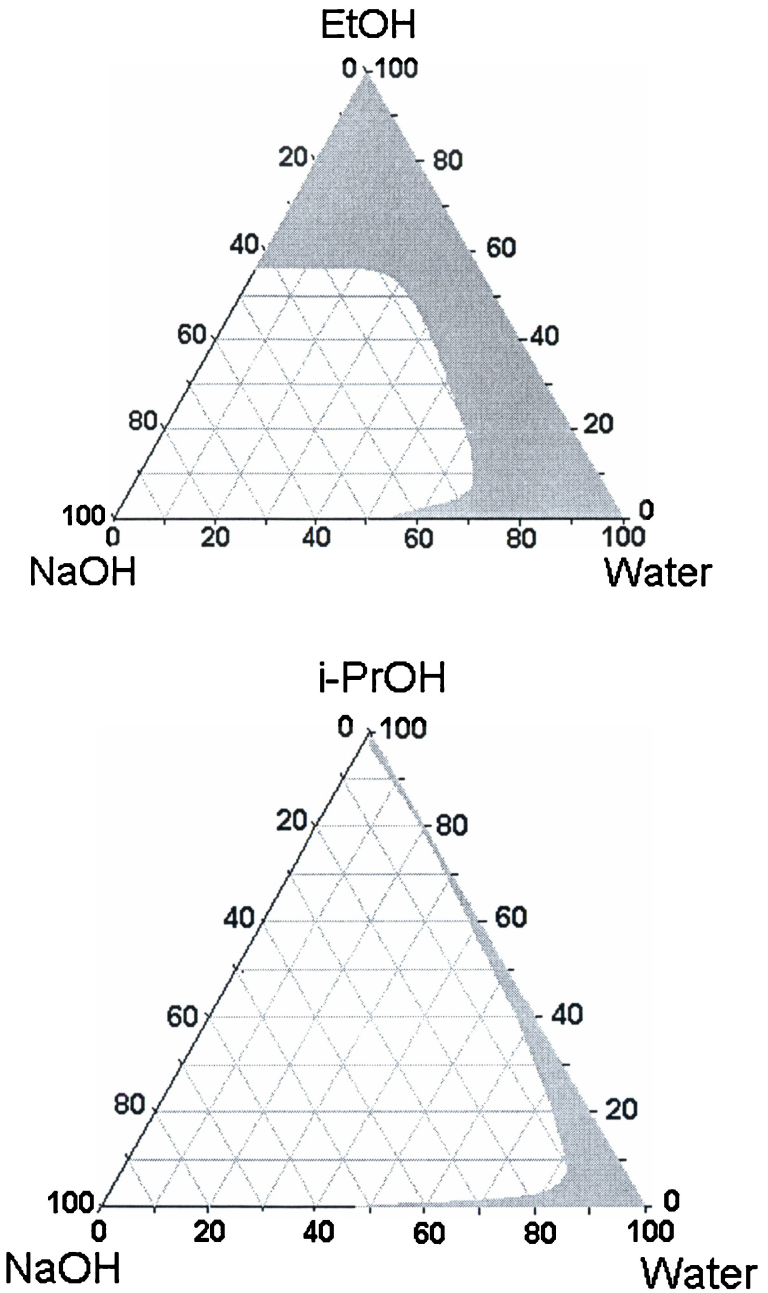

Figure 2.6. Ternary phase diagrams. (Adapted from Peyronel, G. *Gazz. Chim. Ital.* 1949, *79*, 792; Mills, A. L.; Hughes, F. *Chem. & Eng. Data Ser. 2,* 1957, 35.)

This dual optical transducer approach is based on a novel linear relationship, which we observed in the NaOH-ROH-H_2O ternary systems. An optical sensor that bases its transducing mechanism on an indicator chemical equilibrium (e.g., Eq. 2.4) may show a nonlinear relationship between its analytical signal and analyte concentration.[31] When no alcohol is present, absorbance (A) is a function of C_{base}.

$$HInd + OH^- = Ind^- + H_2O \qquad \text{(Eq. 2.4)}$$

Nonlinear relationships between A and C_{base} were observed in the current studies. At a fixed C_{base}, A was found to increase with increased alcohol concentration $C_{alcohol}$. *Experimental* 3-D plots of A vs C_{base} and C_{ROH} for the Sensors **TY1-3** and Sensors **AY1-3** are given in Figures 2.7-2.9.

Several different *empirical* mathematical curve fittings may be used for the calibration plots in the aqueous, *alcohol-free* solutions (Figures 2.10-2.11). A sigmoidal curve fitting function, which we reported earlier for acid sensors in acid-salt-H_2O ternary systems,[31] gave an average value of ±0.990 for the curve fitting correlation factor (R^2) in the current *aqueous* NaOH solutions. A logarithmic curve fitting function (Eq. 2.5) was found to give slightly better fitting with average R^2 values of ±0.999, and could be applied to all six sensors (Sensors **TY1-3** and **AY1-3**). We would like to emphasize that both mathematical curve fitting models are *empirical*, and in the current work, the logarithmic curve fitting function in Eq. 2.5 was employed with different curve fitting constants a, b and c for all six

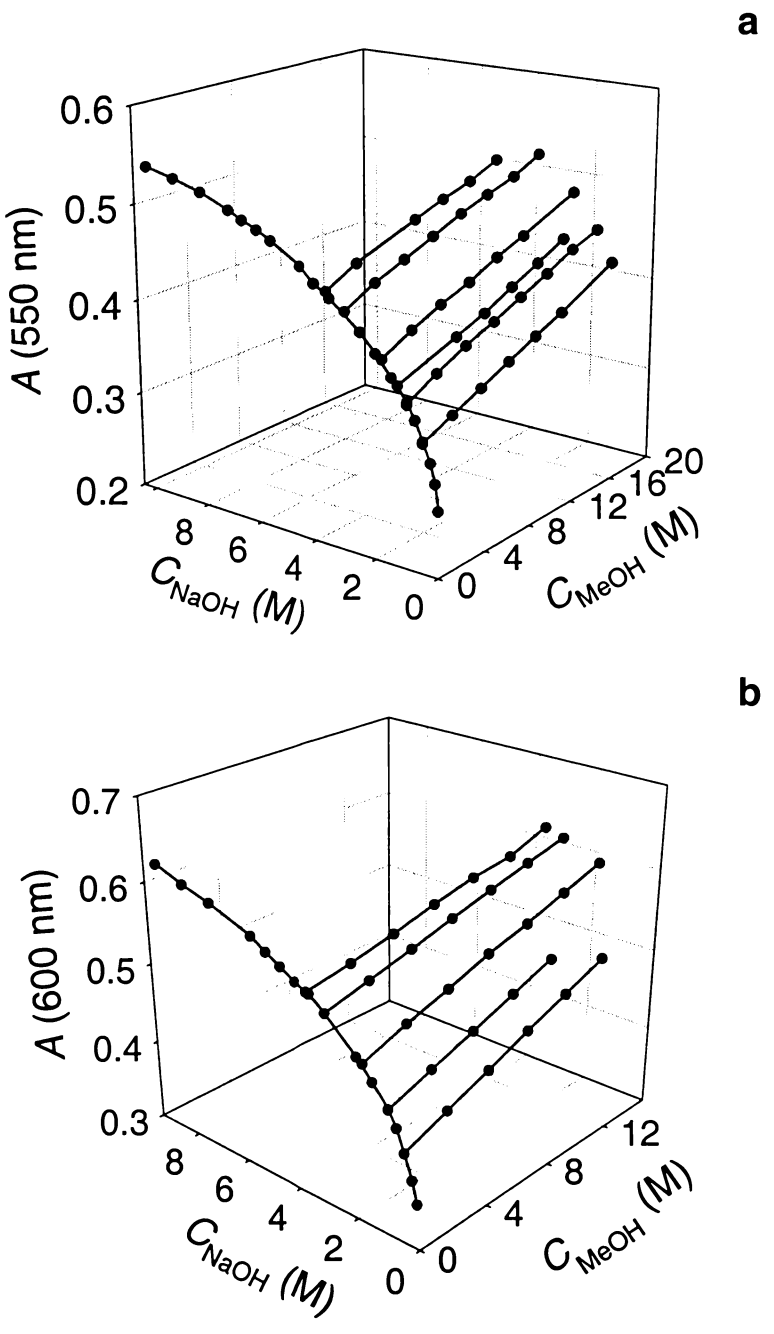

Figure 2.7. Responses of Sensors (a) **TY1** and (b) **AY1** in NaOH-MeOH-H_2O solutions.

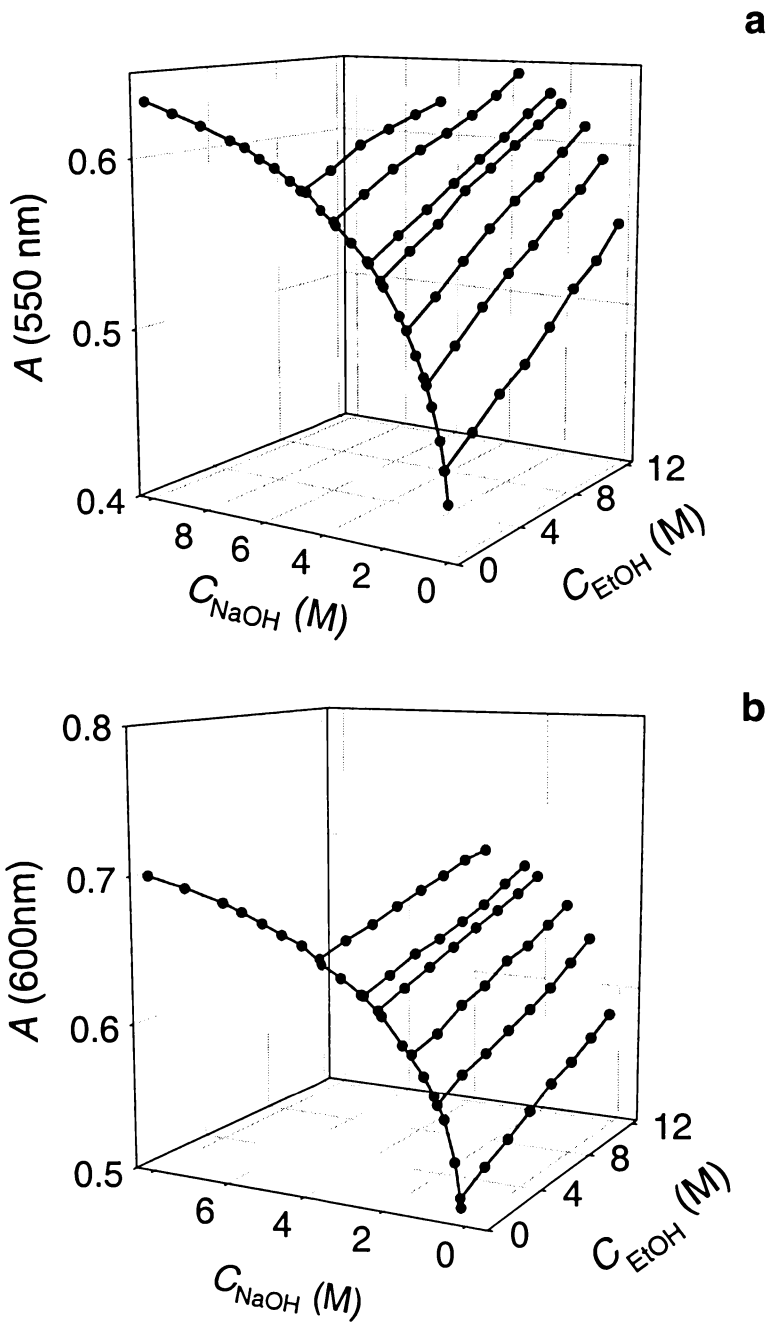

Figure 2.8. Responses of Sensors (a) **TY2** and (b) **AY2** in NaOH-EtOH-H_2O solutions.

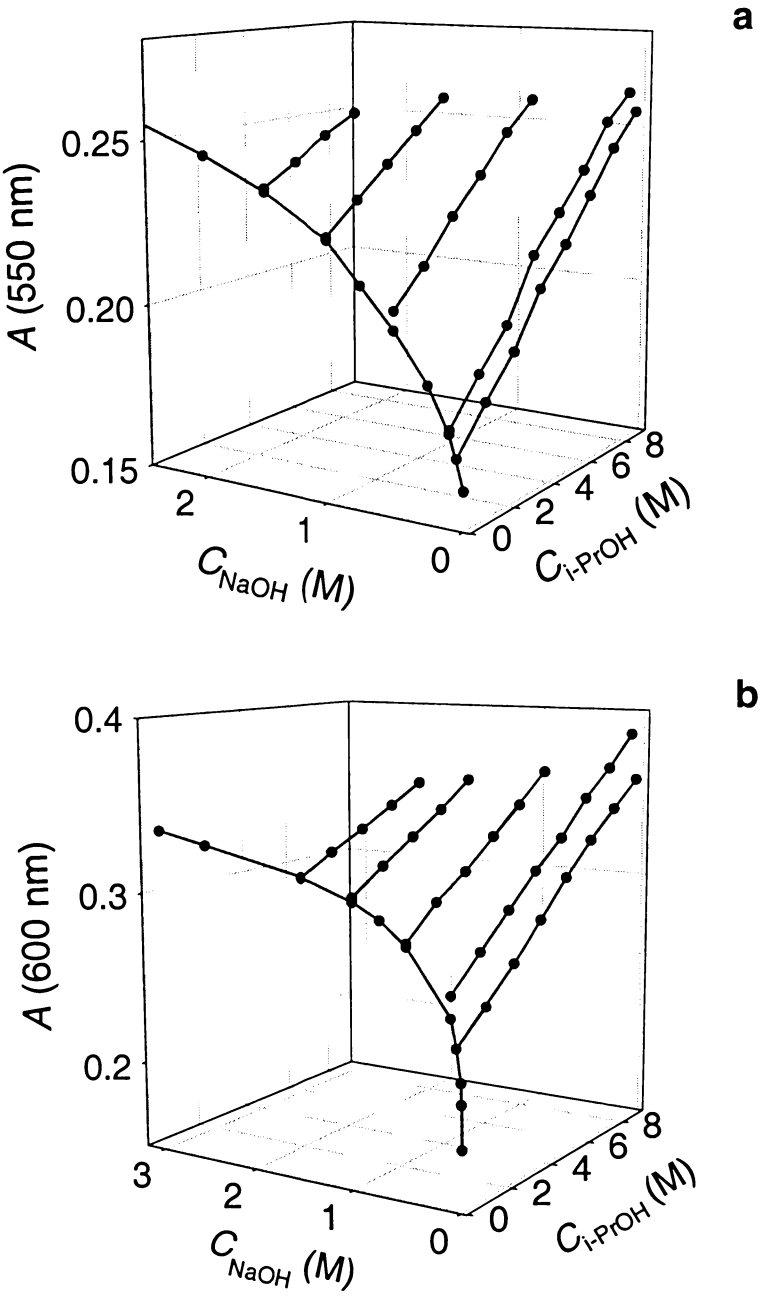

Figure 2.9. Responses of Sensors (a) **TY3** and (b) **AY3** in NaOH-i-PrOH-H_2O solutions.

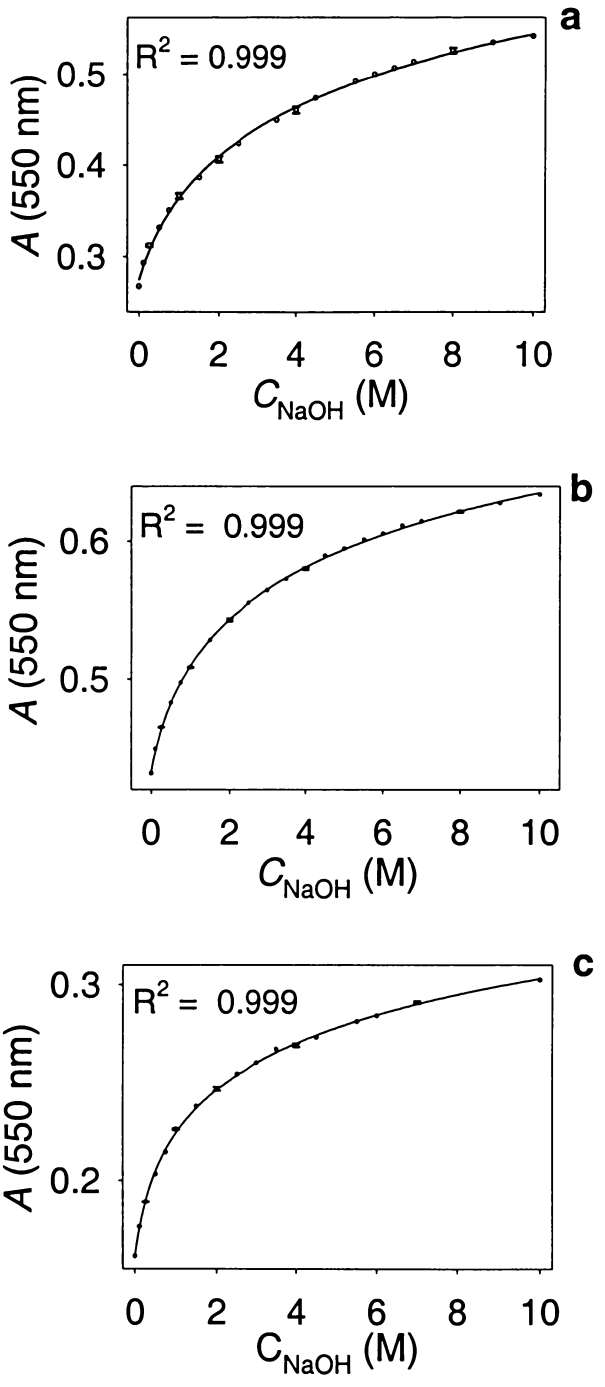

Figure 2.10. Calibration plots of A vs. C_{NaOH} for Sensors (a) **TY1**, (b) **TY2**, and (c) **TY3** in alcohol-free, aqueous solutions.

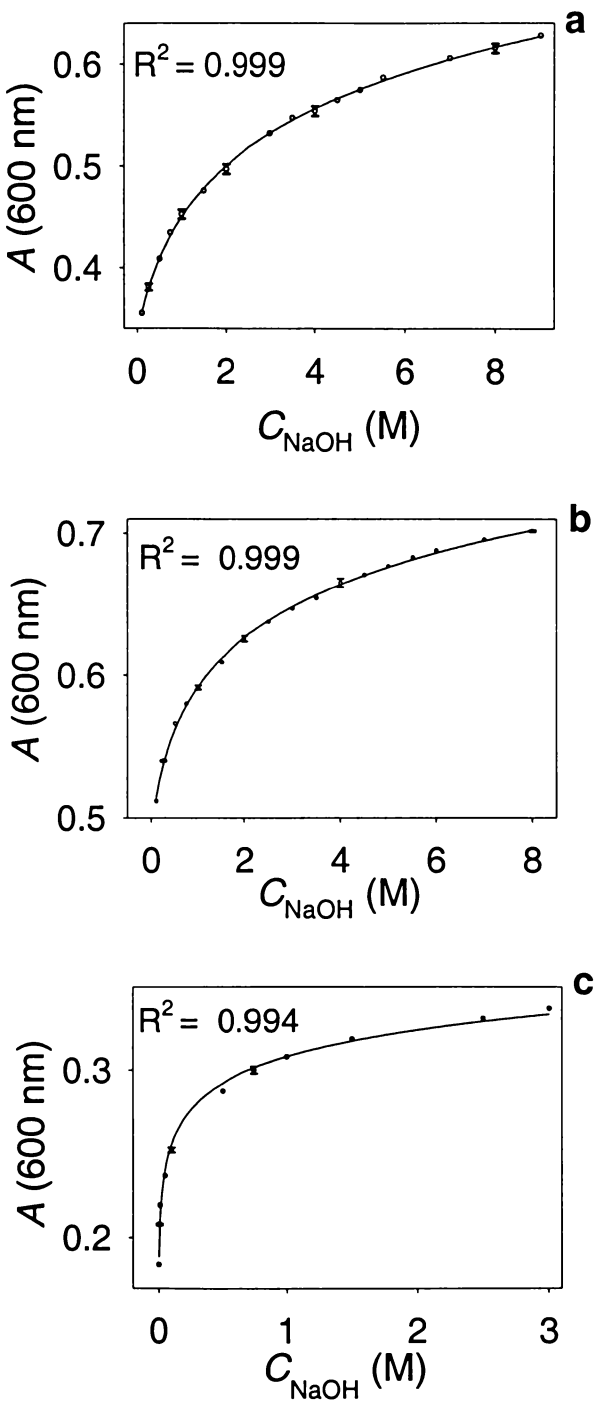

Figure 2.11. Calibration plots of A vs. C_{NaOH} for Sensors (a) AY1, (b) AY2, and (c) AY3 in alcohol-free, aqueous solutions.

sensors.

$$A = f(C_{base}) = c + a \ln(C_{base} - b) \quad \text{(Eq. 2.5)}$$

In NaOH-ROH-H_2O ternary systems, the total sensor absorbance A^t was found to be functions of both base and alcohol concentrations. In such mixed solvent systems, the use of organic solvent leads to an absorbance increase ΔA (Figures 2.12-2.14) from A in *aqueous, alcohol-free* NaOH solution. The total absorbance A^t is thus

$$A^t = A + \Delta A \quad \text{(Eq. 2.6)}$$

We found that, in these NaOH-ROH-H_2O ternary systems, there is a novel linear relationship as shown in Eq. 2.7 for 0-70 v/v% $C_{alcohol}$. $(\partial A/\partial C_{alcohol})_{C_{base}}$, the slope of absorbance change with respect to $C_{alcohol}$ at a fixed C_{base}, is a linear function of C_{base}. This linear relationship in various NaOH-ROH-H_2O solutions is shown in Figures 2.15-2.17.

$$(\partial A/\partial C_{alcohol})_{C_{base}} = d\, C_{base} + e \quad \text{(Eq. 2.7)}$$

This novel linear relationship (Eq. 2.7) could then be used to calculate $C_{alcohol}$ and C_{base}. The change ΔA in mixed aqueous organic solvents can be

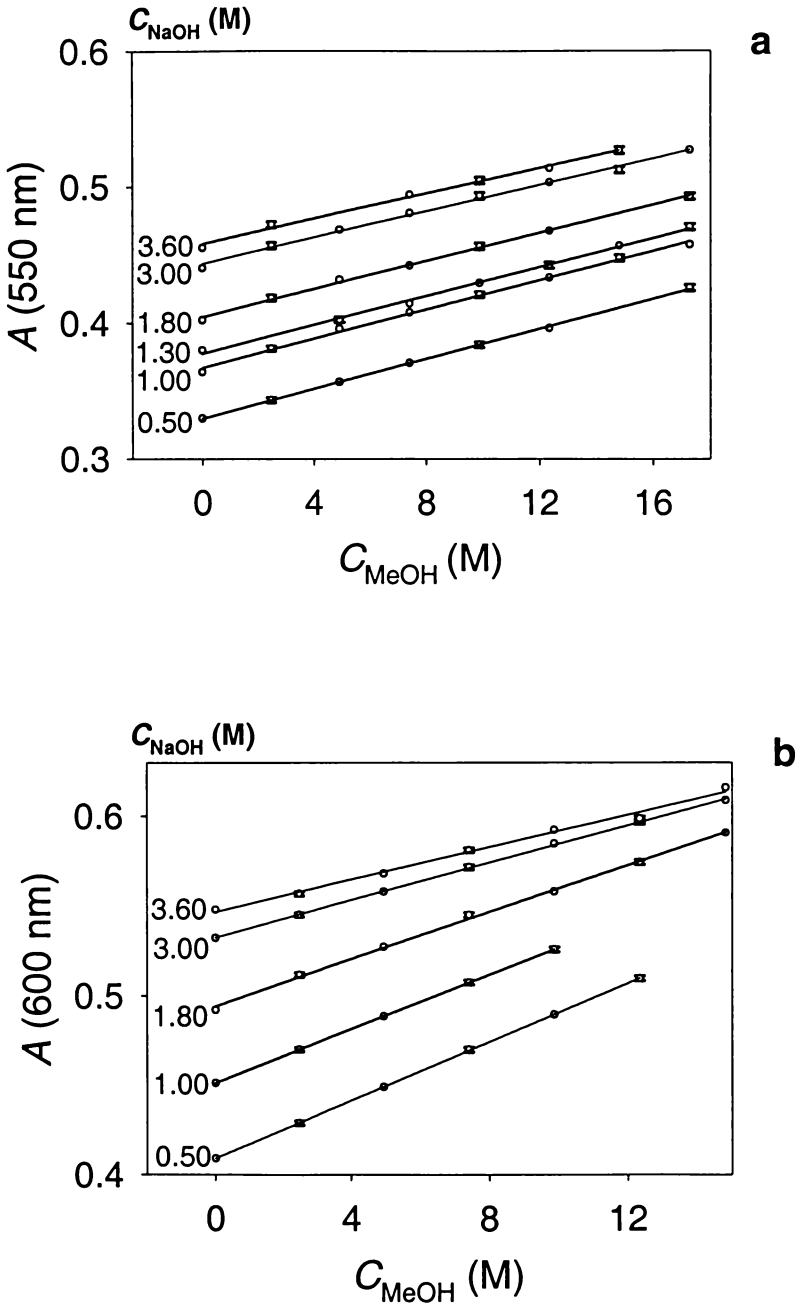

Figure 2.12. Calibration plots of A vs. C_{MeOH} for Sensors (a) **TY1** and (b) **AY1** in NaOH-MeOH-H_2O solutions.

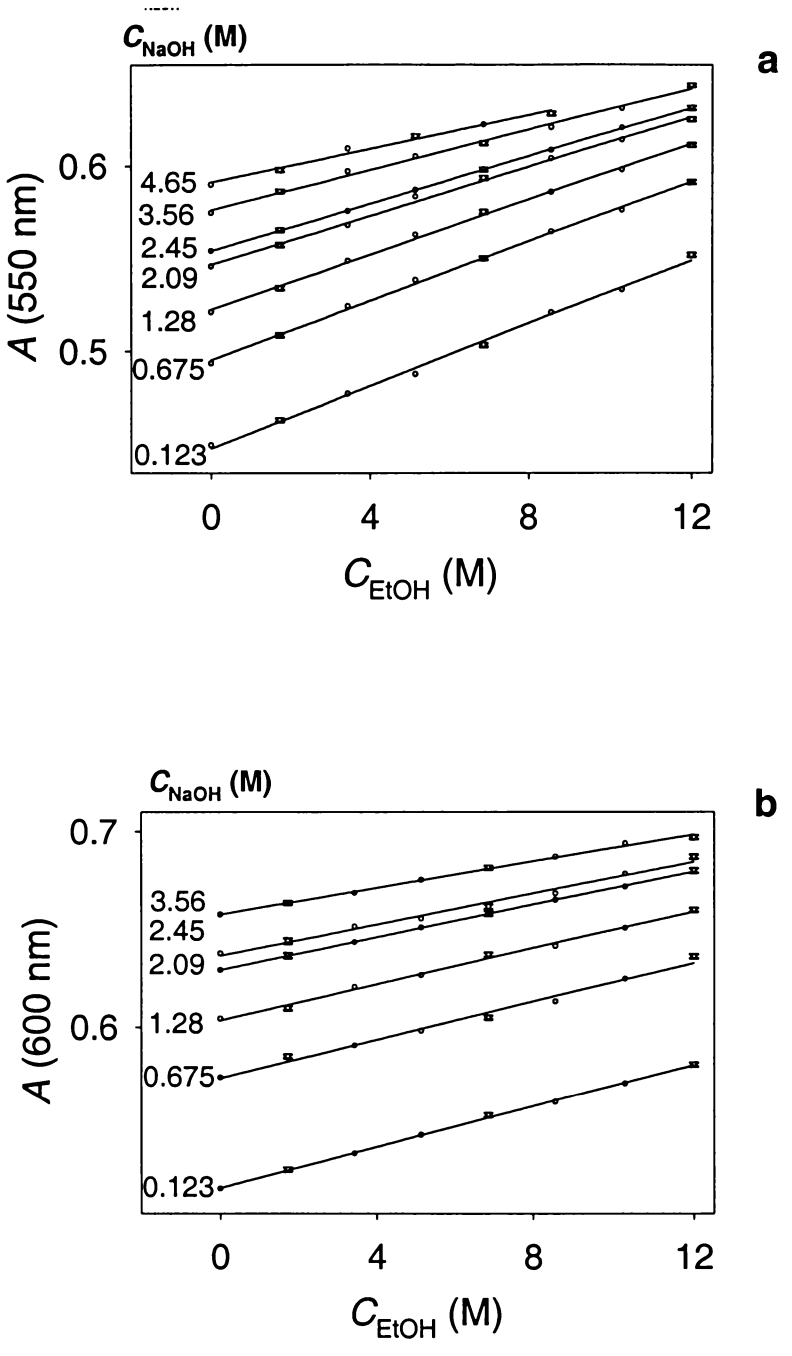

Figure 2.13. Calibration plots of A vs. C_{EtOH} for Sensors (a) **TY2** and (b) **AY2** in NaOH-EtOH-H_2O solutions.

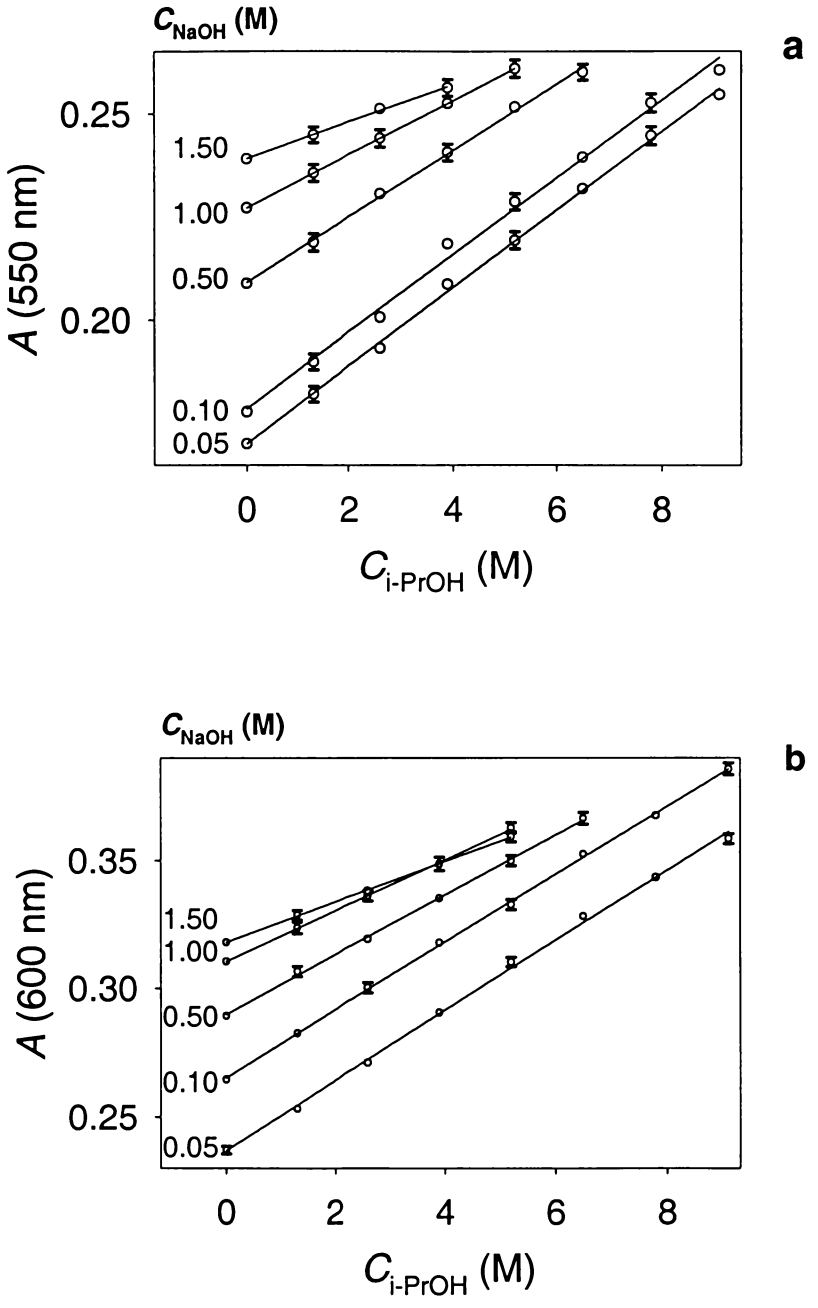

Figure 2.14. Calibration plots of A vs. $C_{i\text{-}PrOH}$ for Sensors (a) **TY3** and (b) **AY3** in NaOH-i-PrOH-H_2O solutions.

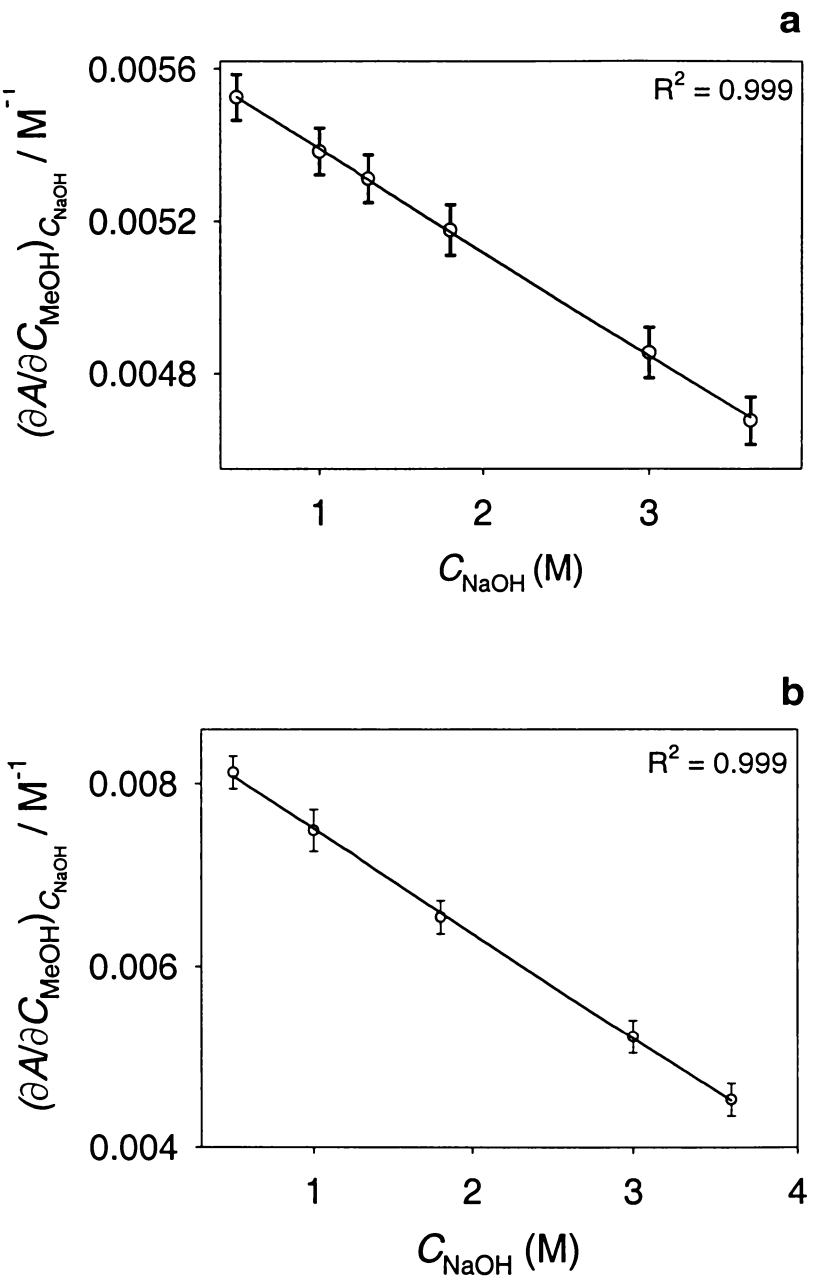

Figure 2.15. C_{NaOH} vs. $(\partial A/\partial C_{MeOH})_{C_{NaOH}}$ plots for Sensors (a) **TY1** and (b) **AY1**.

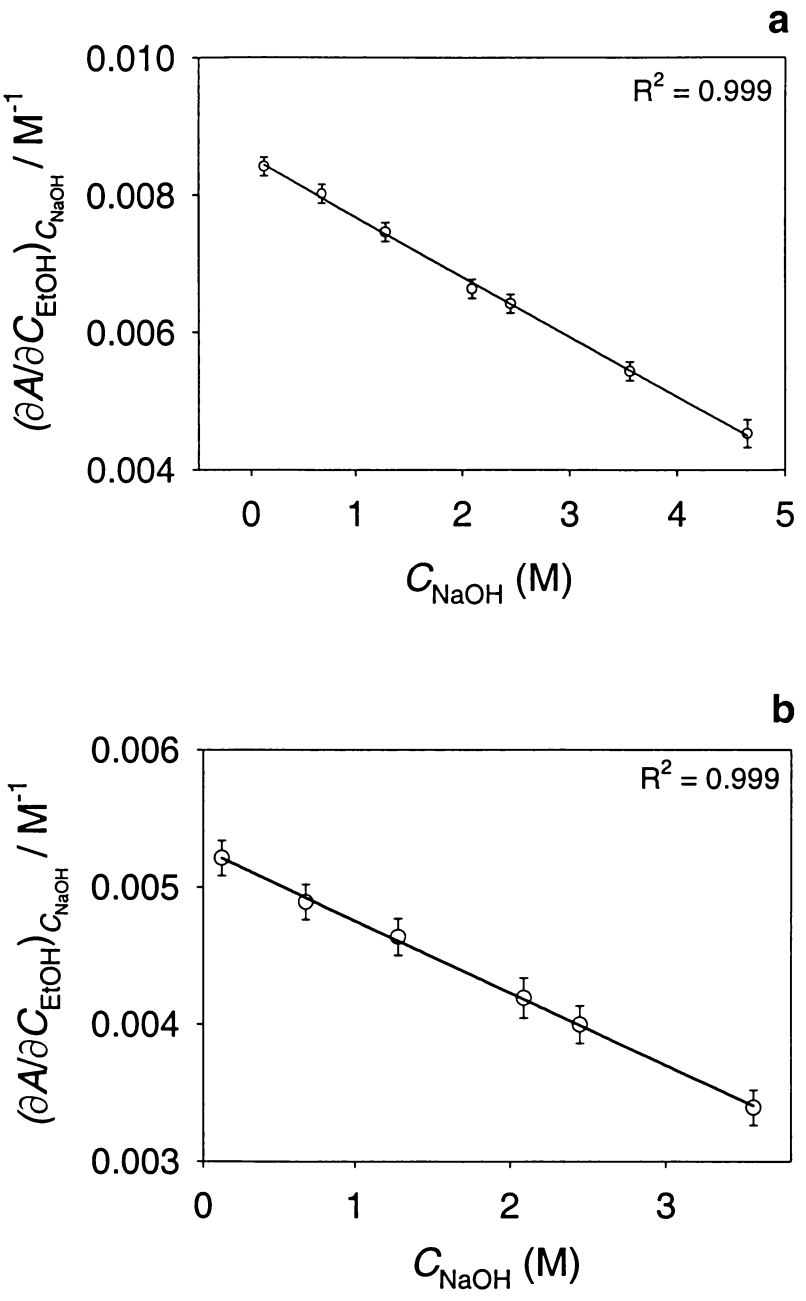

Figure 2.16. C_{NaOH} vs. $(\partial A/\partial C_{EtOH})_{C_{NaOH}}$ plots for Sensors (a) **TY2** and (b) **AY2**.

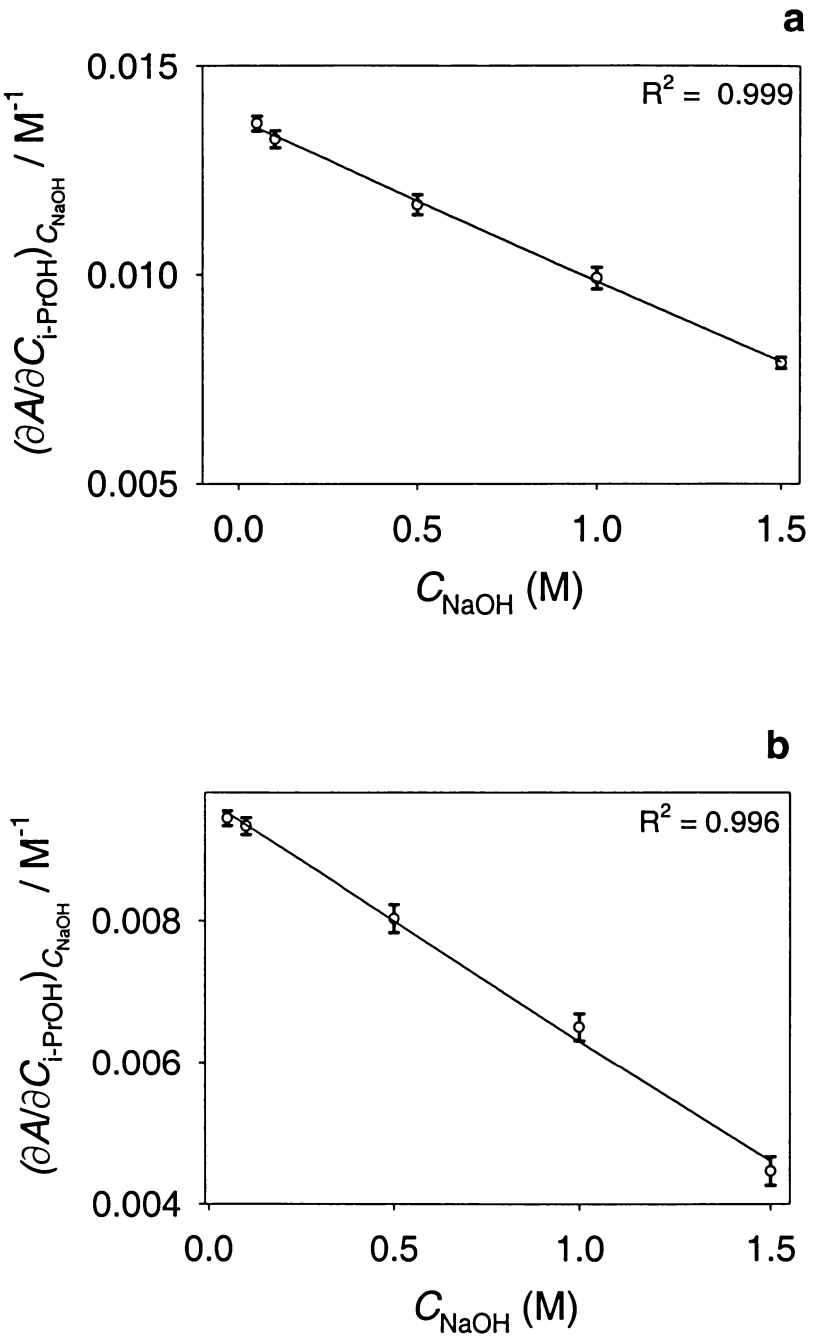

Figure 2.17. C_{NaOH} vs. $(\partial A/\partial C_{i\text{-PrOH}})_{C_{NaOH}}$ plots for Sensors (a) **TY3** and (b) **AY3**.

represented by Eq. 2.8.

$$\Delta A = (\partial A/\partial C_{alcohol})_{C_{base}} \bullet C_{alcohol} \qquad \text{(Eq. 2.8)}$$

Substituting the linear curve fitting Eq. 2.7 into Eq. 2.8 gives ΔA in Eq. 2.9.

$$\Delta A = (e + d\,C_{base})\, C_{alcohol} \qquad \text{(Eq. 2.9)}$$

and thus A^t in Eq. 2.10.

$$A^t = c + a\ln(C_{base} - b) + (e + d\,C_{base})\, C_{alcohol} \qquad \text{(Eq. 2.10)}$$

When two independent transducers are used, we have the following two independent equations (Eqs. 2.11 and 2.12).

$$A^t_1 = c_1 + a_1 \ln (C_{base} - b_1) + (e_1 + d_1\, C_{base})\, C_{alcohol} \qquad \text{(Eq. 2.11)}$$

$$A^t_2 = c_2 + a_2 \ln (C_{base} - b_2) + (e_2 + d_2\, C_{base})\, C_{alcohol} \qquad \text{(Eq. 2.12)}$$

Solving Eqs. 2.11 and 2.12 for the two independent sensors gives C_{base} and $C_{alcohol}$. In essence, this approach converts $(\partial A/\partial C_{alcohol})_{C_{base}}$, an unknown

function of C_{base}, into a linear function ($d\,C_{base} + e$). The parameters d and e could be determined experimentally and, thus, lead to the computed solutions for C_{base} and $C_{alcohol}$. This approach was found to substantially reduce the errors in C_{base} *after* the corrections (Figure 2.18) and give predictions for the $C_{alcohol}$ (Figure 2.19), a subject to be discussed below.

2.3.3 Error Analysis. In the current work an extended range of C_{base} (ca. 0.05 to 3.6 M) in NaOH-ROH-H_2O (Tables 2.1-2.3) was probed to investigate the impact of alcohol on the errors in C_{base} measurements. The concentration range of MeOH, EtOH, and i-PrOH was 0 to 70 v/v%.

Sensors **TY1-3** and **AY1-3** were tested in several NaOH-ROH-H_2O solutions. If no corrections are made, as shown in Figures 2.3-2.5, there are substantial increases in the C_{base} accuracy. In the range of mixed MeOH and EtOH solutions tested, errors in C_{base} were reduced from as much as 95.0% to 15.0% (<10% in most cases). In i-PrOH mixed solutions, errors in C_{base} were reduced from 99.4% to less than 20.5%. In addition, the current approach gives $C_{alcohol}$. Accuracies in $C_{alcohol}$ prediction are shown in Figure 2.19.

Some interesting trends are observed in these NaOH-ROH-H_2O ternary systems: (a) If *no* correction is performed, error in C_{base} measurement increases as the $C_{alcohol}$ is increased (at constant C_{base}). For example, error for Sensor **TY2** increases from 23.2% to 80.9% when C_{EtOH} changes from 10% to 70 v/v% at C_{base} = 1.28 M. (b) Upon applying the dual sensor approach, accuracy in C_{base} prediction increases as the basicity of the solution increases. In other words,

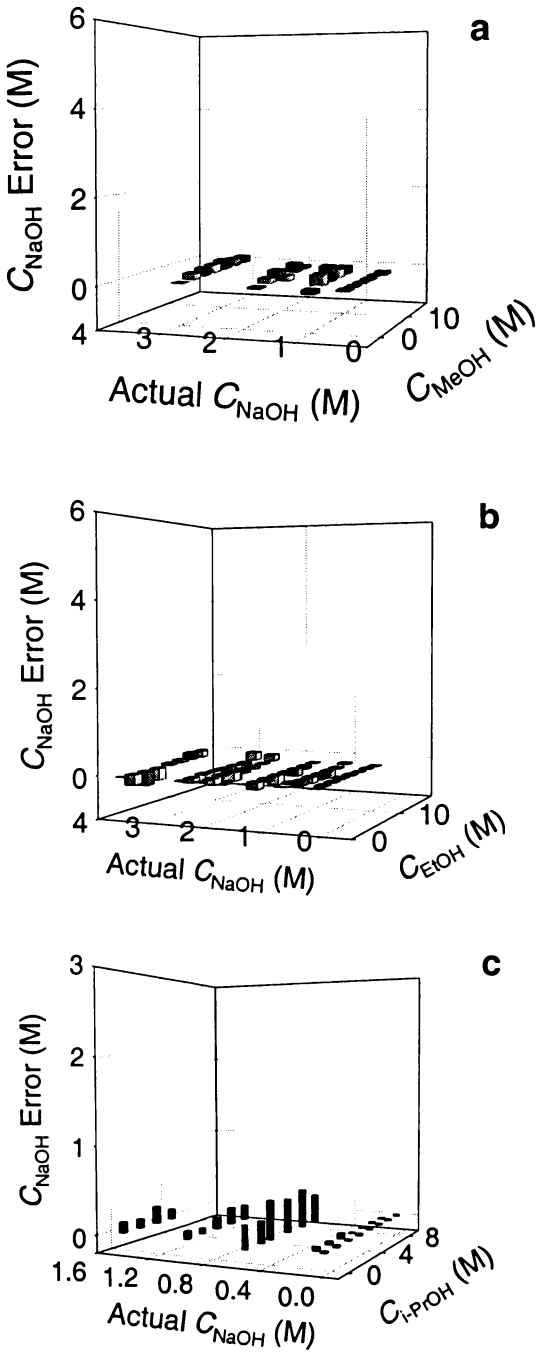

Figure 2.18. Errors in C_{NaOH} *after* corrections using Sensors **TY1-3** and **AY1-3**: (a) NaOH-MeOH-H_2O; (b) NaOH-EtOH-H_2O; (c) NaOH-i-PrOH-H_2O.

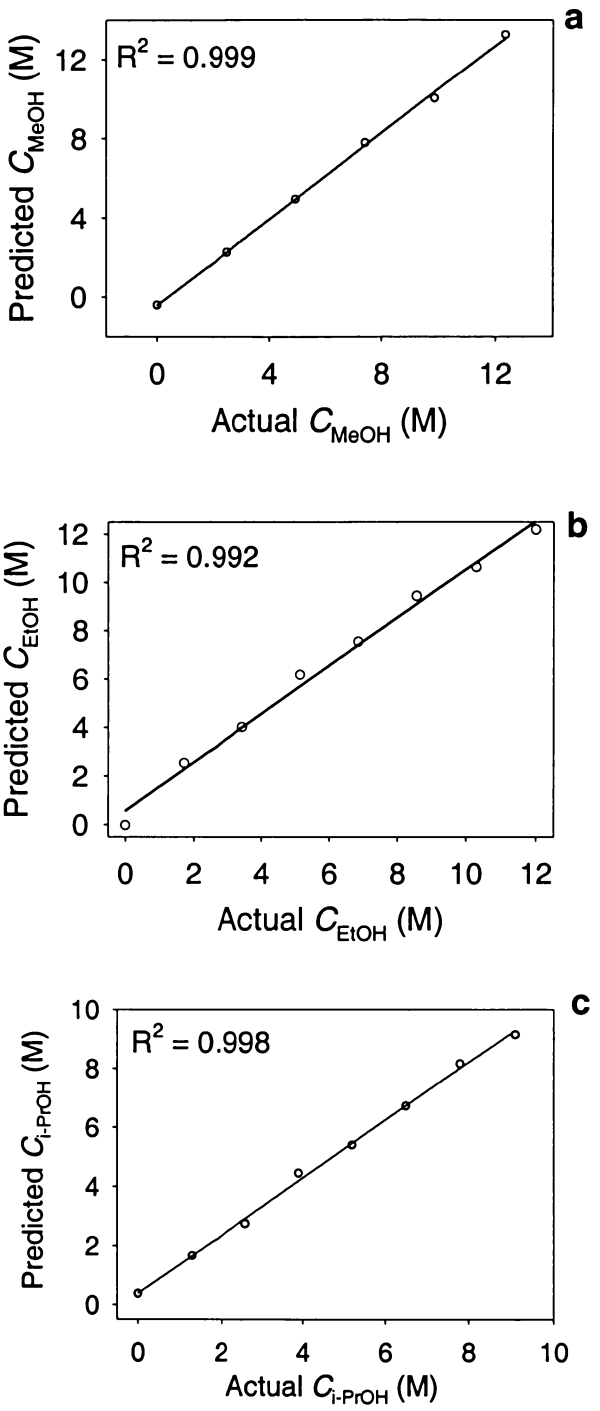

Figure 2.19. Sample plots of actual $C_{alcohol}$ vs. predicted $C_{alcohol}$ in NaOH-ROH-H_2O ternary solutions: (a) 0.50 M NaOH (ROH = MeOH); (b) 1.28 M NaOH (ROH = EtOH); (c) 0.050 M NaOH (ROH = i-PrOH).

Table 2.1. Results of the Dual Sensor Approach for NaOH-MeOH-H_2O Solutions Using Sensors TY1 and AY1[a]

C_{base} (M)	Error (%) in C_{base} by AY1[b]	Error (%) in C_{base} by TY1[b]	Error (%) in C_{base} after dual sensor approach	Precision (%) in C_{MeOH} after dual sensor approach
0.50	30.3–77.8	26.4–80.0	2.0–14.3	72.9–98.5
1.00	25.3–63.8	24.2–73.0	9.6–15.0	75.8–90.0
1.80	22.3–69.8	28.2–70.1	5.6–10.7	86.7–99.1
3.00	14.2–59.1	7.1–68.1	4.5–6.8	92.4–95.8

[a] Standard deviations in C_{base} and C_{MeOH} were ± 0.04 to 0.12 M (3.8 to 7.4%) and ±0.03 to 0.10 M (3.6 to 6.4%), respectively.

[b] % Errors in C_{base} *before* correction.

Table 2.2. Results of the Dual Sensor Approach for NaOH-EtOH-H_2O Solutions Using Sensors TY2 and AY2[a]

C_{base} (M)	Error (%) in C_{base} by AY2[b]	Error (%) in C_{base} by TY3[b]	Error (%) in C_{base} after correction	Precision (%) in C_{EtOH} after correction
0.123	32.8–84.3	51.6–95.0	3.9–15.0	81.8–98.4
0.625	21.2–71.7	30.5–85.9	4.9–14.6	74.7–99.3
1.28	10.2–65.5	23.2–80.9	0.8–14.0	70.6–98.5
2.09	13.0–61.0	19.8–75.3	0.2–8.3	82.8–99.0
2.45	11.3–60.0	18.8–73.8	0.8–13.7	82.2–97.6
3.56	10.4–51.0	18.4–69.0	0.2–8.5	72.4–99.6

[a] Standard deviations in C_{base} and C_{EtOH} were ±0.01 to 0.11 M (3.0 to 7.5%) and ±0.007 to 0.12 M (3.3 to 5.9%), respectively.

[b] % Errors in C_{base} *before* correction via the dual sensor approach using Sensors **AY2** and **TY2**.

Table 2.3. Results of the Dual Sensor Approach for NaOH-i-PrOH-H_2O Solutions Using Sensors TY3 and AY3[a]

C_{base} (M)	Error (%) in C_{base} by AY3[b]	Error (%) in C_{base} by TY3[b]	Error (%) in C_{base} after dual sensor approach	Precision (%) in $C_{i\text{-}PrOH}$ after dual sensor approach
0.05	15.1–99.4	70.0–98.0	16.7–18.6	81.9–99.4
0.10	85.9–99.2	61.0–95.8	9.9–20.5	83.9–92.9
0.50	46.4–95.9	39.2–83.2	20.2–20.5	86.7–97.7
1.00	48.8–90.5	29.8–67.1	5.7–16.0	91.9–98.4
1.50	38.1–73.9	20.7–43.6	6.3–11.8	96.7–98.7

[a] Standard deviations in C_{base} and $C_{i\text{-}PrOH}$ were ±0.007 to 0.13 M (8.0 to 12.3%) and ±0.004 to 0.06 M (3.9 to 7.0%), respectively.

[b] % errors in C_{base} *before* correction via the dual sensor approach using Sensors **AY3** and **TY3**.

there is less error in C_{base} prediction in a more concentrated solution. This trend is particularly obvious for NaOH-EtOH-H_2O solutions. For example, the error in C_{base} prediction drops from a maximum of ca. 15.0% to <8.5% when C_{base} increases from 0.123 to 3.56 M NaOH in the range of 10 to 70 v/v% EtOH. (c) When the dual sensor approach is applied, greater accuracy in the $C_{alcohol}$ prediction is obtained in more concentrated alcoholic solutions. For example, 10 and 70 v/v% solutions of EtOH were predicted with an accuracy of 81.8 and 98.4%, respectively, at 1.23 M C_{base}. (d) Predictions for i-PrOH solutions gave a larger error range than those for EtOH or MeOH solutions. The increased error for the i-PrOH solutions is most likely due to the lower polarity of i-PrOH relative to MeOH and EtOH.

2.3.4 Indicator Selection. The chemical stability of the indicator molecules under hydroxide attack is a vital factor to sensor durability. This is especially important since our sensors primarily work in highly alkaline environments. Literature for base indicators with an appropriate pK_a range (13 to 18) is scarce. In our previous work,[19] a large number of indicators were tested, and Thiazole Yellow GGM, Alizarin Yellow R, Calcion, Arsenazo III, Azoviolet, and Chromothrope 2B were found resistant to hydroxide attack and oxidation by O_2 in air. Thiazole Yellow GGM and Alizarin Yellow R were found to be stable in 10 M aqueous NaOH solution for several weeks.[19]

Thiazole Yellow GGM and Alizarin Yellow R are both azo-dyes. Some azo compounds are highly colored thus making them excellent dyes. The colors

vary with the nature of the aryl group and the substituents.[85] Most azo dyes exhibit color changes at high *p*H (>11), therefore limiting their applications as universal indicators.[91] A detailed description of azo chemistry is presented by Zollinger.[91]

Resonance between the three nitrogens in Thiazole Yellow GGM (Figure 2.20a) exhibits a delocalization of electronic charge which may help resist nucleophilic attach by hydroxide. It has been experimentally proven that some azo-dyes are relatively stable in concentrated hydroxide.[19] A distinct isosbestic point between two absorbance maxima provides evidence for a simple equilibrium between the protonated and deprotonated form of Thiazole Yellow GGM. The azo proton contributes to the acid-base characteristics of the indicator. Safavi and Abdollahi reported a pK_a of 12.92 for Thiazole Yellow GGM in solution while exhibiting a color change from the yellow acid form to the orangish-red base form.[15]

Alizarin Yellow R exists as an anion in the acid form and as a dianion in the base form (Figure 2.20b).[92] The color change of yellow to brownish-red is associated with the dissociation of the phenolic hydroxyl group in alkaline media, forming the phenolate form.[93] The *p*H transition interval in aqueous solution is 10.0 to 12.1 with a reported pK_a range of 10.98 to 11.17.[92,93]

2.3.5 Impact of Sol-Gel Environment on Indicator Equilibria. pK_a values of indicators are usually measured in aqueous solutions. It has been reported that the presence of micelles in sol-gels dramatically alters the pK_a values of

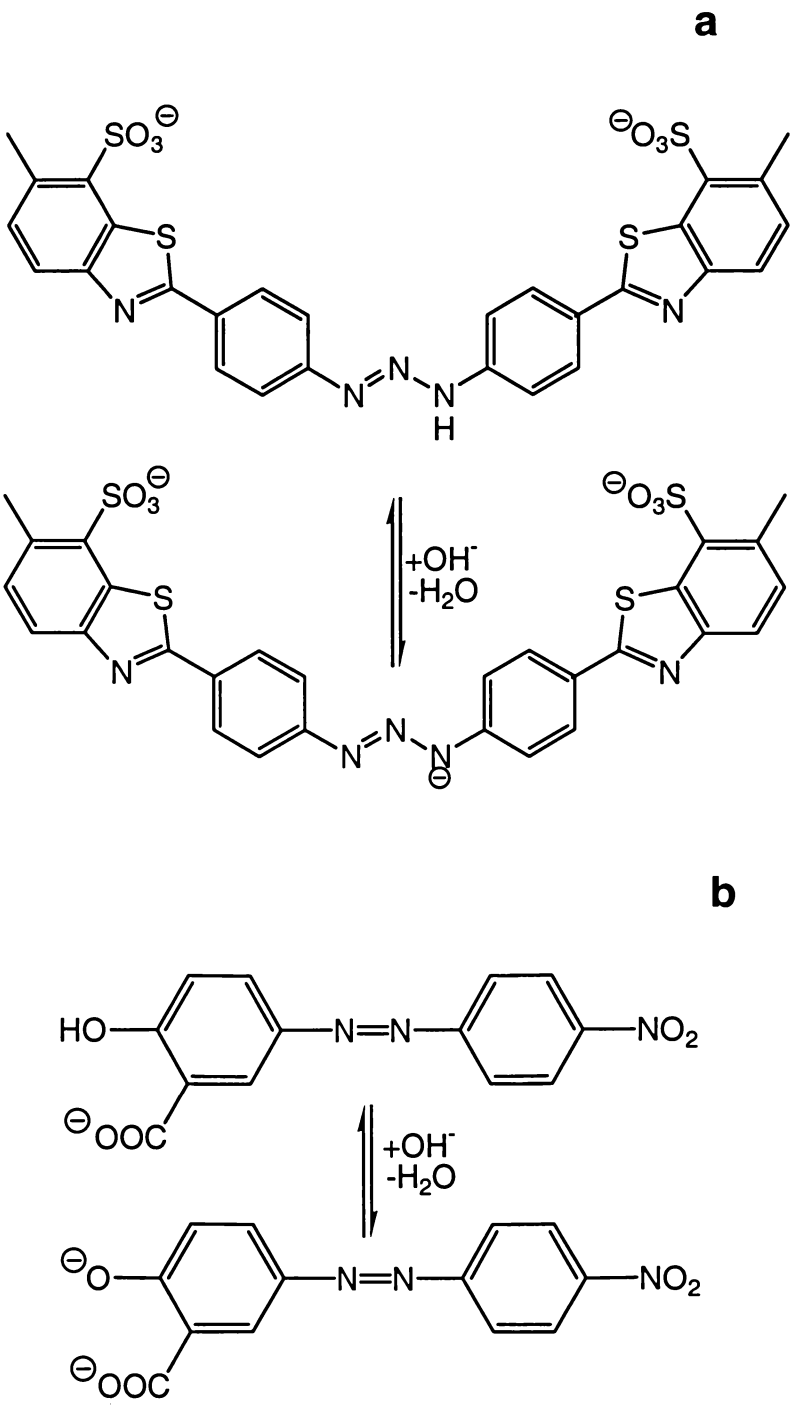

Figure 2.20. Equilibria involving the protonated and deprotonated forms of (a) Thiazole Yellow GGM and (b) Alizarin Yellow R.

indicators.[94] In our current sol-gel sensor thin films, Nafion, a poly(tetrafluoroethylene) polyphenylene ether sulfonate resin, was added to enhance the sensor response time.[1] Its presence in the ($Zr_xSi_yO_{2(x+y)}$)-Nafion composite may also enhance the structural integrity of the sensor film by filling in cracks and providing overall structural support.[19] We were interested in whether the presence of Nafion affects pK_a values of Thiazole Yellow GGM (TY) and Alizarin Yellow R (AY) indicators. The pK_a values of TY and AY in two different supports, ($Zr_{0.66}Si_1O_{3.32}$) and ($Zr_{0.66}Si_1O_{3.32}$)-Nafion, were determined by Eqs. 2.2-2.3 (Table 2.4).

The thermodynamic dissociation constant, K_a, was determined in the current studies by spectroscopic measurement of C_{NaOH} at half ionization (α = 0.5) for the sensors containing Thiazole Yellow indicator (Figure 2.21). Typical plots displaying the transmittance verse wavelength, using Sensors **TY2** and **AY2**, are shown in Figure 2.22. At half ionization, the concentration of the acid form of the indicator is equal to that of the base form, and $pK_a = H_$.[3] The point of intersection involving the acid and base forms of the respective indicator is equivalent to C_{base} at half ionization. The results of current studies are given in Table 2.4. There existed no distinct maxima separated by an isosbestic point for the sensors containing Alizarin Yellow. Therefore, the pK_a was determined by solving for the A located at the midpoint of the A vs C_{base} curve using the wavelength maxima. The A was converted to C_{base} using the curve fitting equation. For both indicators, a lower pK_a was observed in the ($Zr_{0.66}Si_1O_{3.32}$)-Nafion support. For instance, the pK_a of Alizarin Yellow R was 14.57 and 13.86

Table 2.4. Thermodynamic Dissociation Constants for Thiazole Yellow GGM (Sensors TY3 and TY4) and Alizarin Yellow R (Sensors AY3 and AY4) in ($Zr_{0.66}Si_1O_{3.32}$) and ($Zr_{0.66}Si_1O_{3.32}$)-Nafion Composite

Sensor	$[NaOH]_{\alpha = 0.5}$ / (M)	pK_a
($Zr_{0.66}Si_1O_{3.32}$) (**TY4**)	3.04 ± 0.50	14.80 ± 0.08
($Zr_{0.66}Si_1O_{3.32}$) (**AY4**)	2.19 ± 0.41	14.57 ± 0.09
($Zr_{0.66}Si_1O_{3.32}$)-Nafion (**TY3**)	2.18 ± 0.24	14.56 ± 0.06
($Zr_{0.66}Si_1O_{3.32}$) -Nafion (**AY3**)	0.64 ± 0.16	13.86 ± 0.12

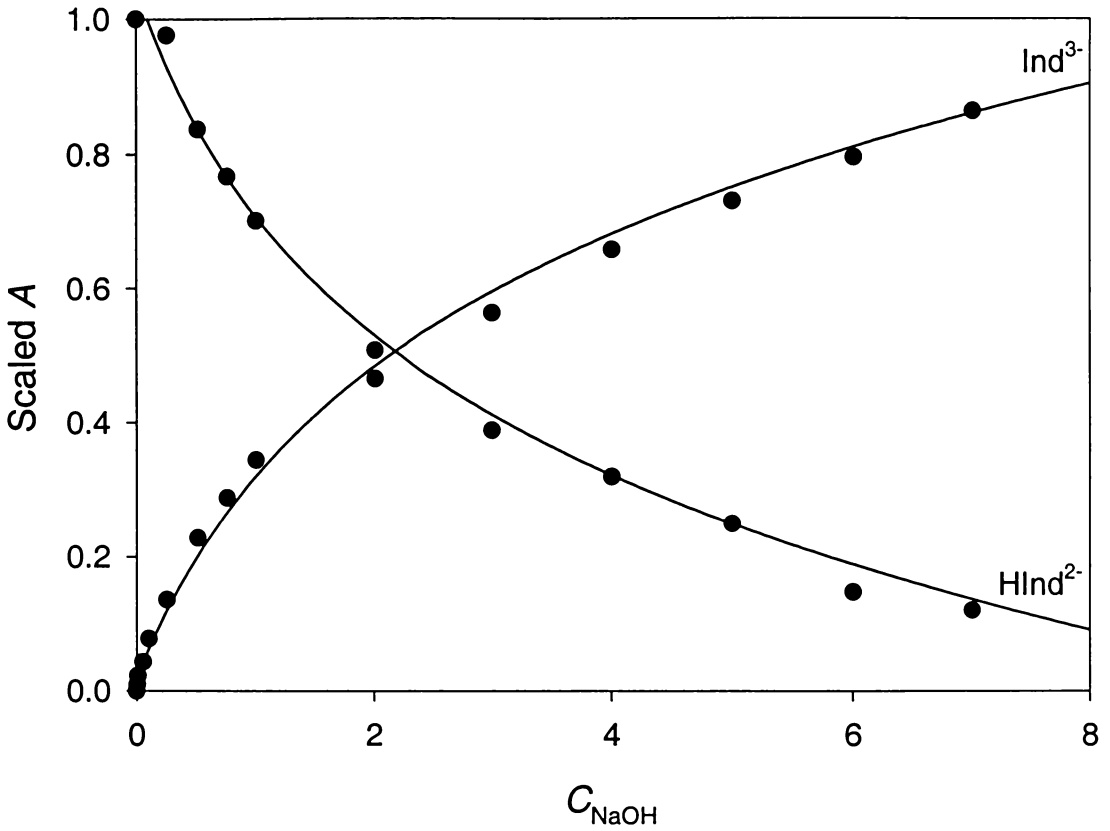

Figure 2.21. Distribution curves for the first ionization of Sensor **TY2** doped in a $(Zr_xSi_yO_{2(x+y)})$-Nafion sol-gel matrix. The curves were fitted by a 5th degree polynomial.

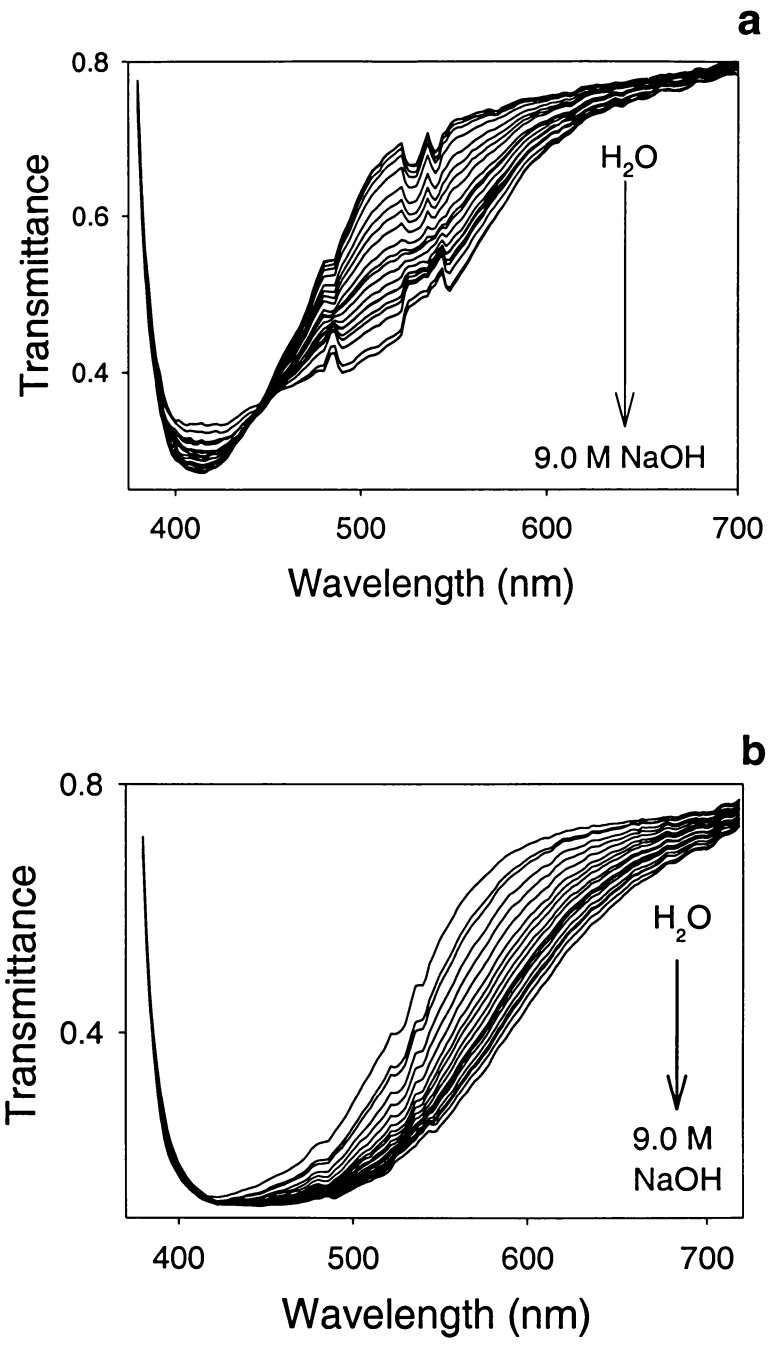

Figure 2.22. Transmittance spectra of a typical (a) Thiazole Yellow sensor and (b) Alizarin Yellow sensor in a ($Zr_xSi_yO_{2(x+y)}$)-Nafion support.

in the ($Zr_{0.66}Si_1O_{3.32}$) and ($Zr_{0.66}Si_1O_{3.32}$)-Nafion matrices, respectively. It is plausible that the shift to higher acidity for the dye infers that Nafion polymer acts as a proton sponge.[94] In other words, protons are being absorbed by the sulfonate groups in the Nafion molecules.

A shift to lower acidity is also observed for the sol-gel encapsulated indicators in comparison to their aqueous solutions. It is not clear why there are such large shifts for both TY and AY doped in Nafion-free, ($Zr_{0.66}Si_1O_{3.32}$) thin films. ZrO_2 is an amphoteric oxide,[95] and in alkaline solutions, it behaves as a weak acid. We speculate that, as a result, it is more difficult for the encapsulated indicator molecules in the ($Zr_{0.66}Si_1O_{3.32}$) thin films to dissociate H^+ ions in an alkaline solution, thus raising their pK_as.

2.4 Concluding Remarks

NaOH-ROH-H_2O (R = Me, Et, i-Pr) mixed solvent systems were studied and a novel linear relationship was observed between ($\partial A/\partial C_{alcohol}$) and C_{base} for high pK_a indicators encapsulated in sol-gel ($Zr_xSi_yO_{2(x+y)}$)-organic polymer composites. This relationship led to a dual transducer approach to give C_{base} and $C_{alcohol}$ with high accuracy and precision. In addition, the selection of indicators with high pK_as, a large dynamic spectral range, and chemical stability to OH^- attack and oxidation was fully evaluated. Refinements in the preparation of Thiazole Yellow and Alizarin Yellow sensors were presented as well.

CHAPTER 3

Characterization of the Materials of the Optical Sensor for Highly Alkaline Solutions and the Sensor Performance Evaluation

3.1 Introduction

Historically zircon ($SiZrO_4$) was known only as a naturally occurring gemstone found in igneous and metamorphic rocks.[96,97] Zircon, because of its chemical stability, is found in several sediment sources such as granite, granodiorite, syenite, monzonite, nepheline syenite, limestone, gneisses, and schiests.[97] Until modern times the identification of zircon was more of an art than a science. Separation of zircon from other minerals is now performed by electrostatic and electromagnetic elutriation.[98] Zircon exists naturally in several arrays of colors with the "colorless form" being the rarest.[96]

Zircon is a member of the nesosilicates. The SiO_4 tetrahedra are isolated and bound to each other only by ionic bonds from interstitial cations. Their structures are generally dependent upon the size and charge of the interstitial cations. Atomic packing of these nesosilicates is generally dense, thus resulting in a high specific gravity and hardness. The independent SiO_4 tetrahedra are not linked in chains or sheets in these cases, and therefore the crystalline nature of nesosilicates is usually equidimensional and void of pronounced cleavage directions.[97]

Zircon has a composition of ZrO_2 (67.2%) and SiO_2 (32.8%) and is known to be very resistant to normal chemical attack.[97] Zircon samples tend to contain a trace amount (typically 1 to 4 wt%) of Hf after the refining process.[97] Zr in zircon has an 8-coordination number with O forming a distorted cubelike polyhedra.[96,97,99,100] Of the eight O atoms surrounding the Zr atom, six belong to different SiO_4 tetrahedra (Figure 3.1).[97]

An entire crystal of zircon is held together primarily by valence forces that do not breakdown until approximately 1500 °C. The Zr and Si atoms are arranged in a diamond type tetrahedral lattice.[96] The lattice symmetry is determined by the tetragonal arrangement of the O atoms and not by the arrangement of the Zr and Si atoms.[96]

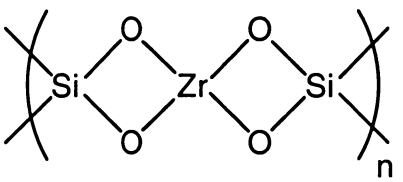

Some uses of zircon are radioactive age determinations,[97] ceramics, glazes, cements, coatings for casting molds, polishing materials, gem stones, catalyst in alkyl and alkenyl hydrocarbon manufacturing, fitted glass in filters, stabilizer in silicone rubbers, and cosmetic creams.[98]

Research has been performed to evaluate zircon stability in high *p*H environments. Glasses containing ZrO_2 are known to be chemically resistant in alkaline solutions.[7,101,102] Kamiya and coworkers explored the chemical durability

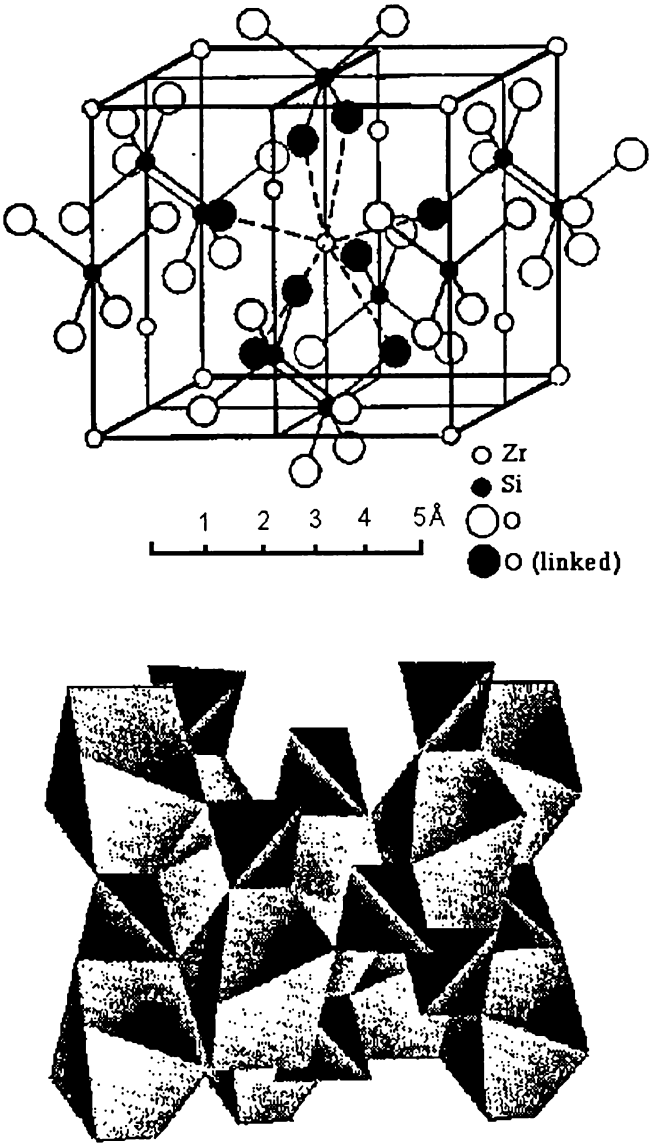

Figure 3.1. Two representations of the structure of zircon $ZrSiO_4$ consisting of independent tetrahedra SiO_2 and distorted ZrO_8 cubes. (Adapted from Klein, C.; Hurlbut Jr., C. S. *Manual of Mineralogy*, 21 ed.; John Wiley & Sons, Inc.: New York, 1977, p. 454; Bragg, W. L. *Atomic Structure of Minerals*; Cornell University Press: Ithaca, New York, 1937, p. 161).

of ZrO_2-SiO_2 glass fibers in alkaline solutions containing up to 33% w/w ZrO_2.[103] They prepared fibrous gels by low temperature sol-gel techniques, and then heated the gels to ~700 °C to form the glass fibers. Fiber diameter reduction as a function of alkali attack over a time interval was the basis of the alkali resistance comparisons. Their work revealed that the chemical durability of the glass fiber increased as the ZrO_2 content was increased.[103]

Baak and coworkers prepared various forms of glasses including ZrO_2-SiO_2 by high temperature melt techniques and subjected the glasses to various levels of alkaline attack.[101] They found that the ZrO_2-containing glasses displayed a substantial improvement in alkaline resistance as compared to the other glasses. They hypothesized that the increased durability was due to the formation of a surface layer containing insoluble sodium zirconosilicates.[101]

An increased stability in alkaline environments for ZrO_2-containing glasses was also explored by Das.[104] He examined the occupancy of surface sites of SiO_2, ZrO_2, and Al_2O_3 for materials prepared from high temperature melts. Both the diffusion coefficient of the alkali ion and the linear rate of extraction of alkali and silica showed a gradual change until a given *p*H was reached, displaying a sharp change.[104] The sharp change for SiO_2 and Al_2O_3-containing glasses occurred at 50% occupancy of the surface sites by alkali ions at a *p*H 9.8 and 11, respectively.[104] In the case of ZrO_2-containing glasses, 50% occupancy would not be reached until *p*H 19. In other words, the solubility of the ZrO_2-containing glass is much less than SiO_2-containing glass at equivalent high *p*H.[104] Therefore, the substitution of SiO_2 with ZrO_2 makes the glasses less susceptible

to chemical attack throughout the high *p*H region as evident by the decrease in the rate of glass extraction.[104] The sharp changes in diffusion and solubility that were present at *p*H 9.8 for pure silica glasses essentially disappear.[104]

ZrO_2 has been found to be virtually insoluble in strong base and to exhibit a low inclination for complete hydrolysis.[105] It has been rationalized that a protective hydrated insoluble ZrO_2 layer is generated in a concentrated base for ZrO_2-containing glasses.[7,105] Thermodynamically, dissolved ZrO^{2+}, Zr^{4+}, and $HZrO_3^-$ ions are energetically unfavorable and exist only below *p*H ~0 and above *p*H ~17.[7] However, hydration of ZrO_2 to form a protective layer is energetically favorable and should occur at all conceivable *p*H ranges. This is the rationale for the enhanced durability.[7]

In our recent work on base sensors, we found that, before the addition of Zr via the alkoxide precursor in the sol-gel process, purely silica sensor films were highly unstable in alkaline solutions. Blending Zr and Si alkoxide precursors in a moisture-controlled environment yielded films of enhanced durability. We thus studied the Si-O-Zr bonding characteristics of our sensor materials to understand their stability to OH^- attack, and explored the mixed metal oxide bonding rationale for the enhancement in the durability.[19] Chemical and physical properties of our sensor films were investigated by solid-state ^{29}Si NMR, reflectance FT-IR, XPS, BET, SEM, and profilometry to gain an insight into the chemistry of the sensor film. These studies are reported here.

We have also evaluated the sensor performance by analysis of response times, hysteresis effects, and durability in NaOH-ROH-H_2O *ternary* solutions (R =

Me, Et, and i-Pr). We previously found that hysteresis is inherently associated to response time.[106] The film morphology (porosity, surface area, and thickness) directly determines the performance of the sensor. By careful manipulation of the independent variables (*p*H, solvent concentration, alkoxide concentration, and drying conditions), the chemistry of the base sensor sol-gel support is controlled which ultimately determines the response kinetics, hysteresis, and durability of our sensors. These studies are also reported.

3.2 Experimental Section

Powders of silica SiO_2 (Powder **1**, Davisil grade 635, 99%, 60-100 mesh, Aldrich), zircon $ZrSiO_4$ (Powder **2**, -325 mesh, 99%, Acros), and zirconia ZrO_2 (Powder **3**, 99+%, Strem) were used as received. Alcoholic solutions were prepared by volumetric dilution % v/v. Hydroxide is known to absorb a small amount of carbon dioxide from the atmosphere; therefore solutions were prepared by gravimetric dilution before each trial to ensure maximum accuracy. Hydroxide solutions were titrated with standard HCl to the phenolphthalein end point to verify their concentrations. EtOH used for the sensor preparation was dried by the standard sodium drying procedures.[78] Thiazole Yellow GGM (TY, 40% dye content, Eastman), Alizarin Yellow R (AY, 80% dye content, Eastman), $Si(OMe)_4$ (99+%, Aldrich), $Zr(O\text{-}n\text{-}Bu)_4$ (80% w/w). in 1-n-BuOH, Aldrich), Nafion (5% Nafion in an alcoholic mixture containing 5% w/w water, Aldrich), $HCONMe_2$ (DMF, 99.9+%, Aldrich), MeOH (99.9%, Fisher), EtOH (absolute, AAPER), i-PrOH (99.9%, Aldrich), HCl standard (0.25 N, LabChem. Inc.), and NaOH

(99.99%, Fisher) were used as received. Data Analysis was conducted by the following programs: Matlab™ (The Math Works, Inc., 3 Apple Hill Drive, Natick, MA 01760-2098; http://mathworks.com), Sigma Plot™ (SPSS Inc., 233 Wacker Drive, 11th floor, Chicago, IL 60606-6307; http://www.spss.com), and Maple™ (Waterloo Maple Inc., 57 Erb Street, W. Waterloo, Ontario, Canada N2L 6C2; http://www.maplesoft.com). Visible spectra were recorded using a visible spectrometer described in Section 1.3.1.[12] Repetition scans were recorded and averaged to minimize the drift error in the instrument.

3.2.1 Preparation of the Sol-Gel Powders.

(a) ZrO_2 (Powder 4). A solution containing H_2O (5 µL), 1.00 M HCl (10 µL), and dry EtOH (200 µL, 3.43 mmol) was stirred at room temperature in a closed vial for 1 min. While stirring vigorously, $Zr(O\text{-}n\text{-}Bu)_4$ (350 µL, 0.889 mmol) was added. The solution was vigorously stirred at room temperature for 2 min. A white precipitate formed in several minutes. The sample was ground with a mortar and pestle.

(b) SiO_2 (Powder 5). A solution containing 0.010 M HCl (134 µL) and MeOH (800 µL, 19.75 mmol) was stirred at room temperature in a vial for 1 min. While stirring, $Si(OMe)_4$ (400 µL, 2.72 mmol) was added. The solution was stirred overnight at room temperature. A clear glass was formed. The sample was ground with a mortar and pestle.

(c) $Zr_{0.66}Si_1O_{3.32}$ (Powder 6). A solution containing H_2O (10 µL) and 1.00 M HCl (5 µL) were stirred at room temperature in a closed vial for 3-5 min. Dry MeOH (150 µL, 3.71 mmol) and $Si(OMe)_4$ (200 µL, 1.36 mmol) were then added to the stirring solution. The vial was kept close and stirred for 10 min in order for pre hydrolysis to occur. While stirring vigorously, $Zr(O\text{-}n\text{-}Bu)_4$ (325 µL, 0.889 mmol) was added and immediately resealed to prevent precipitation of ZrO_2 due to humidity. The solution was vigorously stirred at room temperature for 2 min. A clear glass was formed. The sample was ground with a mortar and pestle.

(d) $Zr_xSi_yO_{2(x+y)}$ (Powders 7-9). Powders **7-9** was prepared in a procedure similar to that in the preparation of Powder **6**. Instead of 200 µL (0.547 mmol), 100 µL (0.273 mmol) and 50 µL (0.137 mmol) of $Zr(O\text{-}n\text{-}Bu)_4$ were used to prepare Powders **7**, **8**, and **9**, respectively. The Zr:Si ratios are 0.66, 0.40, 0.20, and 0.10 for Powders **6**-**9**, respectively.

(e) $Zr_{0.66}Si_1O_{3.32}$-Nafion (Powder 10). A solution containing H_2O (10 µL), and 1.00 M HCl (5 µL) was stirred at room temperature in a closed vial for 3-5 min. Nafion (170 mg) was added by pipet and stirred for ca. 1 min. Dry MeOH (150 µL) and $Si(OMe)_4$ (200 µL) were then added to the stirring solution. The vial was kept close and stirred for 10 min in order for pre-hydrolysis to occur. While stirring vigorously, $Zr(O\text{-}n\text{-}Bu)_4$ (325 µL) was added, and the vial was immediately resealed to prevent precipitation of ZrO_2, as $Zr(O\text{-}n\text{-}Bu)_4$ is very air-sensitive. The solution was vigorously stirred at room temperature until the gel was formed.

(f) $Zr_{0.66}Si_1O_{3.32}$-Nafion-AY (Powder 11). A solution containing H_2O (5 µL), 1.00 M HCl (10 µL), DMF (150 µL), and Alizarin Yellow R (16.0 mg) was stirred at room temperature in a closed vial for 3 to 5 min. Nafion (160 mg) was added and the mixture stirred for ca. 1 min. Dry EtOH (150 µL) and $Si(OMe)_4$ (200 µL) were then added to the stirring solution. The vial was kept close and stirred for 10 min. While stirring vigorously, $Zr(O\text{-}n\text{-}Bu)_4$ (325 µL) was added, and the vial was immediately resealed. The solution was vigorously stirred at room temperature until the gel was formed.

(g) $Zr_{0.66}Si_1O_{3.32}$-Nafion-TY (Powder 12). A solution containing H_2O (10 µL), 1.00 M HCl (5 µL), DMF (125 µL), and Thiazole Yellow GGM (35.5 mg) was stirred at room temperature in a closed vial for 3 to 5 min to insure maximum solubility. Nafion (170 mg) was added by pipet and the mixture stirred for ca. 1 min. Dry MeOH (150 µL) and $Si(OMe)_4$ (200 µL) were then added to the stirring solution. The vial was kept close and stirred for 10 min in order for pre-hydrolysis to occur. While stirring vigorously, $Zr(O\text{-}n\text{-}Bu)_4$ (325 µL) was added, and the vial was immediately resealed. The solution was vigorously stirred at room temperature until the gel was formed.

3.2.2 Instrument

(a) Scanning Electron Microscopy (SEM). An Amray SEM 1830 microscope was used to study surface morphology. The microscope includes the following specifications: a 48505 microscope interface module made by Kevex®, a 500 digital processor made by IXRF® Systems Inc., and an EDS2000 microanalysis

system software package developed by IXRF® Systems Inc. All SEM studies were conducted under the direction of Dr. David B. Beach at Oak Ridge National Laboratory.

(b) Profilometer. An Alpha-Step 500 Surface Profiler was used to determine the thickness (microns) of the thin films deposited upon the glass substrates. Our sensors were too coarse for elipsometry measurements. Covering a half of the sensor film with black wax (a hydrocarbon) and then dipping the sensor into concentrated HF created the step between the glass substrate and the film surface. The portion covered by the black wax was protected from the corrosive HF. The black wax was then removed with hexane and the sensor was washed with alcohol and water, leaving behind a uniform step. A total of 3 sensors with 5 scans per sensor were examined at room temperature. These studies were conducted under the direction of David B. Beach at Oak Ridge National Laboratory.

(c) BET Measurement. A Nova 1000 High Speed Surface Area and Pore Size Analyzer by Quantachrome Corp.® was used to study specific surface area, total pore volume, and pore size distribution. The BET system used in this study consists of a gas storage system, a gas dosing system, a pressure-measuring device, and a sample unit. The sample unit is the destination of the gas. A known amount of gas is dispersed onto the sample system, and a portion of the gas is adsorbed by the sample.

The calibration of the BET instrument was conducted with a Davisil-635 Silica standard. The specific surface area, average pore diameter, and total pore

volume were experimentally determined to be 475 ± 8 m^2/g, 61 ± 6 Å, and 0.720 ± 0.108 cm^3/g, respectively. The reported values by the manufacture are 480 m^2/g, 60 Å, and 0.75 cm^3/g, respectively.

BET surface areas and other BET parameters were calculated from ten points in the relative pressure range 0.04 to 0.36 assuming a cross-sectional area of 0.162 nm^2 for a nitrogen molecule. The amount of nitrogen absorbed at $P/P^o = 0.95$, assuming a liquid density of nitrogen at 77 K of 0.808 g/cm^3, was used to determine the total pore volume of the bulk materials. The BET sample size ranged from 0.070 to 0.120 g.

(d) X-ray Photoelectron Spectroscopy (XPS). An upgraded Perkin-Elmer Phi 5000 Series Electron Spectroscopy for Chemical Analysis System was used to study the bonding characteristics of the mixed metal sol-gel support comprising the sensor films. The apparatus consisted of a Perkin-Elmer diode array X-ray source and a differential ion gun.

XPS samples were prepared by using an adhesive tape to hold the sample to the sample holder. XPS samples ranged from 0.050 to 0.100 g. Calibration of the spectrometer was based upon the In (*3d 5/2*) line binding energy of 443.6 eV.[72] Instrumental factors including imperfections in the electron-velocity analyzer and the monochromator were taken into account.[70] Survey spectra of the samples were recorded for the 0 to 800 eV region to determine the elements that were present in the sample and surface contamination. The step size was 0.25 eV which represents the resolution of the XPS survey spectra. The X-ray source was Mg K_α (1254 eV). A total of 20

sweeps were collected for each sample using a pass energy of 35.75 eV and a work function of 4 eV. The following photoelectron lines were observed: Zr (4*p*), Zr (3*d* 5/2), Zr (3*d* 3/2), Zr (3*p* 3/2), Zr (3*p* 1/2), O (1*s*), O (*KVV*), Si (2*p*), Si (2*s*), and C (1*s*).

The peaks of interest were normalized at the maximum of the photoelectron line in order to more adequately visualize the chemical shifts. Peak location (eV) was determined by the half width at the half intensity. Calibration was performed on all spectra.

(e) ^{29}Si Solid-State NMR. All standard Bloch decay experiments were performed at room temperature using a Varian Inova 400 MHz solid state NMR spectrometer equipped with a Fourier transform unit. A total of 2000 scans were recorded. Individual scans consisted of a $\pi/6$ pulse at a width of 1.6 μs with a 30 s relaxation decay. Exponential multiplication using a line broadening of 100 Hz was performed prior to Fourier transformation. The internal reference was cubic octamer silicic acid trimethylsilyl ester, $Si_8O_{12}(O_8SiMe_3)_8$, which has a singlet at 11.72 ppm and a doublet of doublets at -108.36, -108.64, -109.36, and -109.71 ppm.[107]

(f) FT-IR. A Bio-Rad FTS-60A (serial number 34180) Infrared Spectrometer was used to study the bonding characteristics of the mixed metal polymeric support comprising the sensor films. Reflectance IR measurements were recorded in the mid-IR regime of 400 to 4000 cm^{-1} with a resolution of 8 cm^{-1}. The scan speed was 5 kHz at a delay of 3.0 s. IR samples ranged from 0.075 to 0.100 g.

3.2.3 Sensor Data Collection.

(a) Hysteresis, Kinetic, and Durability Data Collection. Optical data collection was performed using the apparatus described in Section 1.3.1. The chemicals, solutions, and data analysis procedures are described in Section 2.2.1. Sensors **TY5-8** and **AY5-8** were prepared by the procedure in Section 2.2.1-2.2.3.

(b) Kinetics and Hysteresis Experiments. Sensors were stored in water for two days before collecting data. All kinetic data were collected under continuous flowing solutions for a 10-min duration. Data were collected across the positive and negative concentration gradients at room temperature. Sensors were thoroughly washed with de-ionized water between cycles. Response times were the time for the sensor to achieve 90% of the total analytical range. Data were collected and automatically saved as individual files. A program written and operated using UNIX was used to import and script the raw data into Sigma Plot© as a single ASCII file (Appendix A). Individual points on the hysteresis plots were based upon a fixed time domain for both gradients.

(c) Durability Experiments. Sensors **TY6-8** and **AY6-8** were independently used to collect data in NaOH-ROH-H_2O ternary solutions (R = Me, Et, and i-Pr), respectively, for Sensors **TY6**, **7**, and **8** as well as Sensors **AY6**, **7**, and **8**. The C_{NaOH} was 2.00, 2.00, and 0.50 M for MeOH, EtOH, and i-PrOH, respectively. The sensors were monitored spectroscopically in the solution in which they were stored. Transmittance signals were converted to corresponding absorbance values. Individual absorbance values at a specific wavelength were divided by

the absorbance value at the isosbestic wavelength. This was performed in order to compensate for variations in light power or detection.

3.3 Results and Discussion

3.3.1 Physical Characterization of Sensor Films. In the sensor materials containing Nafion and ($Zr_xSi_yO_{2(x+y)}$) (Powders **10-12**, Table 3.1), much lower surface areas and pore volumes were obtained by BET. This suggests that Nafion possibly covered the ($Zr_xSi_yO_{2(x+y)}$) surface extensively, thus reducing the ability of the composite to absorb N_2 on its surface. The average pore diameters of Nafion-containing Powders **10-12** were slightly larger than Powder **6** that did not contain Nafion.

Powder **5** (SiO_2 only) and Powder **6** ($Zr_{0.66}Si_1O_{3.32}$) prepared by acid catalysis have much higher specific surface areas (214 m^2/g for **Powder 5** and 238 m^2/g for Powder **6**) and total pore volumes (0.13 cm^3/g for **Powder 5** and 0.22 cm^3/g for Powder **6**) than Powder **4** (ZrO_2 only; surface area: 57 m^2/g; total pore volume: 0.052 cm^3/g) prepared by acid catalysis. Powders **7-9** also have much higher surface areas and pore volumes (Table 3.1). There is an evident reduction in surface area and total pore volume from pure SiO_2 to pure ZrO_2 samples. It is not clear why such a reduction occurs. However, this observation is consistent with slower OH^- diffusion in "ZrO_2-only films," a topic that has been addressed earlier in our group.[19] Powder **2**, the zircon standard, had a specific surface area of 11 m^2/g, an average pore diameter of 79 Å, and a total pore volume of 0.022 cm^3/g.

Table 3.1. BET Results of the Bulk Samples

Powder	Surface Area (m^2/g)	Avg. Pore Diameter (Å)	Total Pore Volume (cm^3/g)
SiO_2-Davisil grade 635-Aldrich)	475	61	0.72
2 (Zircon-Acros)	11	79	0.022
3 (ZrO_2-Strem)	62	40	0.055
4 (sol-gel ZrO_2)	57	37	0.052
5 (sol-gel SiO_2)	238	26	0.22
6 (Zr/Si: 0.66)	214	25	0.13
7 (Zr/Si: 0.40)	222	25	0.12
8 (Zr/Si: 0.20)	217	23	0.16
9 (Zr/Si: 0.10)	230	26	0.20
10 ($Zr_{0.66}Si_1O_{3.32}$-Nafion)	5	49	0.0059
11 ($Zr_{0.66}Si_1O_{3.32}$-Nafion-AY)	3	33	0.0022
12 ($Zr_{0.66}Si_1O_{3.32}$-Nafion-TY)	3	34	0.0028

To summarize, a high miscibility results in a high homogeneity and effective Si-O-Zr bond formation, and produced films with a high surface area as compared to ZrO_2 composites. This is done by stoichiometrically controlling the hydrolysis rate of the zirconium alkoxide $Zr(O\text{-}n\text{-}Bu)_4$ via prehydrolysis of the silicon alkoxide $Si(OMe)_4$ precursor.

Profilometry measurements showed that the sensor film thickness ranged from 3.4 to 5.0 μm (Figure 3.2). These surface profilers can take measurements in a range of thickness from 100 Å to 0.3 mm.

Scanning electron micrographs (SEM) at 100, 1000, 10,000, and 30,000x magnification are presented in Figures 3.3 and 3.4 for Sensor **AY1**. The acid-catalyzed catalysis in the preparation of this film provides a smooth surface with some inherent crackings. The sensor morphology is dependent upon the sol-gel technique.[19,30] Cracks ranged in size from 0.1 to 1.0 μm.

3.3.2 Chemical Characterization of Sensor Films. Several spectroscopic techniques were used in the current studies to evaluate the sol-gel samples.

(a) X-Ray Photoelectron Spectroscopy (XPS). A correction for charging effects based on an internal calibration using the adventitious C (1*s*) photoelectron line was performed. This was conducted in order to correct the spectrum to the reference binding-energy scale. This thin carbon contamination on the sample surface is suspected to come from diffusion pump oil, air, and/or residual alkoxide precursor hydrocarbons.[72] This contamination is present in all samples prepared by the sol-gel technique. Any shift in this line can be taken as

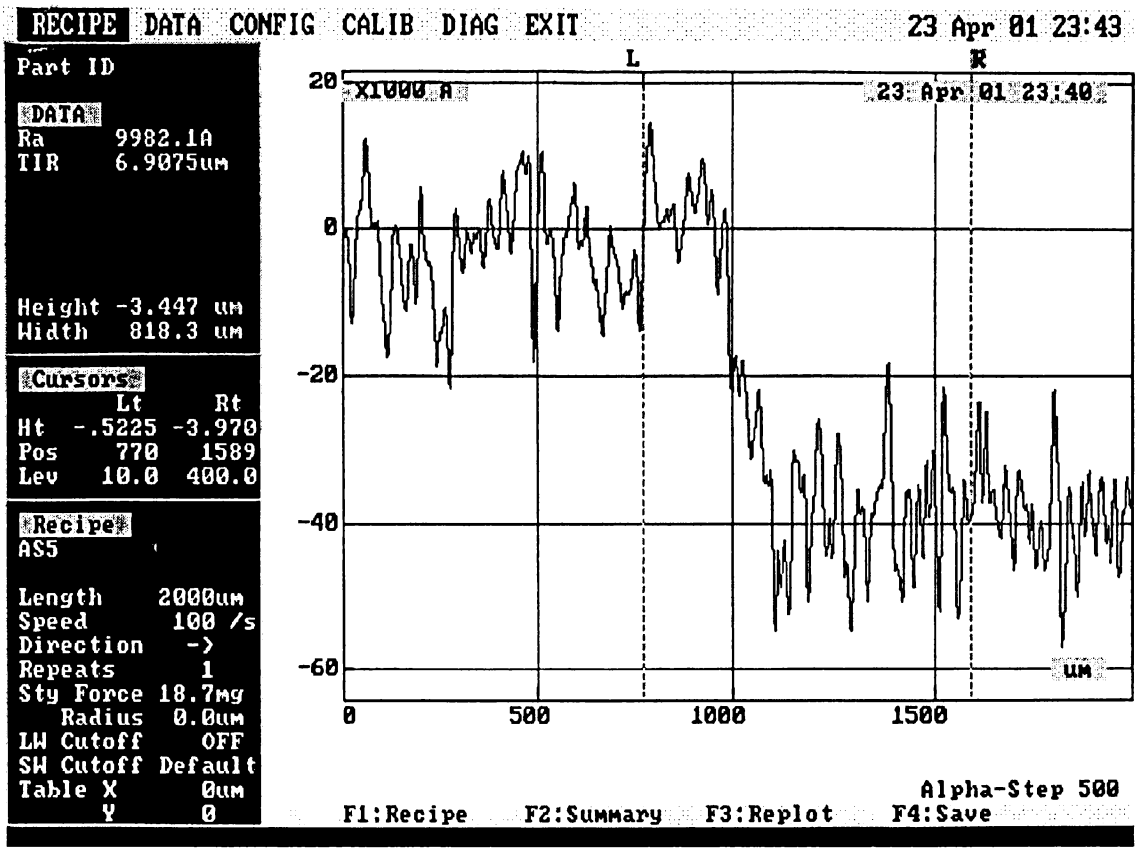

Figure 3.2. An example of a typical spectrum recorded by a profilometer. In this case the step size was appropriately 3.45 μm.

a

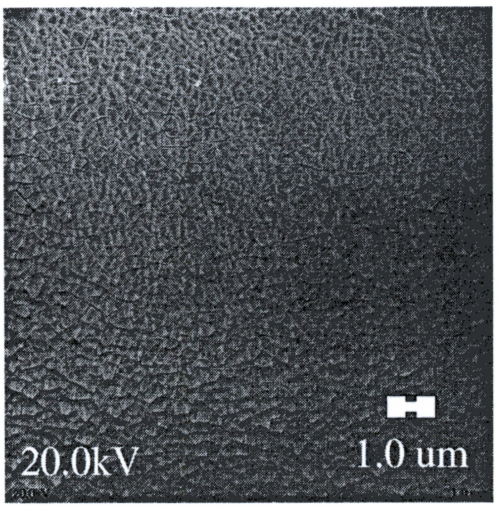

b

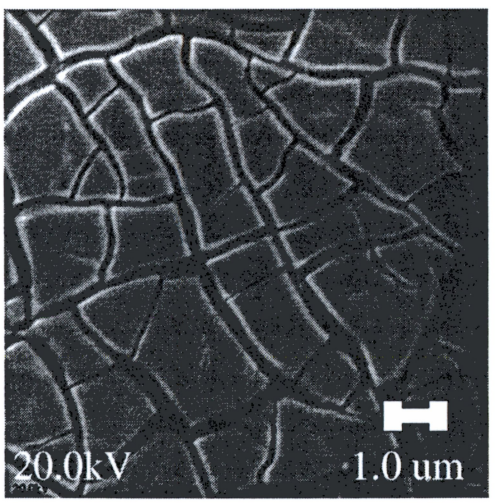

Figure 3.3. SEM images of Sensor **AY1** at (a) 100x magnification and (b) 1000x magnification.

a

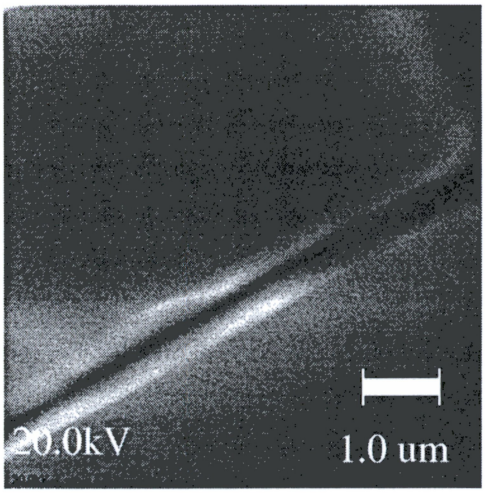

b

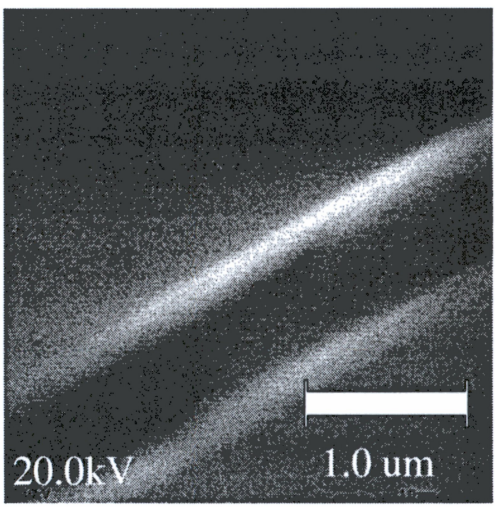

Figure 3.4. SEM images of Sensor **AY1** at (a) 10000x magnification and (b) 30000x magnification.

a measure of static charge.[72] The true binding energy for a photoelectron line is assumed to be $E_b - V$, where E_b is the measured binding energy and V is the correction term due to charging effects of solid samples. V is the difference between the spectrometer ground potential and the surface potential. This is under the condition that differential charging is negligible, and that the entire spectrum is shifted uniformly by the correction term.[108] This also implies that the adventitious C (1*s*) line is at the same location in all samples. This assumption has been checked for all samples containing the C (1*s*) line and no appreciable shift is present between samples. Therefore, calibration was achieved by setting the C (1*s*) binding energy at 284.6 eV.[72,108]

Important features can be obtained from XPS spectra such as chemical shift information, spin splitting, and elemental identification. Chemical shifts due to changing electronic environment are usually small, on the order of a few eV or less, and the overlap of lines due to different elements is unlikely. Every element, except H and He, exhibits photoelectron peaks between 20 to 1200 eV.[70] XPS survey spectra and values are given for Powders **1**-**6** in Figures 3.5-3.7 and Table 3.2. Spin complications can also arise in the case of Zr. For the 3*d* and 3*p* electrons of zirconium, the splittings of the Zr (3*d 5/2*), Zr (3*d 3/2*), Zr (3*p 3/2*), and Zr (3*p 1/2*) photoelectron peaks may occur. Two states with different energies for electrons in a given orbital such as *3d* or 3*p* can result depending upon the spin angular momentum being aligned parallel or anti-parallel to the orbital angular momentum.[70]

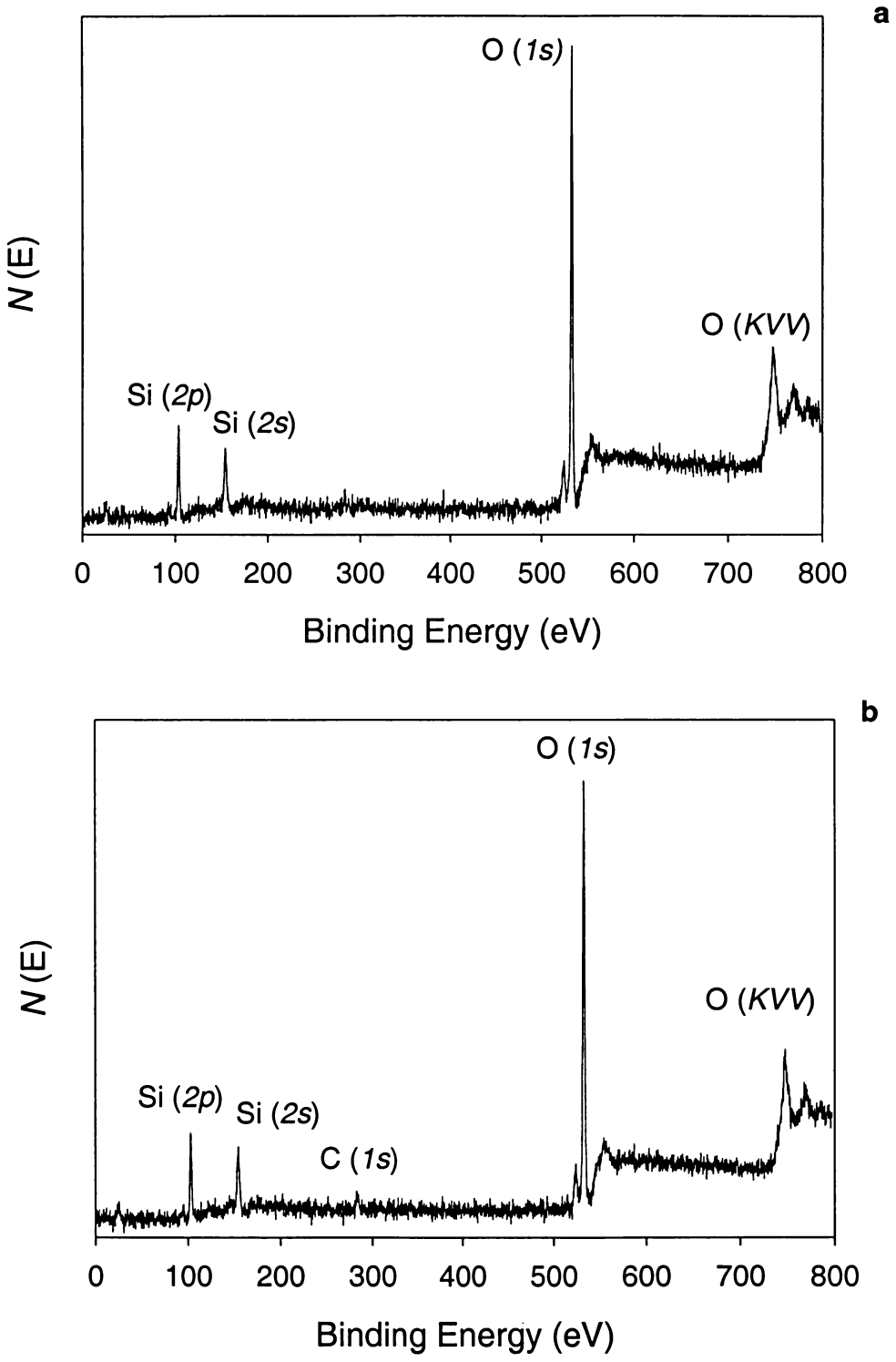

Figure 3.5. The XPS spectra of Powders (a) **1** and (b) **5**.

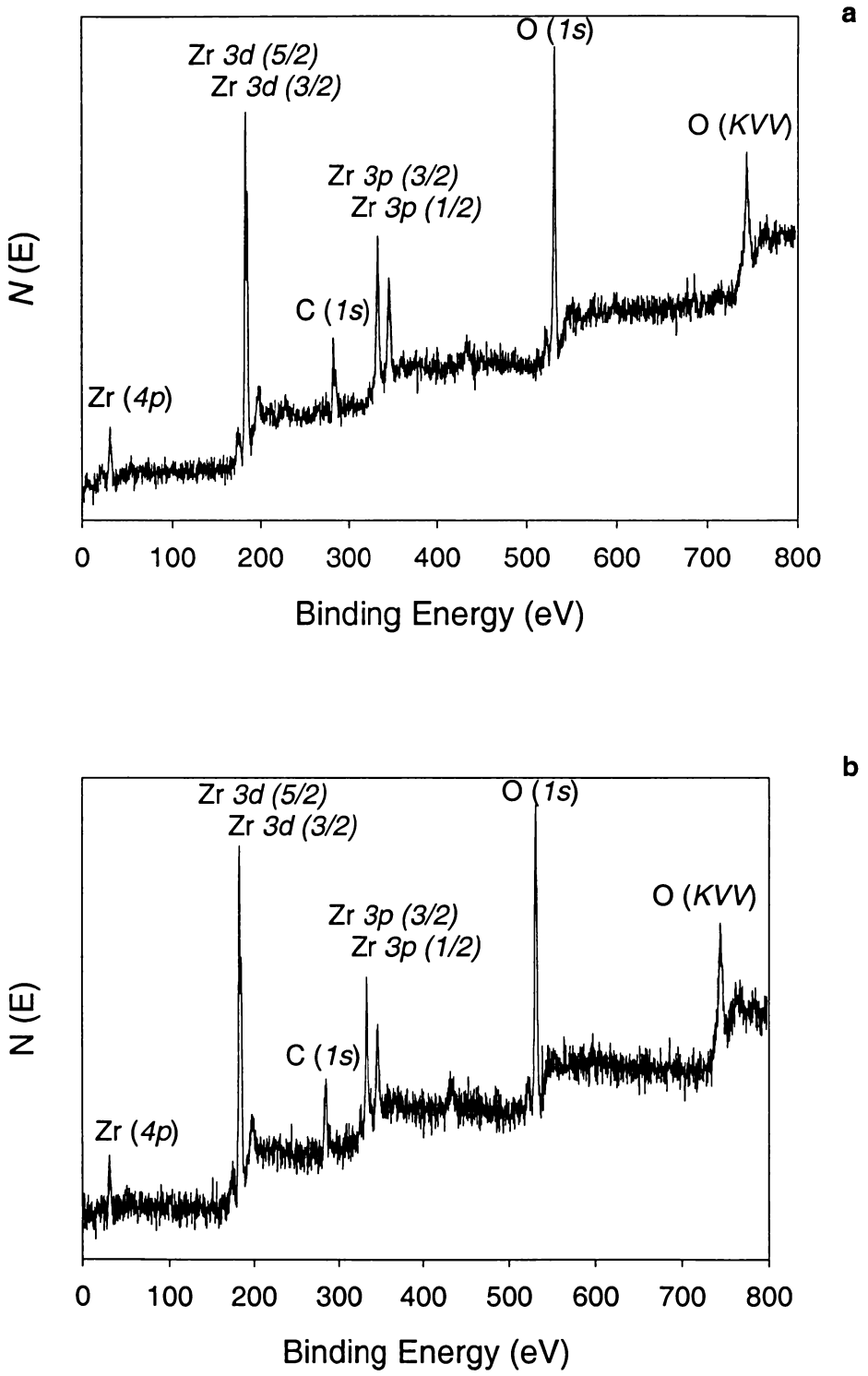

Figure 3.6. The XPS spectra of Powders (a) **3** and (b) **4**.

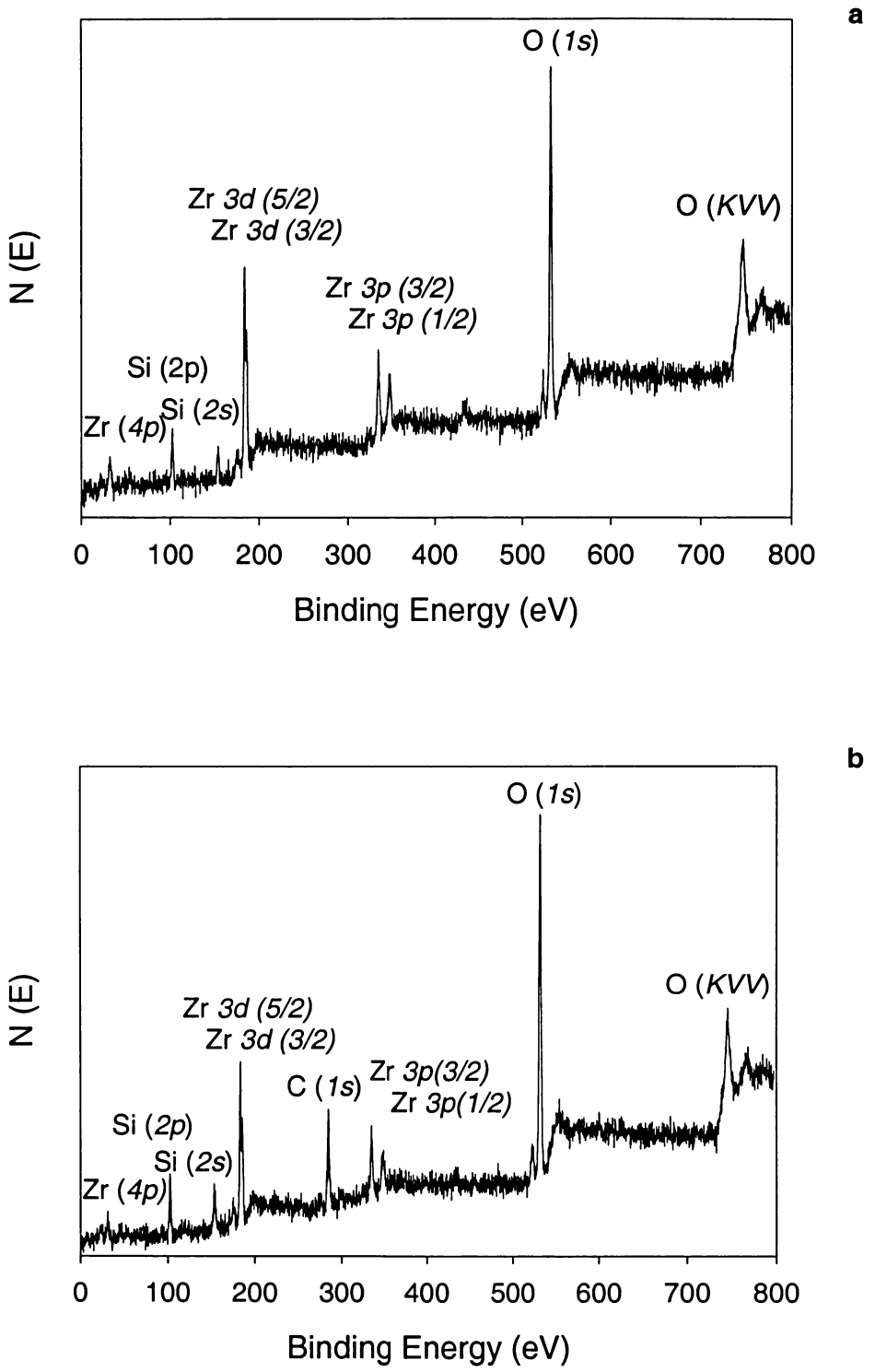

Figure 3.7. The XPS spectra of Powders (a) **2** and (b) **6**.

Table 3.2. Relative XPS Peak Designations (Wagner, C. D.; Riggs, W. M.; Davis, L. E.; Moudler, J. F. *Handbook of X-Ray Photoelectron Spectroscopy*; Perkin-Elmer Corp.: Eden Prairie, MN, 1979.)

Peak Assignment	Relative Location (eV)
Zr (4*p*)	~31
Si (2*p*)	~103
Si (2*s*)	~154
Zr 3*d*(*5/2*)	~183
Zr 3*d*(*3/2*)	~185
C (1*s*)	~285
Zr 3*p*(*3/2*)	~334
Zr 3*p*(*1/2*)	~347
O (1*s*)	~532
O (*KVV*)	~746

Ionic vs covalent character can be analyzed by chemical shift data. Zirconia (ZrO_2) is found to be more ionic than quartz (SiO_2). This difference is due to the larger charge of oxygen in zirconia vs in quartz.[108] However in the case of the mixed oxide ($Zr_xSi_yO_{2(x+y)}$), Zr carries less electron density and Si carries more electron density more covalent, as a result of competition for electrons between Zr (electronegativitiy = 1.4[109]) and Si (electronegativitiy = 1.8[109]) in the mixed oxides. The calculated positive charge on Si is smaller in zircon than in quartz. Zr exhibits the opposite behavior showing a larger calculated positive charge in zircon than in ZrO_2.[108]

Based upon *ab initio* electronic structure calculations using density-functional theory in the local density approximation (DFT-LDA), the ionic charge of each of the ions in the three different oxides could be determined.[108] Oxygen atoms are tricoordinated to one Si and two Zr atoms in zircon. O atoms in silica and zirconia have two Si and four Zr neighbors (assuming monoclinic zirconia), respectively. SiO_4 tetrahedra exist in both silica and zircon. However seven O atoms are bound to one Zr atom in zirconia vs eight in zircon.[100,108,110] According to Guittet and coworkers, the calculated charge (q) on Si was 2.05 and 1.93 eV for silica and zircon, respectively.[108] For Zr the values were 2.76 and 2.85 eV for zirconia and zircon $ZrSiO_4$, respectively.

In our studies, we found that the binding energies (E_b) of Si was smaller in zircon ($Zr_xSi_yO_{2(x+y)}$) than in silica (SiO_2), and the E_b of Zr was larger for zircon ($Zr_xSi_yO_{2(x+y)}$) than in zirconia ZrO_2 (Table 3.3). This trend is in accordance with the changes in charge for Si and Zr. The Si ($2p$) peaks of Davisil grade 635 SiO_2

Table 3.3. XPS Peaks of Powders (step size = 0.25 eV)

Powder	O (1*s*) (eV)	Zr (3*d 5/2*) (eV)	Si (2*p*) (eV)
SiO_2-Standard (**1**)	533.05		103.75
SiO_2-Prepared (**5**)	533.00		103.40
ZrO_2-Standard (**3**)	531.00	182.75	
ZrO_2-Prepared (**4**)	531.00	182.70	
$SiZrO_4$-Standard (**2**)	532.25	183.80	102.60
$(Zr_{0.66}Si_1O_{3.32})$-Prepared (**6**)	532.25	183.70	102.50

(Powder **1**) and sol-gel SiO_2 (Powder **5**) were located at 103.75 and 103.40 eV, respectively. In comparison, the Si (2*p*) peaks for the zircon standard (Powder **2**) and sol-gel $Zr_{0.66}Si_1O_{3.32}$ (Powder **6**) were shifted to 102.60 and 102.50 eV, respectively. A net shift of 1.15 and 0.90 eV to lower E_b from silica to $Zr_{0.66}Si_1O_{3.32}$ mixed oxide in the Si (2*p*) photoelectron peak is given in Figure 3.8.

The Zr (3*d 5/2*) peaks of ZrO_2 standard (Powder **3**) and sol-gel ZrO_2 (Powder **4**) were located at 182.75 and 182.70 eV, respectively, and are essentially the same within resolution of the spectrometer. The Zr (3*d 5/2*) peaks of zircon standard (Powder **2**) and sol-gel $Zr_{0.66}Si_1O_{3.32}$ (Powder **6**) were shifted to 183.80 and 183.70 eV, respectively (Figure 3.9), thus giving a net shift of 1.05 and 1.00 eV to higher E_b from ZrO_2 to $Zr_{0.66}Si_1O_{3.32}$ for the Zr (3*d 5/2*) photoelectron peak.

The trends observed here are in accordance with previously reported experimental chemical shifts of 1.35 and 1.05 eV for Si (2*p*) and Zr (3*d 5/2*) involving SiO_2, ZrO_2, and $Zr_{0.66}Si_1O_{3.32}$, respectively.[108] The similar chemical shifts of Powder **6** and Powder **2** reflect the charge changes induced by mixing the oxides of different ionic and covalent character, and suggest that our mixed oxide $Zr_{0.66}Si_1O_{3.32}$ (Powder **6**) perhaps has a structure similar to that of Powder **2** with extensive Zr-O-Si bonding interaction.

The interaction of O with Si and Zr can be evaluated by carefully monitoring the O (1*s*) photoelectron line shifting. Oxygen is directly connected to both Si and Zr and is important in building a covalence scale.[108] Oxygen present in $Zr_xSi_yO_{2(x+y)}$ samples is more covalent in comparison to more ionic compared

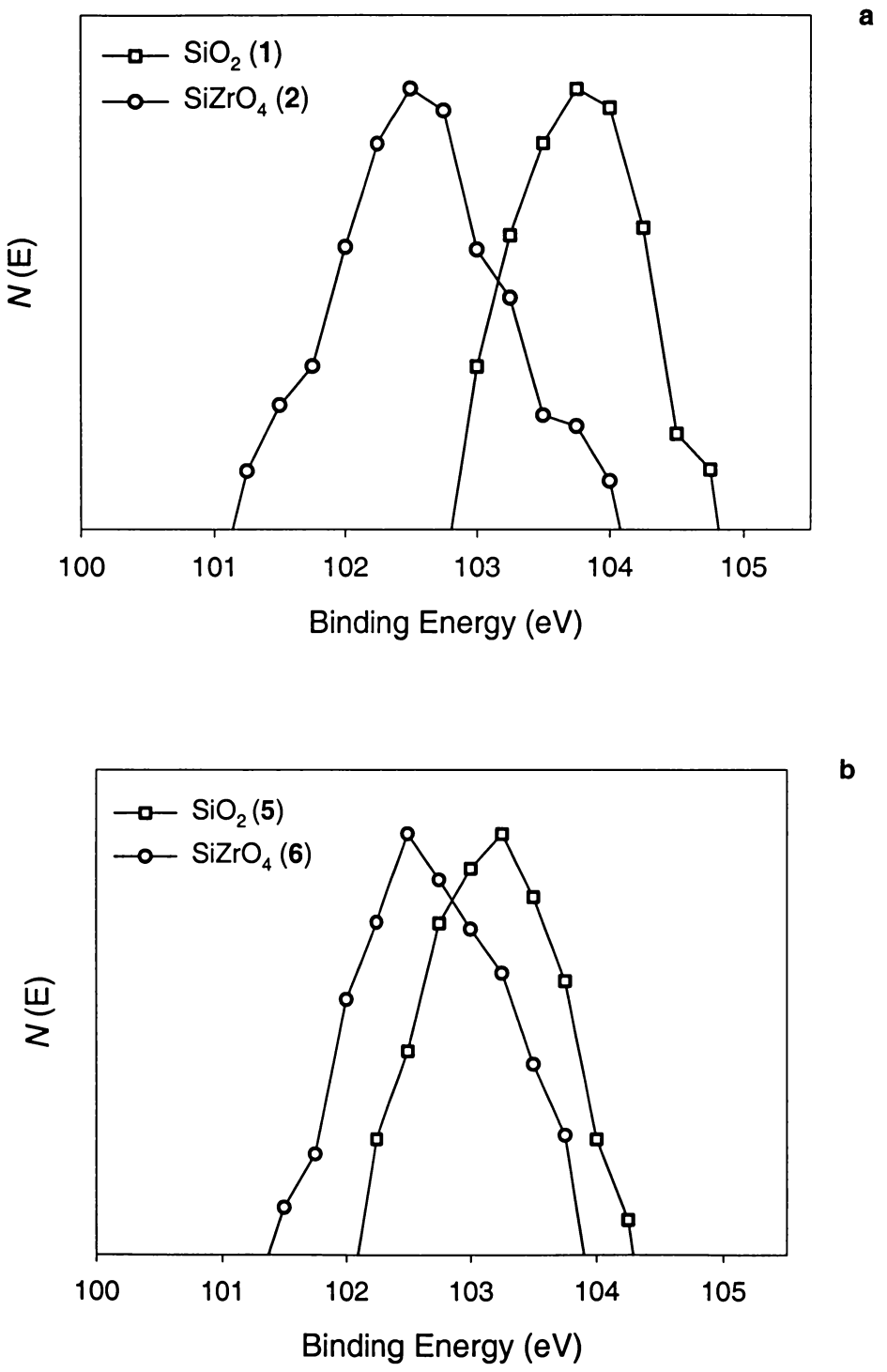

Figure 3.8. Si (2*p*) photoelectron peaks of Powders (a) **1** and **2**, and (b) **5** and **6**.

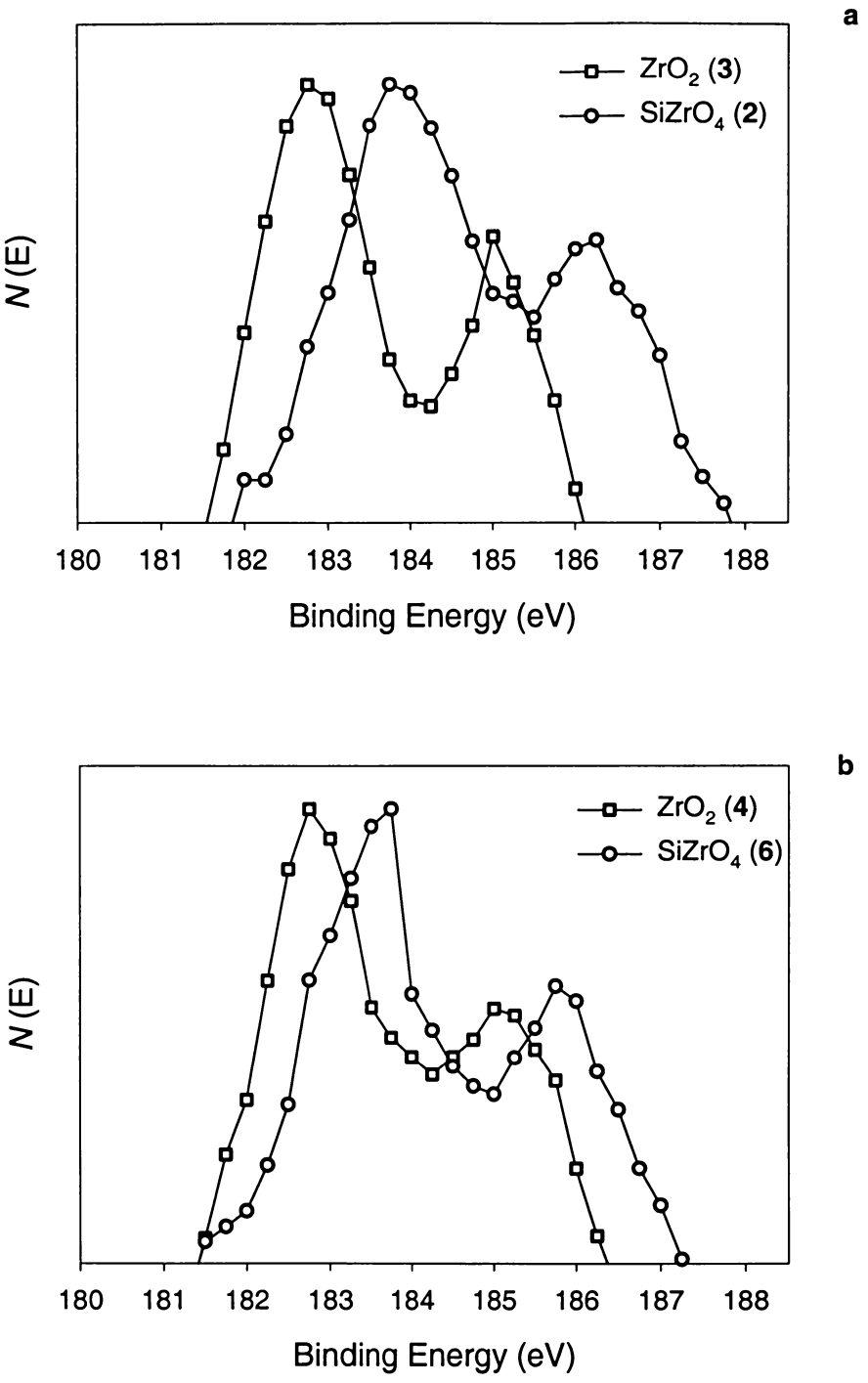

Figure 3.9. Zr (3*d* 5/2) photoelectron peaks of Powders (a) **2** and **3**, and (b) **4** and **6**.

to oxygen in SiO_2.[108] The O (1*s*) photoelectron peak in $Zr_{0.66}Si_1O_{3.32}$ was observed between the ZrO_2 and SiO_2 O (1*s*) values (Tables 3.2 and 3.3, Figure 3.10). The O (1*s*) values of Davisil grade 635 SiO_2 Powder **1** and sol-gel SiO_2 Powder **5** are 533.05 and 533.00 eV, respectively. The O (1*s*) values of ZrO_2 Powder **3** and sol-gel ZrO_2 Powder **4** are 531.00 eV in both samples. The O (1*s*) values of 532.25 eV for $ZrSiO_4$ Powder **2** and $Zr_{0.66}Si_1O_{3.32}$ (Powder **6**) fall between the SiO_2 and ZrO_2 values. The increased ionic character of oxygen in zircon than in silica is evident in the O (1*s*) shift of the former to lower E_b. Such O (1*s*) binding energy shift may reflect Si-O-Zr bonding interaction in zircon.

(b) FT-IR. FT-IR experiments provided evidence as well for Si-O-Zr bonding in zircon. As the Zr:Si ratio was increased from 0.10 to 0.66 from Powders **9**, **8**, **7** to **6**, certain trends were observed in the FT-IR spectra. A FT-IR spectrum of sol-gel SiO_2 Powder **5** is provided in Figure 3.11a as a background. Absorptions from covalent Si-O asymmetric stretching vibrations are assigned to 1296 and 1146 cm^{-1}. Asymmetric stretching vibrations for Si-O have been reported from 1021 to 1220 cm^{-1}.[39,111-115] An absorption centered at 826 cm^{-1} represents the Si-O symmetric stretching vibrational mode. In comparison, values of 800-810 cm^{-1} for Si-O symmetric stretching vibrational mode have been reported for silica.[39,111,113] A very broad band centered at 3460 cm^{-1} (Figure 3.11a) represents the stretching mode of the silanol groups (SiO-H) through hydrogen bonding. A sharp absorption at 1636 cm^{-1} in Powder **5** (Figure 3.11a) is due to the deformation mode of molecular water.[112] These bands have been reported in 3000 to 3700 cm^{-1} and 1630 cm^{-1}, respectively.[39,112,116] Other bands include:

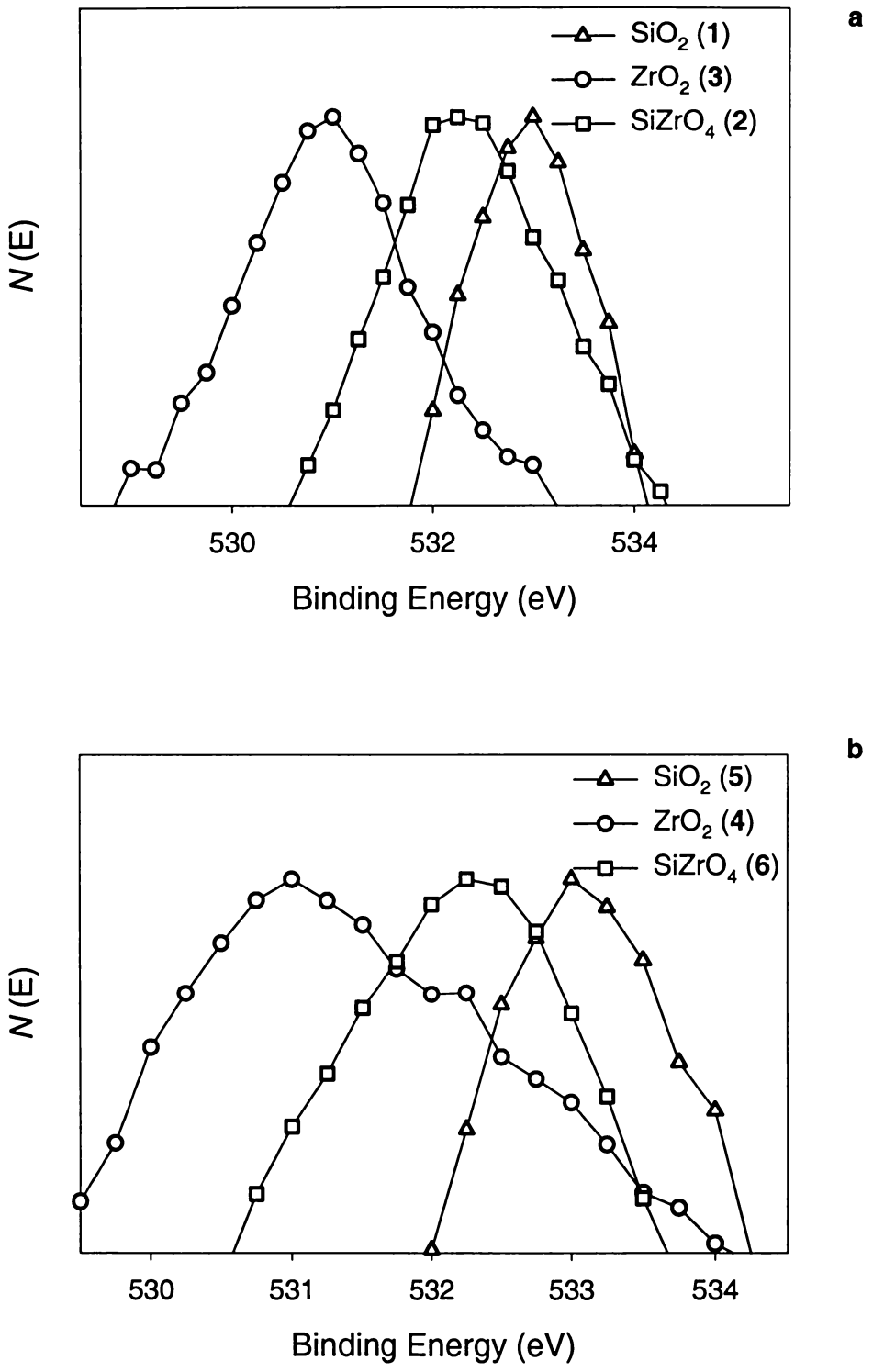

Figure 3.10. O (1*s*) photoelectron peaks of Powders (a) **1-3**, and (b) **4-6**.

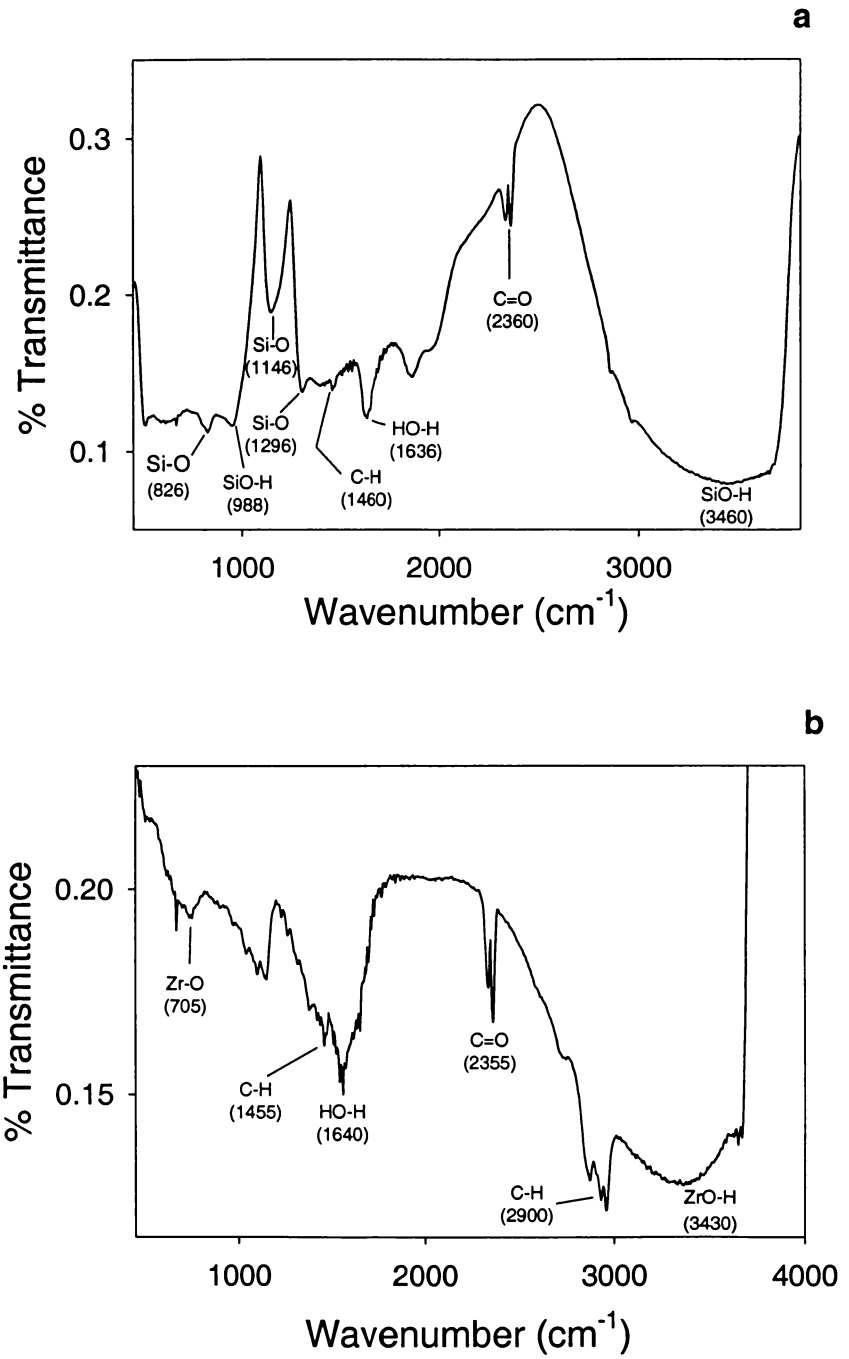

Figure 3.11. The reflectance FT-IR spectra of (a) sol-gel SiO_2 Powder **5** and (b) sol-gel ZrO_2 Powder **4**.

1460 cm^{-1} (C-H scissors or deformation mode region),[39] 2360 cm^{-1} (asymmetric C=O stretches of CO_2),[117] and 2900 cm^{-1} (C-H stretching vibrations).[39] The source of hydrocarbon probably arises from incomplete hydrolysis and condensation of the alkoxide precursor molecules during the sol-gel process.

A FT-IR spectrum of sol-gel zirconia Powder **4** is provided in Figure 3.11b for comparison. A broad and jagged absorption band centered at 737 cm^{-1} is attributed to the ionic Zr-O stretching vibrational mode of zirconia.[111] The superposition of modes has been reported from 400 to 800 cm^{-1}.[111,112,116]

Figures 3.12-3.13 represent Powders **9** (Zr:Si = 0.10), **8** (Zr:Si = 0.20), **7** (Zr:Si = 0.40) and **6** (Zr:Si = 0.66), respectively. In comparison to sol-gel SiO_2 Powder **5**, interesting trends were observed in the FT-IR spectra as the Zr content in these samples increased: (a) A band developed and intensified at 991 cm^{-1}; (b) The intensity of the peak centered at 826 cm^{-1} decreased; (c) The broad band centered at ~3450 to 3500 cm^{-1} remained predominately unperturbed. These observations can be attributed to the formation of more Si-O-Zr bonds as the Zr content increases.[39]

The new band at 991 cm^{-1}, which is related to Si-O-Zr formation, has been reported between 970 and 995 cm^{-1}.[111-115] This band could also be attributed to Si-OH groups of silica.[39] However, the intensity of the broad band centered between ~3450 to 3500 cm^{-1} did not significantly change with increasing Zr content, and the intensity of the band at 991 cm^{-1} did increase with increasing Zr content, thus reducing the likelihood that the band at 991 cm^{-1} was from Si-OH stretches. Such a phenomenon has been observed in the literature.[113] The

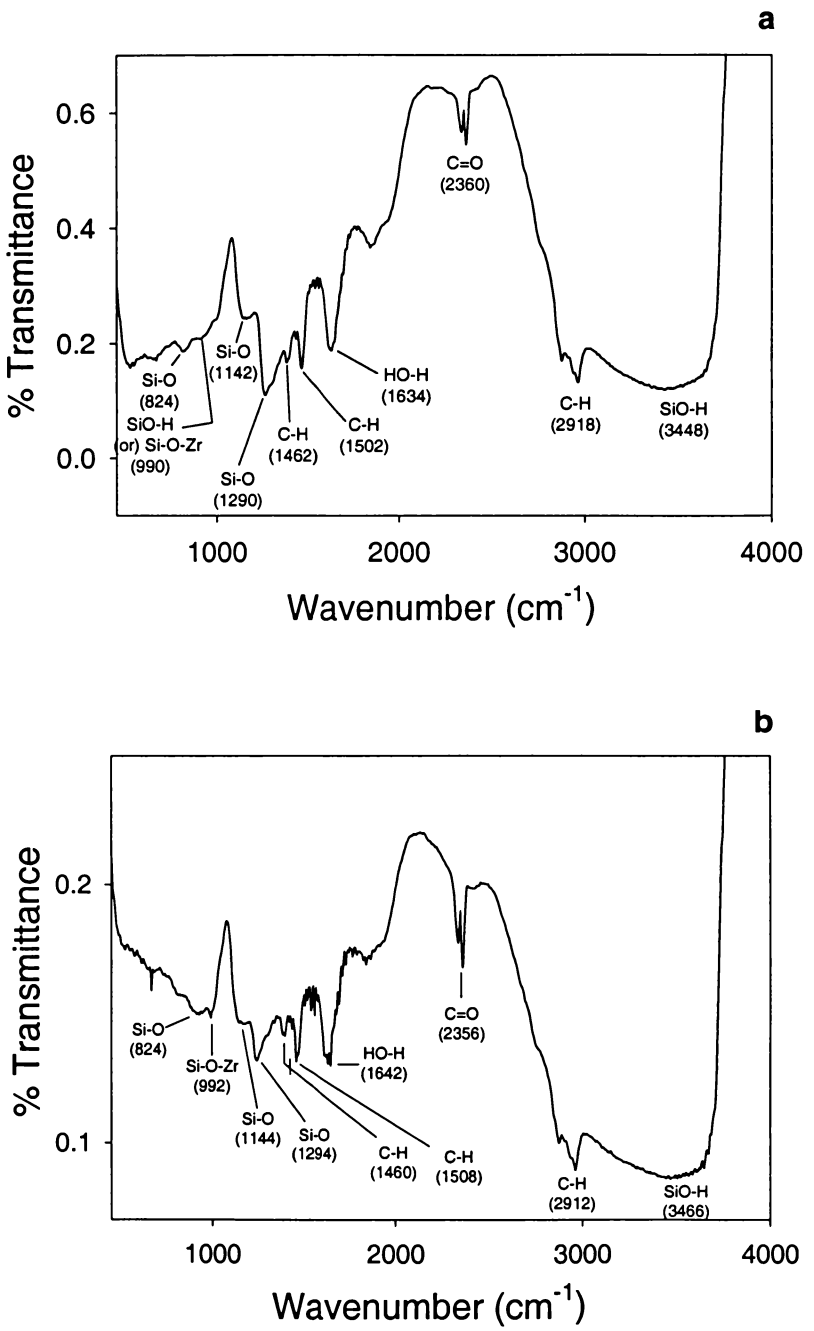

Figure 3.12. The reflectance FT-IR spectra of (a) Powder **9** ($Zr_{0.10}Si_1O_{2.20}$) and (b) Powder **8** ($Zr_{0.20}Si_1O_{2.40}$).

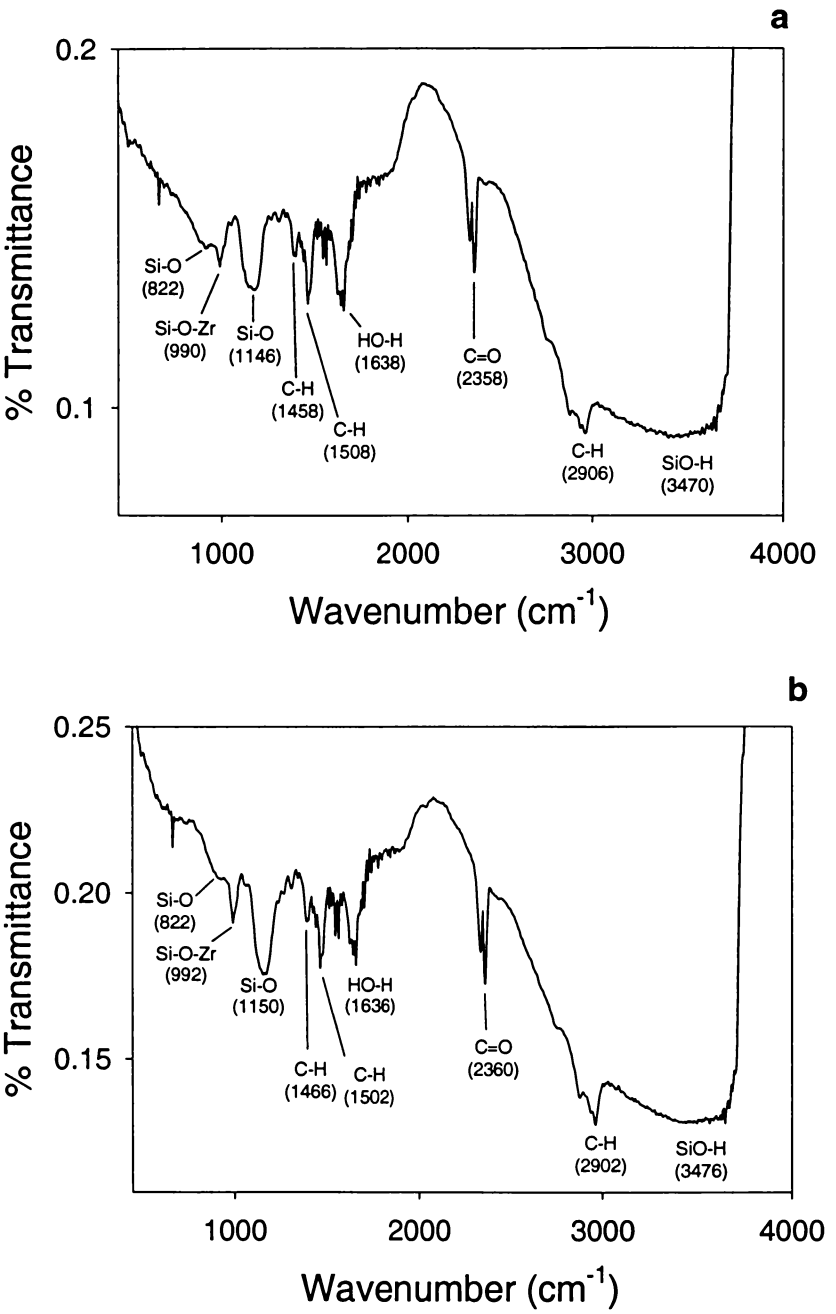

Figure 3.13. The reflectance FT-IR spectra of (a) Powder **7** ($Zr_{0.40}Si_1O_{2.80}$) and (b) Powder **6** ($Zr_{0.66}Si_1O_{3.32}$).

maxima for the Si-O-Si stretching vibrations are located at 1146 and 1296 cm^{-1}. It is reasonable to speculate that the shift to a lower wavenumber at 991 cm^{-1} is due to the replacement of Si atoms with the heavier Zr atoms. Si-OM (M = heavier atom than silicon) stretching vibrations have been reported at 945 cm^{-1} for M = Sn and at 950 cm^{-1} for M = Ti.[112,118,119] However, the assignment of the band at 991 cm^{-1} remains a topic of debate.[120]

Such shifts after heavy atom substitutions may be understood by the Hooke's Law governing vibrations. Two atoms separated by a bond can be regarded as a simple harmonic oscillator similar to two masses separated by a spring. Hooke's Law (Eq. 3.1) relates the frequency of oscillation, atomic masses, and the force constant of the bond. The force constant *f* is approximately 5 x 10^5 dyne/cm for single bonds and approximately two and three times of this value for double and triple bonds, respectively.[69] The frequency given by the Hooke's Law is inversely proportional to the square root of the reduced mass:

$$\nu = \frac{1}{2\pi c}\left[\frac{f}{(M_x M_y)/(M_x + M_y)}\right]^{1/2} \qquad \text{(Eq. 3.1)}$$

where ν is the vibrational wavenumber (cm^{-1}), c is the velocity of light (cm/s), M_x and M_y are the masses of atom x and atom y (g), and f is the force constant (dyne/cm).

Mutin and coworkers[113] have attributed a broad peak around 800 cm^{-1} in the IR spectra of their mixed oxides $Zr_xSi_yO_{2x+2y}$ to the network Si-O-Si symmetric bond stretching vibrations, and the decrease in intensity of this peak when Zr content increases in the mixed oxides to the degradation of the silicate network as Zr^{4+} ions are incorporated into the matrix.[113] The band centered at 826 cm^{-1} in our samples, and its decrease as the Zr content increases may also be attributed to the degradation of the Si-O-Si network as Zr^{4+} ions substitute Si ions in the network.

The formation of the new band at 991 cm^{-1}, the constancy of the 3450-3500 cm^{-1} band, and the decrease in intensity of the band centered at 826 cm^{-1} are all consistent with the formation of a Si-O-Zr matrix.

(c) ^{29}Si Solid-State NMR. The ^{29}Si isotope with spin of ½ exists in nature at 4.70% abundance, and its NMR is valuable for sol-gel research. Difficulties in ^{29}Si NMR however are known due to low sensitivity of the nucleus, low abundance, and long T_1 relaxation times of the ^{29}Si nucleus. The introduction of Fourier transform technique (FT-NMR) has helped surmount some of the inherent problems.

NMR studies of the sensitivity of ^{29}Si nucleus to their neighbors through two bond interactions have been well documented for aluminosilicates. For instance, the chemical shift of a Si atom with 4 (-OSi) groups around it (labeled Q^4) is usually found between ~102 and 117 ppm. As a (-OSi) group is replaced with one (-O-Al; labeled Q^3), two (-O-Al; labeled Q^2), three (-O-Al; labeled Q^1), and four (-O-Al, labeled Q^0) groups, a shift to ~97-107, ~92-99, ~85-94, and ~82-

92 ppm, respectively, takes place.[107] Hence, a broad spectrum may indicate the existence of a mixture of Q^{0-4} Si nuclei. This implies that the chemical shift of ^{29}Si nuclei in aluminosilicates depends upon the number of Al atoms in the second coordination sphere of the Si atoms.[107]

The effect of substituting Si atoms with Zr atoms upon ^{29}Si chemical shift is more ambiguous. However the effect of Zr substitution of Si atoms in mixed oxides $Zr_xSi_yO_{2(x+y)}$ on ^{29}Si chemical shift is expected to be similar in nature to that of Al. The straightforward identification of Si-O-Zr bonds in oxides $Zr_xSi_yO_{2(x+y)}$ is difficult by ^{29}Si solid-state NMR, as the peaks of $(SiO)_x{}^{29}Si(OZr)_{4-x}$ (x = 1-3) groups may be mixed with those of $(SiO)_3{}^{29}Si$-OH (Q^3) groups. The shift of the latter {from $[Si(OSi)_4]$} is greater in magnitude than for Si-O-Zr, but a mixture of the two could possibly exist.[113] In addition, variations in Si-O-Si bonding angles may also affect the chemical shift.[113] In the case of our studies, a broadening of the spectral peak was observed, as the Zr content was increased, and this was consistent with previously reported observations.[112,113,121,122]

In sol-gel SiO_2 Powder **5**, two overlapping peaks are present (Figure 3.14). The peaks at -106.3 and -112.8 ppm most likely represent the Q^3 $[Si(OSi)_3O^-]$ and Q^4 $[Si(OSi)_4]$ phases of silica, respectively. When the Zr content was increased from Powders **8**, **7** to **6** (Figure 3.15), a total chemical shift of 7.4 ppm was observed. This downfield shift could be an evidence of increased Si-O-Zr bonding just as a similar trend for the substitution of Si with Al was observed earlier.[107] The ^{29}Si resonances of Powders **8** ($Zr_{0.20}Si_1O_{2.40}$), **7** ($Zr_{0.40}Si_1O_{2.80}$),

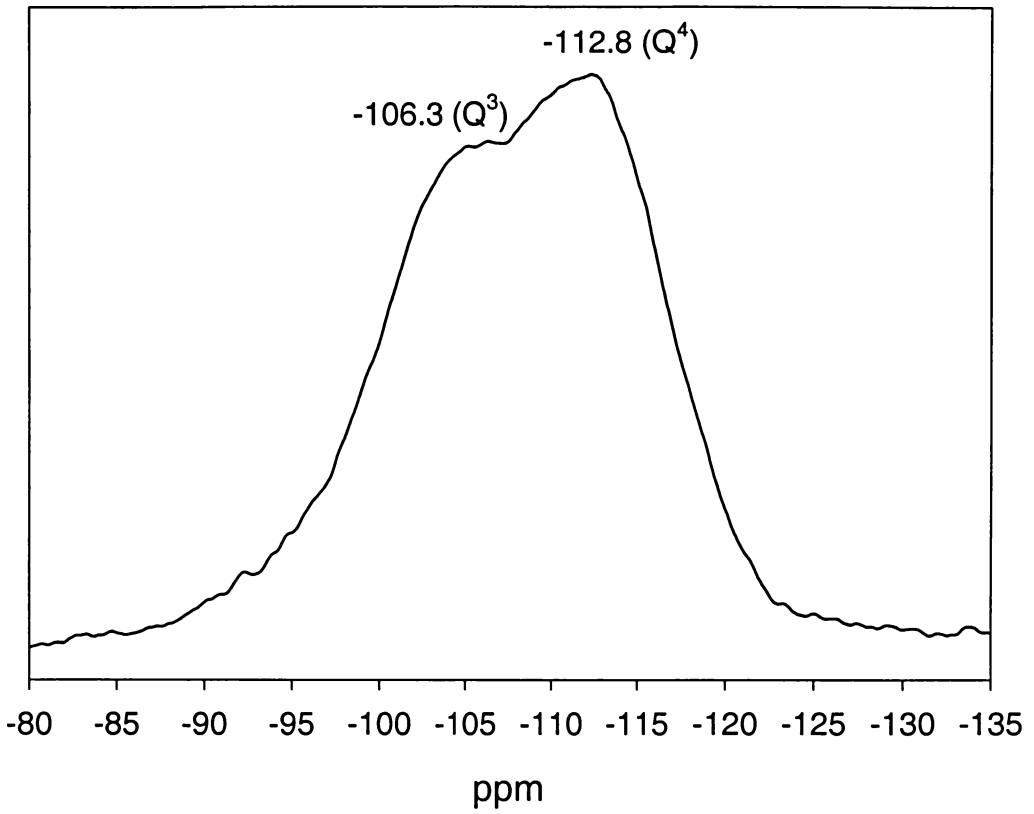

Figure 3.14. Solid-state ^{29}Si NMR spectrum of sol-gel SiO_2 Powder **5**.

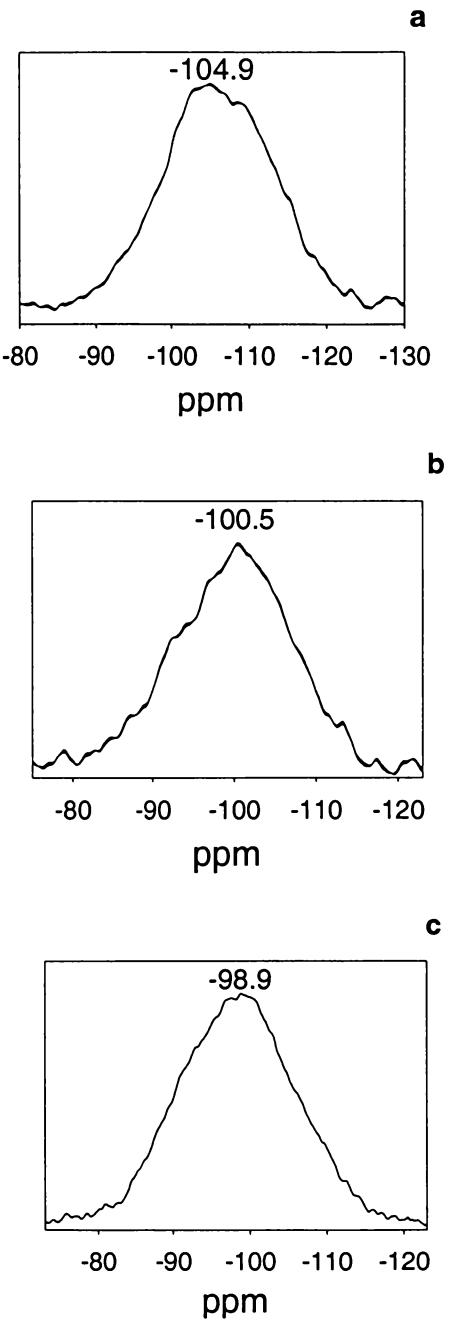

Figure 3.15. Solid-state ^{29}Si NMR spectra of (a) Powder **8** ($Zr_{0.20}Si_1O_{2.40}$), (b) Powder **7** ($Zr_{0.40}Si_1O_{2.80}$), and (c) Powder **6** ($Zr_{0.66}Si_1O_{3.32}$).

and **6** ($Zr_{0.66}Si_1O_{3.32}$) were centered at -104.9, -100.5, and -98.9 ppm, respectively, and were shifted from the peak at -106.3 ppm in Powder **5**. A plot depicting the chemical shift vs Zr:Si ratios is given in Figure 3.16. Si-O-Zr bonds of mixed oxides of lower Zr content (Powders **8** and **9**) cannot be ascertained from the ^{29}Si solid-state NMR, as the ^{29}Si peak shift by Zr is small in the mixed oxides and cannot be separated from that of Si-O-Si.[113] In comparison, a chemical shift of -98.5 ppm has been reported for a sol-gel mixed oxide $Zr_xSi_yO_{2(x+y)}$ containing 0.50:0.50 Zr:Si.[113]

For comparative measures the ^{29}Si NMR spectra (Figure 3.17) of commercial SiO_2 Powder **1** and zircon $ZrSiO_4$ Powder **2** were obtained. In the case of Powder **2**, a sharp peak was observed at -84.8 ppm. Values ranging from -89.3 to -82.0 ppm have been reported for the ^{29}Si nucleus in zircon,[114,115,123] due to the presence of the Q^3 and Q^4 phases, respectively, of silica in zircon.

The application of ^{17}O NMR would provide more sensitivity for evaluating Si-O-Zr bonding in mixed metal oxide $Zr_xSi_yO_{2x+2y}$ systems. Sanchez and coworkers[112] were able to observe well-resolved spectra of zirconium silicates using ^{17}O MAS NMR. Distinct peaks located at 410, 290, and 170 ppm were assigned to OZr_3, OZr_4, and OZrSi moieties, respectively.[112] The natural abundance of ^{17}O is low (0.037%)[113] and the elevated costs of ^{17}O enriched water inhibit further testing in our studies. Complexity of synthesis involving hydrolysis of alkoxides by ^{17}O enriched water provides yet another challenge.[113]

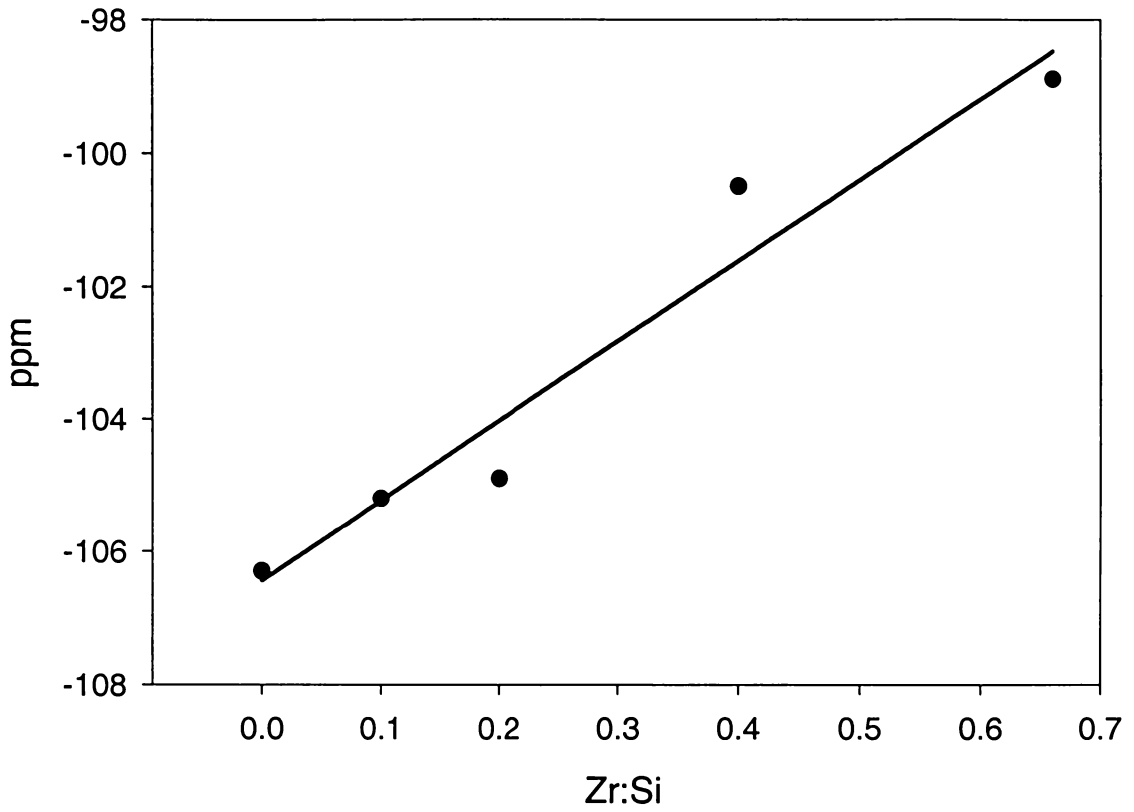

Figure 3.16. Comparisons of solid-state ^{29}Si NMR chemical shifts vs Zr:Si ratios for Powders **6-9**.

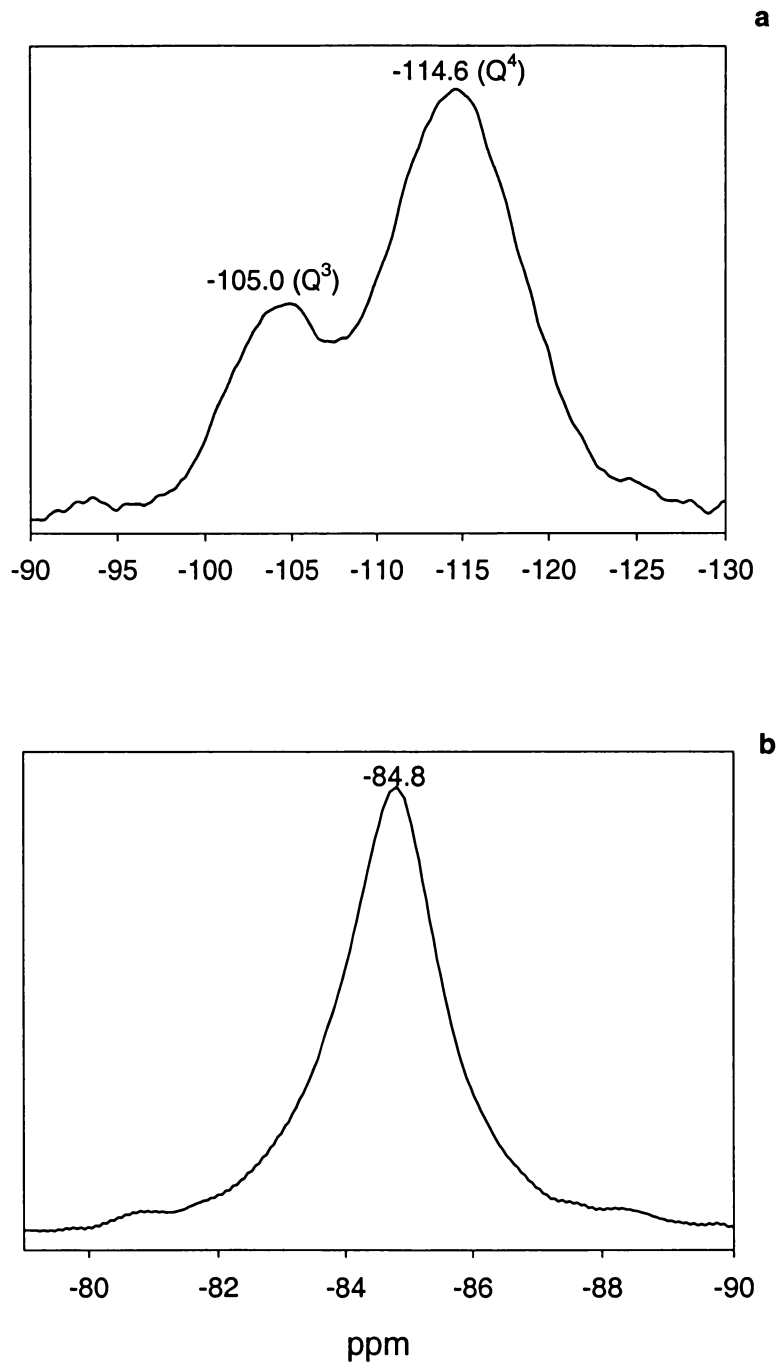

Figure 3.17. Solid-state ^{29}Si NMR spectra of (a) Powder **1** (SiO_2) and (b) zircon Powder **2** ($ZrSiO_4$).

3.3.3 Sensor Performance. The kinetics, hysteresis and durabilities of our base sensors in NaOH-ROH-H_2O ternary media were evaluated, and compared with those in aqueous NaOH solutions.

(a) Kinetic and Hysteresis Studies of Optical Sensors in NaOH-ROH-H_2O (R = Me, Et, and i-Pr) Ternary Media. Porosity of sol-gel solids can be controlled by manipulation of *p*H and drying conditions in the gel formation process.[124] In sol-gel formation, *p*H strongly influences the kinetics of the agglomeration of the colloidal suspension. Therefore the structures of the xerogels are *p*H dependent.[39,125-127] High *p*H yields condensed particulate sols of larger pores and lower surface areas. In contrast, low *p*H yields highly branched sols and dense xerogels with high surface areas.

Sensor films tested in the current studies were prepared by acid-catalyzed hydrolysis in order to produce films with small pores (25 to 50 Å, as revealed in powders prepared by similar procedures). By the use of the acid-catalyzed technique, we were able to minimize indicator leaching from the mixed-metal oxide support. Previously, base-catalyzed hydrolysis was explored and found to produce sensors with fast response times at the expense of increased leaching of the indicator.[18]

The use of Nafion, poly(tetrafluoroethylene)polyphenylene ether sulfonate resin, has been observed to drastically reduce the response time of these sensors.[18] The role of Nafion here is not clear. The hydrophilicity of this perfluorinated resin may help decrease the response time (along with the hydrophilic oxide lattices). Complete dehydration by prehydrolysis of the

$Si(OMe)_4$ and the water-rich Nafion solution in an acidic medium was needed to prevent phase segregation upon the addition of $Zr(O\text{-}n\text{-}Bu)_4$.

A general response time of 1 min or less is required of "real-time" chemical sensors according to Wolfbeis.[2] Sensor **TY5** response times were found to decrease from 12 to <6 s from 0.050 to 3.00 M *aqueous* NaOH solutions and Sensor **AY5** decreased from 60 to <6 s (Table 3.4 and Figure 3.18). In NaOH-ROH-H_2O solutions (R = Me, Et, and i-Pr), a similar trend was observed. For instance, Sensor **TY5** response times decreased from 38 to <6 s (R = Me) and 15 to 6 s (R = Et) from 0.050 to 3.00 M NaOH solutions (Figures 3.19 and 3.20). In NaOH-i-PrOH-H_2O solutions, response times were longer. For Sensors **TY5** and **AY5**, response times range from 78 to 33 s and 84 to 66 s (Figure 3.21), respectively, in 0.050 to 1.00 M NaOH solutions, respectively.

In the current studies, indicator dye molecules that were encapsulated in the sol-gel matrics, experienced "free" molecular tumbling and thus faster chemical kinetics relative to dyes that were chemically grafted to sol-gel substrates.[125] However, the diffusion kinetics of our thin films involves three basic diffusion zones (a) the bulk solution; (b) thin diffusion boundary; and (c) the internal diffusion of the analyte throughout the porous silica membrane.

The sol-gel substrate is primarily composed of mesopores and micropores.[39] Diffusion through the mesoporous region is substantially faster than that across the microporous region.[128] Therefore, the steep rise in the *A* vs time in Figures 3.18-3.21 is probably associated with diffusion through the

Table 3.4. Kinetic Data Based Upon the Time in Seconds to Reach 90% of the Analytical Signal (grad = concentration gradient)

NaOH (M)	TY5 (+ grad)	TY5 (- grad)	AY5 (+ grad)	AY5 (- grad)
0.050 [a]	12	30	60	198
0.10 [a]	9	54	45	171
0.50 [a]	<6	42	23	150
1.00 [a]	<6	25	<6	135
1.50 [a]	<6	21	<6	78
3.00 [a]	<6	22	6	51
0.50 [b]	38	39	33	45
1.50 [b]	6	15	<6	43
3.00 [b]	<6	33	8	45
0.50 [c]	15	15	53	42
1.50 [c]	<6	<6	54	39
3.00 [c]	6	<6	50	37
0.050 [d]	78	21	84	63
0.10 [d]	86	22	69	51
1.00 [d]	33	9	66	39

[a] aqueous solution, [b] 50% v/v MeOH-H_2O solution, [c] 50% v/v EtOH-H_2O solution, [d] 50% v/v i-PrOH-H_2O solution

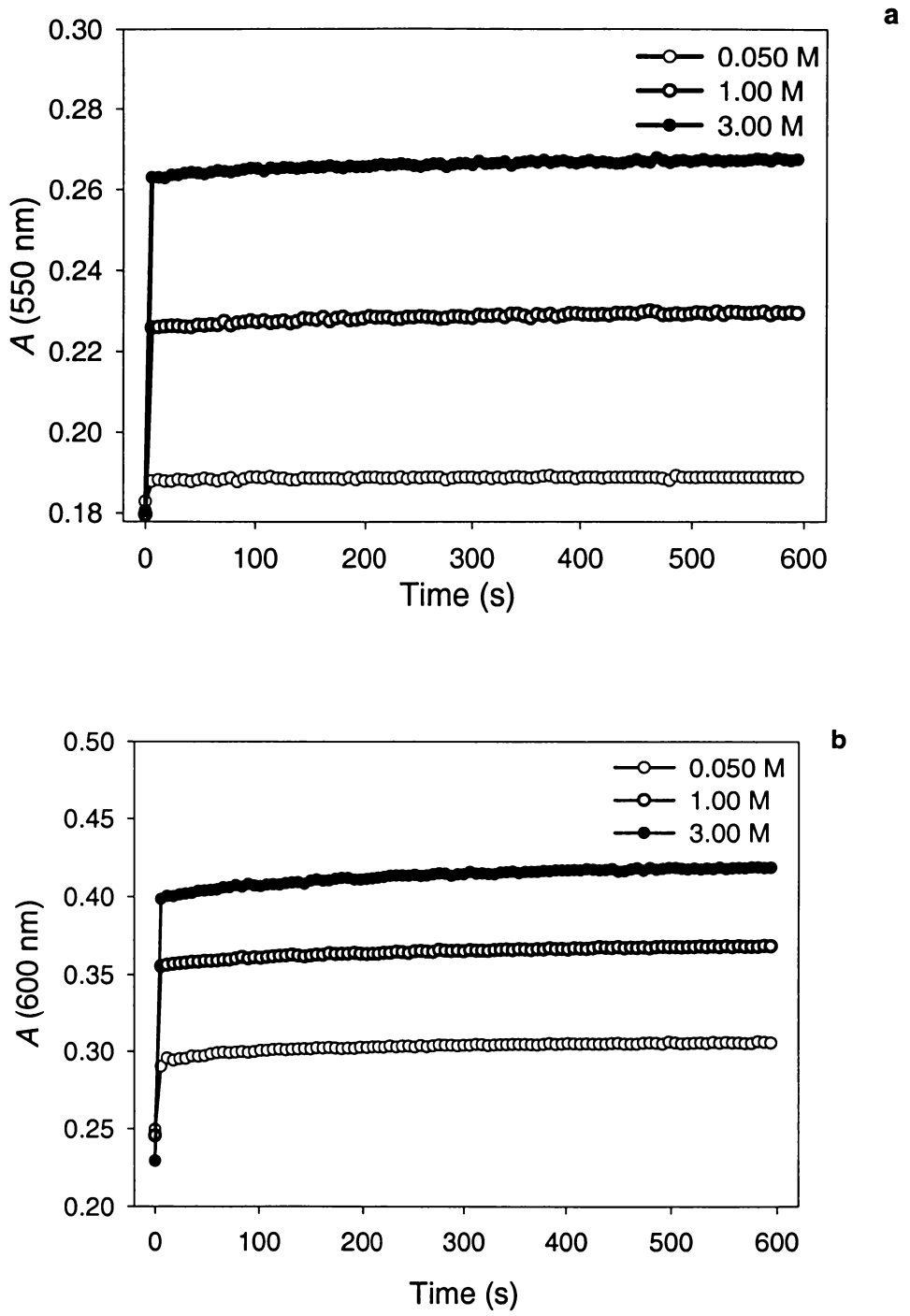

Figure 3.18. Sensor response kinetics during the positive concentration gradient in aqueous NaOH solutions for Sensors (a) **TY5** and (b) **AY5**.

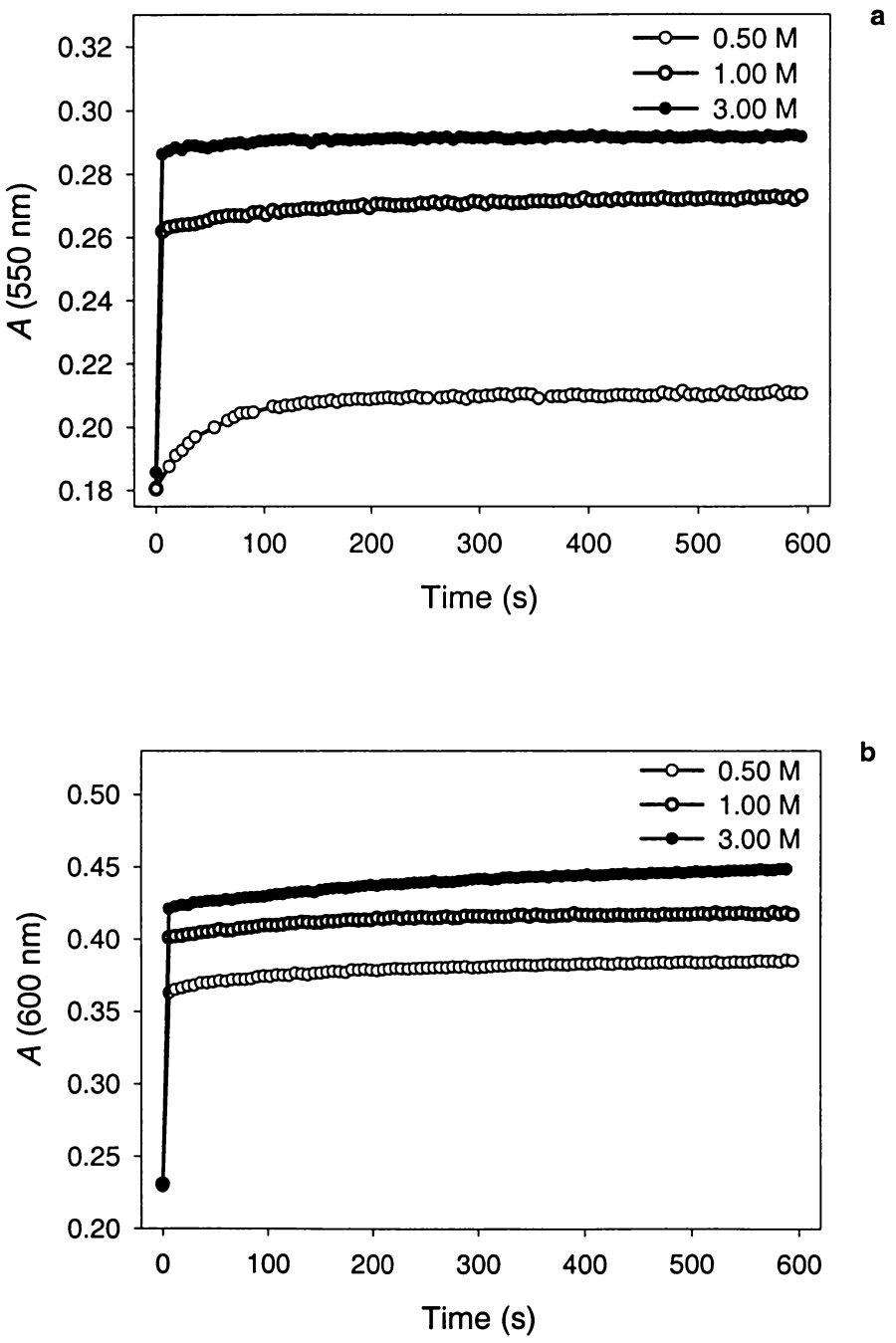

Figure 3.19. Sensor response kinetics during the positive NaOH concentration gradient in 50% v/v MeOH-H_2O solutions for Sensors (a) **TY5** and (b) **AY5**.

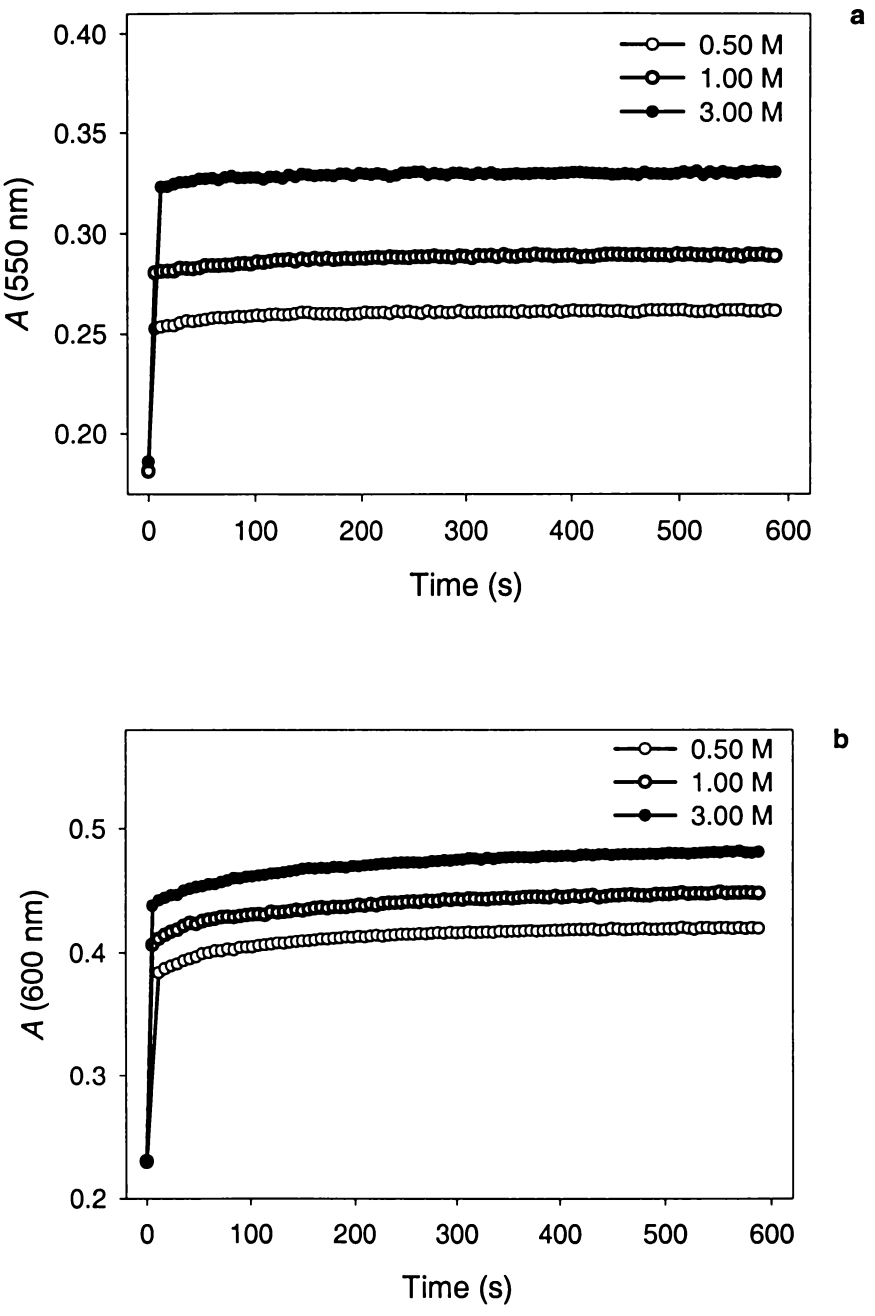

Figure 3.20. Sensor response kinetics during the positive NaOH concentration gradient in 50% v/v EtOH-H_2O solutions for Sensors (a) **TY5** and (b) **AY5**.

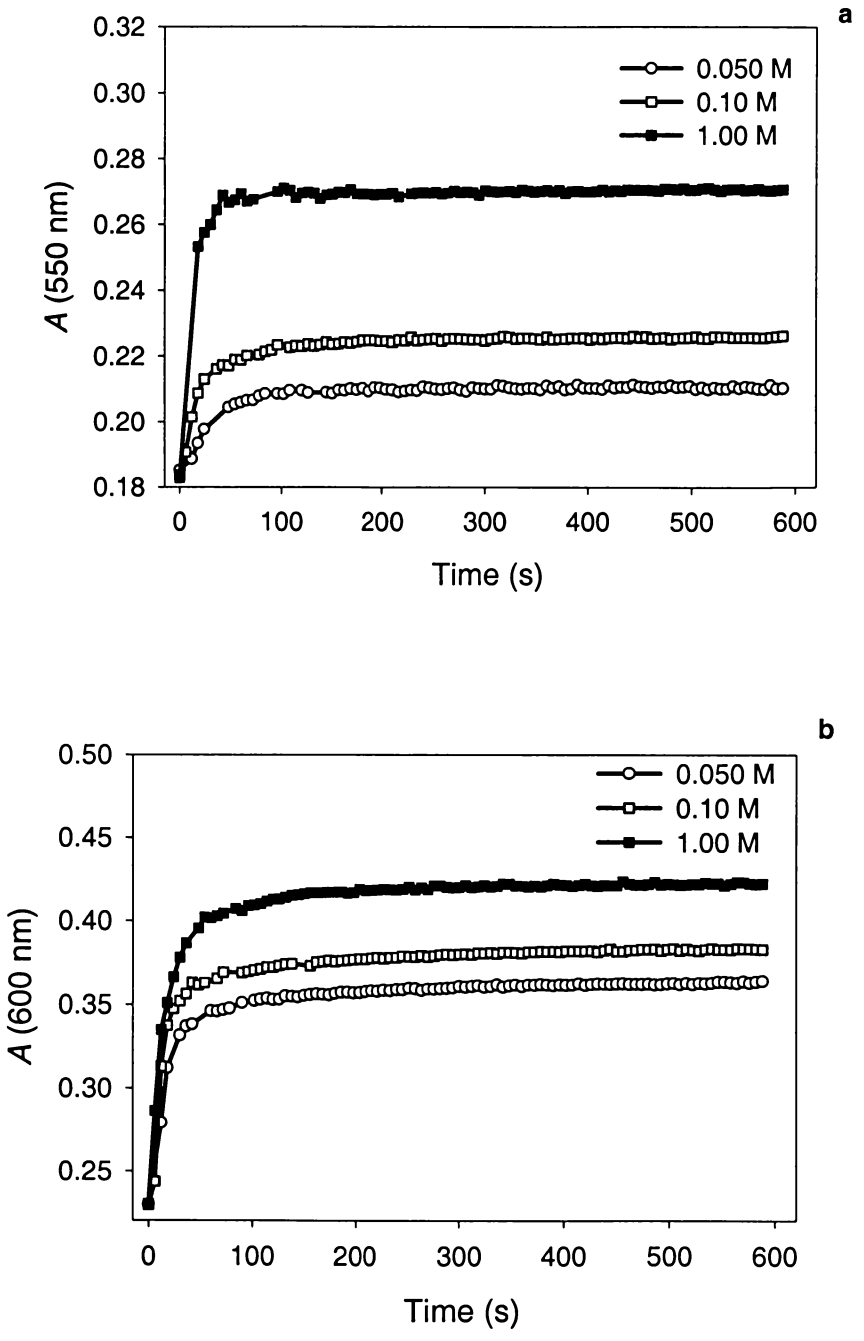

Figure 3.21. Sensor response kinetics during the positive NaOH concentration gradient in 50% v/v i-PrOH-H_2O solutions for Sensors (a) **TY5** and (b) **AY5**.

mesoporous regions, and the leveling off of the curve is due to the diffusion through microporous regions.

Surface interactions and geometric restrictions are two processes that affect the diffusion rate through the pores of the sol-gel.[124,128] Within the microporous regions, wall collision, collisions with other molecules, and narrow necks influence the diffusion rate of the analyte. The constrained geometry of the micropores has been found to severely limit the efficiency of molecular transport.[128] Even in systems displaying no interaction between the analyte and the walls of the silica, transport was slow through the microporous region as compared to the mesoporous region.[128]

Porous silicas are heterogeneous in nature and the influence of transport through the porous structures on binding rates has not been well established (especially for pores of 4.0 nm or less in size). It has been shown that diffusion through a porous sol-gel membrane is slower than in solution.[129-131] Rivera and Harris[128] were able to show that the rate of transport into a film decreased as the degree of interaction between the analyte and the walls of the silica surface increased. In other words, adsorption inhibited the transport of the molecules through the pores. Kinetic parameters were correlated to chemical interactions at the silica surface. By derivatizing the silica surface, Rivera and Harris were able to correlate diffusion kinetics with surface interactions.[128] For instance, the rates of transport through the pore network were found to vary inversely with the strength of the surface interaction.[128] The film thickness of the silica was found not to affect the diffusion rate, implying that kinetics of transport is controlled by

the microporous region of the silica film.[128] Other studies displaying similar observations have been reported.[124] Zerda and coworkers[124] indicated that the surface layer may determine the pore diffusion coefficient when molecules are in close proximity within micropores. Hydrogen bonding between a polar analyte and the silica surface could be attributed to the decreased kinetics due to a reduction in the pore diameter.[124]

The buffering power of the media is important regarding its ability to replenish exhausted hydroxide at the diffusion layer surrounding the silica. As hydroxide diffuses into the sensor membrane an adjoining thin depleted layer is momentarily produced that must be replenished with hydroxide from the bulk (Figure 3.22). The sensor kinetics can be greatly affected by the buffering power of the bulk solution. In solutions of large buffering power, the thin layer next to the sensor membrane is quickly replenished by the bulk solution. Highly concentrated solutions of hydroxide have large buffering powers as compared to diluted hydroxide solutions. In other words, buffering power increases with hydroxide concentration as depicted in Figure 3.23.[132] The buffering power of water is a function of *p*H. The logarithm of the buffer power per liter of water is a linear function up to *p*H 13.6. Beyond *p*H 13.6, there is a non-linear dependence approaching a limiting value of 0.84 corresponding to a buffer power of 7.08 mol/L.[132] The increase in sensor response times from water → MeOH-H_2O (50:50 v/v%) → EtOH-H_2O (50:50 v/v%) → i-PrOH-H_2O (50:50 v/v%) solutions (Table 3.4) in the current studies suggested a reduction in buffering power in these solutions.

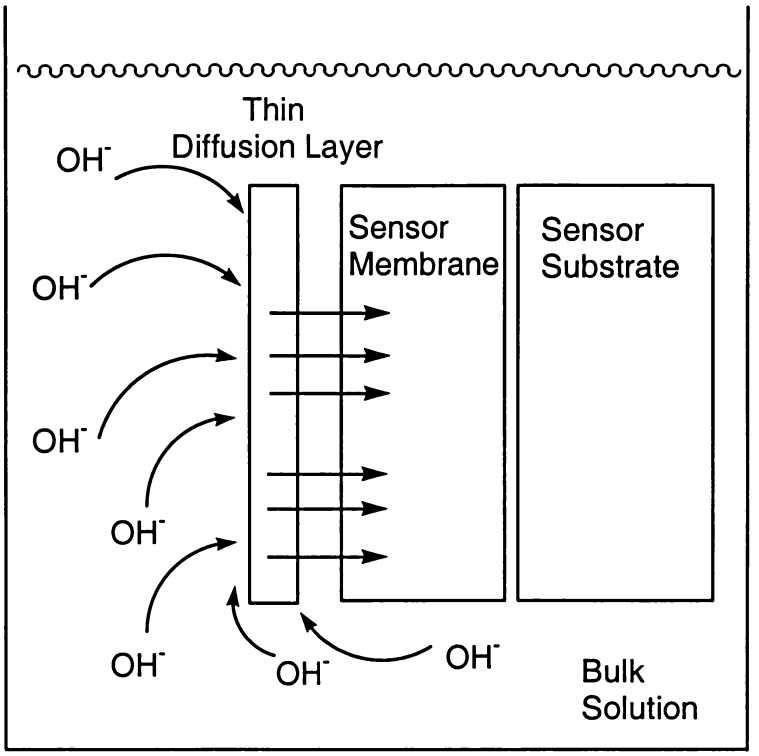

Figure 3.22. Three basic zones of hydroxide diffusion.

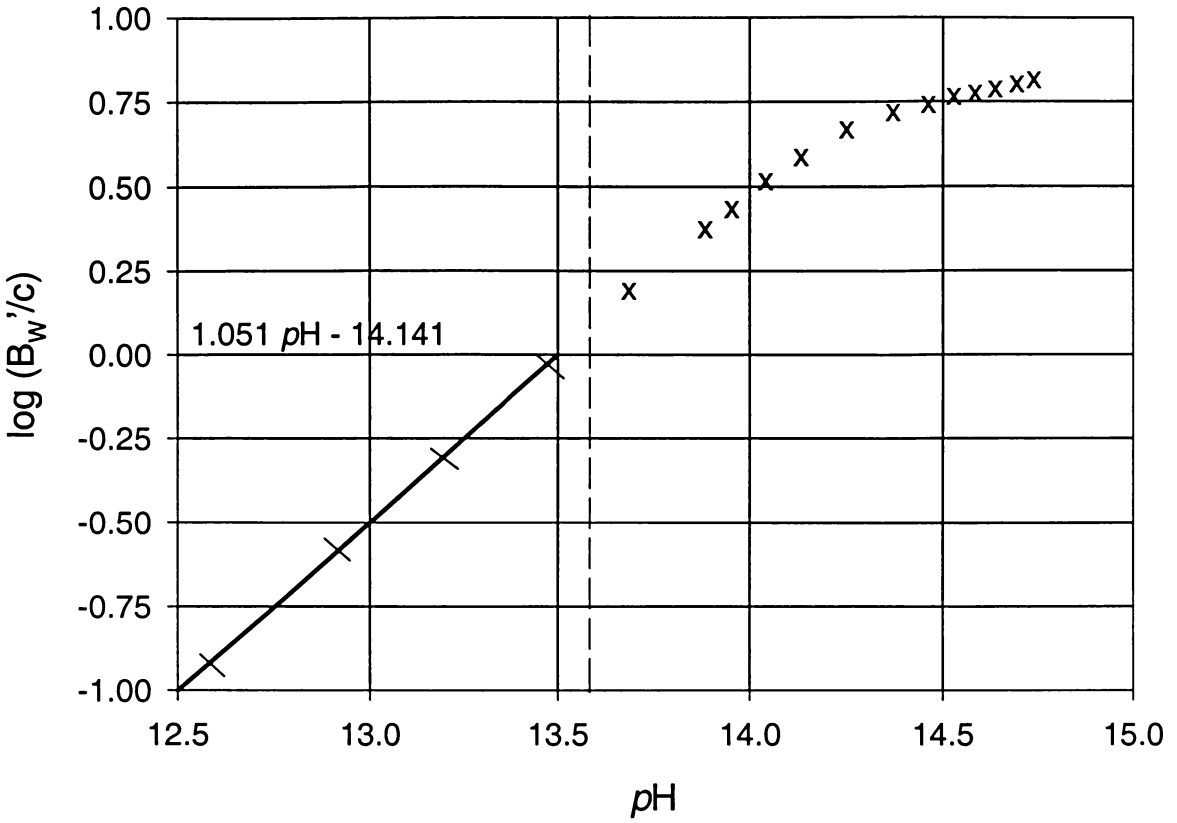

Figure 3.23. The logarithm of the buffer power per liter of water (B_W'/c) as a function of *p*H in the alkaline region. Below *p*H = 13.6 the logarithm is a linear function of *p*H with the equation given in the graph. Above this *p*H there is a non-linear dependence. The logarithm appears to reach a limiting value of 0.84. (Adapted from Rilbe, H. *pH and Buffer Theory-A New Approach*; John Wiley & Sons: New York, 1996, pp. 135-139.)

Across the negative concentration gradients, response times tended to decrease as C_{base} was increased. For instance, as C_{base} was varied from 0.050 to 1.00 M NaOH in *aqueous* solutions, response times decreased from 198 to 51 s for Sensor **AY5** and 54 to 21 s for Sensor **TY5** (Figure 3.24). Again in NaOH-ROH-H_2O ternary solutions with same C_{base}, the response times increased from R = Me, Et, to i-Pr (Table 3.4).

The studies here reveal that sensor kinetics is very much dependent upon both the magnitude and direction of the *p*H change. Low buffering power of the deionized water or alcohol-H_2O mixed solvents probably limits the diffusion of the hydroxide across the sensor element. The initial continuous flowing aqueous solutions caused a quick (few seconds) and significant drop in the *p*H of the sensor element. However, the residual hydroxide within the film was much slower (minutes) to diffuse outward. It has been experimentally observed that the use of neutral buffer solutions (e.g., $HPO_4^{2-}/H_2PO_4^-$) significantly decreases the response time in the negative gradient.[18]

Previous work in our group focused on analysis of variance (ANOVA) as a statistical tool to identify sources of variation in acid sensors.[106] The major source of analytical error, based upon the total variance, was found to be the hysteresis of the sensor response.[106]

Hysteresis effects upon the sensor performance were examined here in NaOH-ROH-H_2O solutions (R = Me, Et, and i-Pr). The magnitude of hysteresis was found to vary with C_{base}, $C_{alcohol}$, and the sensor response time. In the case of Sensor **TY5** in aqueous NaOH solutions, the error due to hysteresis as a

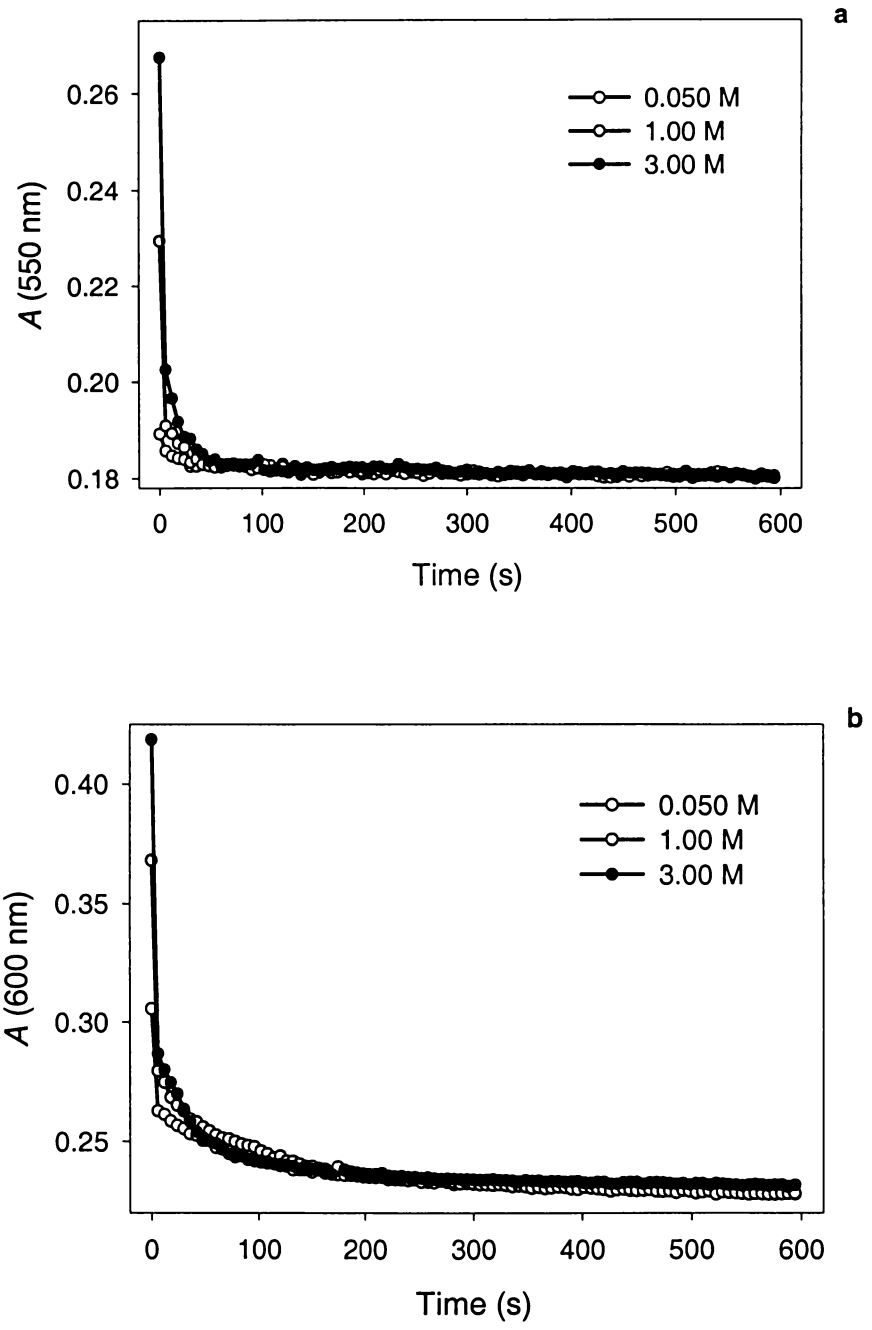

Figure 3.24. Sensor response kinetics during the negative NaOH concentration gradient in *aqueous* solutions for Sensors (a) **TY5** and (b) **AY5**.

function of total analytical range increased from 2.7 to 10.9% as the C_{base} was decreased from 1.50 to 0.10 M. The error change was 3.2 to 8.5% using Sensor **AY5** (Figure 3.25) in the same solutions. When C_{NaOH} was decreased from 1.50 to 0.50 M, Sensors **TY5** and **AY5** exhibited an increase in error from 2.2 to 10.8% and from 5.7 to 6.1%, respectively, in 50% v/v NaOH-MeOH-H_2O solutions (Figure 3.26). In 50% v/v NaOH-EtOH-H_2O solutions with the same C_{base} (1.50 to 0.50 M), Sensors **TY5** and **AY5** exhibited an increase in error from 3.2 to 11.7% and from 4.5 to 5.1%, respectively, (Figure 3.27). In 50% v/v NaOH-i-PrOH-H_2O solutions with the same C_{base} (1.50 to 0.50 M), a noticeable increase in the magnitude of the hysteresis was observed (Figure 3.28). When C_{NaOH} was decreased from 0.10 to 0.050 M in these i-PrOH-containing solutions, Sensors **TY5** and **AY5** exhibited an increase in error due to hysteresis from 15.0 to 20.5% and 9.0 to 12.3%, respectively.

The studies here show the following general trends: (a) As the *p*H of the solution was increased the response time and magnitude of hysteresis decreased; (b) As the solvent was altered from aqueous to MeOH, EtOH, and i-PrOH, the response time and magnitude of hysteresis increased.

The difference in buffering powers among the solutions and severazl other factors contribute to an ineffective mass transport between the bulk, thin diffusion layer, and the sensor membrane. The factors[133] influencing sensor kinetics and hysteresis include (a) matrix quantity; (b) particle size; (c) indicator solution concentration; (d) direction and magnitude of *p*H change; (e) shape and morphology of sensor substrate; (f) temperature of analyte solution; (g) transition

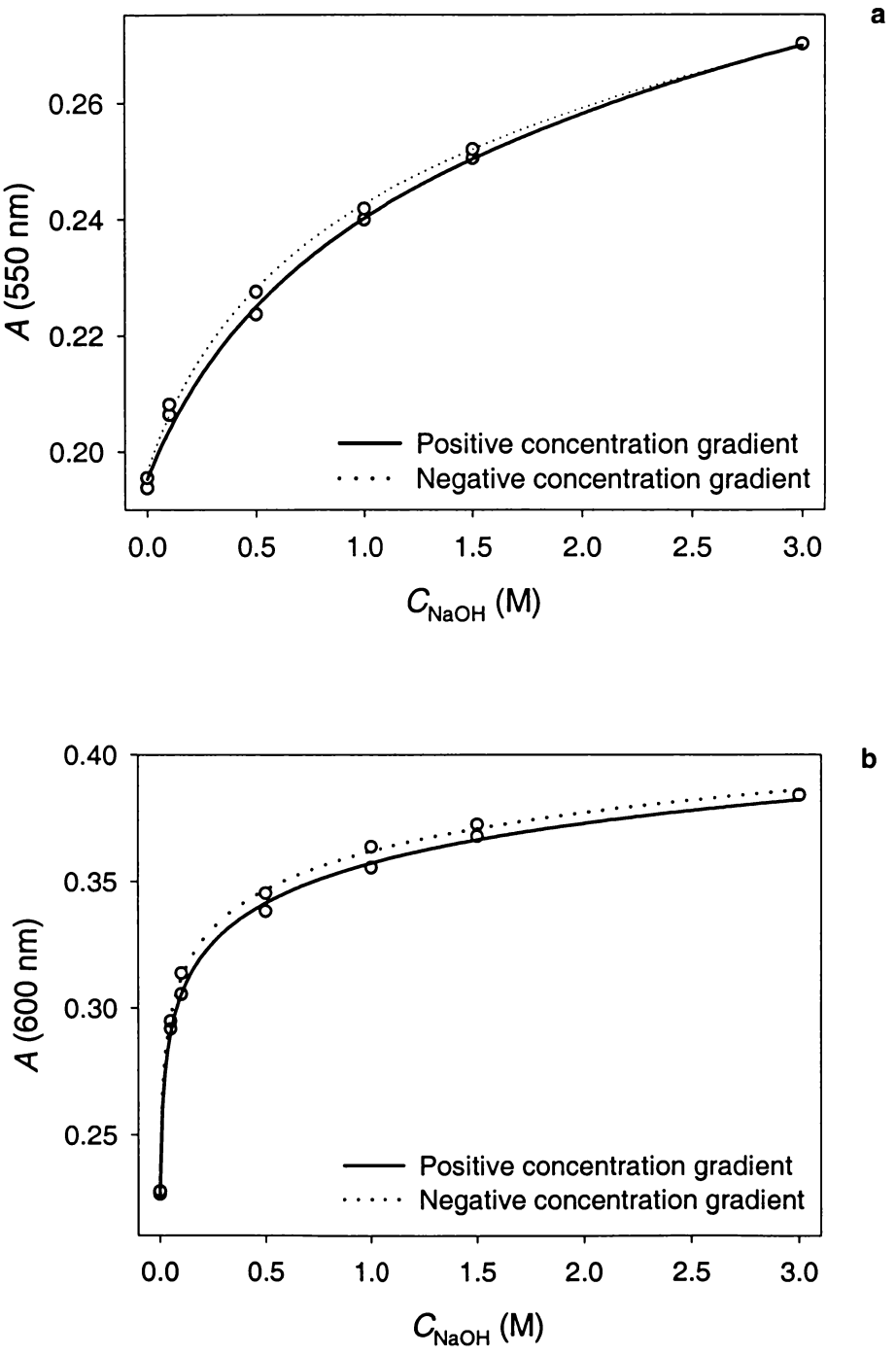

Figure 3.25. Hysteresis profile for Sensors (a) **TY5** and (b) **AY5** in aqueous NaOH solutions.

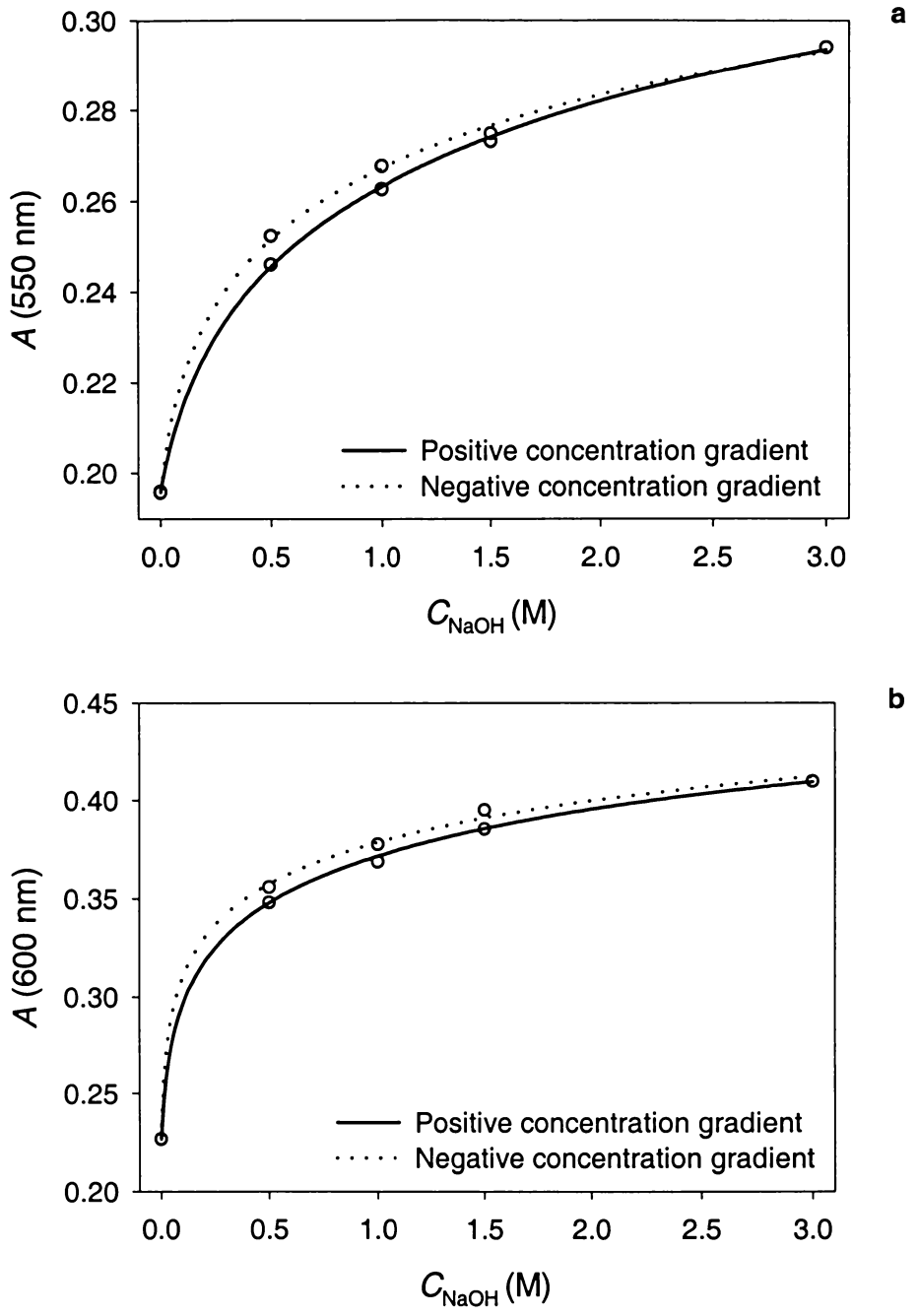

Figure 3.26. Hysteresis profile for Sensors (a) **TY5** and (b) **AY5** in NaOH-MeOH-H_2O 50% v/v solutions.

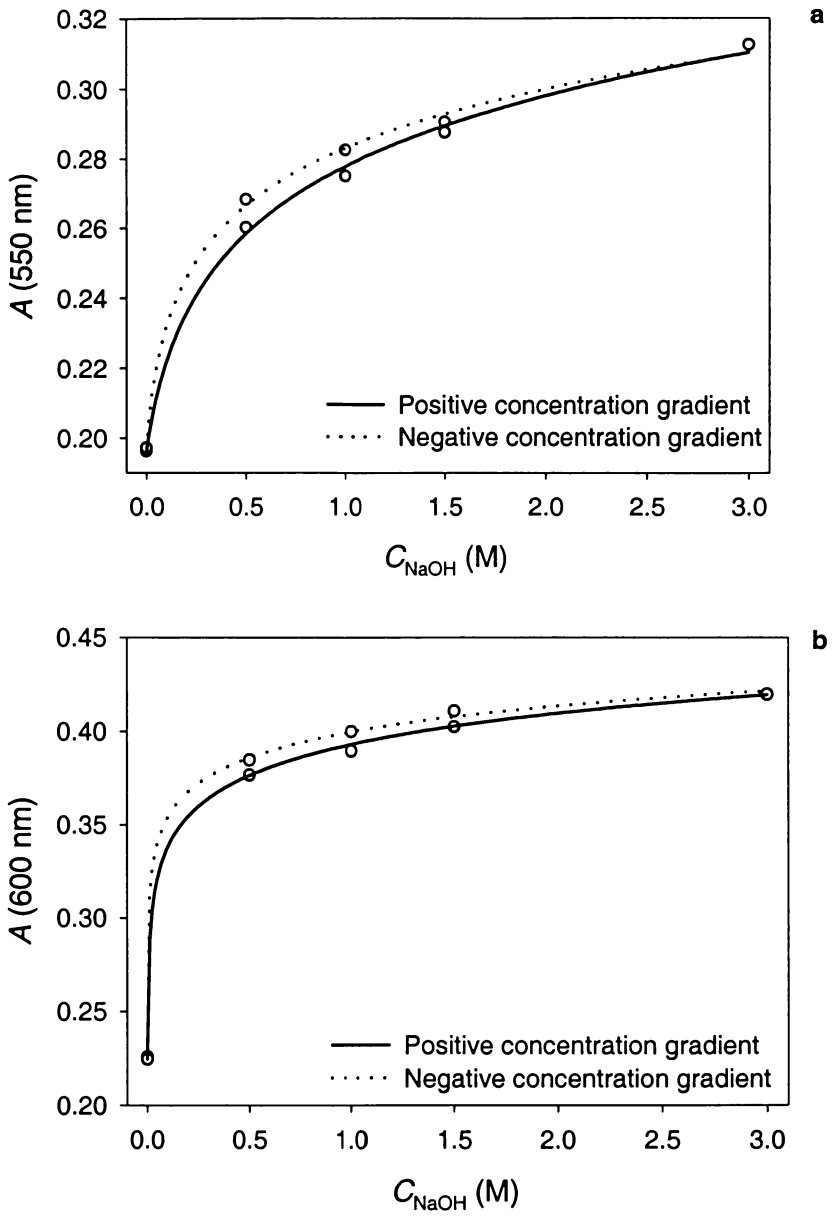

Figure 3.27. Hysteresis profile for Sensors (a) **TY5** and (b) **AY5** in NaOH-EtOH-H_2O 50% v/v solutions.

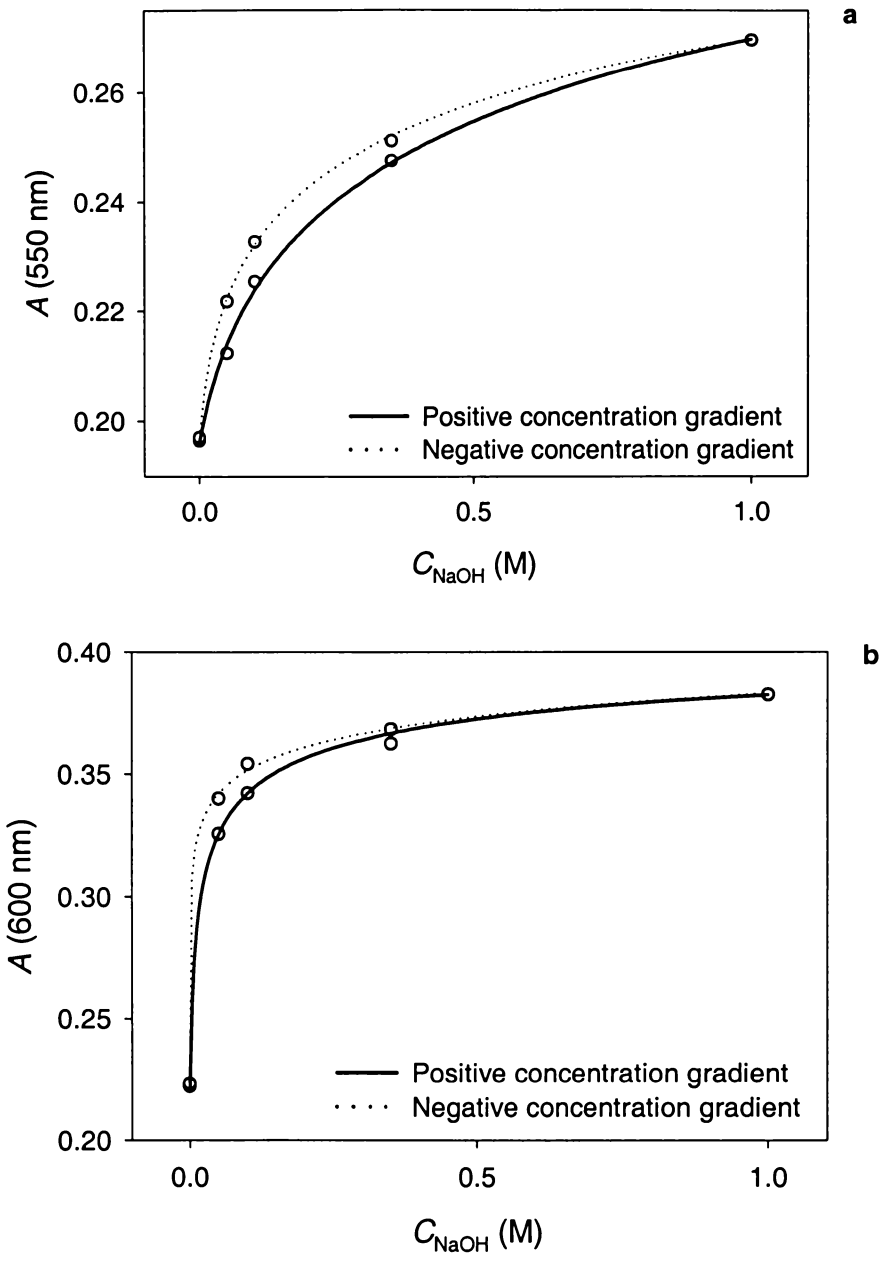

Figure 3.28. Hysteresis profile for Sensors (a) **TY5** and (b) **AY5** in NaOH-i-PrOH-H_2O 50% v/v solutions.

interval of the indicator. Hysteresis was observed since there was not an alignment between the positive and negative concentration gradients (Figures 3.25-3.28). If the positive and negative gradients coincided, there would have been no hysteresis.

The magnitude of hysteresis is a direct function of sensor response time.[134] As response times increase so does the magnitude of hysteresis. According to Bousse and coworkers, hysteresis effects present a greater obstacle than long-term drift.[134] Göpel and coworkers have stated that differences in the output value of a sensor are determined by the approach on both sides of the output value.[135]

(b) Durability Studies of Optical Sensors in NaOH-ROH-H_2O Media. Periodic testing of Sensors **TY6-8** and **AY6-8** were performed in order to evaluate the long-term durability of the sensors. The sensors remained in constant contact with the NaOH-ROH-H_2O solutions (R = Me, Et, and i-Pr) over the course of several days. The potential indicator leaching could be observed spectroscopically and thus provide insight on the durability of the sensors.

Sensors **TY6-8** and **AY6-8** were found to be durable in NaOH-ROH-H_2O solutions (R = Me, Et, and i-Pr, respectively, for Sensors **6-8**) for approximately 120 days in their alkaline environments (Figures 3.29-3.31). Standard deviations were 2.38, 1.46, and 4.04% for Sensors **TY6-8** in MeOH-, EtOH-, and i-PrOH-containing solutions, respectively. Standard deviations were 2.20, 2.18, and 2.38% for Sensors **AY6-8** in these solutions, respectively. Enhanced indicator leaching or breakdown (standard deviation as large as 10 to 15%) resulted at

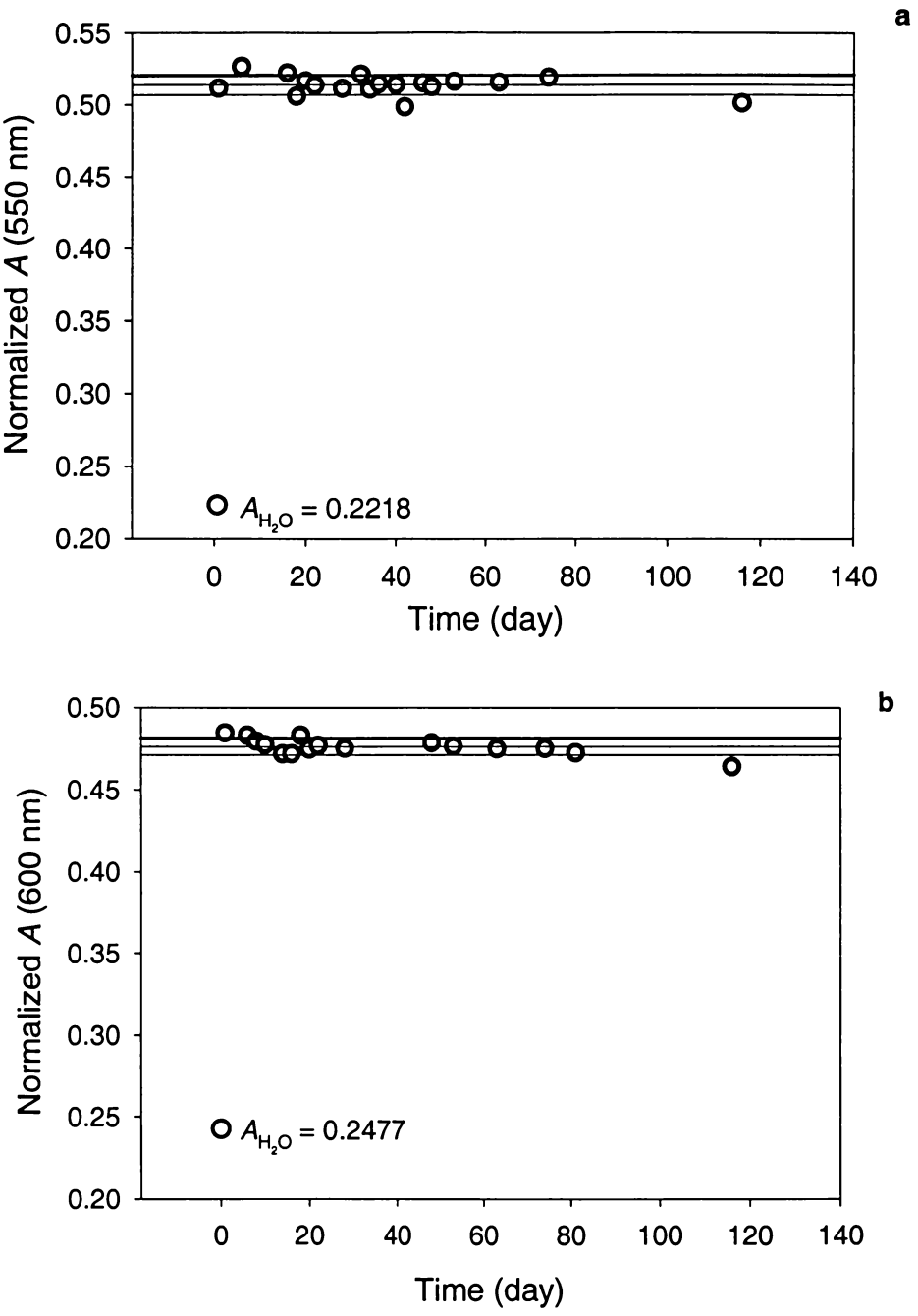

Figure 3.29. Durability of Sensors (a) **TY6** and (b) **AY6** in 2.00 M NaOH-MeOH-H_2O 50% (v/v) solutions.

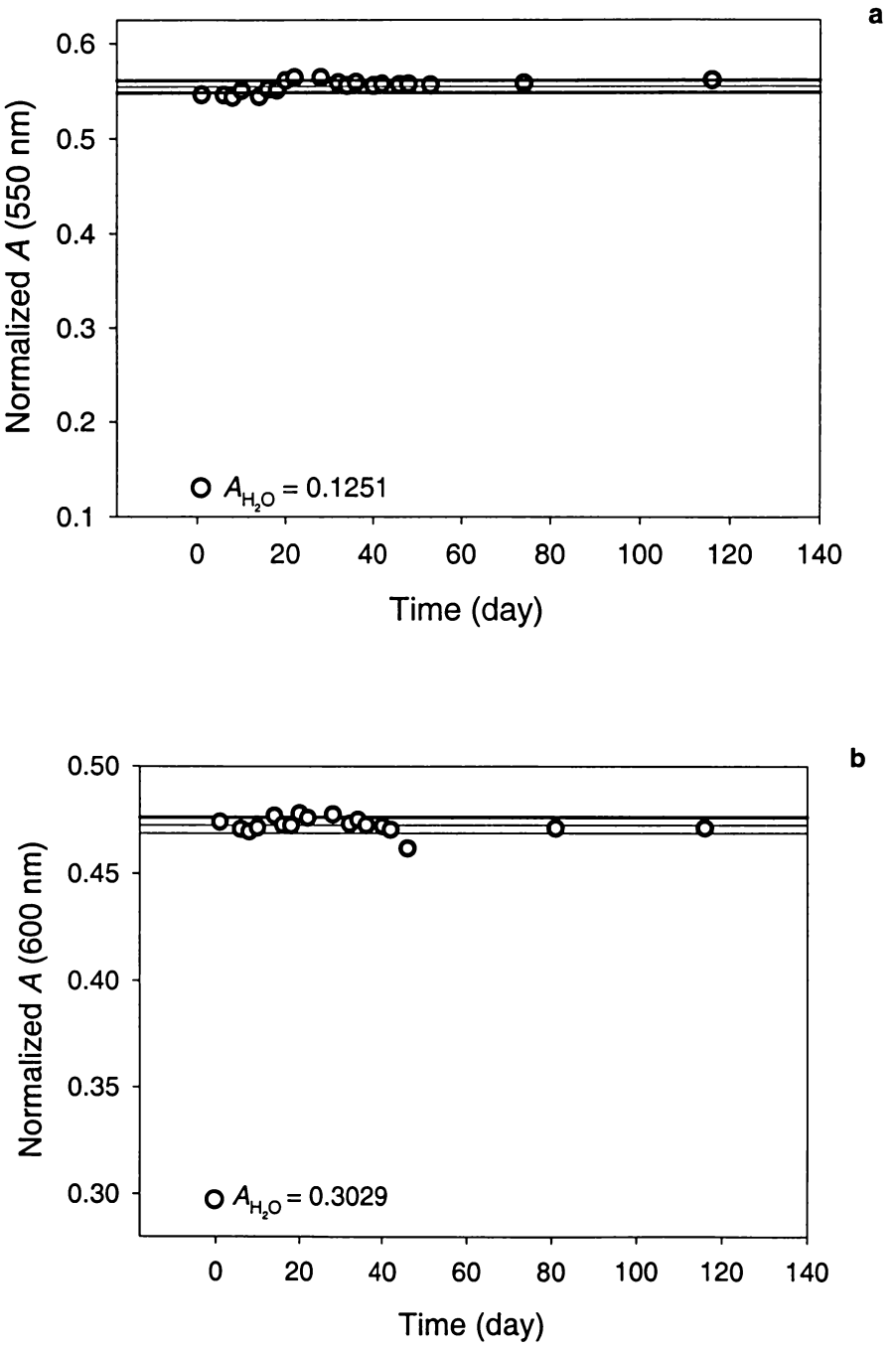

Figure 3.30. Durability of Sensors (a) **TY7** and (b) **AY7** in 2.00 M NaOH-EtOH-H_2O 50% (v/v) solutions.

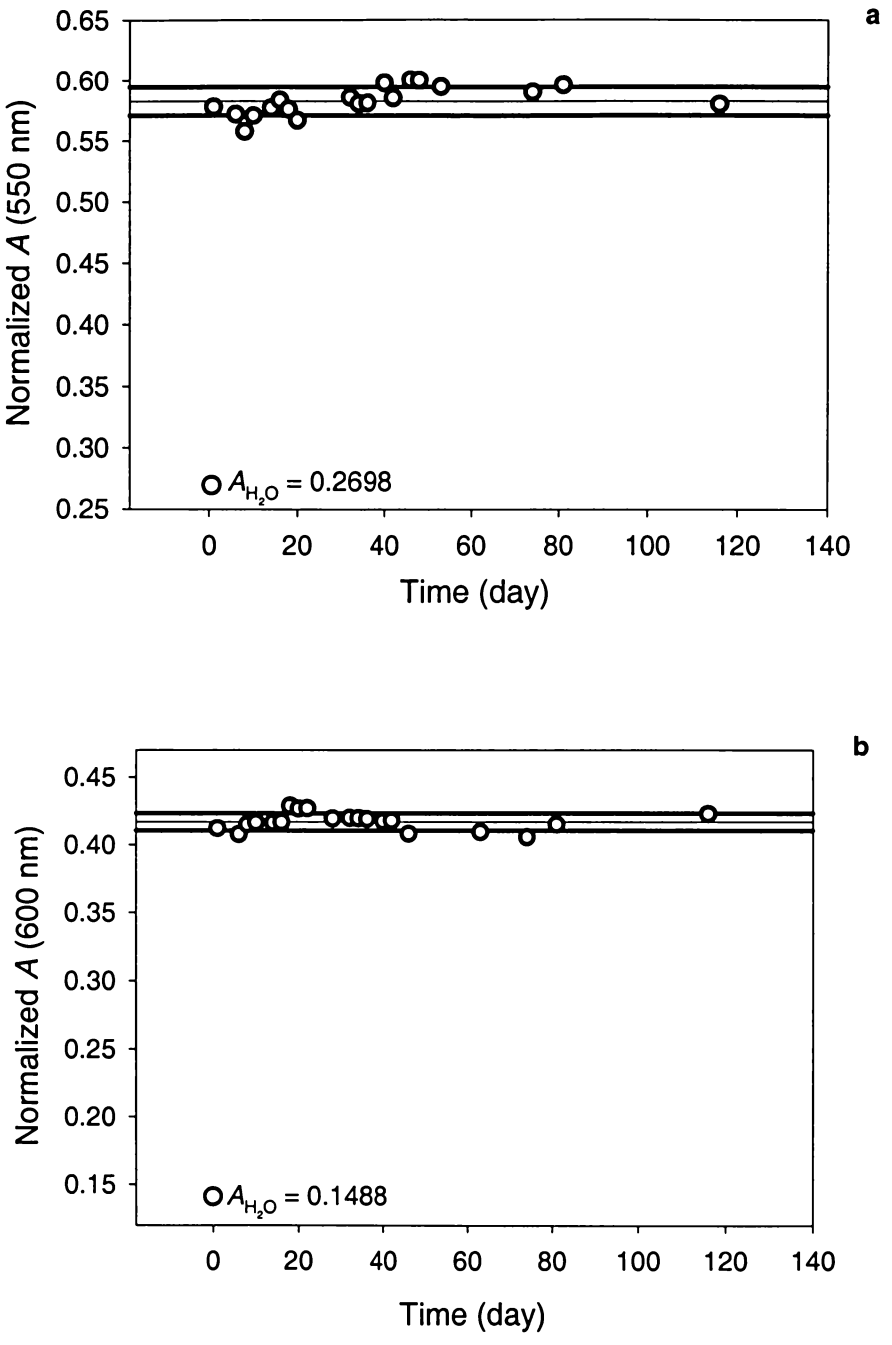

Figure 3.31. Durability of Sensors (a) **TY8** and (b) **AY8** in 0.50 M NaOH-i-PrOH-H_2O 50% (v/v) solutions.

some time interval during day 120 to 150.

3.4 Concluding Remarks

The film morphology (porosity, surface area, and thickness) and chemistry directly determine the performance of the sensor. The presence of Si-O-Zr linkages are suspected to increase the stability of the sensor films in concentrated alkaline media in which silica dissolves readily. The sensor materials in the current studies were evaluated by XPS, ^{29}Si solid-state NMR, and FT-IR techniques. It was found that these sensors were stable for approximately 120 days, exhibited short response times (typically <10 s), and were fully reversible with minimal hysteresis effects in NaOH-ROH-H2O solutions (R = Me, Et, and i-Pr).

CHAPTER 4

High-Acidity Determination in Salt-Containing Acids by Optical Sensors. The Scope of a New Dual-Transducer Approach

4.1 Introduction

Optical sensors constitute one major category of chemical sensors, and they are often used in systems containing more than one chemical.[34-37,73-75] In these multi-component systems, sensor response is often affected by changes in ionic strength by chemicals other than the analyte. This is particularly significant for optical sensors that are based on indicator equilibria as their transducing mechanism. In addition, the sensor response to changes in ionic strength (by chemicals other than the analyte) is often indistinguishable from that by the analyte. An accurate measurement of each component in these multi-component systems is of intense current interest.

Several approaches have been developed to correct ionic strength in optical sensing for the *p*H region and solutions of low-to-medium ionic strength *I*.[34-37,73-75] Seitz and coworkers[74,75] previously reported a sensor for *p*H via an optical reflectance device coupled to the swelling of a polystyrene membrane. The resultant sensor was inexpensive with modest power requirements. The sensor was stable provided that the membrane was kept moist at all times. The changing ionic strength affected the turbidity of the membrane and the extent to which the protonated polymer swelled. The sensor was only viable through the

*p*H range 4 to 10.

A sensor has been reported[36] that is based upon multiple analytes forming a sensor array. Data acquisition is obtained by using a charge-coupled device (CCD). The response to multiple analytes (Ce^{3+}, Ca^{2+} and *p*H at low concentrations) can be thought of as a primitive "electronic tongue." Polystyrene beads were embedded with an assortment of indicator molecules to mimic taste buds.[36]

Sensors reported by Wolfbeis and Offenbacher[35] have been developed in order to measure both the *p*H and ionic strength by using two different *p*H determinations. One of the two sensors is based upon a *p*H indicator embedded within a micro-environment. In this case, the dissociation constant of the indicator is highly sensitive towards changes in the ionic strength of the solution. The second sensor is desensitized to changes in salt concentration by surrounding the indicator with charged ammonium groups. Additional changes in ionic strength have essentially no effect upon the second sensor. A limitation of this approach is that only ionic strength determinations near the neutral *p*H range can be investigated.[35]

Another sensor, developed by Lübbers and Opitz,[34] was based upon fluorescent photometric techniques for continuously measuring the ionic strength and hydrogen ion activities of a solution. The correction is based upon using two different *p*H fluorescent indicator systems in order to develop two independent equations to measure both the *p*H and ionic strength. The determination of the

ionic strength was restricted between 0.1 to 1 M and *p*H measurements had to be in the range of 6.5-8.5.[34]

Pittner and coworkers[37] developed a technique for measuring the ionic strength of a solution by metal island coated swelling polymer over mirror system (MICSPOMS). By monitoring the slope of the narrow-bandwidth reflection minimum, the analyte responsible for the swelling action could be observed. This technique was sensitive only across the range of 0.05 to 1 M salt concentration and near neutral *p*H.[37]

Due to the acid error effect, *p*H meters cannot be used to accurately determine the acidity of solutions greater than 0.1 M. In such solutions, the *p*H response of the glass electrode displays a negative error (opposite of the alkaline error effect, Figure 4.1). As a result the *p*H measurement in this region is greater than the true *p*H. There are many conflicting theories on the origin of the acid error effect.[136-138]

We recently reported a dual-transducer optical sensor approach to measure acid concentrations in salt-containing, concentrated strong acids such as $CaCl_2$-HCl solutions. The sensors in this approach are based upon indicators encapsulated in silica sol-gel thin films.[19,30-32,51,52,106,139-142]

The dual-transducer approach was developed in part to address the need for sensors for concentrated strong acids such as HCl: (a) These acids are amongst the largest volume chemicals manufactured in the world, and are widely used in many chemical processes.[23,24] Rapid and reliable methods for their on-line determination and quality control are limited. (b) Concentrated strong acids

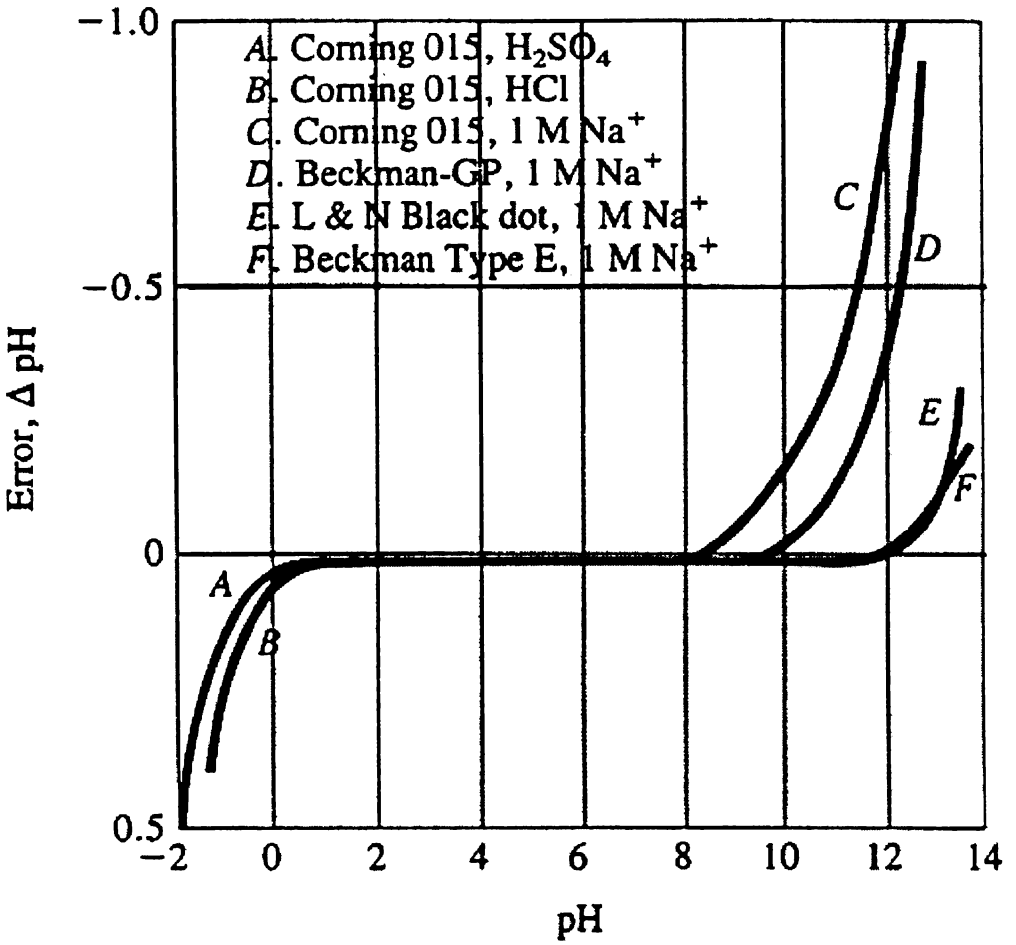

Figure 4.1. Acid and alkaline error for selected glass electrodes at 25 °C. (Bates, R. G. *Determination of pH: Theory and Practice*, 2nd ed.; John Wiley & Sons: New York, 1973, p. 365.)

such as HCl are often used in the presence of, e.g., salts, and the ionic strength changes by these salts complicate the acidity measurement. This dual-transducer approach was based on a novel linear relationship[18] between $\left(\partial A/\partial C_{salt}\right)_{C_{acid}}$ and $\left(dA/dC_{acid}\right)_{C_{salt}=0}$ (Eq. 4.1) for indicator-doped sol-gel sensors. The two sensors used in this approach have distinct ionic strength dependencies, and the signal arrays are deconvoluted to give C_{acid} and C_{salt}.

$$\left(\partial A/\partial C_{salt}\right)_{C_{acid}} = \beta \cdot \left(dA^{o}/dC_{acid}\right)_{C_{salt}=0} \qquad \text{(Eq. 4.1)}$$

Previous work in our group[18] on this dual-transducer approach concentrated on the linear relationship in Eq. 4.1 and the development of the approach for one salt ($CaCl_2$) demonstrated for *one* acid concentration (5 M). In the current work, we studied the use of this approach to estimate C_{acid} at 2 to 9 M in HCl-LiCl-H_2O, HCl-$CaCl_2$-H_2O, and HCl-$AlCl_3$-H_2O solutions.

4.2 Experimental Section

Visible spectra were recorded using the spectrometer discussed in Section 1.1.3 with a xenon flashlamp as the light source. Solutions of HCl, HCl-LiCl-H_2O, HCl-$CaCl_2$-H_2O, and HCl-$AlCl_3$-H_2O were prepared by gravimetric dilution and titrated with NaOH standards (Fisher) to the phenolphthalein end point. Bromocresol Purple (BCP, 90% dye content, Aldrich), Bromocresol Green (BCG, 95% dye content, Eastman), Neutral Red (NR, 60% dye content,

Eastman), $Si(OMe)_4$ (99+%, Aldrich), MeOH (Certified ACS, Fisher), cetyltrimethylammonium bromide (CTAB, Aldrich), Nafion (5% Nafion in an alcoholic mixture containing 5% w/w water, Aldrich), HCl (37.5%, Certified ACS, Fisher), and $AlCl_3 \cdot 6H_2O$ (99%, Acros) were used as received. $CaCl_2.2H_2O$ (Certified ACS, Fisher) and LiCl (99% anhydrous, Acros) were kept at 45 °C for one and two weeks, respectively, prior to use. Data analysis was conducted with Sigma Plot™ (SPSS Inc., 233 S. Wacker Drive, 11th Floor, Chicago, IL 60606-6307; http://www.spss.com), Matlab™ (The MathWorks, Inc., 3 Apple Hill Drive, Natick, MA 01760-2098; http://www.mathworks.com), and Maple (Waterloo Maple™ Inc., 57 Erb Street, W. Waterloo, Ontario, Canada N2L 6C2; http://www.maplesoft.com) programs. Sensor slides were cut and processed after the sol-gel spin coating, as discussed in Section 1.4.5.

4.2.1 Preparation of Sensors BCG1-3.[30] A solution of H_2O (60 µL), HCl solution (0.01 M, 17 µL), methanol (130 µL, 3.21 mmol), CTAB (4.0 mg, 0.011 mmol), and Bromocresol Green (55.3 mg, 0.0792 mmol) was allowed to stir for 5 min in a glass vial at room temperature to completely dissolve CTAB and BCG. $Si(OMe)_4$ (200 µL, 1.36 mmol) was then added and the solution was stirred for 50 min at room temperature. The solution was then spin coated onto individual glass substrates. The spin coating process lasted about 30 s at a spinning rate of 3000 rpm for each thin film generated. The sensors were cured for 5 days in air at room temperature, and then placed in an oven at 45 °C for 15 days.

4.2.2 Preparation of Sensors BCP1-3.[30] They were prepared by a procedure similar to that used in the preparation of Sensors **BCG1-3** except that 60.0 mg (0.111 mmol) of Bromocresol Purple indicator was used.

4.2.3 Preparation of Sensors NR1-3.[30] A mixture of HCl solution (0.01 M, 110 µL), methanol (40 µL, 0.99 mmol) and Neutral Red (15.1 mg, 0.0523 mmol) was allowed to stirr at room temperature to give a dark purple solution. Nafion® solution (160 mg) was then added while stirring at room temperature. The solution became more viscous. $Si(OMe)_4$ (300 µL, 2.03 mmol) was added and the solution was stirred for 2 h at room temperature. The solution was then spin coated onto individual glass substrates. The spin coating process lasted about 45 s at a spinning rate of 3000 rpm for each thin film generated. The sensors were cured 7 days in air at room temperature then placed in an oven at 45 °C for 4 days. The films containing Nafion were found to degrade if the sensors were left in the oven for too long.

4.2.4 Sensor Conditioning. The cured sensors were placed in water for two days followed by concentrated HCl for one day and finally in distilled water for one day. This procedure was performed at room temperature in air. When no appreciable leeching of dye was observed spectrometrically, the sensors were cut for testing.

4.2.5 Measurement Procedure. The sensor element, an indicator-doped film coated onto a glass slide, was mounted in a Teflon cell, leaving a 0.7 mm space along the optical path for contact with the flowing liquid sample. A regular sanded glass slide without any coating was used as a blank. The apparatus used for the measurement was reported earlier in Chapter 1. Between each individual test, the cell was washed thoroughly with distilled water to prevent contamination between the samples. The salt-HCl solution was flowed through the sensor cell. The average of several repetition scans was used for each test to minimize the effect of spectral drift. Standard deviations were calculated from the random errors in five separate tests for several samples.

4.2.6 Characterization. An Alpha-Step 500 Surface Profilometer X187401 was used for the film thickness analysis. A Nova 1000 High Speed Surface Area and Pore Size Analyzer by Quantachrome Corp.® was used for Brunauer-Emmett-Teller (BET) gas adsorption analysis to measure the specific surface area, pore volume, and pore size distribution of sol-gel sensor materials.

4.3 Results and Discussion

4.3.1 Salt Selection. The three main criteria for the selection of salts to be used in conjunction with HCl were cation valence, solubility, and optical transparency of the salt-HCl solutions. By using chloride salts we were able to have a three-component system in each case: Cl^-, H^+, and metal (Li^+, Ca^{2+}, or Al^{3+}) ions. A univalent, divalent, and trivalent salt was investigated individually. Due to the

common-ion effect, salt solubility was crucial to having mono-phase solutions concentrated in acid and salt. LiCl, $CaCl_2$, and $AlCl_3$ were chosen for their relatively high aqueous solubilities (1 g/1.3 mL, 1 g/1.5 mL, and 1 g/0.9 mL, respectively).[143] In addition, the solutions of these salt-HCl solutions have little or no color to minimize visible spectral interference.

4.3.2 Characterization of the Sensor Materials. Profilometry measurements showed that the sensor film thickness ranged from 3.4 to 5.0 μm. In these measurements, a diamond stylus was scanned over the film surface. The stylus was attached to an arm that rotates about a flexure pivot to give smooth and stable scanning across the film surface. The aberrations were recorded by a detector and plotted. There were two baselines, film surface and substrate surface, and they were separated by a step which gave the film thickness. These surface profilers have a resolution of 1 Å in a range of thickness from 100 Å to 0.3 mm.

Brunauer-Emmett-Teller (BET) method was used to examine the surface area, average pore distribution, and total pore volume of the sol-gel materials. Due to the limited mass of the sensor film, we used the bulk sol-gel samples for the BET measurements (Table 4.1). These bulk materials were prepared by procedures similar to those to give the sensor films except that the sol-gel was not cast to films. The blank and BCG encapsulated sol-gel Powders **13-15** were found to be mesoporous based on their isotherm plots. The surface area of Powders **13-15** ranged 226 to 238 m^2/g with an average pore size distribution of

Table 4.1. BET Results of the Bulk Samples

Sensor Bulk	Surface Area (m^2/g)	Average Pore Diameter (Å)	Total Pore Volume (cm^3/g)
Davisil-635 Silica Standard	475	61	0.72
Bulk **1**	238	26	0.22
Bulk **2**	226	25	0.14
Bulk **3**	227	25	0.14
Bulk **4**	7	36	0.0062
Bulk **5**	14	43	0.015

25 to 26 Å. The total pore volume ranged from 0.14 to 0.22 cm^3/g.

In the NR sensor materials containing Nafion and SiO_2 (Powders **16-17**, Table 4.1), much lower surface areas and pore volumes were obtained. This suggests that Nafion either covered the SiO_2 surface extensively or formed a Nafion/SiO_2 polymer blend, thus reducing the ability of the SiO_2 polymer to absorb N_2 on its surface.

4.3.3 The Salt-Effect and Dual Optical Transducer Approach. It has long been known that when a soluble salt is added to an aqueous acidic solution, the water activity decreases. Water is removed from the bulk solution in order to solvate the cations and anions of the salt.[33] A net shift in the indicator equilibrium takes place in order to replenish the water.

LiCl, $CaCl_2$ and $AlCl_3$, M^+, M^{2+}, and M^{3+} salts, respectively, were chosen for the current studies to give solutions of different ionic strength. We observed that when a large amount of each of these three salts was added to an acid solution of a fixed concentration, the absorbances of the Bromocresol Purple (Sensors **BCP1-3**), Neutral Red (Sensors **NR1-3**), and Bromocresol Green (Sensors **BCG1** and **3**) varied proportionally to the amount of the added salt. Such linear plots are shown in Figures 4.2-4.4. 3D experimental plots of A (A = absorbance of the sensor in a salt-containing HCl solution) vs C_{acid} and C_{salt} are given in Figures 4.5-4.7. In high ionic strength solutions, as expected, the magnitude of change in sensor response varies with different salts in the solutions. The experimentally observed salt-free (C_{salt} = 0 M) A^0 vs C_{acid} plots are

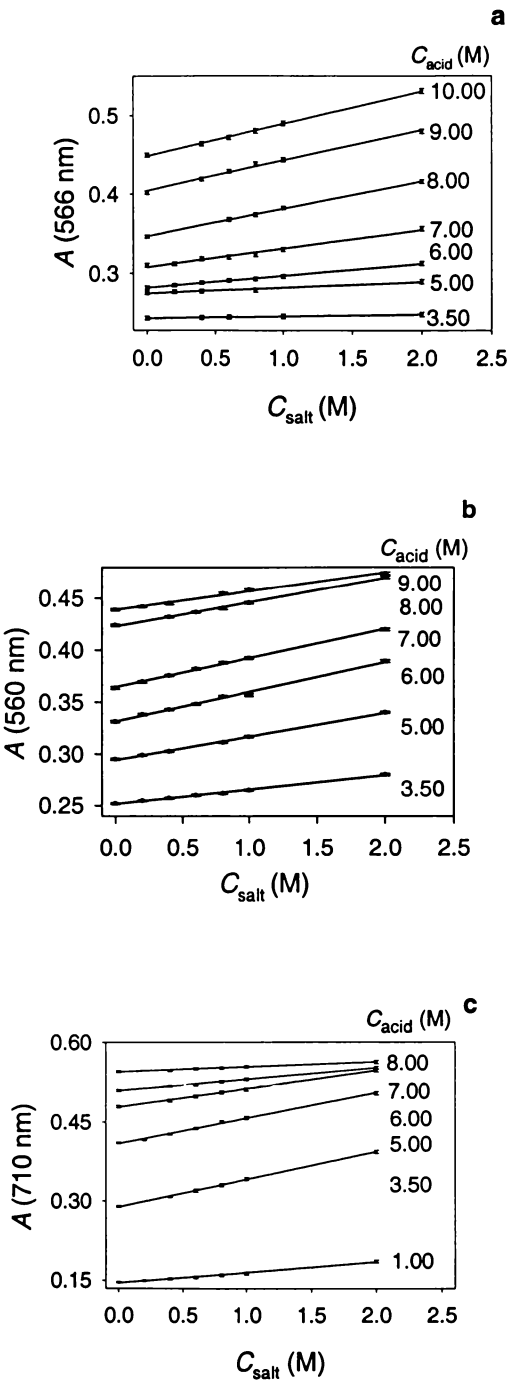

Figure 4.2. Sensors (a) **BCG1**, (b) **BCP1**, and (c) **NR1** in HCl-LiCl-H_2O solutions.

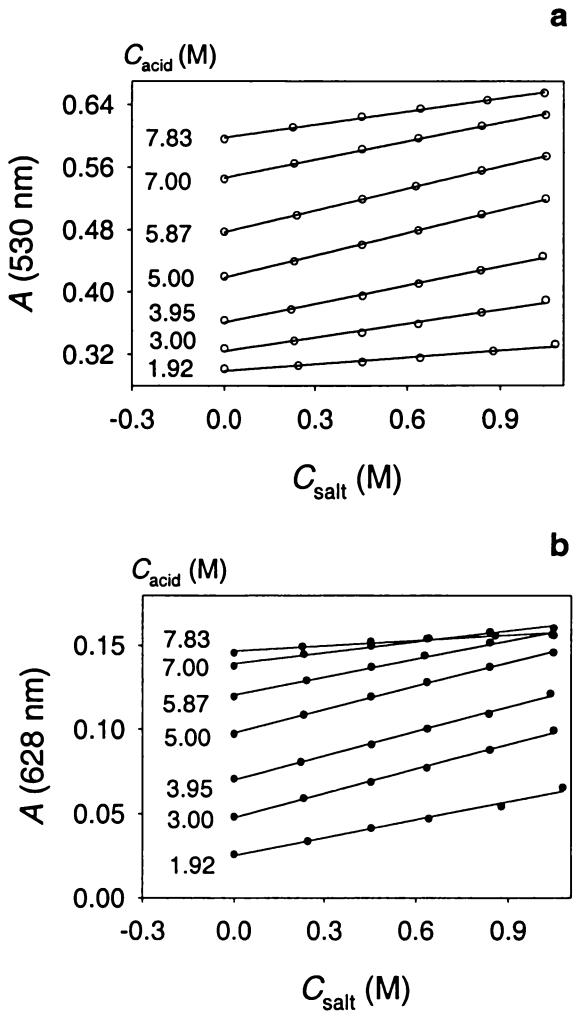

Figure 4.3. Sensors (a) **BCP2** and (b) **NR2** in HCl-$CaCl_2$-H_2O solutions.

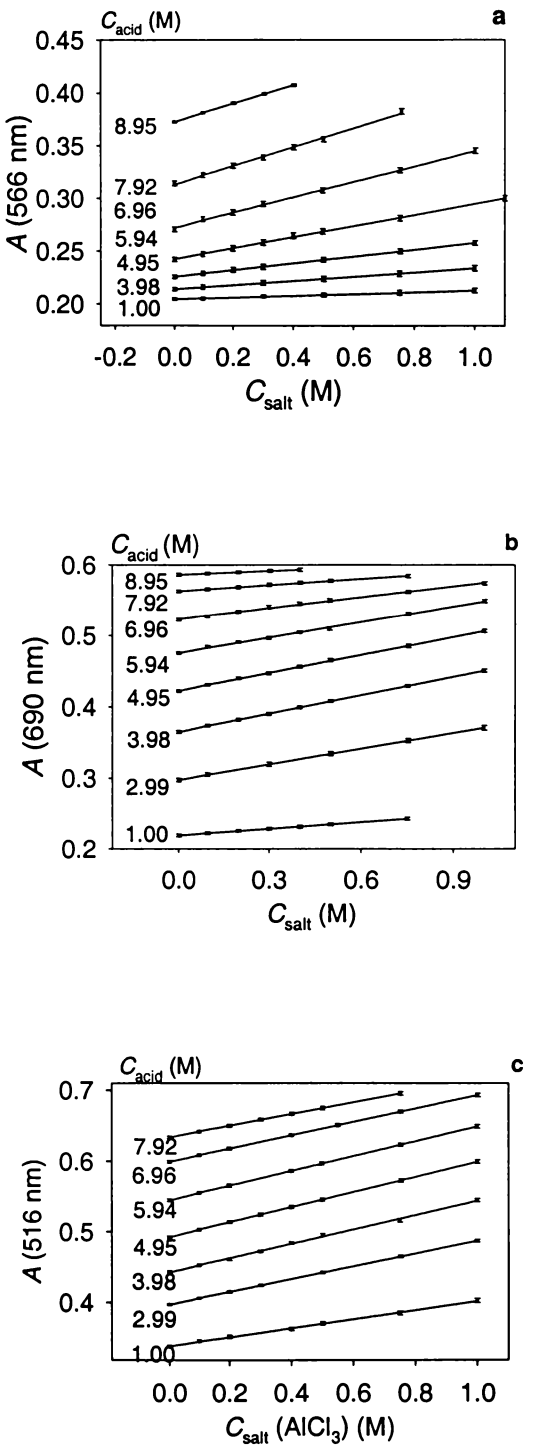

Figure 4.4. Sensors (a) **BCG3**, (b) **NR3**, and (c) **BCP3** in HCl-$AlCl_3$-H_2O solutions.

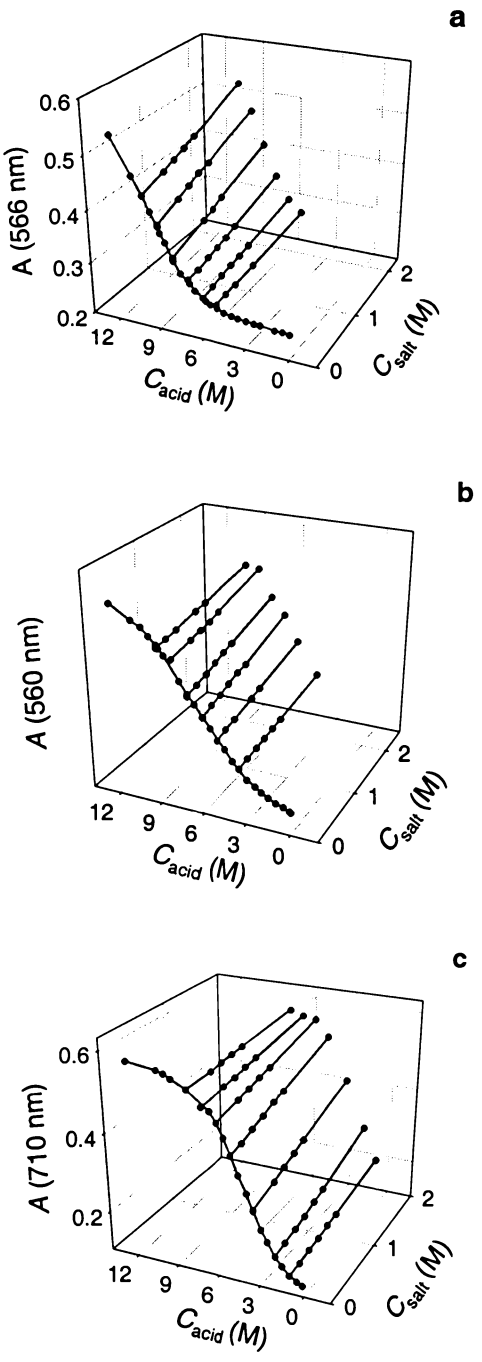

Figure 4.5. Sensors (a) **BCG1**, (b) **BCP1**, and (c) **NR1** in HCl-LiCl-H_2O solutions.

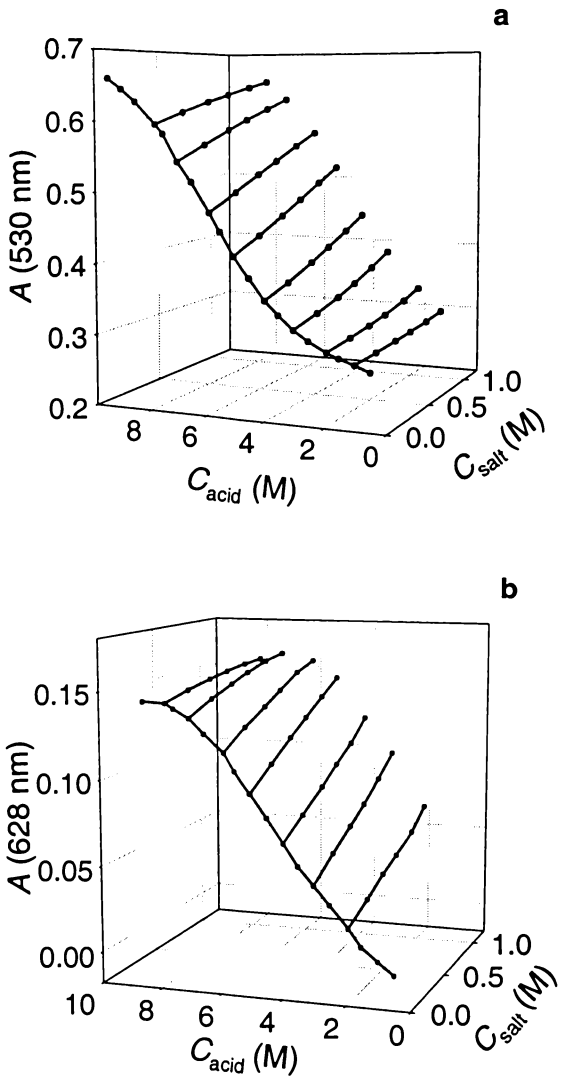

Figure 4.6. Sensors (a) **BCP2** and (b) **NR2** in HCl-$CaCl_2$-H_2O solutions. (Allain, L. R. Ph.D Dissertation, "Optical Sensors in Harsh Environments: Determination of Concentrated Strong Acids and Bases for Process Control," The University of Tennessee, Knoxville, 1999, p. 120, and p. 122.)

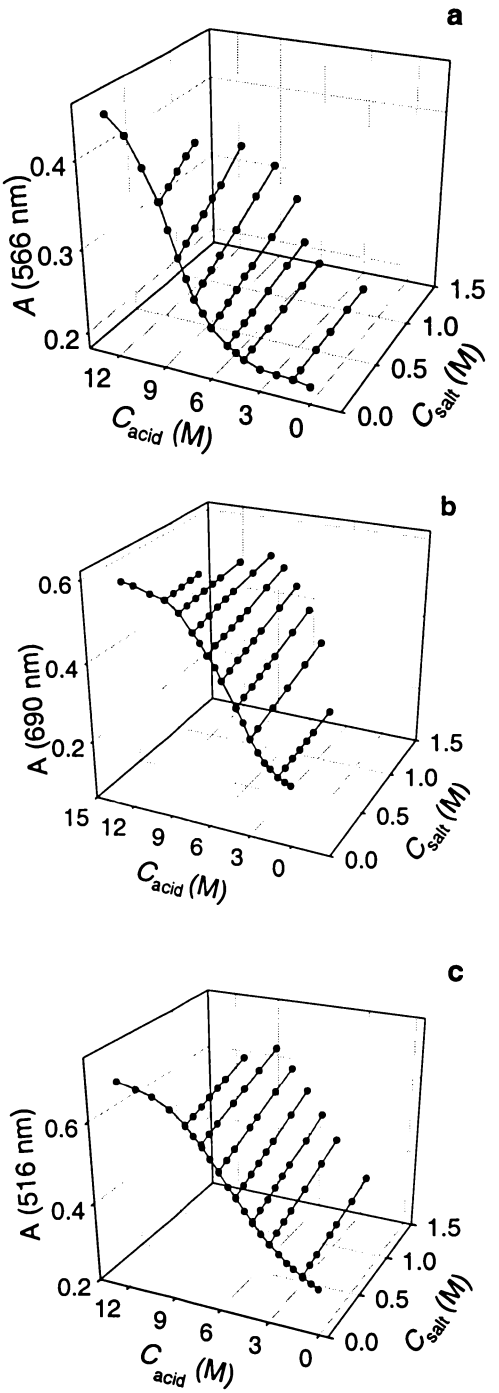

Figure 4.7. Sensors (a) **BCG3**, (b) **NR3**, and (c) **BCP3** in HCl-$AlCl_3$-H_2O solutions.

different from each other for these eight sensors (Sensors **BCP1-3**, **NR1-3**, and **BCG1** and **3**).

As was found earlier in our group,[18] the slope of A vs C_{salt} at a given acid concentration, $\left(\partial A/\partial C_{salt}\right)_{C_{acid}}$, is proportional to the respective tangent of the A^0 vs C_{acid} plot, $\left(dA^0/dC_{acid}\right)_{C_{salt}=0}$, for a salt-free acid solution using these sensors (Appendix B).[18] A linear relationship was observed between the slopes of A vs C_{salt} plots (Figures 4.2-4.4) and the first derivatives of A^0 vs C_{acid} curves (Figures 4.8-4.10) for each of these eight sensors in HCl-LiCl-H_2O, HCl-$CaCl_2$-H_2O and HCl-$AlCl_3$-H_2O solutions. Such linear plots for Sensors **BCP1**, **NR1** and **BCG1** sensors in HCl-LiCl-H_2O solutions, Sensors **BCP2** and **NR2** in HCl-$CaCl_2$-H_2O solutions, and Sensors **BCP3**, **NR3** and **BCG3** sensors in HCl-$AlCl_3$-H_2O solutions are shown in Figures 4.11-4.13, respectively. In other words, there exists a new relationship in Eq. 4.1.

The ranges of error in Figures 4.11-4.13 as percentages of the dynamic ranges are 0.122-6.89% in $\left(dA^0/dC_{acid}\right)_{C_{salt}=0}$ and 0.165 to 8.83% in $\left(\partial A/\partial C_{salt}\right)_{C_{acid}}$. The origin of this, to our knowledge, previously unknown relationship for these eight sensors is not clear. It forms the basis in the current work to estimate acid (C_{acid}) and salt concentration (C_{salt}) in salt-containing concentrated strong acid.

In salt-free ($C_{salt}=0$) acid solutions, the plot of A vs C_{acid} (e.g., Figures 4.8-4.10) for each of these eight sensors is *best* fitted by an *empirical sigmoid* curve

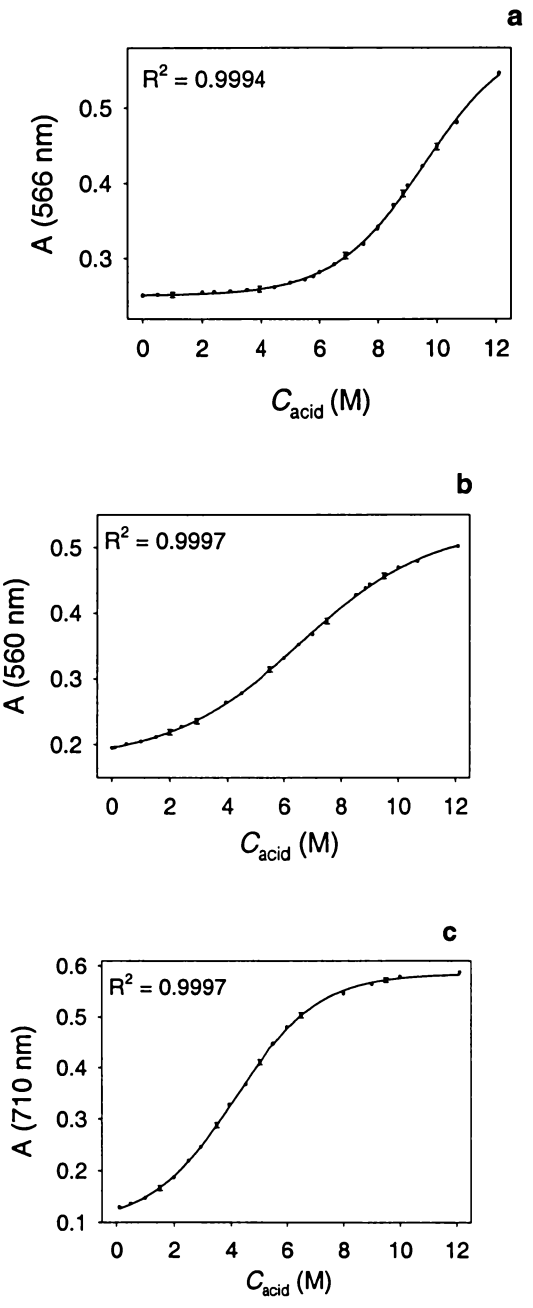

Figure 4.8. Calibration plots for Sensors (a) **BCG1**; (b) **BCP1**; and (c) **NR1** in salt-free, HCl solutions.

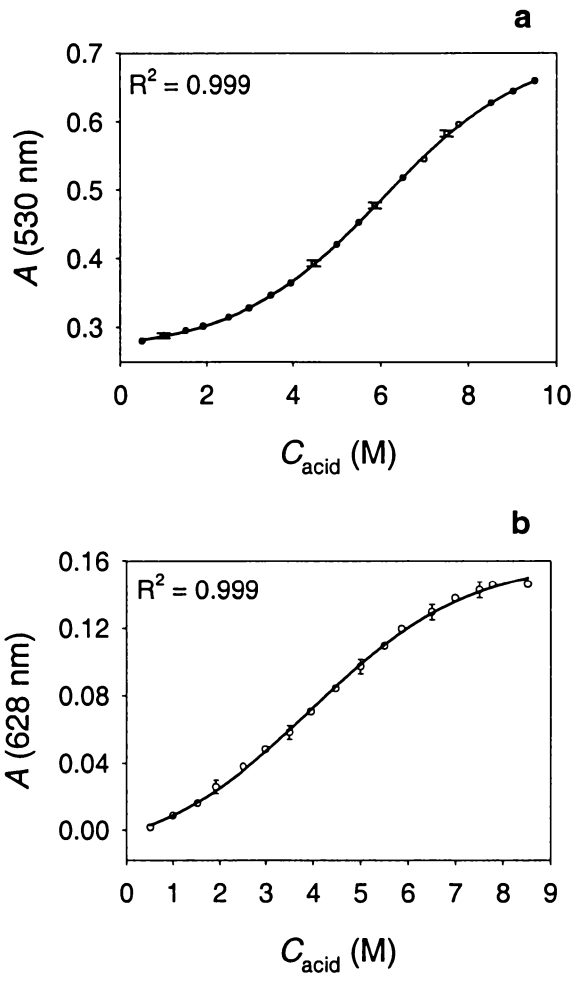

Figure 4.9. Calibration plots for Sensors (a) **BCP2** and (b) **NR2** in salt-free, HCl solutions.

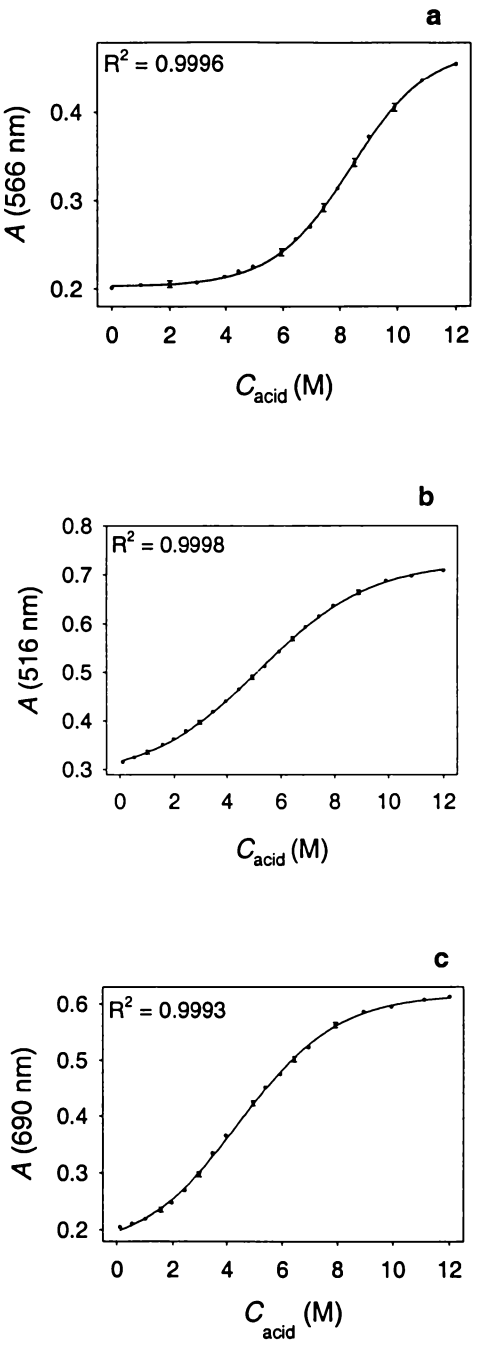

Figure 4.10. Calibration plots for Sensors (a) **BCG3**, (b) **BCP3**, and (c) **NR3** in salt-free, HCl solutions.

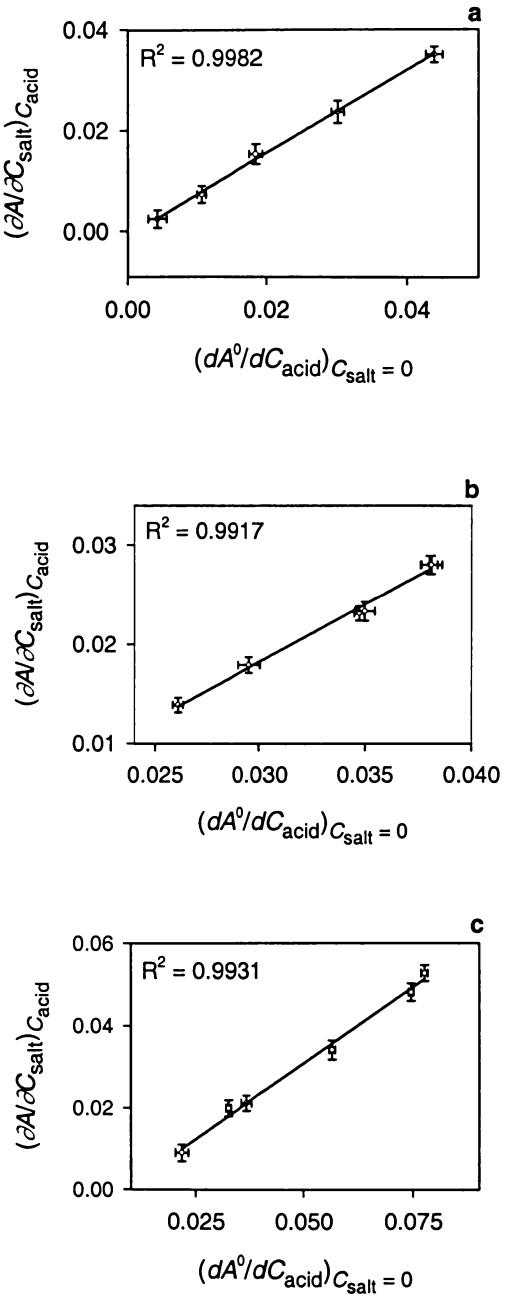

Figure 4.11. Plot of $\left(dA^0/dC_{acid}\right)_{C_{salt}=0}$ vs. $\left(\partial A/\partial C_{salt}\right)_{C_{acid}}$ in HCl-LiCl-H_2O solutions: Sensors (a) **BCG1**, (b) **BCP1**, and (c) **NR1** (unit: $mol^{-1}.L$).

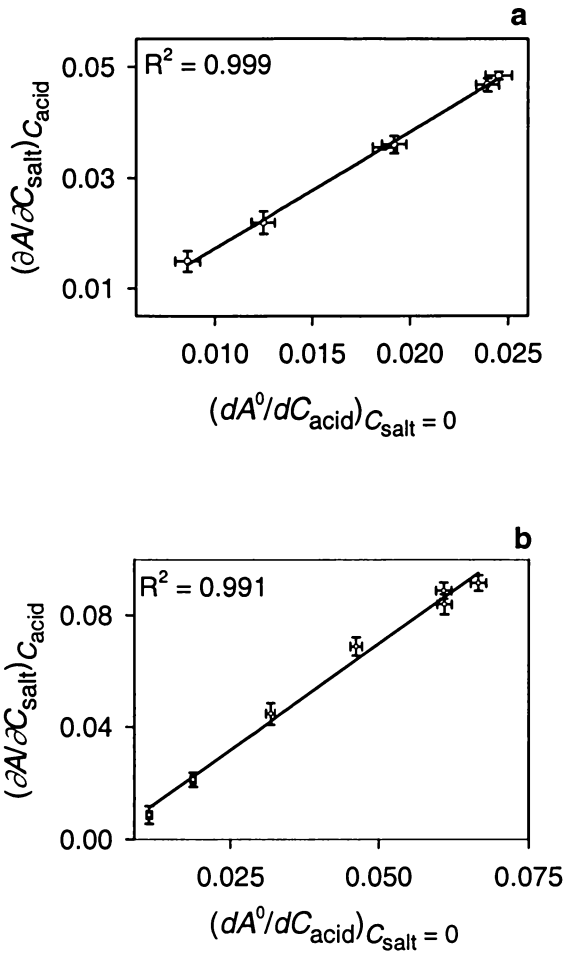

Figure 4.12. Plot of $\left(dA^0/dC_{acid}\right)_{C_{salt}=0}$ vs. $\left(\partial A/\partial C_{salt}\right)_{C_{acid}}$ in HCl-$CaCl_2$-H_2O solutions: Sensors (a) **BCP2** and (b) **NR2**; (unit: $mol^{-1}.L$). (Allain, L. R. Ph.D Dissertation, "Optical Sensors in Harsh Environments: Determination of Concentrated Strong Acids and Bases for Process Control," The University of Tennessee, Knoxville, 1999, p. 123, and p. 125.)

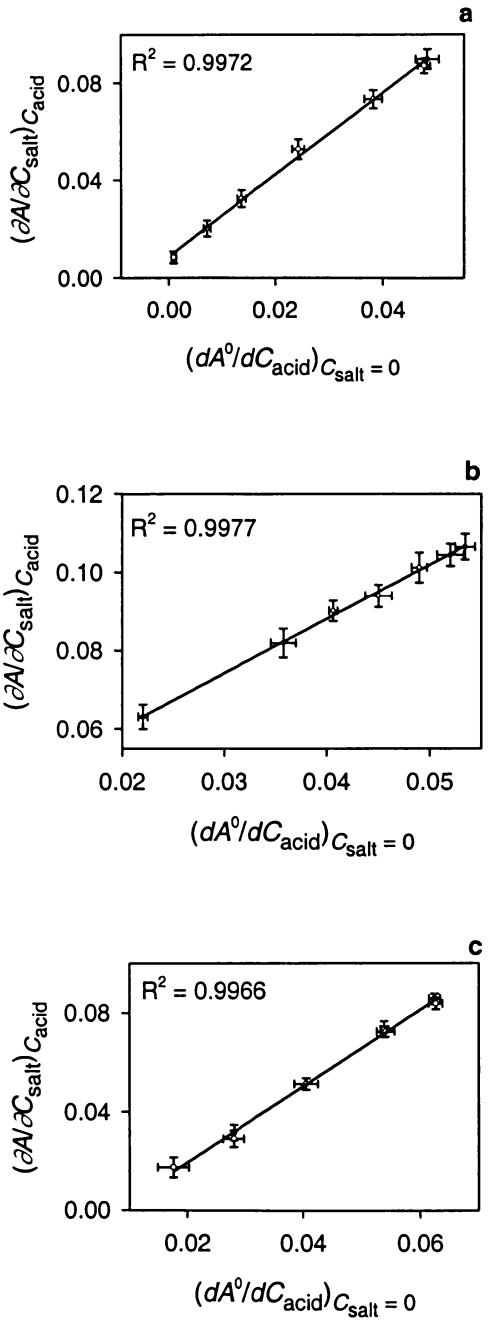

Figure 4.13. Plots of $\left(dA^0/dC_{acid}\right)_{C_{salt}=0}$ vs. $\left(\partial A/\partial C_{salt}\right)_{C_{acid}}$ in HCl-$AlCl_3$-H_2O solutions: Sensors (a) **BCG3**, (b) **BCP3**, and (c) **NR3** (unit: $mol^{-1}.L$).

in Eq. 4.2.

$$A^0 \text{ (salt - free acid)} = f(C_{acid}) = B + \frac{a}{1 + e^{(b - C_{acid})/c}} = B + \frac{a}{1 + x} \quad \text{(Eq. 4.2)}$$

($x = e^{(b - C_{acid})/c}$; B, a, b and c are constants for *each* indicator from the curve fit)

The addition of a salt to an acid solution will lead to an increase ΔA (salt) in absorbance, which, in our systems, is proportional to the salt concentration C_{salt} (Figures 4.2-4.4):

$$\Delta A \text{ (salt)} = \left(\partial A / \partial C_{salt}\right)_{C_{acid}} \cdot (C_{salt} - 0) = \left(\partial A / \partial C_{salt}\right)_{C_{acid}} \cdot C_{salt} \quad \text{(Eq. 4.3)}$$

The total absorbance A in a salt-containing acid is thus:

$$\begin{aligned} A &= A^0 \text{ (salt - free acid)} + \Delta A \text{ (salt)} \\ &= f(C_{acid}) + \left(\partial A / \partial C_{salt}\right)_{C_{acid}} \cdot C_{salt} \end{aligned} \quad \text{(Eq. 4.4)}$$

$\left(\partial A / \partial C_{salt}\right)_{C_{acid}}$ is the slope of the change in A vs added salt (C_{salt}), and is a constant at a given C_{acid} in our systems. However, this slope is an unknown function of C_{acid}. Using the relationship in Eq. 4.1 observed in the current

studies, $\left(\partial A/\partial C_{salt}\right)_{C_{acid}}$ can be replaced by $\beta\left(dA^0/dC_{acid}\right)_{C_{salt}=0}$. Furthermore, $\left(dA^0/dC_{acid}\right)_{C_{salt}=0}$ could be replaced by $df(C_{acid})/dC_{acid}$ using Eq. 4.2 to give Eq. 4.5.

$$\begin{aligned} A &= f(C_{acid}) + \beta\cdot\left(dA^0/dC_{acid}\right)_{C_{salt}=0}\cdot C_{salt} \\ &= f(C_{acid}) + \beta\cdot\left(df(C_{acid})/dC_{acid}\right)\cdot C_{salt} \\ &= f(C_{acid}) + \beta\cdot f'(C_{acid})\cdot C_{salt} \qquad \left(f'(C_{acid}) = df(C_{acid})/dC_{acid}\right) \end{aligned} \qquad \text{(Eq. 4.5)}$$

In other words, the relationship in Eq. 4.1 converts an unknown function in Eq. 4.4 to a function (Eq. 4.5) of absorbance A with C_{acid} and C_{salt}. This non-linear equation (Eq. 4.5) is based on the empirical sigmoid curve $f(C_{acid})$ in Eq. 4.2 that best fits experimental A^0 vs salt-free C_{acid} plot (e.g., Figures 4.8-4.10) for each sensor.

By using two different (and thus independent) transducers 1 and 2, the following two equations and two variables (C_{acid} and C_{salt}) are obtained:

$$A_1 = f_1(C_{acid}) + \beta_1\cdot f_1'(C_{acid})\cdot C_{salt} \qquad \text{(Eq. 4.6)}$$

$$A_2 = f_2(C_{acid}) + \beta_2\cdot f_2'(C_{acid})\cdot C_{salt} \qquad \text{(Eq. 4.7)}$$

In the current case, the first derivative of the empirical sigmoid curve

$f(C_{acid})$ (Eq. 4.2) is

$$f'(C_{acid}) = {df(C_{acid})}/{dC_{acid}} = \frac{a \cdot x}{c(1 + x)^2} \quad \text{(Eq. 4.8)}$$

($x = e^{(b - C_{acid})/c}$; a, b and c are constants for each indicator from the curve fit)

Thus Eqs. 4.6-4.7 turn into Eqs 4.9-4.10.

$$A_1 = B_1 + \frac{a_1}{1 + x_1} + \beta_1 \cdot \frac{a_1 \cdot x_1}{c_1(1 + x_1)^2} \cdot C_{salt} \quad \text{(Eq. 4.9)}$$

$$A_2 = B_2 + \frac{a_2}{1 + x_2} + \beta_2 \cdot \frac{a_2 \cdot x_2}{c_2 \cdot (1 + x_2)^2} \cdot C_{salt} \quad \text{(Eq. 4.10)}$$

A different version of Eqs 4.9 and 4.10 were developed earlier by our group for $CaCl_2$ in 5 M HCl.[18] The solutions to this set of equations could be obtained through a series of iterations. A program was written in Matlab (Appendex C)[18] to calculate C_{acid} and C_{salt} for given A_1 and A_2. An initial C_{acid}(est) was obtained from A vs C_{acid} curve for the salt-free HCl. For a given A_i of sensor i, the iteration program yields a curve of C_{acid}(est) vs C_{salt}(est). The interception of the two independent curves for the two sensors gives C_{acid} and C_{salt}. The use of combinations of sensors for C_{acid} and C_{salt} determination in a *salt*-containing

HCl solutions are given in Figure 4.14 as an example.

4.3.4 Scope of the New Dual-Sensor Approach and Error Analysis.

Previously in our group[18] accurate C_{acid} measurements in concentrated salt-containing acids at one acid concentration (5 M HCl) was studied for one salt ($CaCl_2$) to demonstrate the approach. In the current work an extended range of C_{acid} (ca. 2 to 9 M) with LiCl, $CaCl_2$, and $AlCl_3$ was probed to extend the scope of the approach and to investigate the impact of acid concentration on the errors in C_{acid} measurements. The concentration range of anhydrous LiCl, $CaCl_2 \cdot 2H_2O$, and $AlCl_3 \cdot 6H_2O$ was 8.50 to 85.0, 25.0 to 120.0, and 24.0 to 241 g/L, respectively.

Sensors **BCG1** and **3**, **BCP1-3**, and **NR1-3** were tested in several salt-HCl solutions (salt = LiCl, $CaCl_2$, or $AlCl_3$). If corrections are made, there are substantial increases in the C_{acid} accuracy. In the range of solutions tested (ca. 2 to 9 M HCl, 0 to 2 M salt) errors in C_{acid} were reduced from as much as 48.3% to less than 8.9% in all cases. C_{acid} prediction accuracies before Figures 4.15-4.17) and after (Figures 4.18-4.20) correction, as well as C_{salt} prediction accuracies (Figures 4.21-4.23) for the three HCl-salt solutions studied are given in Tables 4.2-4.4.

Some interesting trends are observed in acid-salt containing solutions: (a) If *no* correction is performed, error in C_{acid} measurement increases as the C_{salt} is increased (at constant C_{acid}). For example, error for Sensor **NR1** increases from 1.6 to 23.4% when C_{LiCl} changes from 0.20 to 2.00 M (and C_{HCl} is held constant

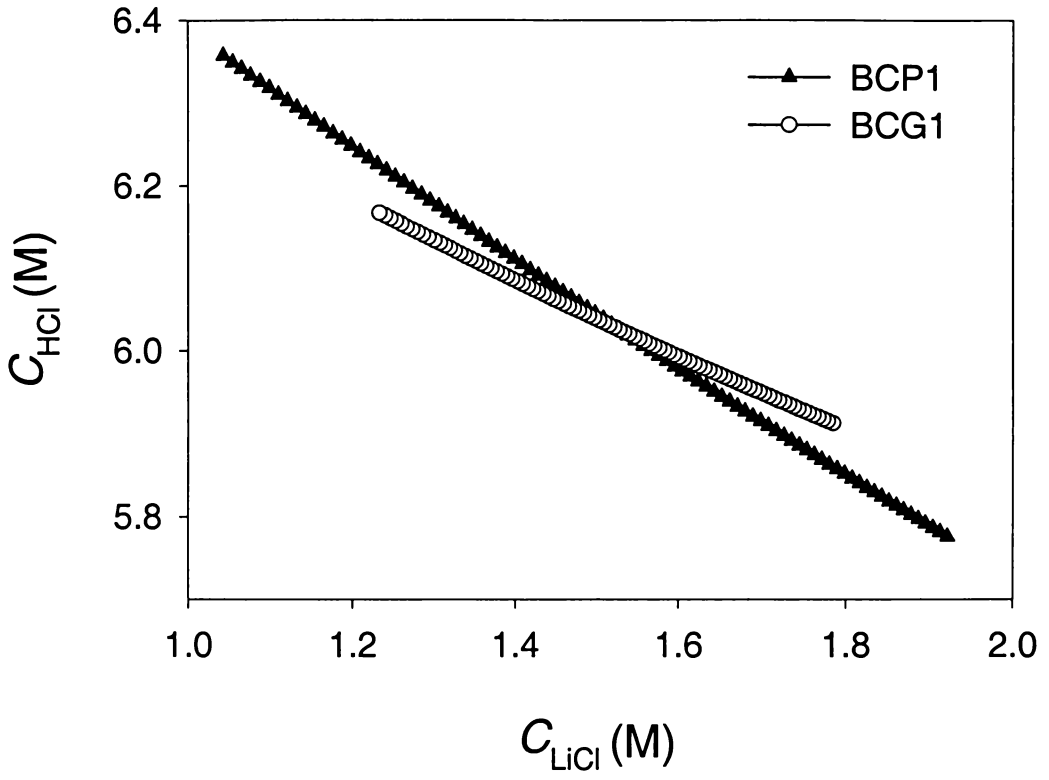

Figure 4.14. Typical representation of the plots of computed (C_{salt}, C_{acid}) pairs for given *A* readings from Sensors **BCP1** and **BCG1** in a HCl-LiCl-H_2O solution.

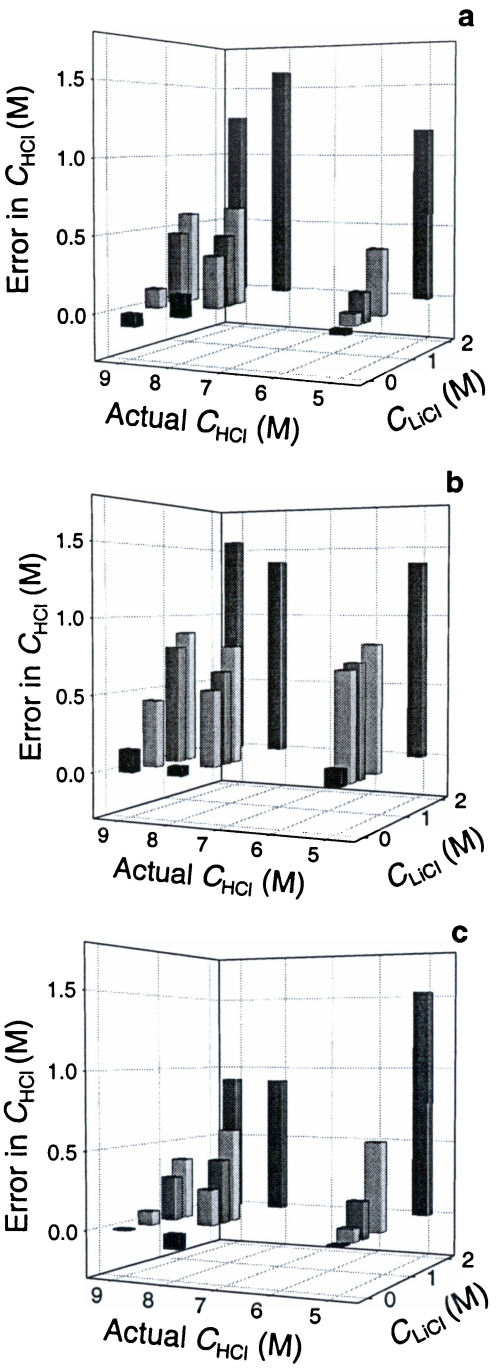

Figure 4.15. Errors in C_{HCl} measurement in HCl-LiCl-H_2O solutions using Sensors (a) **BCP1**, (b) **BCG1**, and (c) **NR1** without correction (standard deviations: 0.03-0.07, 0.07-0.10, 0.08- 0.10 M HCl, respectively).

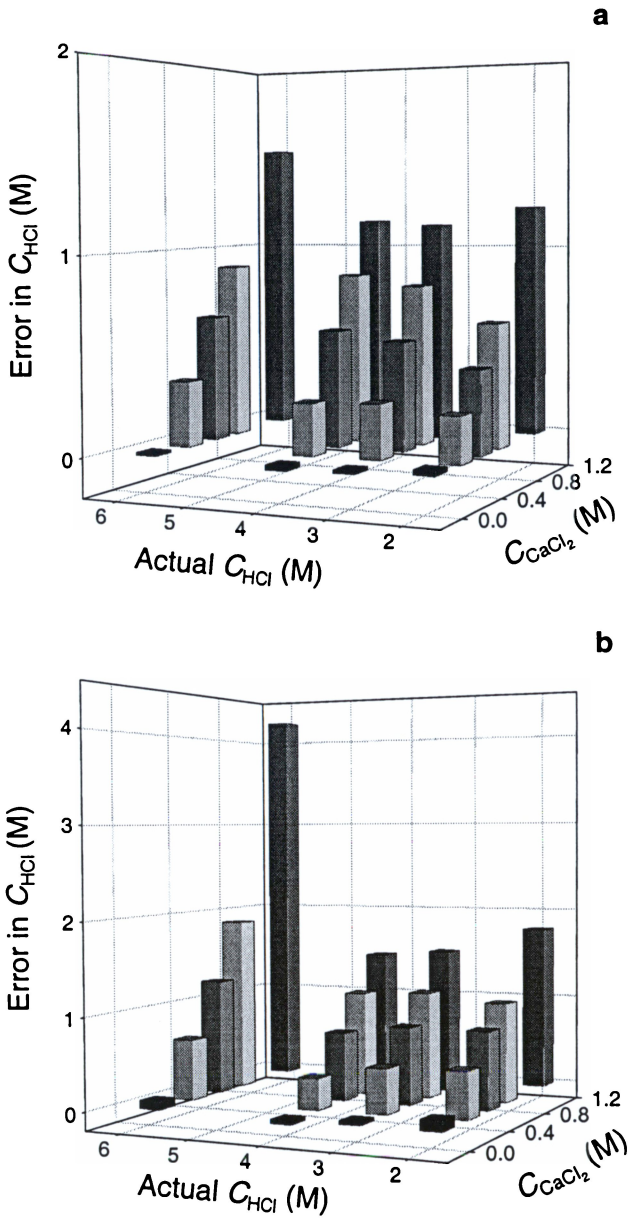

Figure 4.16. Errors in C_{HCl} in HCl-$CaCl_2$-H_2O solutions using Sensors (a) **BCP2** and (b) **NR2** *before* correction (standard deviations = 0.03-0.05 and 0.03-0.05 M HCl, respectively).

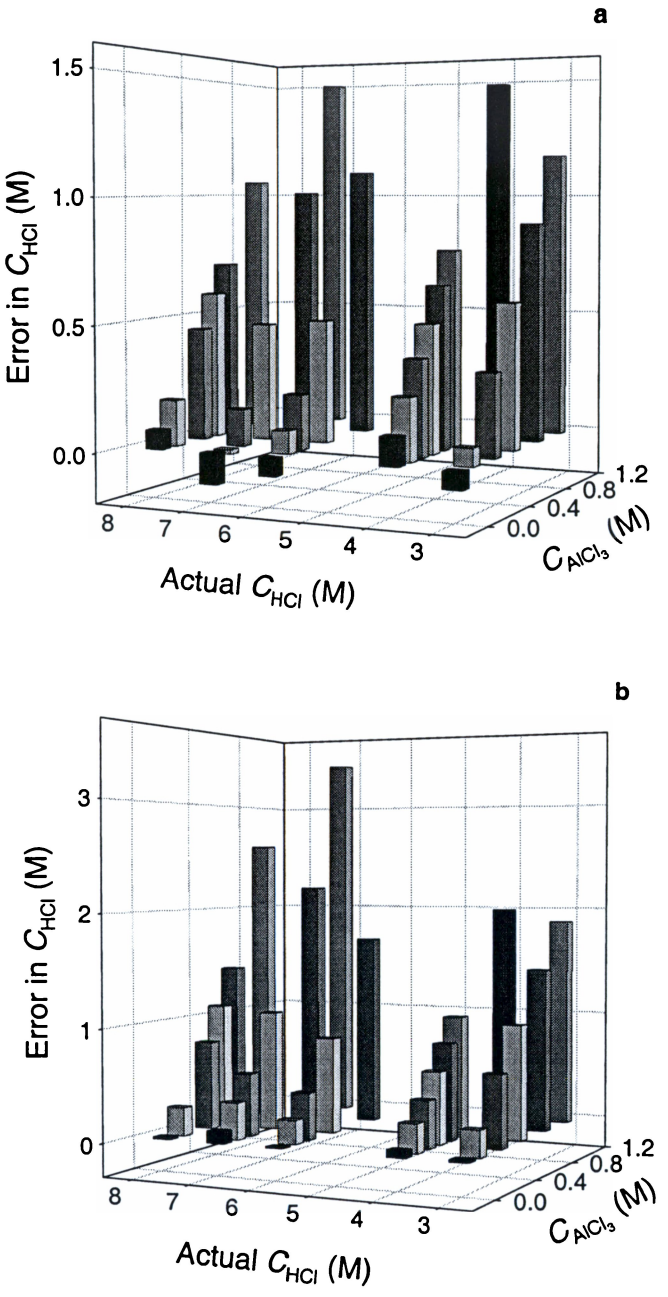

Figure 4.17. Errors in C_{HCl} in HCl-$AlCl_3$-H_2O solutions using Sensors (a) **NR3**; and (b) **BCP3** *before* correction (standard deviations = 0.02-0.05 and 0.03-0.06 M HCl, respectively).

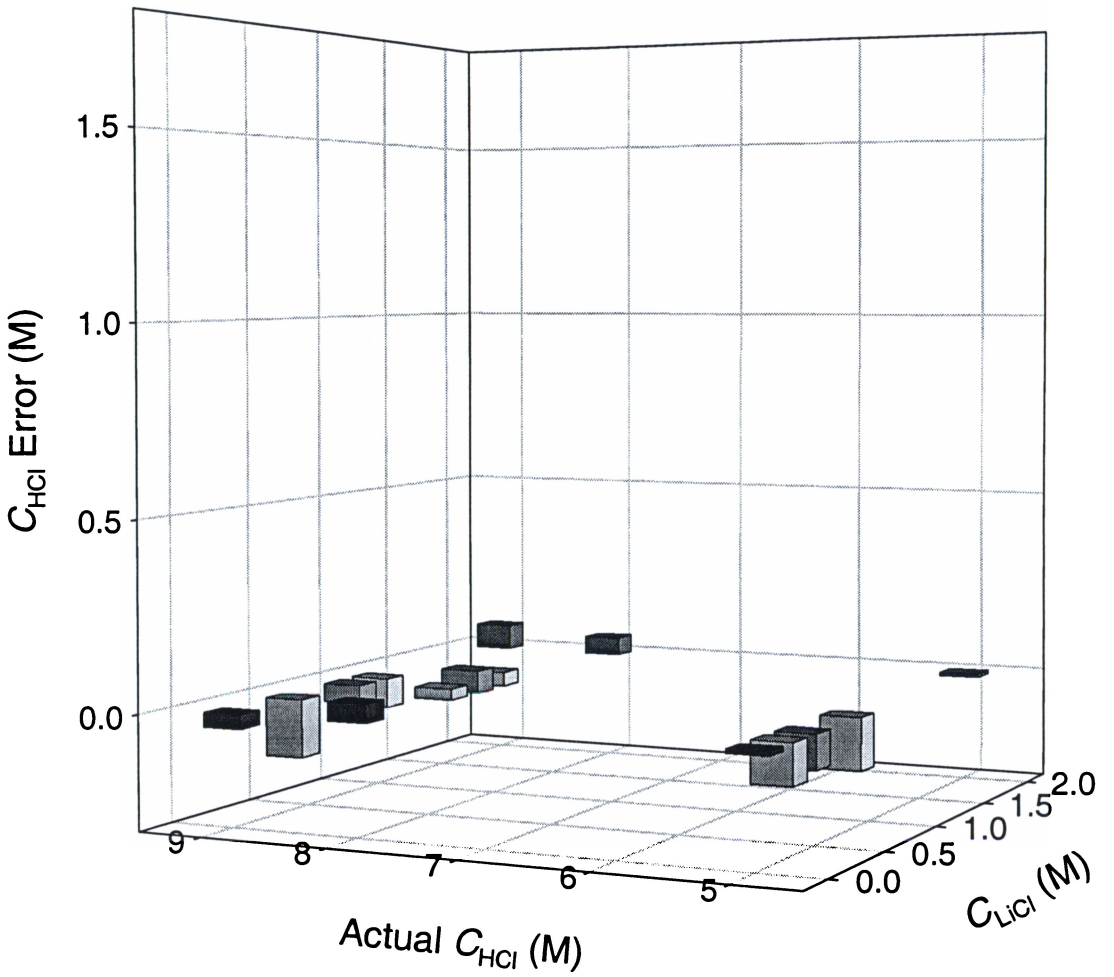

Figure 4.18. Errors in C_{HCl} after corrections were made for the presence of LiCl in HCl-LiCl-H_2O solutions using combinations of Sensors **BCP1**, **BCG1** and **NR1** (standard deviation 2.79-6.70%).

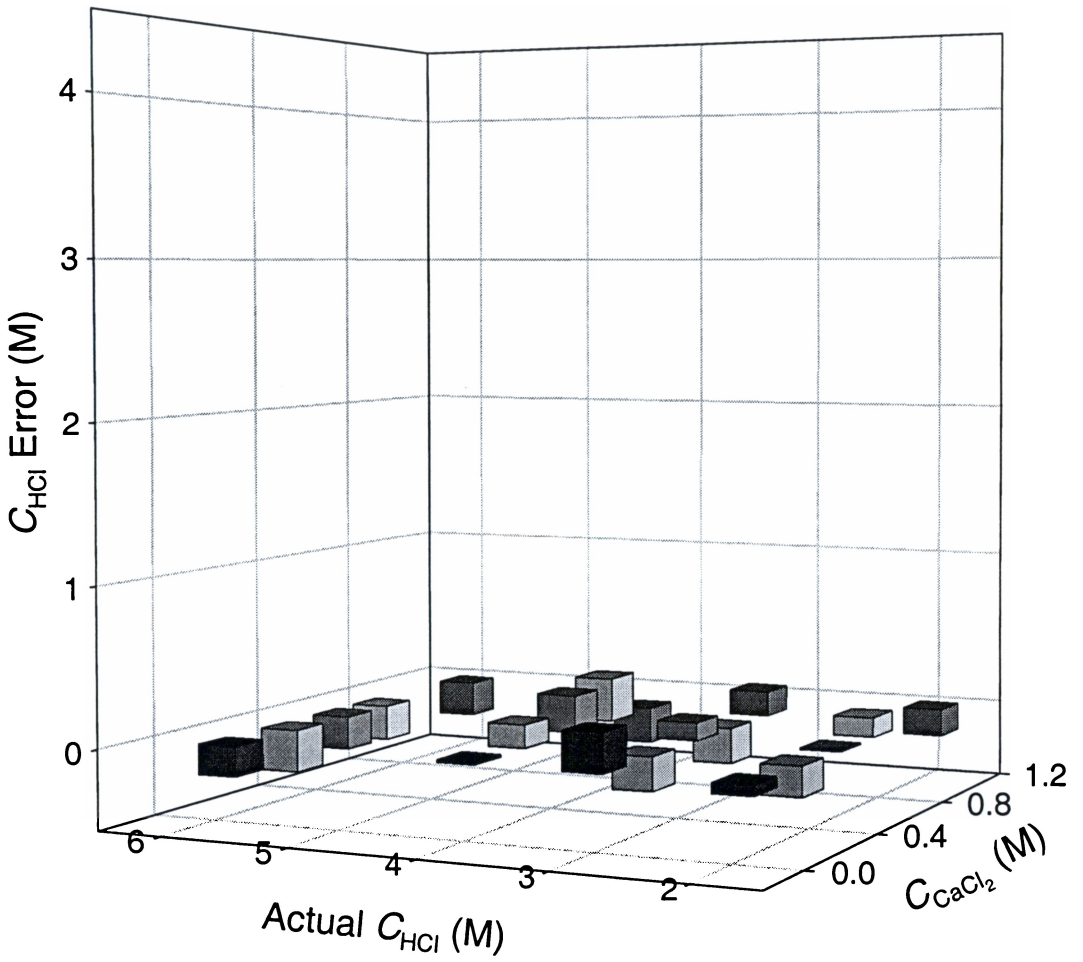

Figure 4.19. Errors in C_{HCl} after corrections were made for the presence of $CaCl_2$ in HCl-$CaCl_2$-H_2O solutions using Sensors **BCP2** and **NR2**. The standard deviation was 0.02-0.19 M HCl.

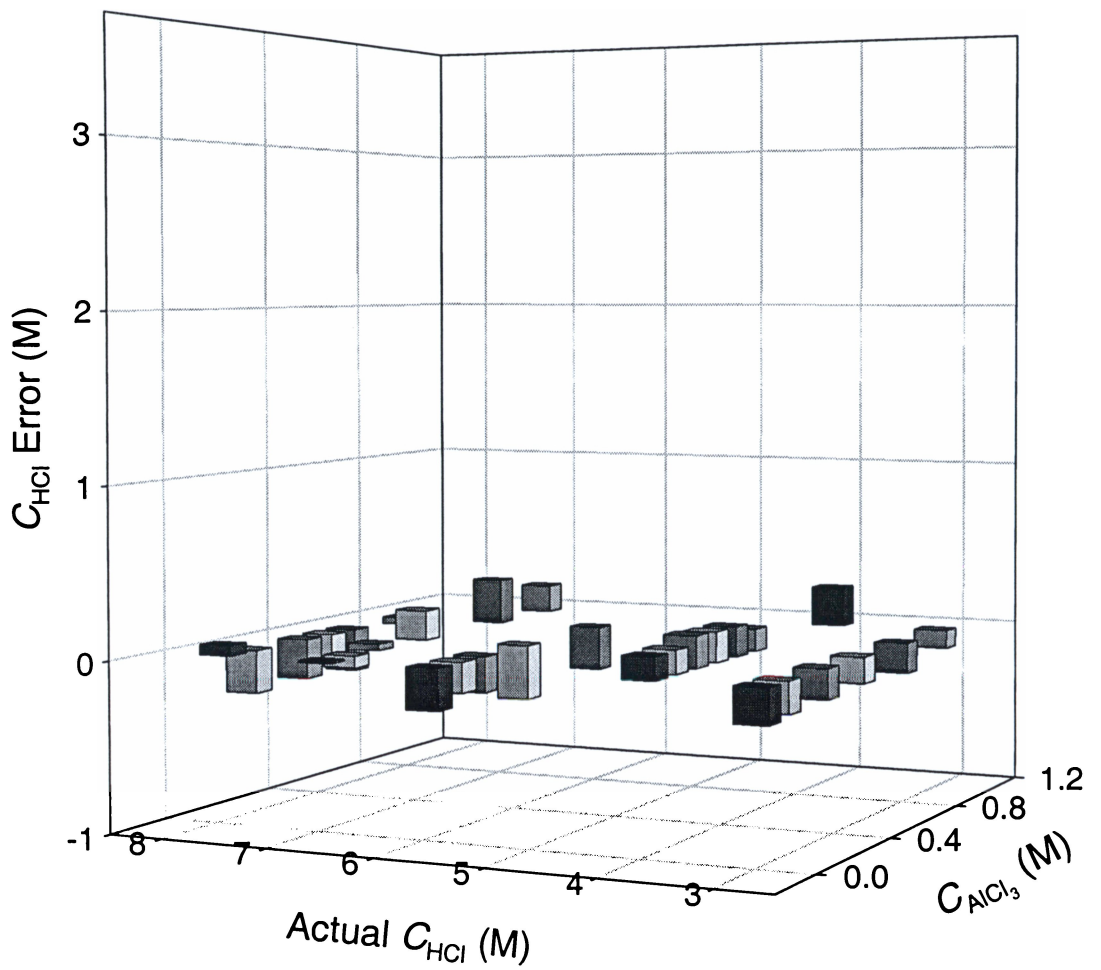

Figure 4.20. Errors in C_{HCl} after corrections were made for the presence of $AlCl_3$ in HCl-$AlCl_3$-H_2O solutions using Sensors **BCP3** and **NR3** (standard deviation 0.05-0.11 M HCl).

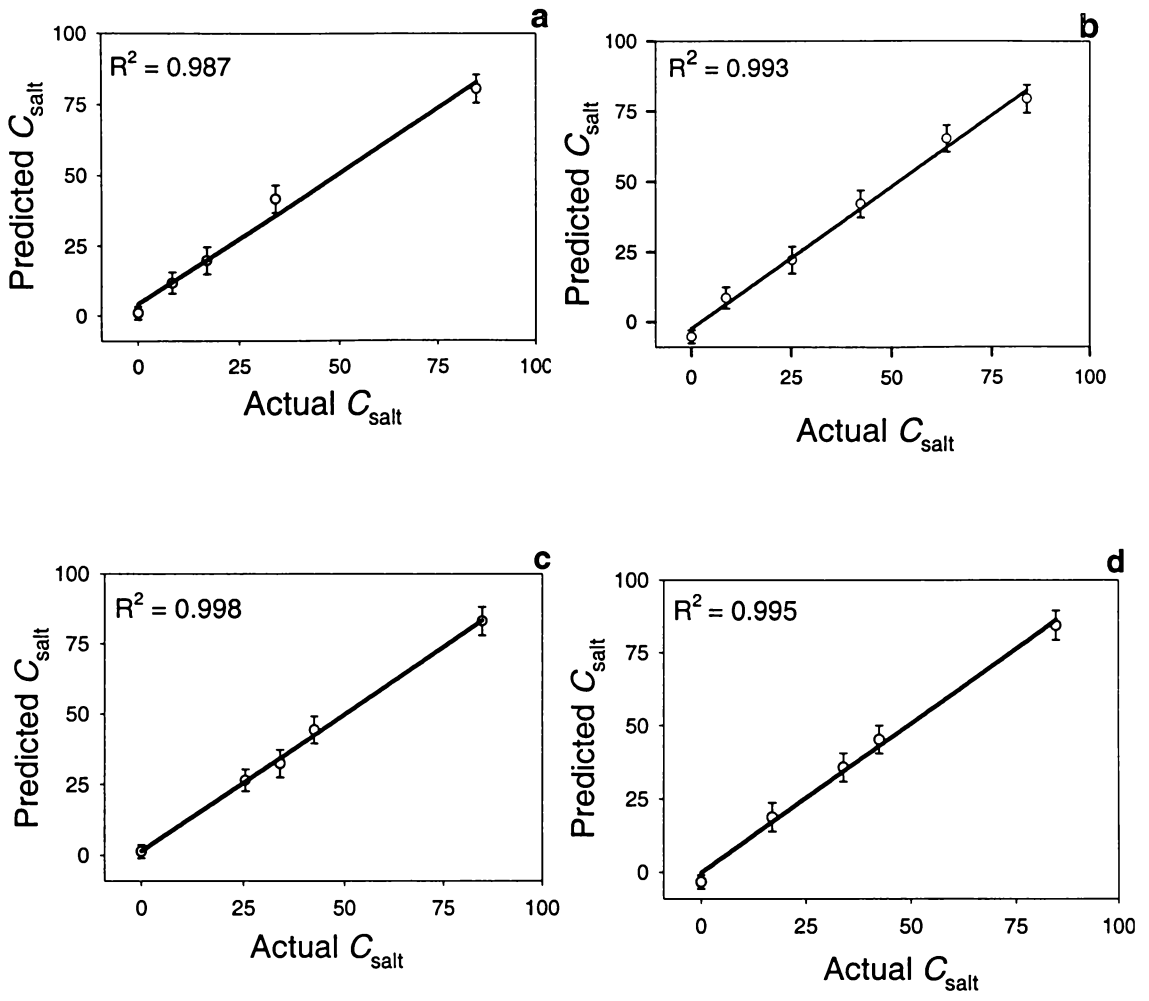

Figure 4.21. Validation plots of predicted vs. actual C_{salt} ($g.L^{-1}$) in HCl-LiCl-H_2O solutions. Predicted values were computed via a signal deconvolution algorithm using the data from Sensors (a) **BCP1** and **NR1**; (b) **BCG1** and **BCP1**; (c) **BCG1** and **NR1**; (d) **BCG1** and **BCP1**. The C_{HCl} was (a) 5.00; (b) 6.00; (c) 8.00; and (d) 9.00 M, respectively.

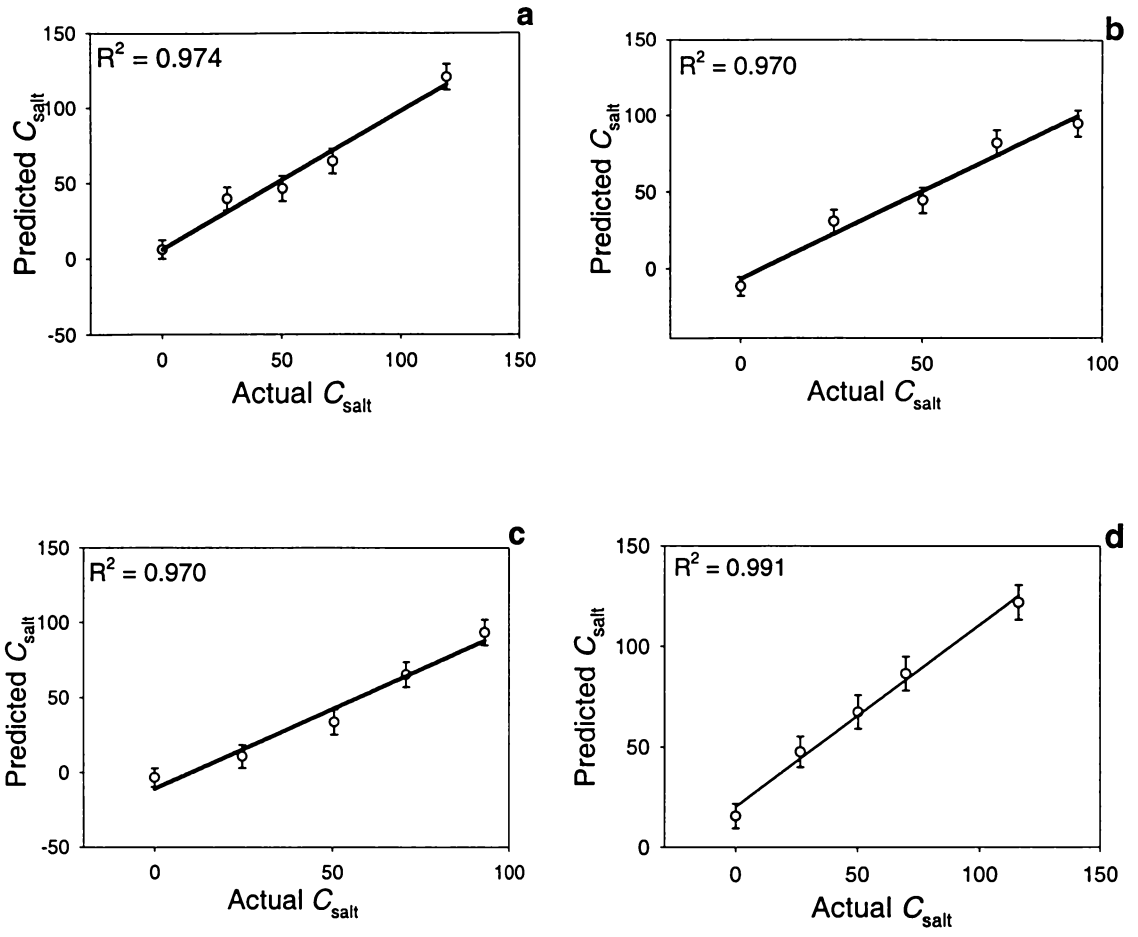

Figure 4.22. Validation plots of predicted vs. actual C_{salt} ($g.L^{-1}$) in HCl-$CaCl_2$-H_2O solutions. Predicted values were computed via a signal deconvolution algorithm using the data from Sensors **NR2** and **BCP2**. The C_{HCl} was (a) 1.916; (b) 2.997; (c) 3.952 M, and (d) 4.997 M, respectively.

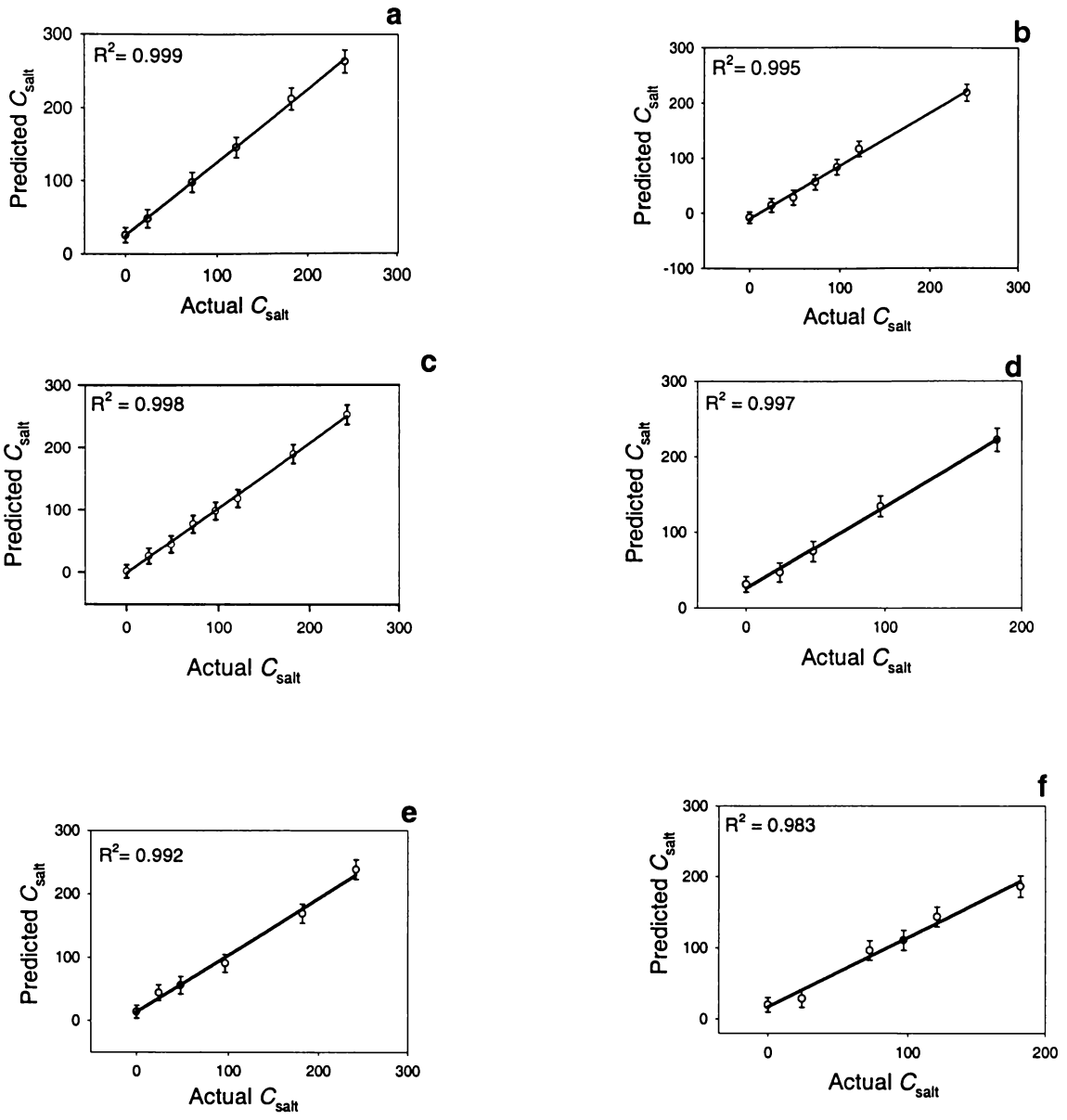

Figure 4.23. Validation plots of predicted vs. actual C_{salt} ($g.L^{-1}$) in HCl-$AlCl_3$-H_2O solutions. Predicted values were computed via a signal deconvolution algorithm using the data from Sensors **NR3** and **BCP3**. The C_{HCl} was (a) 2.99; (b) 3.96 M; (c) 4.95; (d) 5.94; (e) 6.96; and (f) 7.92 M, respectively.

Table 4.2. Comparisons for the HCl-LiCl-H_2O Solutions[a]

C_{HCl} (M)	Error (%) in C_{HCl} *before* Correction (BCP1)	Error (%) in C_{HCl} *before* Correction (BCG1)	Error (%) in C_{HCl} *before* Correction (NR1)	Error (%) in C_{HCl} *after* Correction	Accuracy (%) in C_{LiCl} *after* Correction
5.00	1.5-19.1	12.1-21.6	1.6-23.4	0.2-2.7[b]	61.0-94.9[b]
8.00	4.1-16.8	6.0-14.9	2.8-10.2	0.4-0.7[c]	95.5-98.0[c]
9.00	1.4-12.5	4.7-14.8	1.0-9.2	0.5-1.7[d]	89.3-99.5[d]

[a] Standard deviations in C_{HCl} and C_{LiCl} were 0.05-0.13 M and 1.18-2.84 g/L, respectively.

[b] Combination of Sensors **BCP1** and **NR1**

[c] Combination of Sensors **BCG1** and **NR1**

[d] Combination of Sensors **BCG1** and **BCP1**

Table 4.3. Comparisons for the HCl-$CaCl_2$-H_2O Solutions[a,b]

C_{HCl} (M)	Error (%) in C_{HCl} *before* Correction (BCP2)	Error (%) in C_{HCl} *before* Correction (NR2)	Error (%) in C_{HCl} *after* Correction	Accuracy (%) in C_{CaCl_2} *after* Correction
1.92	10.8-38.9	20.5-48.3	0.5-8.9	55.0-98.9
3.00	8.4-27.4	13.7-34.4	3.6-7.0	80.8-98.4
3.95	6.2-22.5	7.9-27.7	0.4-6.4	53.8-99.5
5.87	5.4-20.8	10.2-41.8	3.1-4.4	66.2-94.9

[a] Sensors **BCP2** and **NR2**.

[b] Standard deviations in C_{HCl} and C_{CaCl_2} were 0.02-0.19 M and 4.48-6.15 g/L, respectively.

Table 4.4. Comparisons for the HCl-$AlCl_3$-H_2O Solutions[a,b]

C_{HCl} (M)	Error (%) in C_{HCl} *before* Correction (BCP3)	Error (%) in C_{HCl} *before* Correction (NR3)	Error (%) In C_{HCl} *after* Correction	Accuracy (%) in C_{AlCl_3} *after* Correction
2.99	7.4-38.7	2.3-28.1	3.5-6.5	65.5-91.0
3.96	6.1-40.0	5.9-26.9	3.1-5.5	60.0-96.2
5.94	3.4-22.3	1.6-20.5	2.9-5.1	61.0-77.7
6.96	4.5-32.7	2.1-17.6	0.2-3.7	83.4-98.4
7.92	3.2-24.5	2.2-11.7	0.5-3.1	67.8-97.5

[a] Sensors **BCP3** and **NR3**.

[b] Standard deviations in C_{HCl}.

at 5.00 M). (b) Upon applying the dual sensor approach, accuracy in C_{HCl} measurement increases as the acidity of the solution increases. This trend is particularly obvious for $AlCl_3$-HCl solutions. For example, from 2.99 to 7.92 M HCl, the error in C_{acid} prediction (0.10 to 1.00 M $AlCl_3$) drops from 3.5-6.5 to 0.5-3.1%. (c) When the dual sensor approach is applied, greater accuracy in the C_{salt} prediction is obtained in more concentrated salt solutions. For example, C_{AlCl_3} of 0.10 and 1.00 M were predicted with an accuracy of 80.8 and 98.4%, respectively, at 3.00 M C_{HCl} (Table 4.4).

4.4 Concluding Remarks

The dual-transducer approach reported here provides easy measurements of acid and salt concentrations in salt-containing concentrated strong acids. The effect of ionic strength on the optical sensor response can be a significant source of error if not corrected in the acidity measurement. The approach developed here is based on a novel linear relationship between $\left(\partial A/\partial C_{salt}\right)_{C_{acid}}$ and $\left(dA^0/dC_{acid}\right)_{C_{salt}=0}$. In essence, the approach reported here converts $\left(\partial A/\partial C_{salt}\right)_{C_{acid}}$, an unknown function of C_{acid}, into $\beta\left(dA^0/dC_{acid}\right)_{C_{salt}=0}$. Both β and $\left(dA^0/dC_{acid}\right)_{C_{salt}=0}$ could be be determined experimentally, and thus lead to the computed solutions for C_{acid} and C_{salt}. If similar relationships exist between other analytes, the approach could be potentially applicable in their analysis. In addition, the approach here can be potentially applied to the

development of sensors coupled to a single multiplex CCD (charge-coupled device) spectrometer to coordinate and analyze multiple measurements automatically.

CHAPTER 5

Single Optical Sensors Containing Dual Transducers – Cocktail Sensors

5.1 Introduction

Ionic strength contributions from salts or organic solvents in ternary acidic or basic systems can lead to significant errors if not taken into account. Novel mathematical models have been developed to address the C_{salt} contributions to C_{acid} predictions and the $C_{alcohol}$ contributions to C_{base} predictions, respectively. As shown in Chapters 2 and 4, if not accounted, large errors can result in the prediction of C_{acid} or C_{base}, respectively. A dual-sensor approach containing *two* independent sensors was developed to gather data to solve the mathematical equations. This Chapter focuses on the use of a single optical sensor containing two transducers for the measurement of more than one analyte instead of using the dual sensor approach.

Two well-known drawbacks of C_{acid} or C_{base} determination by *p*H sensitive dyes are their narrow dynamic ranges and non-linear responses.[1] Non-linear responses can be addressed by the mathematical curve fitting models in Chapters 2 and 4. *p*H indicators generally encompass a sensitivity range of approximately 2 *p*H units. To address this issue, multiple indicators or a single

*p*H indicator that exhibits multiple dissociations can be doped within a single sol-gel matrix.[1]

Gupta and Sharma developed a fiber optic sensor consisting of three immobilized *p*H indicators (Cresol Red, Bromophenol Blue, and Chlorophenol Red).[144] The long-range fiber optic sensor was based on evanescent wave absorption and sol-gel immobilization via dip-coating upon a sanded fiber core.[144] Advantages of such a sensor included: (a) *p*H equilibrium of the test solutions is not affected by the probe itself; (b) the *p*H of the solution is not affected by the small amount of immobilized indicator; and (c) the sensor can be used for multiple analyte sensing.[144] This sensor gave linear and reproducible *p*H responses through a limited, mild *p*H range (4.5 to 13.0).[144]

Lin and Liu developed an optical *p*H sensor consisting of four sol-gel immobilized sulphonephthalein indicators (Bromocresol Purple, Bromocresol Green, Phenol Red, and Thymol Blue).[145] The sensors were made by dip-coating of a sol solution containing the indicators, onto both sides of a glass microscope slide.[145] Data were collected using a specially designed UV-visible spectrometer setup.[145] A linear response over a range of 4.5 *p*H units could be obtained within a mild *p*H range.[145] They found that a linear response could be observed for mixed indicators provided that the indicators had a $\triangle pK_a \leq 1.7$.[145] They noted that indicators were chosen so that the absorbancies of each indicator changed in the same direction as the solution acidity was increased.[145] By this arrangement, a monotonic linear plot could be generated based upon the absorbance and C_{acid}.[145]

Mohr and Wolfbeis developed an optical sensor based upon the covalent attachment of an azo-dye to a transparent film consisting of a thin membrane of cellulose on top of a polymer support.[146] The sensor was sensitive through a *p*H range of 0.5 to 11.28,[146] and it was found to be durable for years with operation lifetime of weeks. The sensor was reproducible, and exhibited 30-60 s response times.[146] Other similar studies involving sol-gel or cellulose supports have been reported.[147-150]

Multiple analyte detection is of intense current interest.[56,151-156] Fiber optic sensors with discrete sensing sites for *p*H, pCO_2, and pO_2 in blood samples have been developed using fluorescing sensing sites coupled to a CCD video camera.[151] The development of a dual-label time-resolved fluorometric immunoassay for the simultaneous detection of two different proteins in samples of potatoes has been achieved.[152] Studies have been performed involving combined imaging and chemical sensing using a single optical imaging fiber in order to analyze multiple components in biological systems.[56,154,155]

We recently developed dual-sensor approaches for simultaneous measurements of C_{acid} and C_{salt} as well as C_{base} and $C_{alcohol}$. In these approaches, two independent optical sensors, each containing one encapsulated indicator, were used to obtain two variables, C_{acid} and C_{salt} or C_{base} and $C_{alcohol}$. We have explored co-encapsulating two independent indicators into one optical sensor. In such an approach, a single optical sensor with two transducers immobilized therein could be used to measure two variables. We report here

such a cocktail approach that can used to determine the contribution of C_{salt} and C_{acid} to the total ionic strength of an acidic saline solution.

Reported studies with cocktail sensors dealt with mixtures of indicators that responded throughout different pK_a ranges.[1,144,146] We have been interested in determinations of C_{salt} and C_{acid} in extremely acidic environments, and in such measurements, indicators need to respond throughout the same pK_a regions. This fundamental difference sets our cocktail sensors apart from other reported cocktail sensors.

A successful peak deconvolution method is established to *deconvolute A* into the individual components, $A_{form\ I,\ Ind\ X} + A_{form\ I,\ Ind\ Y}$. The contribution of C_{HCl} to each component of the cocktail sensor could be evaluated by this deconvolution method. Through the deconvolution the cocktail sensor could be used to determine the C_{salt} and C_{acid} in HCl-$CaCl_2$-H_2O (C_{HCl} = 5 to 9 M, C_{CaCl_2} = 0 to 1 M) solutions. A complete indicator analysis is presented for Bromocresol Purple and Fast Green FCF including K_{a1}, pK_{a1}, and ε determinations in the solution and encapsulated sol-gel matrices.

5.2 Experimental Section

Visible spectra of the indicators in solution were collected using a Hewlett Packard 8452A Diode Array Spectrometer. Visible spectra of the films were recorded using the visible spectrometer described in Section 1.3.1.[12] Repetition scans were recorded and averaged to minimize the drift error in the instrument.

Hydroxide solutions were prepared by gravimetric dilution before each trial to ensure maximum accuracy. Hydroxide solutions were titrated with standard HCl to the phenolphthalein end point to verify their concentrations. HCl solutions were prepared by dilution and titrated with standard NaOH to the phenolphthalein end point.

$Si(OMe)_4$ (99+%, Aldrich), $Zr(O\text{-}n\text{-}Bu)_4$ (80% wt. in 1-n-BuOH, Aldrich), Nafion (5% Nafion in an alcoholic mixture containing 5% w/w water, Aldrich), $HCONMe_2$ (DMF, 99.9+%, Aldrich), MeOH (99.9%, Fisher), EtOH (dry, absolute, AAPER)[78], HCl standard (0.25 N, LabChem. Inc.), NaOH (99.99%, Fisher), Thiazole Yellow GGM (TY, 40% dye content, Eastman), Alizarin Yellow R (AY, 80% dye content, Eastman), Bromocresol Purple (BCP, 90% dye content, Aldrich), Fast Green FCF (FG, 99% dye content, Aldrich), Bromocresol Green (BCG, 95% dye content, Eastman), cetyltrimethylammonium bromide (CTAB, Aldrich), and HCl (37.5%, Certified ACS, Fisher) were used as received. Data analysis was conducted with Sigma Plot (SPSS Inc., 233 S. Wacker Drive, 11th Floor, Chicago, IL 60606-6307; http://www.spss.com), Matlab (The MathWorks, Inc., 3 Apple Hill Drive, Natick, MA 01760-2098; http://www.mathworks.com), and Maple (Waterloo Maple Inc., 57 Erb Street, W. Waterloo, Ontario, Canada N2L 6C2; http://www.maplesoft.com) programs. Preparation of the sanded microscope slide glass substrate is described in Section 1.4.5. A 75 mm x 25 mm glass slide was coated with the sol-gel solution and then cut into approximately five sensors (25 mm x 12 mm). All data in Section 5.3.3 were processed using the Matlab programs that are listed in Appendix C.

5.2.1 Preparation of the Sensors

(a) Sensor TY9. A solution containing H_2O (10 µL), 1.00 M HCl (5 µL), DMF (125 µL), and Thiazole Yellow GGM (29 mg) was stirred at room temperature in a closed vial for 3 to 5 min. Nafion (148 mg) was added by pipet and stirred for ca. 1 min. Dry MeOH (150 µL) and $Si(OMe)_4$ (200 µL) were then added to the stirring solution. The vial was kept closed and stirred for 10 min. While stirring vigorously, $Zr(O\text{-}n\text{-}Bu)_4$ (275 mg) was added, and the vial was immediately resealed. The solution was vigorously stirred at room temperature for 2 min. The solution was then immediately spin-coated (3000 RPM) onto a glass substrate (75 mm x 25 mm) for ca. 1 min. This sensor was used to give the background.

(b) Sensor AY9. A solution containing H_2O (5 µL), 1.00 M HCl (10 µL), DMF (150 µL), and Alizarin Yellow R (18.0 mg) was stirred at room temperature in a closed vial for 3 to 5 min. Nafion (154 mg) was added and the solution stirred for ca. 1 min. Dry EtOH (150 µL) and $Si(OMe)_4$ (200 µL) were then added to the stirring solution. The vial was kept close and stirred for 10 min. While stirring vigorously, $Zr(O\text{-}n\text{-}Bu)_4$ (290 mg) was added, and the vial was immediately resealed. The solution was vigorously stirred at room temperature for 10 min. The solution was then immediately spin-coated (3000 RPM) onto a glass substrate (75 mm x 25 mm) for ca. 1 min. This sensor was used to give the background.

(c) Sensor AYTY1. A solution containing H_2O (5 µL), 1.00 M HCl (10 µL), DMF (150 µL), Thiazole Yellow GGM (23.0 mg), and Alizarin Yellow R (15.0 mg) was stirred at room temperature in a closed vial for 3 to 5 min. Nafion (160 mg) was added to the solution which was stirred for ca. 1 min. Dry EtOH (200 µL) and $Si(OMe)_4$ (200 µL) were then added to the stirring solution. The vial was kept close and stirred for 10 min. While stirring vigorously, $Zr(O\text{-}n\text{-}Bu)_4$ (293 mg) was added, and the vial was immediately resealed. The solution was vigorously stirred at room temperature for 70 min. The solution was then spin-coated (3000 RPM) onto a glass substrate (75 mm x 25 mm) for ca. 1 min.

(d) Sensor BCP4. H_2O (120 µL), HCl solution (0.01 M, 34 µL), methanol (260 µL), and Bromocresol Purple (112 mg) was allowed to stir for 2 min in a glass vial at room temperature to insure complete solubility of all the components. $Si(OMe)_4$ (400 µL) was then added and the solution was stirred for 50 min at room temperature. The solution was then spin-coated (3000 RPM) onto a glass substrate (75 mm x 25 mm) for ca. 1 min. This sensor was used to give the background.

(e) Sensor BCG4. This sensor was prepared by a procedure similar to that used in the preparation of Sensor BCP4 except that 130 mg of Bromocresol Green indicator was used to give Sensor BCG4. This sensor was used to give the background.

(f) Sensor FG1. A solution containing 0.01 M HCl (100 µL), MeOH (40 µL), and Fast Green FCF (6.2 mg) was stirred at room temperature in a vial for 3-5 min. Nafion (160 mg) was added by pipet and stirred for ca. 1 min. $Si(OMe)_4$ (300 µL)

was then added to the stirring solution. The solution was stirred at room temperature for 2 h. The solution was then spin-coated (3000 RPM) onto a glass substrate (75 mm x 25 mm) for ca. 1 min. This sensor was used to give the background.

(g) Sensor NR4. This sensor was prepared by a procedure similar to that used in the preparation of Sensor **FG1** except that 18 mg of Neutral Red indicator was used to give Sensor **NR4**. This sensor was used to give the background.

(h) Sensor BCPBCG1. A solution containing H_2O (120 µL), HCl (0.01 M, 34 µL), Bromocresol Purple (25 mg), and Bromocresol Green (25 mg) was stirred at room temperature for 2 min. MeOH (260 µL) and $Si(OMe)_4$ (400 µL) were then added in that order to the stirring solution. The solution was stirred at room temperature for 50 min. The solution was then spin-coated (3000 RPM) onto a glass substrate (75 mm x 25 mm) for ca. 1 min.

(i) Sensors BCGFG1 and BCPFG1. These sensors were prepared by a procedure similar to that used in the preparation of Sensor **BCPBCG1** except the following blends were used: 60 mg of Bromocresol Green and 7 mg of Fast Green FCF for **BCGFG1**, and 51 mg of Bromocresol Purple indicator and 7 mg of Fast Green FCF indicator for **BCPFG1** were used, respectively, to give these sensors.

(j) Sensor NRBCP1. A solution containing 0.01 M HCl (100 µL), MeOH (40 µL), Neutral Red (16 mg), and Bromocresol Purple (60 mg) was stirred at room temperature in a vial for 3-5 min. Nafion (160 mg) was added by pipet and the solution stirred for ca. 1 min. $Si(OMe)_4$ (400 µL) was then added to the stirring

solution. The solution was stirred at room temperature for 2 h. The solution was then spin-coated (3000 RPM) onto a glass substrate (75 mm x 25 mm) for ca. 1 min.

(k) Sensors NRFG1 and NRBCG1. These sensors were prepared by a procedure similar to that used in the preparation of Sensor NRBCP1 except the following blends were used: 19 mg Neutral Red and 7 mg of Fast Green for NRFG1, and 19 mg of Neutral Red indicator and 49 mg of Bromocresol Green indicator for NRBCG1 were used, respectively, to give these sensors.

5.2.2 Curing of the Sensors. Sensors **TY9**, **AY9**, and **AYTY1** were cured for 5 days in air at room temperature, and then placed in an oven at 45 to 50 ^{o}C for 5 days. Nafion in the sensors was found to degrade if the sensors were left in the oven for over 5 days. Sensors **BCP4**, **BCG4**, **FG1**, **NR4**, **BCPFG1**, **BCPBCG1**, **NRBCP1**, **NRFG1**, **NRBCG1**, and **BCGFG1** were cured for 3 days in air at room temperature, and then placed in an oven at 45 to 50 ^{o}C for 8 days.

5.2.3 Conditioning of the Sensors. Sensors **TY9**, **AY9**, and **AYTY1** were placed in H_2O for 1 day followed by 3 M NaOH for 1 day and finally placed in H_2O for 1 day. Sensors **BCP4**, **BCG4**, **FG1**, **NR4**, **BCPFG1**, **BCPBCG1**, **NRBCP1**, **NRFG1**, **NRBCG1**, and **BCGFG1** were placed in H_2O for 1 day, followed by 3 M HCl for 1 day, and finally placed in H_2O for 1 day till no appreciable leaching of dye was observed spectrometrically before they were used for testing.

5.3 Results and Discussion

5.3.1 Studies of Dissolved and Encapsulated Acid Indicators in Highly Acidic Solutions.

We used two criteria in our selection of indicators for sensors in concentrated strong acids: (1) They are stable in solutions such as 1 to 11 M HCl; (2) There is at least one equilibrium between different forms of the indicator in these highly acidic solutions, and these forms of indicators can be observed by visible spectroscopy. Several indicators were tested in the range of 1 to 11 M HCl. Bromocresol Purple (BCP), Bromocresol Green (BCG), Neutral Red (NR), and Fast Green FCF (FG) were found to be stable while having a high sensitivity.

(a) Bromocresol Purple Dissolved in Highly Acidic Solutions. Bromocresol Purple is a member of the sulfonephthalein dyes. Sulfonephthalein indicators contain the sulfonic group and are very soluble in aqueous solutions.[157] Three forms of this indicator exist depending upon the *p*H of the environment (Figures 5.1a and 5.2). The phenolic form **III** (λ_{max} = 591 nm) predominates in basic solutions (*p*H > 6.8).[6,158] **III** is converted to the hydroquinonic form **II** (λ_{max} = 433 nm) throughout a moderate *p*H range (6.8 to 5.2).[6,158] A range of pK_{a_2} (6.05 to 6.3) determinations have been reported.[6,158-160] The color change is purple to yellow upon converting form **III** to **II**.[6,158]

The hydroquinonic form **II** converts to sulfonic form **I** (λ_{max} = 534 nm) in extreme acidity.[157,161,162] The color change is yellow to violet. Gupta and Reed reported a pK_{a_1} of -2.13 (*p*H = -0.75 ± 0.02) on the Hammett acidity scale.[162] Aragoni and coworkers reported pK_{a_1} to be -2.00 ± 0.01(*p*H = -0.75) on the

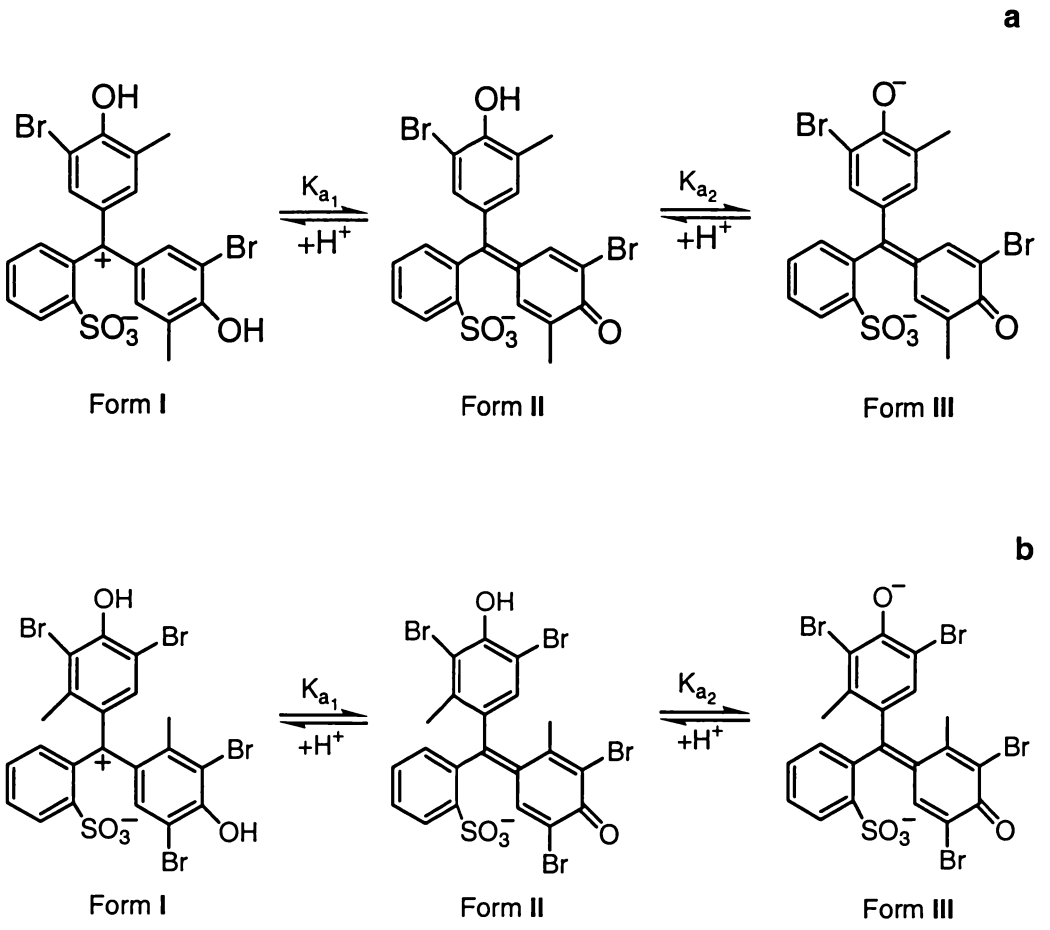

Figure 5.1. The acid-base equilibrium of (a) Bromocresol Purple and (b) Bromocresol Green.

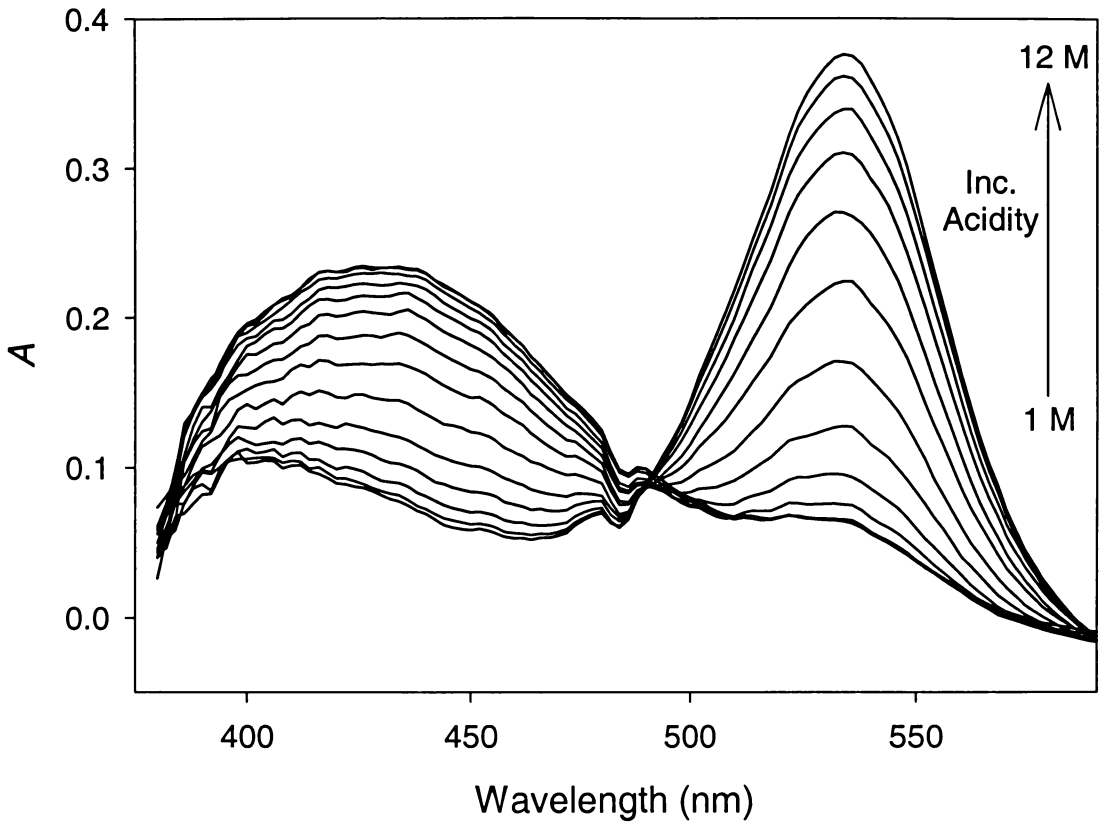

Figure 5.2. The optical spectrum of Sensor **BCP4** in aqueous HCl solutions.

Hammett acidity scale.[161]

We were able to spectrometrically monitor the change of form **II** to **I**, and measured the pK_{a_1} of the indicator dissolved in solution. The K_{a_1} value for the indicator was calculated from two different methods and compared. Method 1 (depicted in Figure 5.3a) involved using optical spectral measurements to construct a scaled absorbance vs C_{HCl} plot for two distribution curves for the first ionization of the indicator. The absorbances at 432 nm (**II**) were scaled to those at 534 nm (**I**) in order to compensate for the difference in the extinction coefficients. The point of intersection corresponded to the K_{a_1} value. Method 2 (depicted in Figure 5.3b) involved determining $A_{1/2\ ionization}$ on the A vs C_{HCl} curve that sufficed $[H_2Ind] = [Hind^-]$, $[(A_{max}-A_{min}/2) + A_{min})]$. $A_{1/2\ ionization}$ could then be entered into the mathematical curve fitting equation to give the C_{HCl} at the half ionization. Extrapolation of the curve-fitting equation to infinite acid dilution and infinite acidity could be used to determine A_{max} and A_{min} at the analytical wavelength.

Upon analysis via both methods the point of half ionization in solution, was determined to be 6.14 ± 0.16 M HCl (pK_{a_1} = -0.79 ± 0.01, H_o = -2.18 ± 0.07).

Molar extinction coefficients (ε) in the indicator-acid solutions for the H_2Ind form of Bromocresol Purple could be calculated by optical measurements and Beer's Law. A_{max} at 534 nm could be extrapolated from the experimental points using the curve-fitting equation in Eq 4.2 . At A_{max} the indicator should exist solely in the H_2Ind form. The total concentration of indicator (Ind_T) in the solution

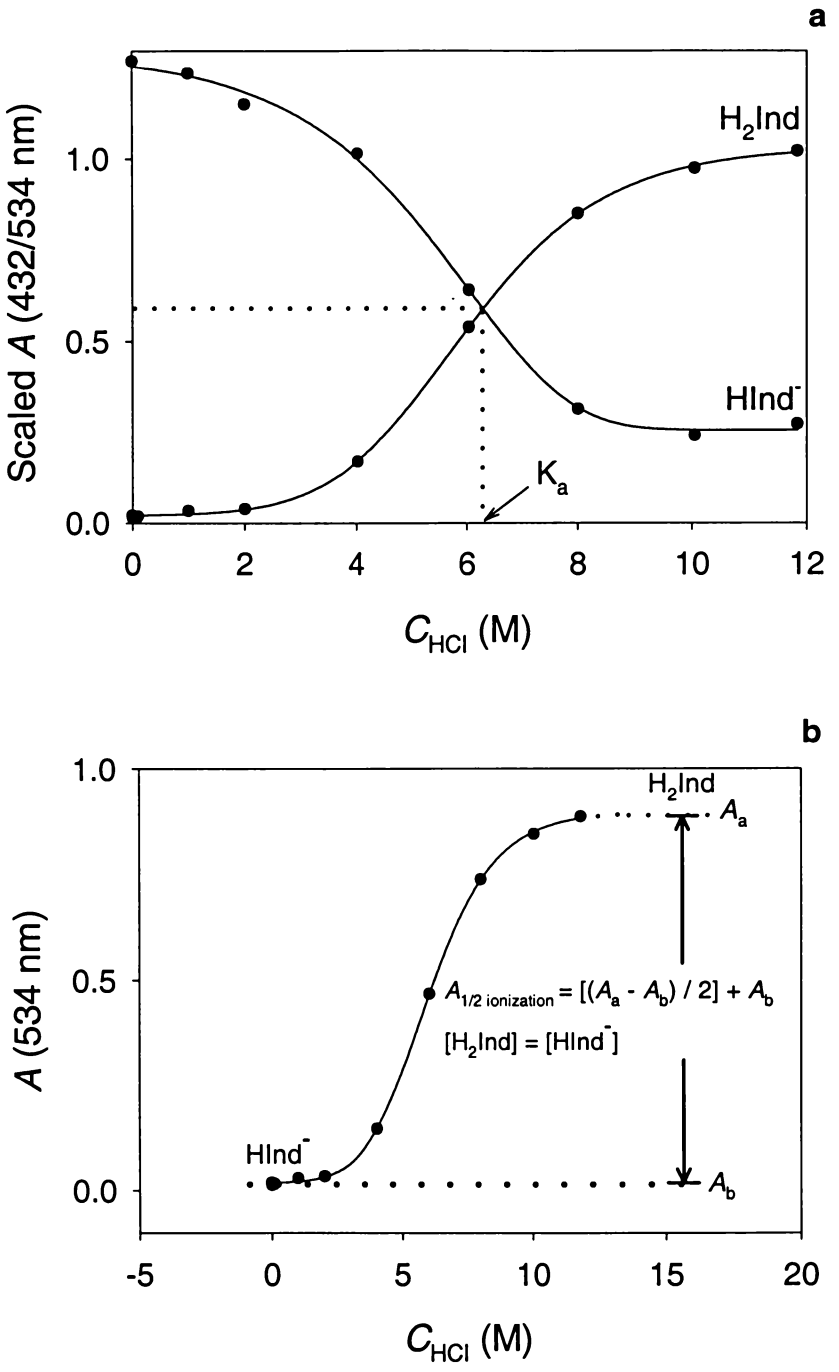

Figure 5.3. Determination of K_{a_1} for Bromocresol Purple in solution by (a) Method 1 and (b) Method 2.

was known, since the indicator was weighed before dissolving into solution. Thus, [Ind_T] equals to [H_2Ind] at A_{max}. The ε value at the selected wavelength is determined by graphical estimation for the indicator dissolved in solution. A list of selected ε values of the H_2Ind form of Bromocresol Purple is given in Table 5.1. The pK_{a_1}'s, analytical wavelength (534 nm), and isosbestic point (484 nm) were approximately the same in solution and in the encapsulated sol-gel solid, which is discussed below. The ε values, for the indicator dissolved in solution could be used for the indicator encapsulated in the sol-gel. Gravimetric determination of the [Ind_T] in a sol-gel film was found to be difficult.

(b) Bromocresol Purple Encapsulated in a Sol-Gel Solid and Tested in Highly Acidic Solutions. For Bromocresol Purple, the wavelength of maximum sensitivity, i.e., analytical wavelength, was found to be 534 nm in both solution and encapsulated sol-gel solid. The K_{a1} value of Bromocresol Purple in the encapsulated sol-gel matrix was calculated via method 1 (Figure 5.4). The point of intersection was at 6.10 M HCl, corresponding to a pK_{a_1} = -0.79 (H_o = -2.18).

(c) Bromocresol Green Dissolved in Highly Acidic Solutions. Bromocresol Green has a similar structure to Bromocresol Purple.[157] Bromocresol Green (BCG) is also a member of the sulfonephthalein dyes. This indicator exists in three different protonated forms and experiences two color change sequences (Figure 5.1b).[6] The phenolic form **III** predominates in slightly acidic to basic solutions (pH > 5.4). **III** is converted to the hydroquinonic form **II** in the acidic pH range. Several pK_{a_2} (4.68 to 4.90) determinations have been reported.[157-160]

Table 5.1. Molar Extinction Coefficients (ε) of Fast Green FCF, Bromocresol Purple, and Bromocresol Green as Determined Optically in Solution (x 10^4 L mol^{-1} cm^{-1})

Indicator Form	534 nm	564 nm	628 nm
FG, $HInd^-$	1.43	3.69	16.4
BCP, H_2Ind	7.45	0.813	0
BCG, H_2Ind	2.17	3.53	0.214

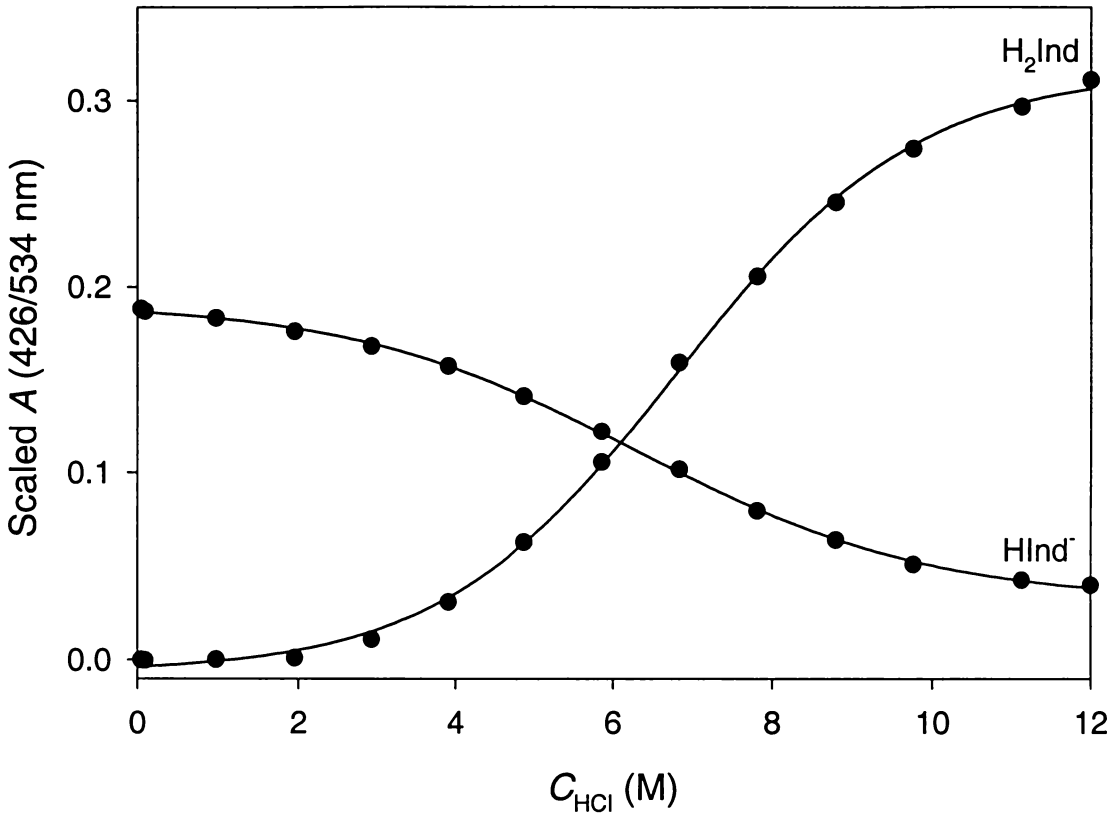

Figure 5.4. Distribution curves for the first ionization of Sensor **BCP4**.

Form **II** is converted to the sulfonic form **I** in extremely acidic conditions. A pK_{a_1} of -4.4 ± 0.1 on the Hammett acidity scale has been reported recently by Aragoni and coworkers.[161] They chose HCl to study the pK_{a_1} of BCG for the non-oxidizing nature of HCl, even though HCl does not completely produce the diprotonated form of the dye.[161] Determination of the pK_{a_1} of BCG was found to be difficult because of the upper limits of acidity of HCl.[162] In addition, it was not clear whether the dye exists in the fully protonated form in highly concentrated HCl. Therefore, H_0 was extrapolated using the scale reported by Paul and Long.[163] Another study did not give the pK_{a_1} of BCG but the value was predicted to be approximately -2.7 on the Hammett acidity scale.[162] **III** → **II** → **I** chemical changes results in a color sequence of blue → yellow → violet.[6,158]

(d) Bromocresol Green Encapsulated in a Sol-Gel Solid and Tested in Highly Acidic Solutions. We were able to spectrometrically monitor (Figure 5.5) the change from **II** to **I** in Bromocresol Green (BCG) encapsulated in sol-gel matrix in concentrated HCl solutions. This measurement gave a plot (Figure 5.6) of scaled absorbance vs C_{HCl} for two distribution curves for the first ionization of sol-gel encapsulated BCG. The absorbances at 450 nm (**II**) were scaled with those at 560 nm (**I**) in order to eliminate extinction coefficient differences between the two forms of BCG. The two curves intersected at 9.81 ± 0.48 M HCl, and this corresponded to a pK_{a_1} of –3.60 ± 0.10 on the Hammett acidity scale (-0.99 ± 0.02 using theoretical *p*H).[163,164] The point of half ionization of BCG in solution was determined to be 10.05 ± 0.06 (pK_{a_1} = -1.00 ± 0.01, H_o = -3.68 ± 0.10).

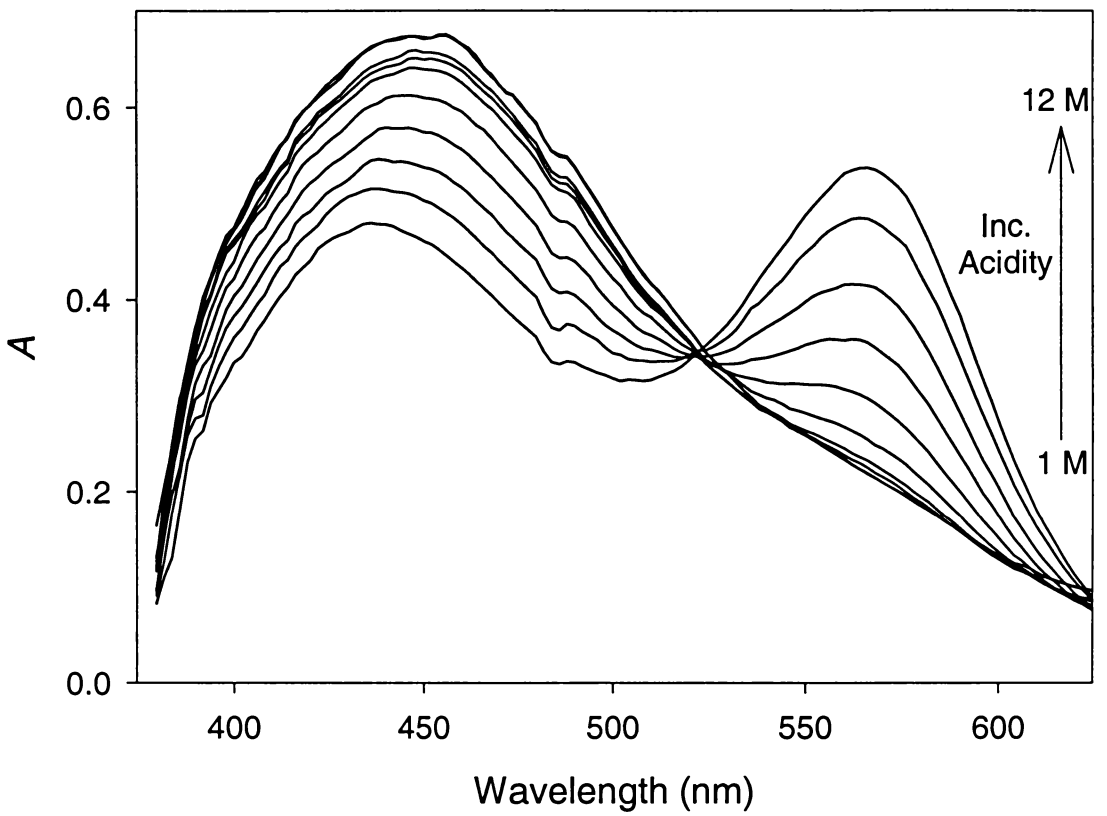

Figure 5.5. The optical spectrum of Sensor **BCG4** in aqueous HCl solutions.

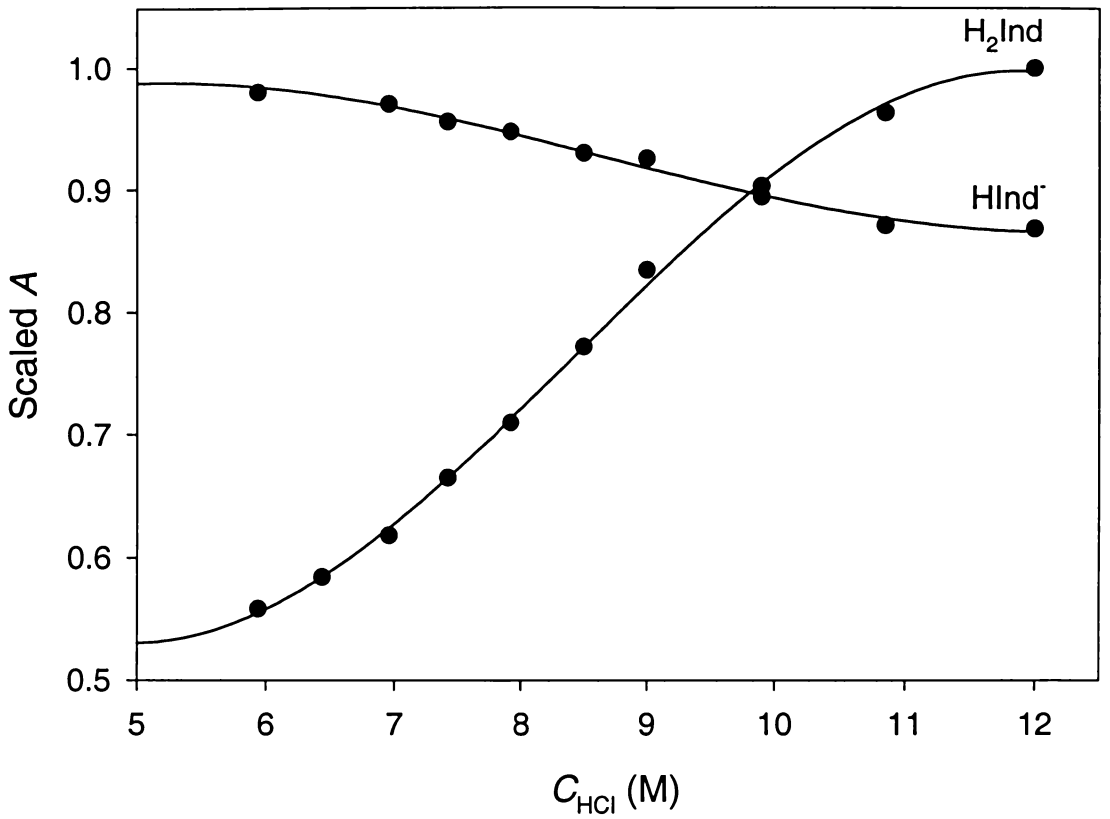

Figure 5.6. Distribution curves for the first ionization of Sensor **BCG4**. The curves were fitted by a 3rd degree polynomial.

The pK_{a_1} of –3.6 ± 0.1, on the Hammett acidity scale, for Bromocresol Green (BCG) encapsulated in sol-gel matrix in the current study falls between -4.4 ± 0.1[161] and -2.7,[162] two values reported earlier for the indicator dissolved in solution. The sol-gel films of the BCG sensors were prepared with *a small amount* of the surfactant cetyltrimethylammonium bromide [$Me(CH_2)_{15}NMe_3^+Br^-$, CTAB; CTAB/Si molar ratio = 8.1×10^{-3} : 1; CTAB/BCG ratio = 1 : 7],[1] which was found to enhance the film strength and thus BCG sensor durability.[30] Recently Avnir and coworkers studied in detail the effect of doped surfactants on properties of *p*H indicators.[94,165] CTAB was found to form micellar aggregates (at CTAB/Si molar ratio = 4.8×10^{-3} : 1) within the SiO_2 sol-gel glass. At CTAB/BCG = 2950-590 : 1 ratios[165], the *p*H indicating range of BCG was found to shift from 3.8 to 5.4 in CTAB-free solution[157,159] to 1.5 to 3.8 in the CTAB micellar aggregates-SiO_2. In the current studies, the effect of encapsulated CTAB on pK_{a_1} of BCG was investigated. A CTAB-free BCG sensor (Sensor **BCG5**) was prepared in a procedure similar to the procedure to give Sensors **BCG1-3** except that CTAB was not used. The intersection for the scaled absorbance vs C_{HCl} for two distribution curves for the first ionization of CTAB-free Sensor **BCG5** was 9.64 M HCl (Figure 5.7). The difference between two intersection values of the *CTAB-containing* BCG sensor and *CTAB-free* BCG is ~0.17 M, which is within the standard deviation (±0.48 M HCl) of the trials. We were thus not able to determine whether CTAB in our Sensors **BCG1-3** has a noticeable effect upon pK_{a_1} value of encapsulated BCG in highly acidic media, perhaps because of a

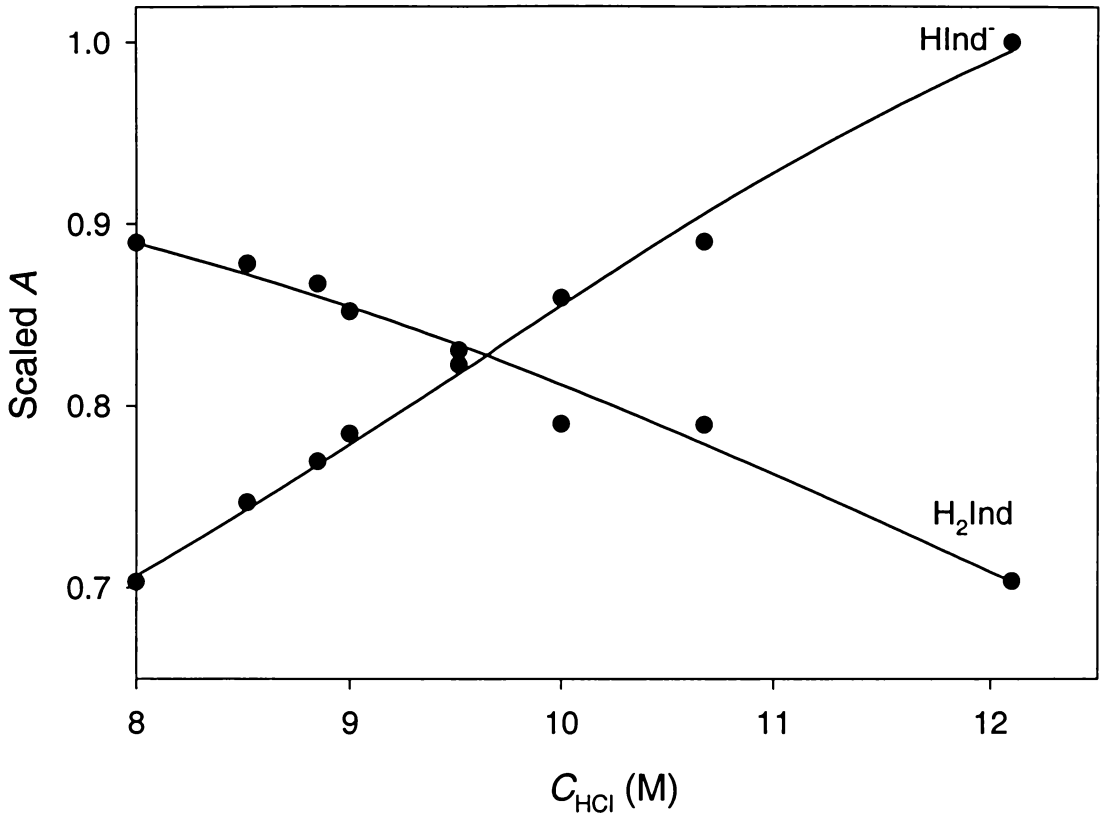

Figure 5.7. Distribution curves for the first ionization of a *CTAB free*-BCG Sensor **BCG5**. The curves were fitted by a 3rd degree polynomial.

small CTAB/BCG ratio in the Sensors **BCG1-3**. There is on average one CTAB molecule per 7 molecules of BCG indicator in our Sensors **BCG1-3**.

(e) Neutral Red. Neutral Red (NR) was found not to be a good candidate for a cocktail sensor study, which is discussed in Section 5.3.2. However, NR was found to be an attractive indicator for single-indicator systems as discussed in Chapter 4.

NR is a readily water-soluble aminophenazine derivative. As many as five forms of NR can exist from *p*H 13 to -8.4 on the H_0 acidity scale (Figure 5.8).[166] From *p*H 7.4 to 13, the yellow uncharged NR V exists.[6,166-169] Around pH 7.5 to 0 the red NR^+ **IV** predominates.[166-169] The pK_{a_4} of **IV** to **V** conversion has been determined from a range of 6.75 to 7.40.[160,166-168,170] The conversion of **IV** to the blue NR^{++} **III** has been reported at a range of pK_{a_3} values (0.20 to -0.7 or 0.63 to 5 M $[H^+]$).[163,164,166,171] Upon conversion to the Hammett acidity scale, *p*H 0.20 and –0.7 are approximate to 0.08 and -1.75.[163,164] Bisset and Dines were able to provide supporting Raman and NMR data in order to confirm the structure of **III**.[170]

NR^{++} can be converted to NR^{+++} **II** (green) and then to NR^{++++} **I**.[166] **I** is reportedly difficult to be observed.[166] The corresponding pK_{a_2} and pK_{a_1} values, as determined in concentrated H_2SO_4 solutions, are -3.38 ± 0.04 (7.10 M H_2SO_4) and -9.5, respectively.[163,166] The determination of pK_{a_1} involved a theoretical approximation.[166]

The change from **IV** to **III** for a NR sensor in concentrated HCl (Figure 5.9)

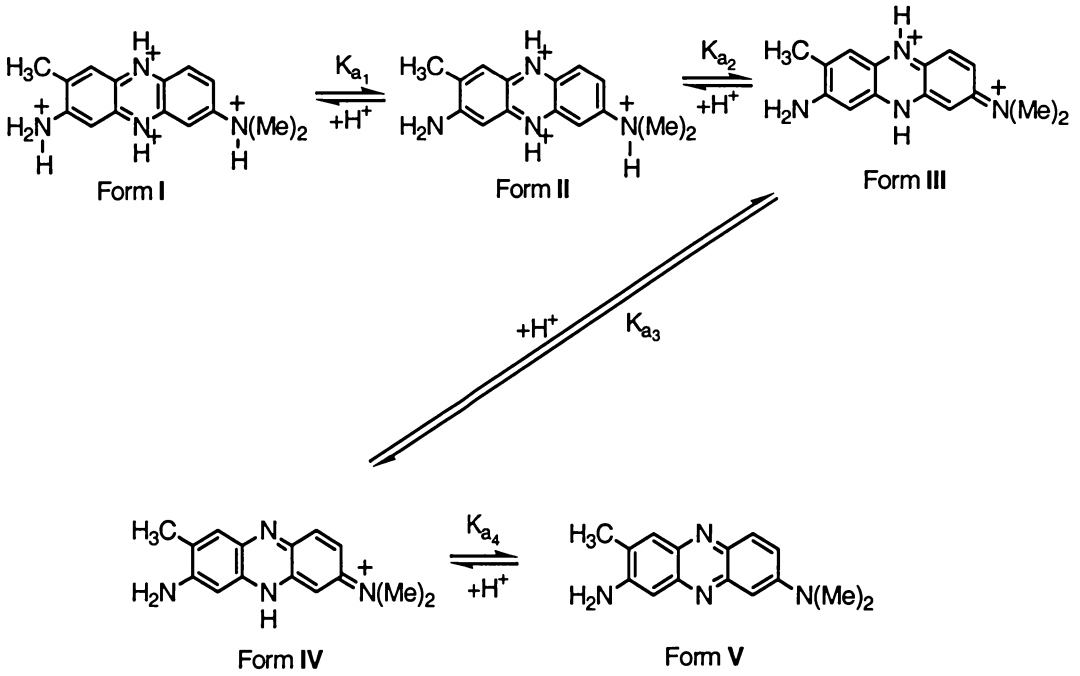

Figure 5.8. The acid-base equilibrium of NR.

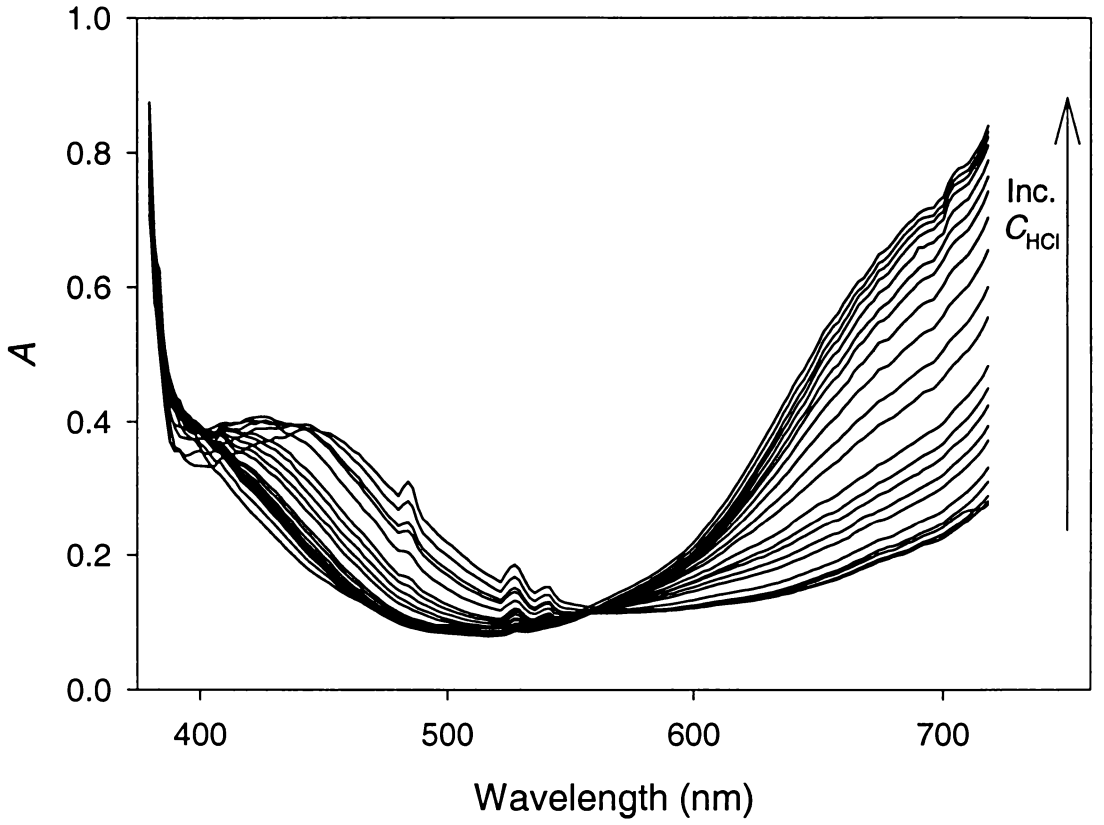

Figure 5.9. Typical spectra of Sensor **NR4** in HCl solutions.

was evaluated in a procedure similar to that for the BCG sensors. The two maxima, 450 nm (**IV**) and 680 nm (**III**) were used to give an intersection at C_{HCl} = 5.88 ± 0.29 M (Figure 5.10), therefore giving a pK_{a_3} of –2.07 ± 0.1 on the H_0 acidity scale (-0.77 ± 0.02 using theoretical pH).[163,164] A noticeable transition occurred from red to blue, both in soluble NR and the NR-composite using HCl solutions ranging from 0 to 10 M.

Our NR sensors were prepared with Nafion, a hydrophilic poly(tetrafluoroethylene) polyphenylene ether sulfonate resin which was found to shorten the NR sensor response time and enhance the sensor durability. No CTAB or other surfactant was used in the preparation of the NR sensors. Comparing to NR dissolved in solution, a shift to higher acidity (lower pK_a) was observed for the indicator encapsulated with Nafion in our sensor sol-gel matrix. The presence of the organic polymer phase has been known to significantly lower an indicator pK_a value, much more so than the oxide phase.[19] It is plausible that the shift to higher acidity for NR infers that Nafion polymer acts as a proton sponge.[94,165] In other words, protons are being adsorbed by the sulfonate groups of the Nafion molecules.

In our current studies, an error analysis revealed that the standard deviations (random errors of trials of each sensor) for NR, BCP, and BCG sensors were 0.02 to 0.05, 0.03 to 0.07, and 0.07 to 0.10 M HCl, respectively. The standard deviations of the Nafion-containing NR sensors are within the same proximity as the Nafion-free BCG and BCP sensors. It is thus not clear if the

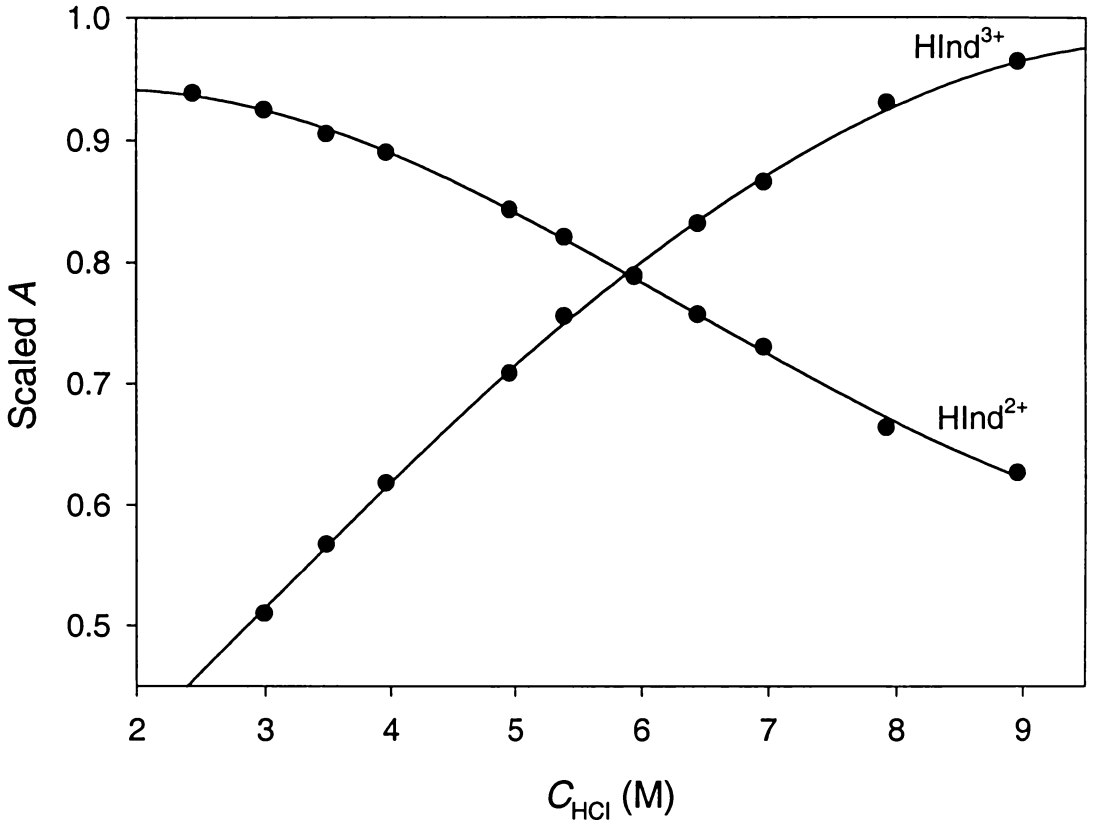

Figure 5.10. Distribution curves for the first ionization of Sensor **NR4**. The curves were fitted by 3rd degree polynomial.

presence of Nafion in the NR sensors noticeably contributes to the standard deviation under highly acidic conditions.

(f) Fast Green FCF. Fast Green (FG) was found not to be a good candidate for a cocktail sensor study and is further reasoned in Section 5.3.2. Fast Green FCF is more commonly referred to as Food Green 3. Optical studies relating to Fast Green FCF is limited in the literature. Fast Green FCF is commonly used as a food-coloring agent due to its high solubility in water and alcohol.[98] In concentrated alkaline solutions the dye exists in the bright blue, basic form **III** (Ind^{2-}).[98] Upon increasing acidity (*p*H 10 to 6), the $Hind^{-}$ form **II** appears due to the protonation of the phenolic-O.[172] The pK_{a_2} of Fast Green FCF has been reported at 8.1 ± 0.5.[172] The green form **II** has a reported λ_{max} at 624 to 628 nm.[98,172] Upon increasing acidity, **II** gains a proton through the unsaturated amine group to form the dull orangish-yellow, H_2Ind form **I**.[98,172] To our knowledge no pK_{a_1} values have been reported in the literature. A representation of the equilibrium of Fast Green FCF is given in Figure 5.11. A plot of *A* vs wavelength is given in Figure 5.12.

We were able to spectrometrically monitor the conversion of **II** to **I** and determine pK_{a1}, K_{a1}, and the wavelength dependent ε-values (reported in Table 5.1) by using the techniques described for Bromocresol Purple. The analytical wavelength of **II** and **I** were found to be 624 and 458 nm, respectively, in solution, as well as 628 and 454 nm, respectively, in the sol-gel solid. The point of intersection in solution was determined to be 0.25 ± 0.06 M HCl ($pK_{a_1} = 0.60 \pm$

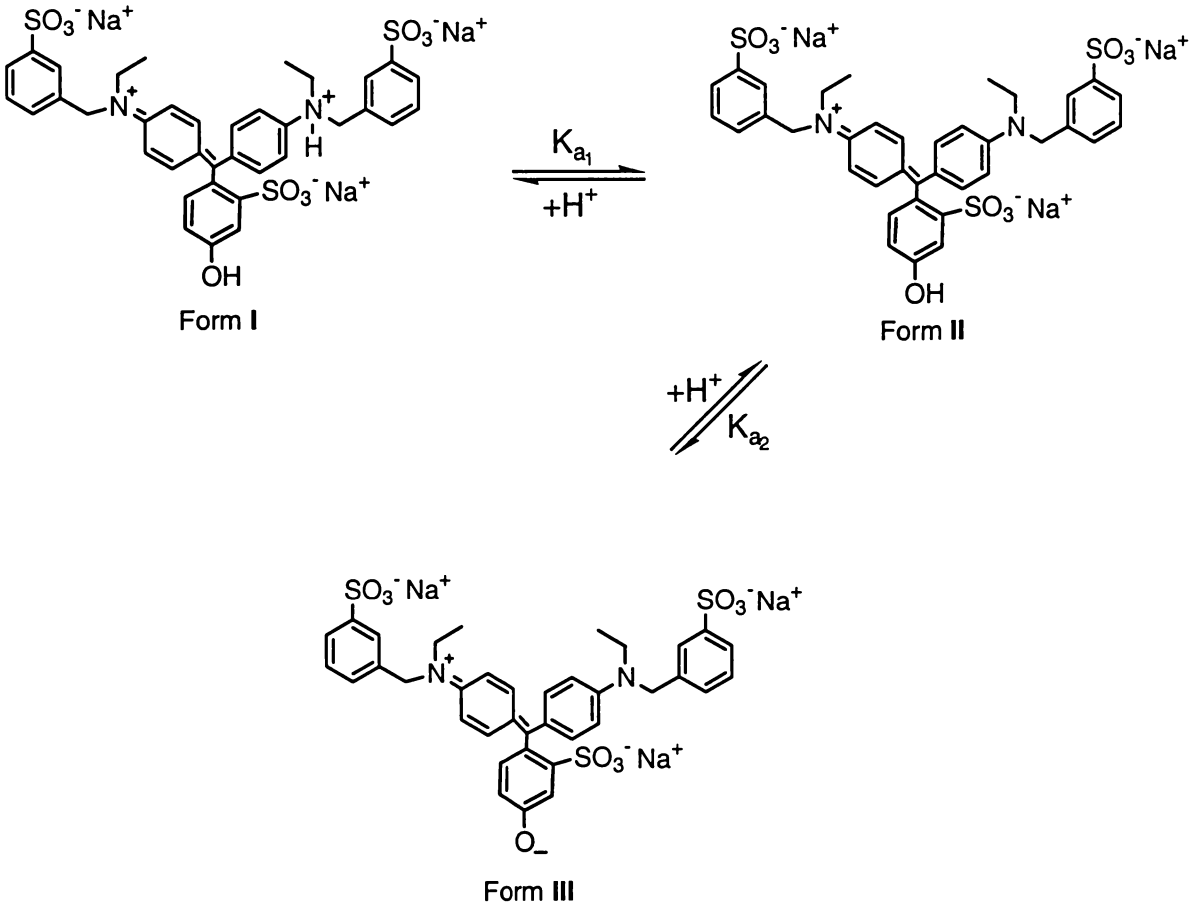

Figure 5.11. The acid-base equilibrium of FG.

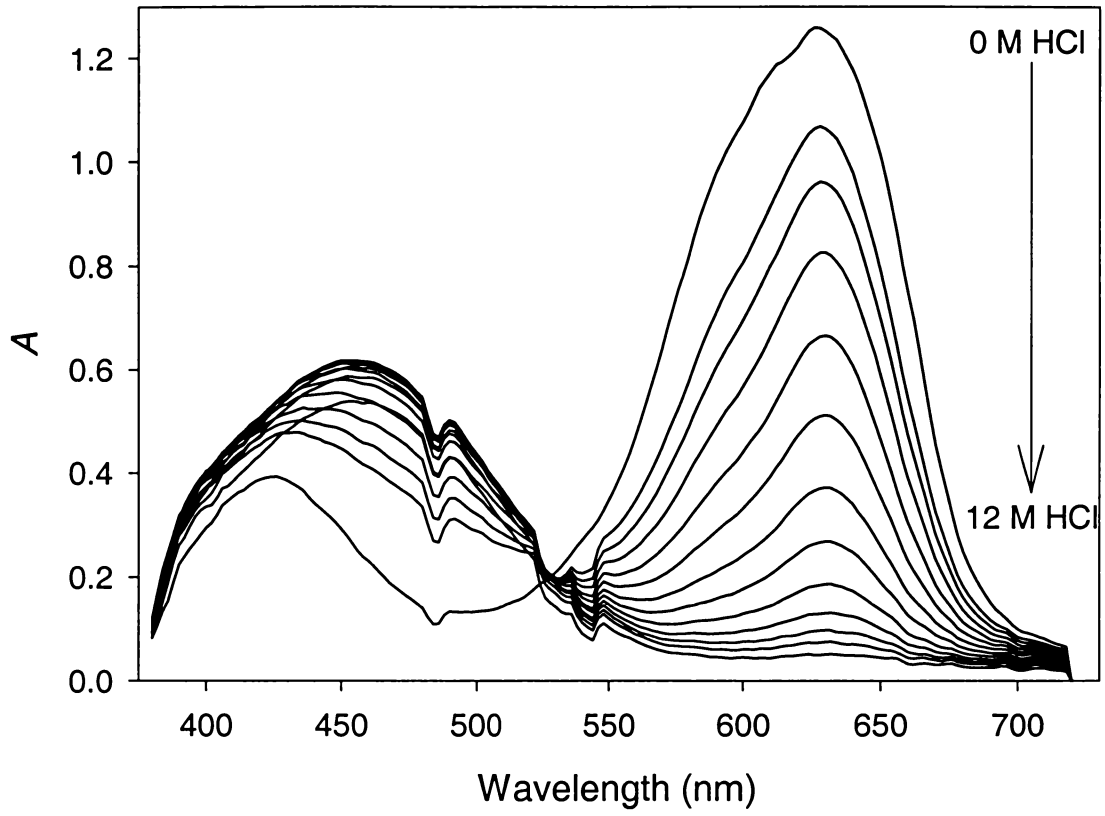

Figure 5.12. The optical spectrum of Sensor **FG1** in aqueous HCl solutions.

0.10, H_o = 0.55 ± 0.16). However, in the sol-gel solid, K_{a1} was determined to be 5.56 (pK_{a_1} = -0.75, H_o = -1.95, Figure 5.13).

In contrary to the preparation of sensors containing Bromocresol Green or Bromocresol Purple, Nafion was used in the preparation of Fast Green FCF sensors in order to improve physical integrity of the sensor films and response times. The effect of Nafion upon pK_a shifts of indicators in these sol-gel solids was discussed earlier.

5.3.2 Spectral Deconvolution of Cocktail Sensors. By the use of the cocktail sensors, we were able to obtain plots composed of two absorbing components. The optical sensors containing two indicators were prepared via a sol-gel synthetic route. Both indicators are active throughout the same general pH range; therefore the separation of the total absorbance (A_T) into the individual component absorbances was needed. Beer's Law was used to adequately deconvolute A_T into $A_{indicator1} + A_{indicator2}$ at a given wavelength.

Limitations to Beer's Law include:[8] (1) deviations in highly concentrated solutions, (e.g. in >0.10 M HCl solutions); (2) poor monochromaticity of the radiation beam resulting in analytical wavelength shifting; (3) instrumental stray light; (4) Solvent interactions through, e.g., H-bonds; (4) shifts in chemical equilibria; (5) decomposition; and (6) changes in solution refractive index. These limitations lead to non-linear deviations in the A vs concentration and contribute to the overall error.[8]

The cocktail base Sensor **AYTY1** could not be studied because of nearly

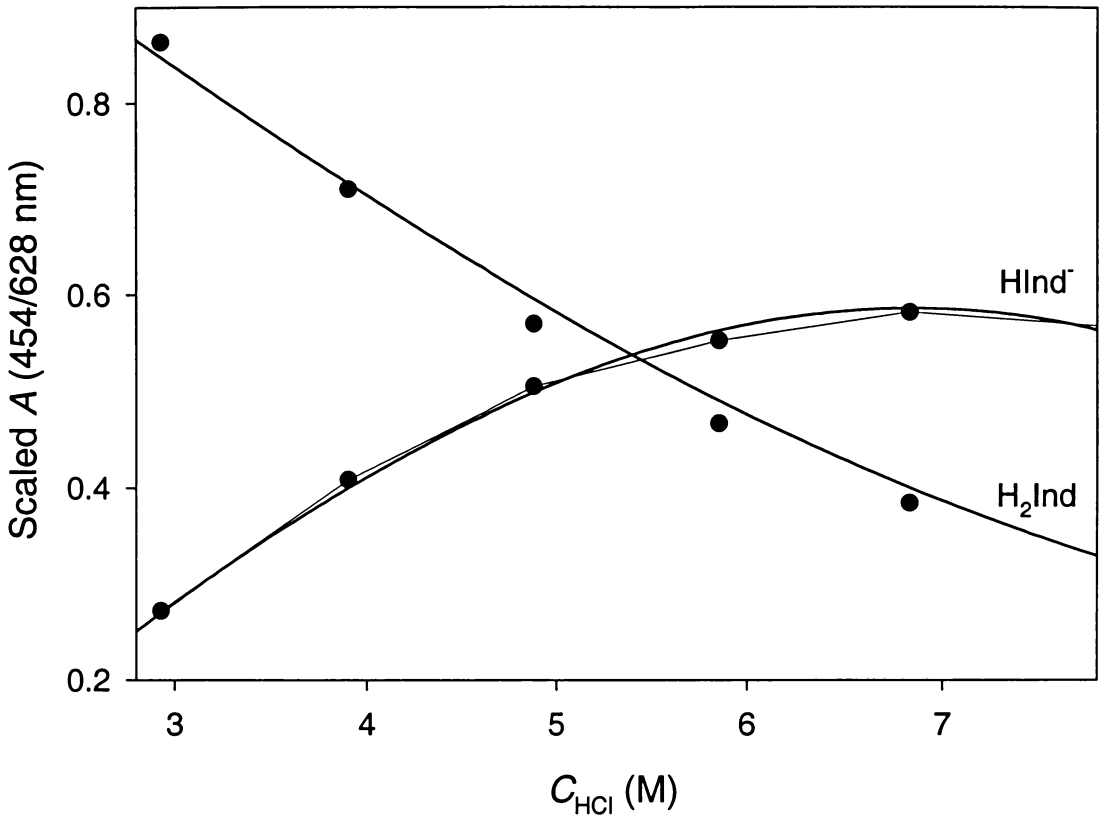

Figure 5.13. Distribution curves for the first ionization of Sensor **FG1** encapsulated in a sol-gel matrix.

identically overlapping *A*-values (Appendix D). The isosbestic points of Sensors **TY9** and **AY9** provided little separation to deconvolute Sensor **AYTY1**. The deconvolution of peaks with little separation was difficult to perform. Therefore, we focused our efforts on the deconvolution of individual absorbances associated with the acid sensors.

Cocktail sensors involving four acid indicators that have been used in our acidity determination for concentrated strong acids were studied. Attempts to prepare, cure, and condition sensors containing Neutral Red co-encapsulated with another indicator (BCG, BCP, and FG) were unsuccessful. In each case, uncontrollable leaching was too severe to give stable, precise measurements. Fast Green FCF sensors suffered slower kinetics, hence an increased magnitude of hysteresis. Sensors **BCP4** and **BCG4** had response times of <5 s and <10 s, respectively, to reach 90% of the analytical signal. In comparison, Sensor **FG1** had a response time of ~3 min to reach 90% of the analytical signal. We thus chose cocktail sensors involving BCP and BCG to perform the spectral deconvolution.

Optical spectra (*A* vs wavelength) consisting of a single sol-gel, encapsulated indicator representing an equilibrium between a H_2Ind and $Hind^-$ form are given in Figures 5.2, 5.5, and 5.12, for Sensors **BCP4**, **BCG5**, and **FG1**, respectively. The optical spectra of cocktail Sensors **BCPBCG1**, **BCPFG1**, and **BCGFG1** are given in Figures 5.14-5.16, respectively. For example, Sensor **BCPBCG1** is the combination of two indicators, Bromocresol Purple and Bromocresol Green. A_T can be deconvoluted to give the concentration of each

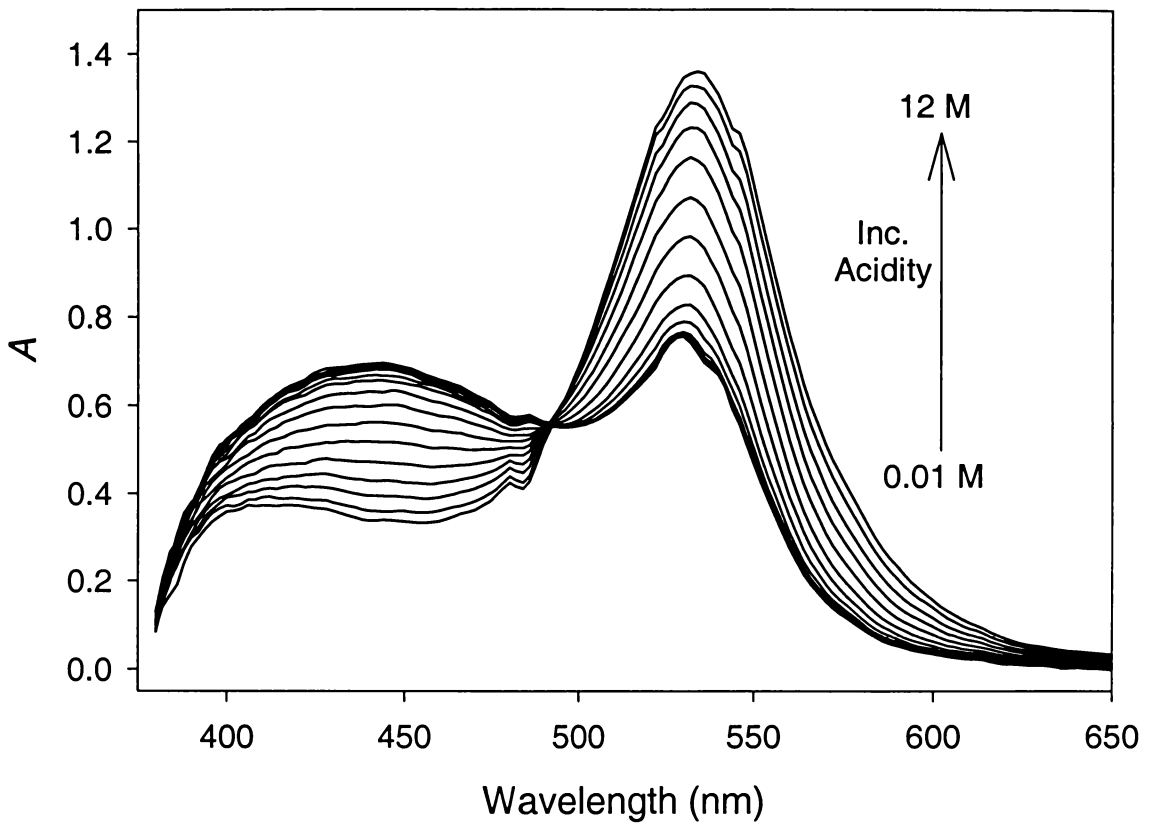

Figure 5.14. The optical spectrum of Sensor **BCPBCG1** in aqueous HCl solutions.

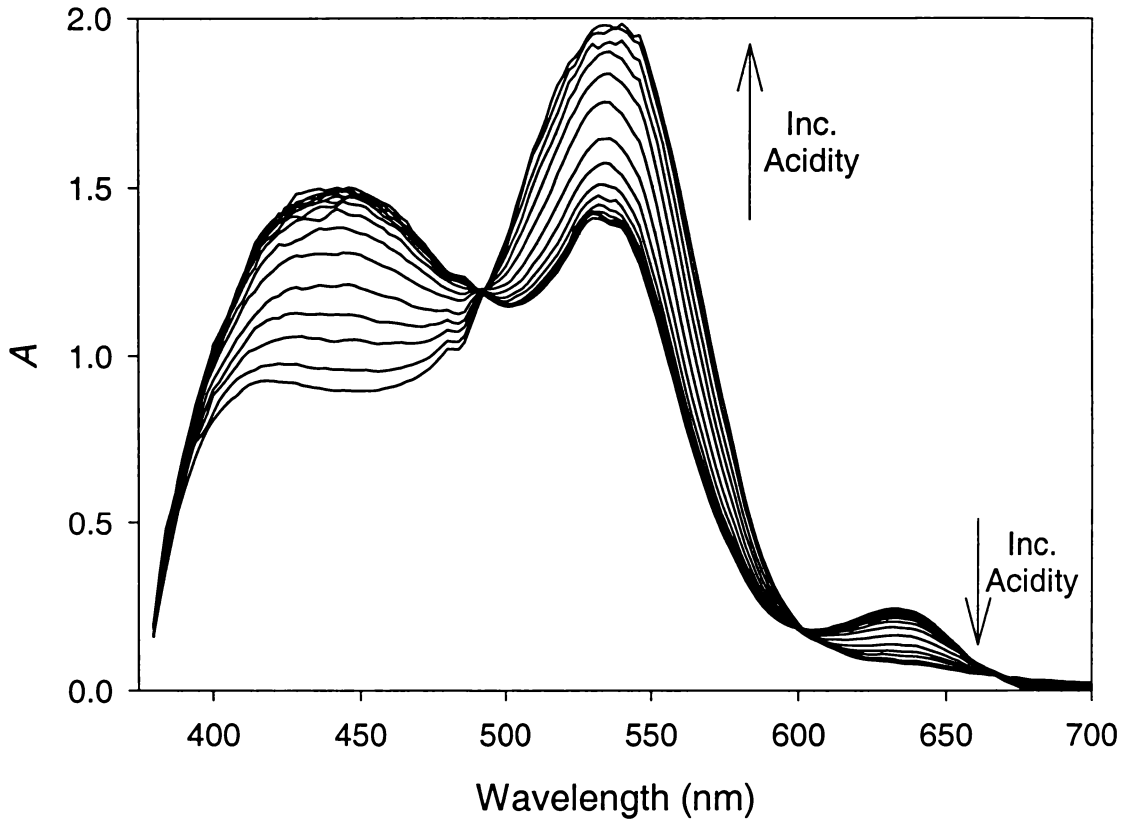

Figure 5.15. The optical spectrum of Sensor **BCPFG1** in aqueous HCl solutions (0.1 to 1 M HCl).

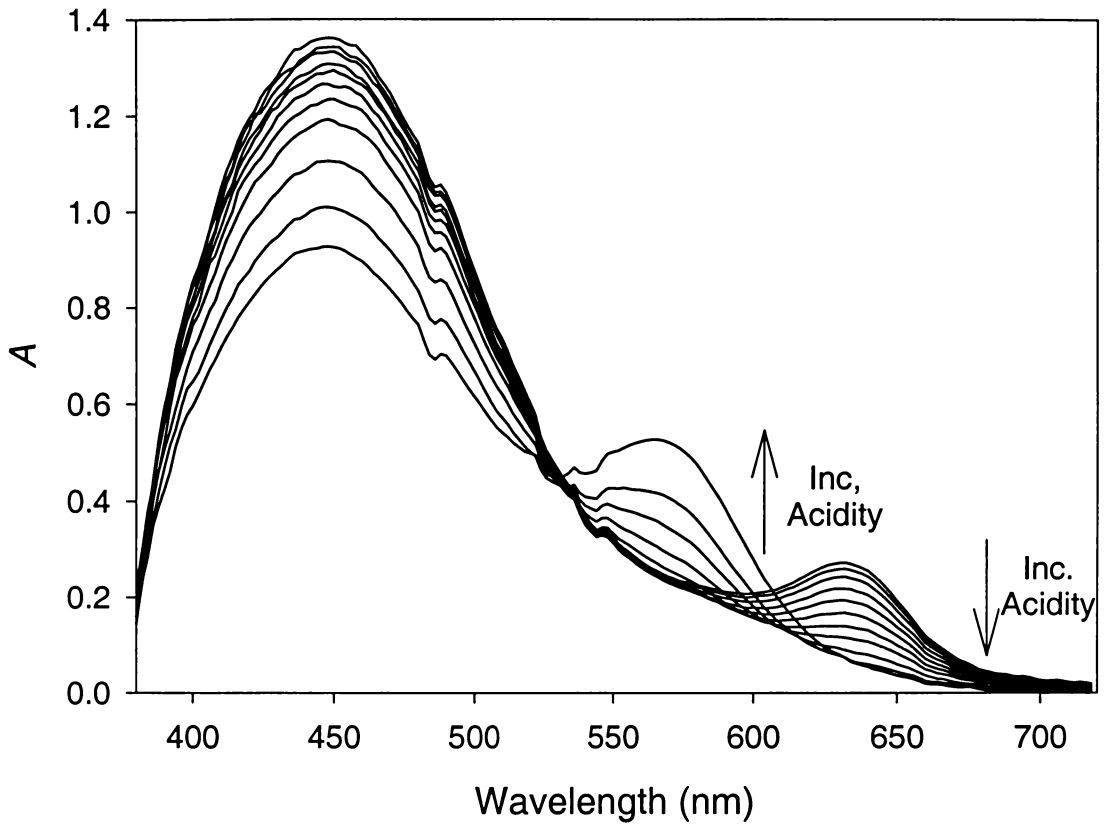

Figure 5.16. The optical spectrum of Sensor **BCGFG1** in aqueous HCl solutions (0.1 to 1 M HCl).

indicator by using two different wavelengths. Sensor **BCPBCG1** contains BCP and BCG that exhibit an analytical wavelength at 534 nm and 564 nm, respectively, for the H_2Ind absorbing forms (form **I**).

The wavelength dependent ε-values for BCP and BCG (as determined for the indicators dissolved in solution and reported in Table 5.1), an optical path length of 4.3 μm (0.0043 cm) (Figure 1.3 in Chapter 1), and the A_T for Sensor **BCPBCG1** (Figure 5.14) can be used to solve for the $C_{form\ I,\ BCG}$ and $C_{form\ I,\ BCP}$ as well as $A_{form\ I,\ BCG}$ (λ_1) and $A_{form\ I,\ BCP}$ (λ_2) using $\varepsilon(\lambda_1)bC_{form\ I,\ BCG}$ and $\varepsilon(\lambda_2)bC_{form\ I,\ BCP}$, respectively. The optical path length of the adsorbing species is the average thickness (b) of Sensor **BCPBCG1** as determined by a surface profiler. These relationships are given in Eqs. 5.1 and 5.2.

$$A_T(\lambda_1) = \varepsilon(\lambda_1)bC_{form\ I,\ Ind\ X} + \varepsilon(\lambda_1)bC_{form\ I,\ Ind\ Y} \qquad \text{(Eq. 5.1)}$$

$$A_T(\lambda_2) = \varepsilon(\lambda_2)bC_{form\ I,\ Ind\ X} + \varepsilon(\lambda_2)bC_{form\ I,\ Ind\ Y} \qquad \text{(Eq. 5.2)}$$

The $C_{form\ I,\ BCG}$ ranged from 9.78×10^{-4} mol.L^{-1} to 3.52×10^{-3} mol.L^{-1} in 1 to 12 M HCl solutions, respectively. The $C_{form\ I,\ BCP}$ ranged from 2.00×10^{-3} mol.L^{-1} to 3.22×10^{-3} mol.L^{-1}, respectively. The estimated total volume of the Sensor **BCPBCG1** film as determined by the sensor dimensions was 0.0129 cm^3 (1.29×10^{-5} L). The total amount of each indicator (Ind_T) within the sensor film was estimated to be 4.54×10^{-8} and 4.15×10^{-8} mol for indicators BCG and BCP,

respectively.

5.3.3 Salt Study Using a Cocktail Sensor. The $A_{\text{form I, BCG}}$ (λ_{564}) and $A_{\text{form I, BCP}}$ (λ_{534}) values calculated from Eqs. 5.1-5.2 can then be plotted as a function of C_{HCl} in a process similar to that in Chapter 4 for the single indicator-containing sensors. These plots can then be *best* fitted by an *empirical sigmoid* curve that is similar to that used in Chapter 4, Section 3.4 (Eq. 4.2) to give the A vs C_{HCl} plot of each absorbing species. The A_T and *deconvoluted component absorbances* ($A_{\text{form I, Ind X or Y}}$) are given as a function of C_{HCl} for Sensor **BCPBCG1** in Figure 5.17. The following most sensitive analytical wavelengths were chosen for each indicator: BCP (λ_{534}, form **I**) and BCG (λ_{564}, form **I**). With the ionic strength contributions of C_{acid} as a function of A for each indicator, one can then attempt to determine the contributions of C_{acid} and C_{salt} to the total ionic strength of a salt-containing concentrated, strong acid system.

In Chapter 4 we developed a novel mathematical relationship to correct for the salt contributions to ionic strength. This dual-transducer (two sensors) approach was based on a novel linear relationship between $\left(\partial A/\partial C_{salt}\right)_{C_{acid}}$ and $\left(dA/dC_{acid}\right)_{C_{salt}=0}$ (Eq. 4.1) for indicator-doped sol-gel sensors. The two sensors used in this approach have distinct ionic strength dependencies, and the signal arrays are decomposed to give C_{acid} and C_{salt}. Here we attempt to apply the mathematical models to cover cocktail sensors (single sensor with two indicators)

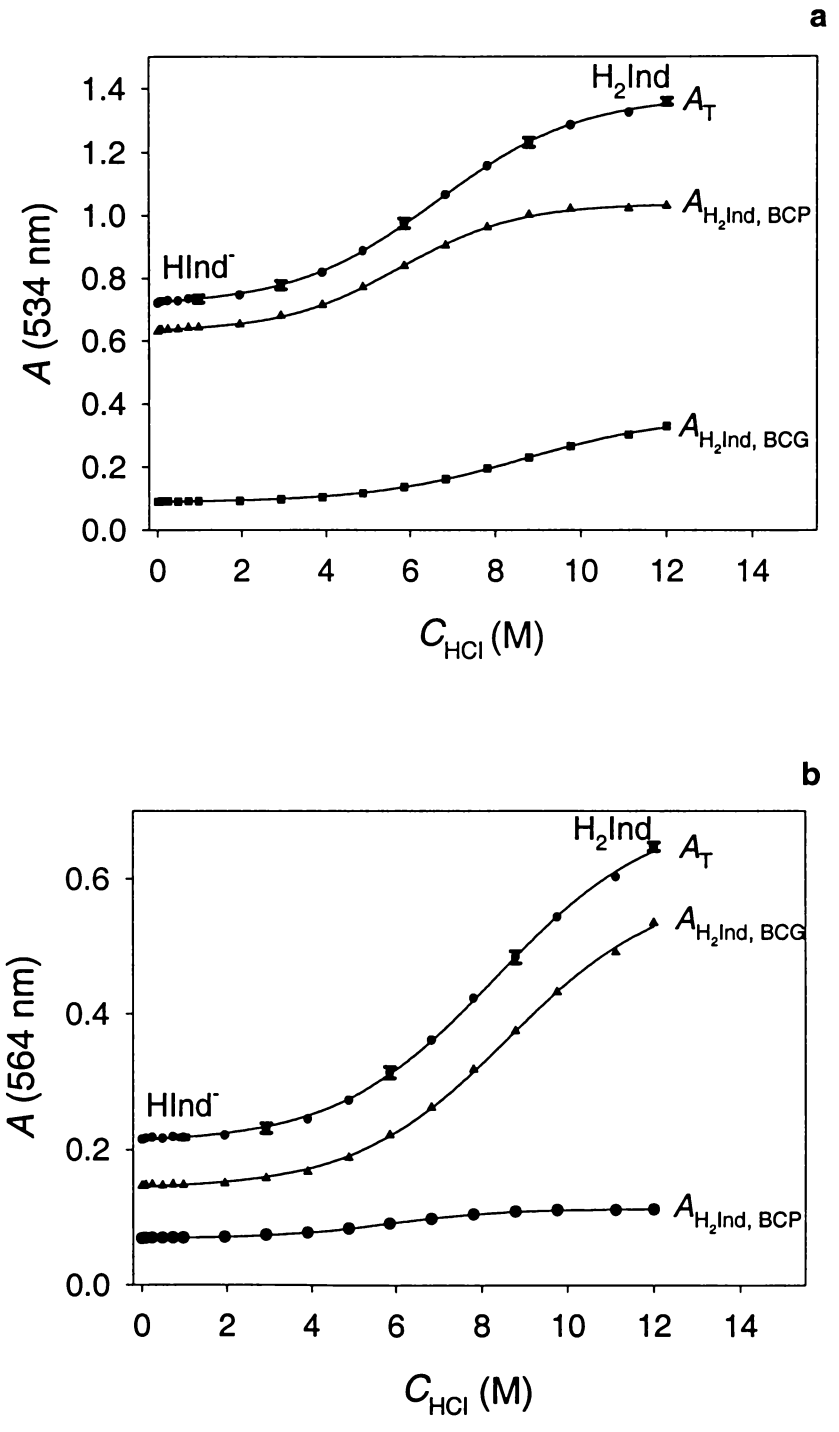

Figure 5.17. Deconvoluted plots of A vs. C_{HCl} at (a) 534 nm and (b) 564 nm for each transducing component using the cocktail Sensor **BCPBCG1**.

in order to minimize the error in C_{acid} prediction and gain an approximation of the C_{salt} in a saline-acidic system.

We observed that when a large amount of $CaCl_2$ was added to an acid solution at a fixed C_{acid}, the absorbance of Sensor **BCPBCG1** varied proportionally to the amount of the added salt. 3-D experimental plots of *deconvoluted A* (*A* = absorbance of the sensor in a $CaCl_2$-containing HCl solution) vs C_{acid} and C_{salt} are given in Figure 5.18. The *deconvoluted A* represents the $A_{form\ I,\ BCG}$ (λ_{564}) and $A_{form\ I,\ BCP}$ (λ_{534}) for the HCl-$CaCl_2$-H_2O ternary systems. We then applied the linear relationship in Eq. 4.1, and these plots are given in Figure 5.19.

Before corrections were performed in 5.00 M HCl solutions containing $CaCl_2$, prediction errors ranged from 1.79 to 16.9 and 1.10 to 8.50% for the BCP and BCG components, respectively, of Sensor **BCPBCG1**. After the corrections were performed, C_{HCl} prediction errors were reduced to 1.63 to 8.23%. The average reduction in error after the correction was ~56.3 and ~10.2%. A greater degree of error reduction was obtained in higher C_{salt} solutions (0.40 to 1.0 M $CaCl_2$). In those solutions, the error in C_{HCl} predictions could be reduced by as much as 76.6 and 53.5% for BCP and BCG components, respectively.

More concentrated of HCl-$CaCl_2$-H_2O solutions could be corrected as well. In the case of 9.00 M HCl solutions of HCl-$CaCl_2$-H_2O, C_{HCl} prediction errors were reduced from 0.71 to 9.0 and 0.33 to 10.1% for the BCP and BCG components, respectively, to <4.15% after correction. Comparisons of errors in

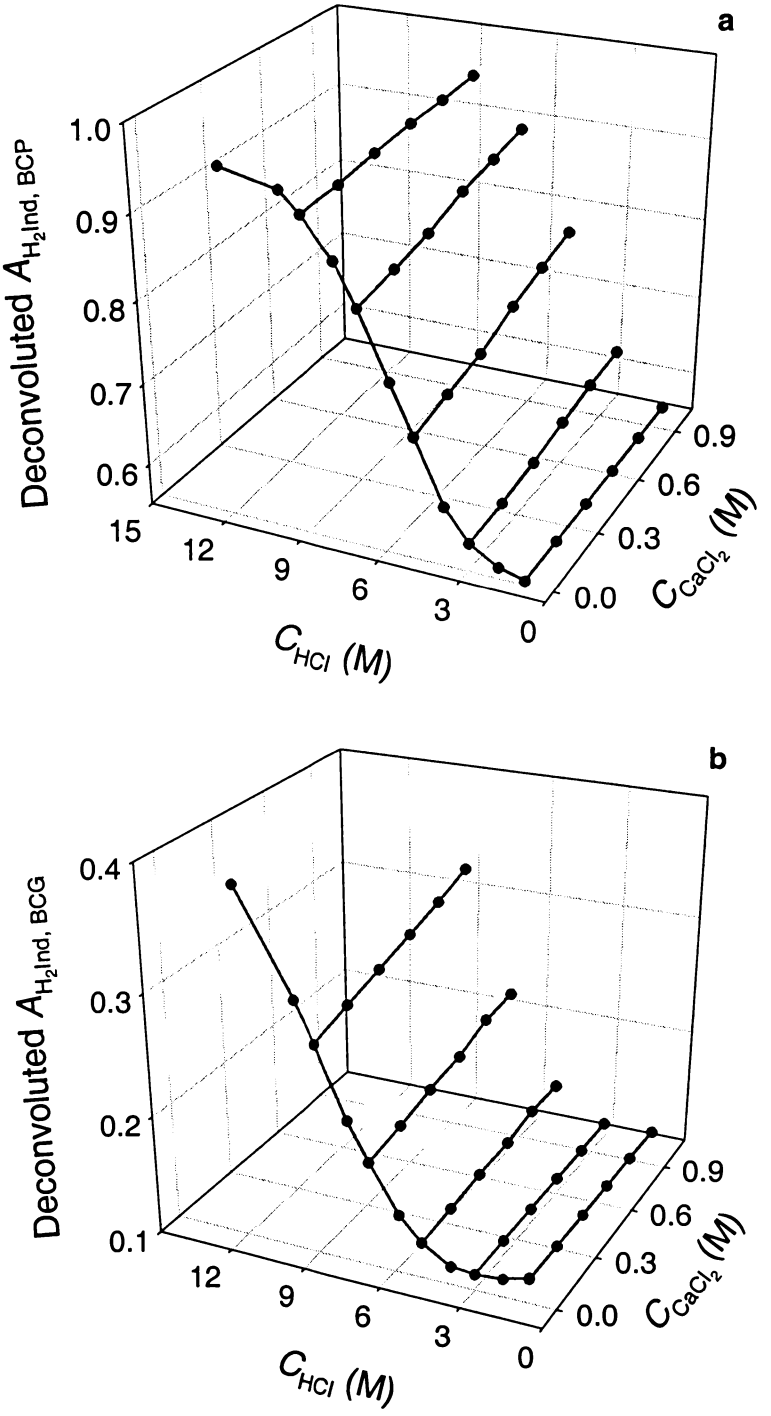

Figure 5.18. Deconvoluted spectra for (a) BCP and (b) BCG in cocktail Sensor **BCPBCG1** in HCl-$CaCl_2$-H_2O solutions.

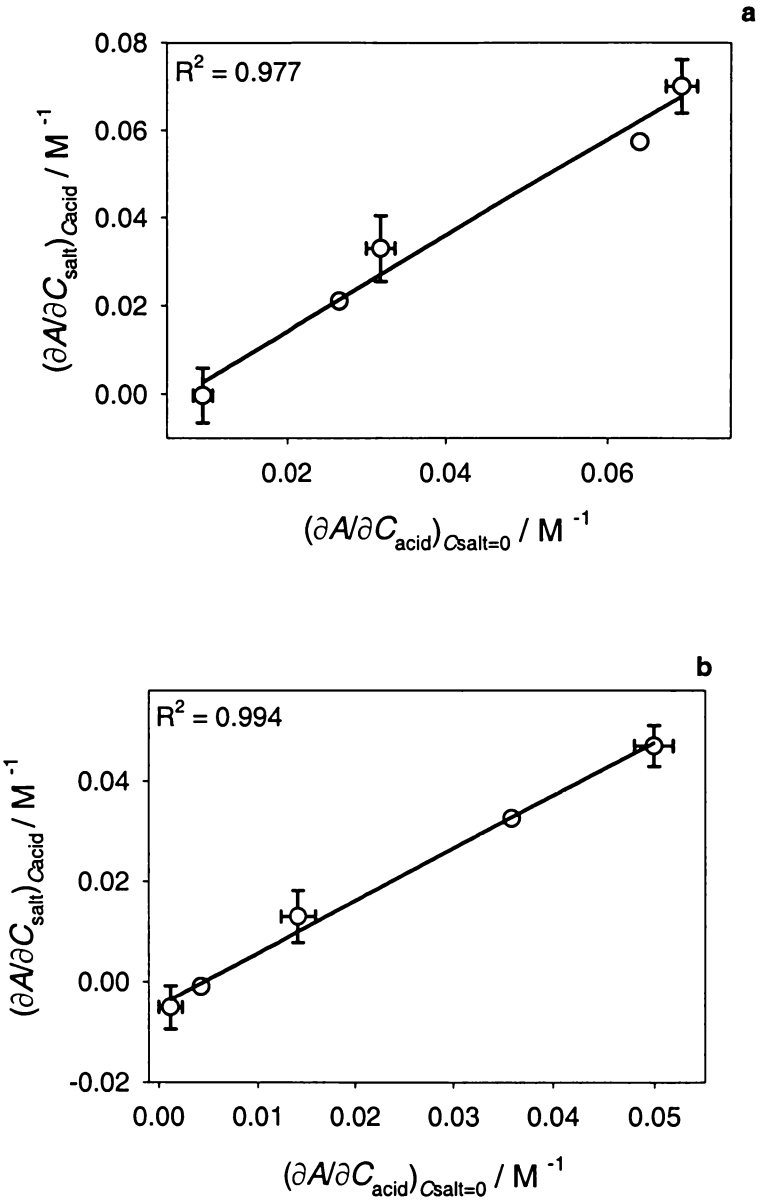

Figure 5.19. Plot of $\left(dA^{o}/dC_{acid}\right)_{C_{salt}=0}$ vs. $\left(\partial A/\partial C_{salt}\right)_{C_{acid}}$ in HCl-$CaCl_2$-H_2O solutions for (a) BCP and (b) BCG in the cocktail Sensor **BCPBCG1**.

C_{HCl} before and after the corrections are given in Figure 5.20 for HCl-$CaCl_2$-H_2O solutions (5 to 9 M HCl and 0 to 1 M $CaCl_2$).

Reductions in the C_{HCl} error could not be accomplished at the lower ends of the acidity range (1 to 3 M HCl) due to the compressed analytical range of the cocktail sensor.

Predictions were also made for the C_{salt} in the HCl-$CaCl_2$-H_2O (C_{HCl} = 5 to 9 M, C_{CaCl_2} = 0 to 1 M) solutions and are presented in Figure 5.21. Reliability of predicted C_{salt} values was lower than that achieved by the optical sensors containing a single indicator discussed in Chapter 4.

In contrast to the dual sensor approach containing a single indicator (Chapter 4), cocktail sensors exhibit a greater degree of error. We speculate that the following factors contribute to the increase in error: (1) errors associated with the deconvolution of overlapping absorbances; (2) reductions in the amount of indicators used to prepare the sensors, and thus the cocktail sensor sensitivity; (3) larger error due to two components of A_T; and (4) smaller dynamic ranges of the cocktail sensor in comparison to single transducer sensors in Chapter 4.

The total amount of each indicator used in the cocktail sensor preparations was reduced (to approximately one half) as compared to the optical sensors containing a single indicator. The reduction in the amount of both indicators was needed for two reasons: (1) to minimize spectral saturation and (2) to form homogeneous sol solutions with an appropriate solvent to Si-alkoxide ratio to make a uniform sensing film. These modifications led to a reduction in the analytical window. As mentioned above, two indicators at each A_T data point

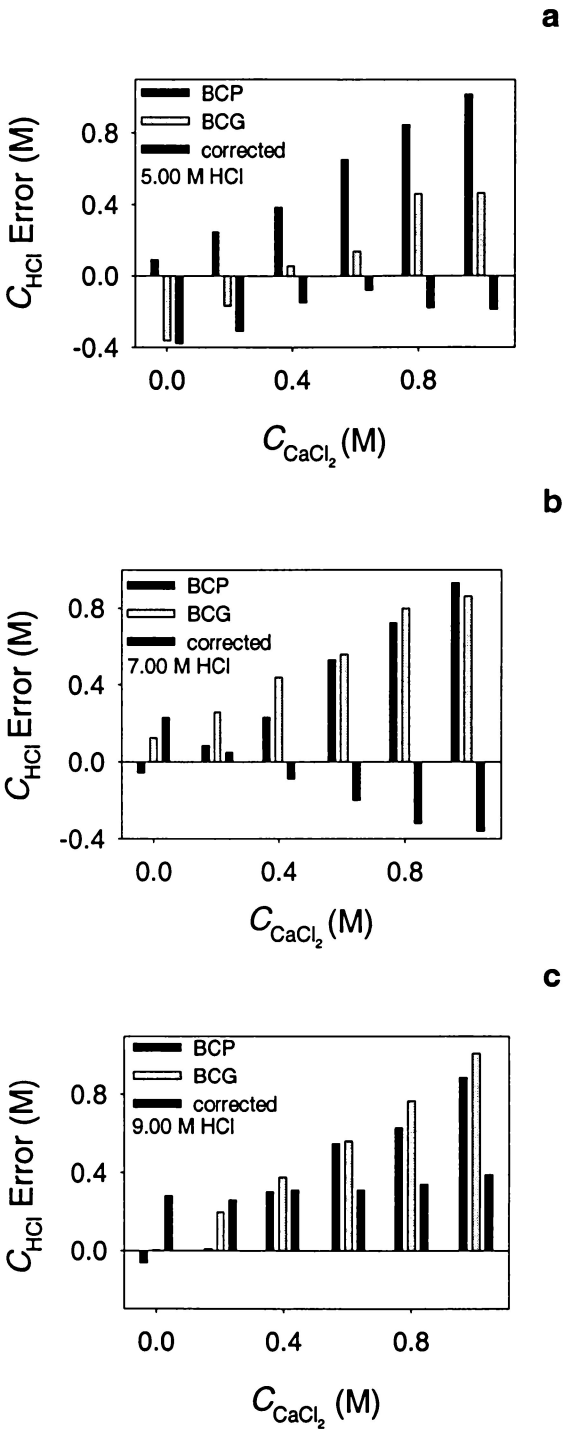

Figure 5.20. Comparison of errors in C_{acid} measurements before and after the corrections for (a) 5.00, (b) 7.00, and (c) 9.00 M HCl in HCl-$CaCl_2$-H_2O solutions.

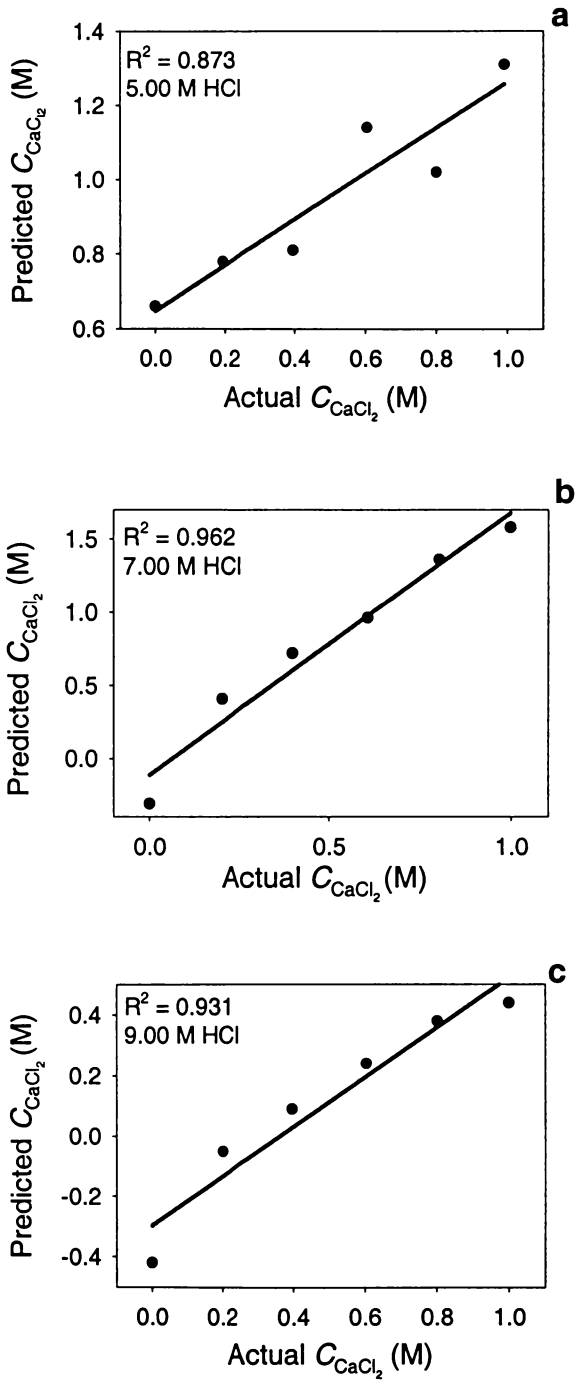

Figure 5.21. C_{salt} predictions via the dual-transducer approach; (a) BCP and (b) BCG components of Sensor **BCPBCG1**.

contribute to the overall error of the data point in a cocktail sensor, in contrast to optical sensors containing a single indicator. As a result of the additional error, curve-fitting correlation factors (R^2) are lower with the derivative plots (Figure 5.19) for the cocktail sensors. These less precise derivative plots ultimately led to larger errors in the C_{acid} and C_{salt}.

5.4 Concluding Remarks

A successful peak deconvolution method was established to *deconvoluted A* into the individual components, $A_{form\ I,\ Ind\ X} + A_{form\ I,\ Ind\ Y}$. The contribution of C_{HCl} to each component of the cocktail sensor could be evaluated. The deconvolution of the cocktail sensor could then be used to determine C_{salt} and C_{acid} in HCl-$CaCl_2$-H_2O (C_{HCl} = 5 to 9 M, C_{CaCl_2} = 0 to 1 M) solutions. However errors in C_{salt} and C_{acid} are larger than those determined by the optical sensors containing a single indicator. Indicator analysis studies for BCP, BCG, NR, and FG were presented.

REFERENCES

(1) Lin, J. *Anal. Chem.* **2000**, *19*, 541.

(2) Wolfbeis, O. S. *Fresenius J. Anal. Chem.* **1990**, *337*, 522.

(3) Rochester, C. H. *Acidity Functions*; Academic Press: New York, 1970.

(4) Alberty, R. A.; Silbey, R. J. *Physical Chemistry*; John Wiley & Sons: New York, 1997, pp 363-378.

(5) Janata, J. *Anal. Chem.* **1987**, *59*, 1351.

(6) Bates, R. G. *Determination of pH: Theory and Practice*, 2nd ed.; Johy Wiley & Sons: New York, 1973, pp 15-99, 138-152.

(7) Paul, A. *J. Mater. Sci.* **1977**, *12*, 2246.

(8) Skoog, D. A.; West, D. M.; Holler, F. J. *Analytical Chemistry an Introduction*, 6th ed.; Saunders College Publishing: Philadelphia, 1994, pp 84-85, 168-223, 337-338, 403-167.

(9) Phelan, M. K.; Barlow, C. H.; Kelly, J. J.; Jinguji, T. M.; Callis, J. B. *Anal. Chem.* **1989**, *61*, 1419.

(10) Wolfbeis, O. S. *Fiber Optic Chemical Sensors and Biosensors*; CRC Press: Boca Raton, FL., 1991, pp 267.

(11) Janata, J. *Anal. Chem.* **2000**, 150A.

(12) Allain, L. R.; Xue, Z.; Roberts, M. J. *J. Process Anal. Chem.* **1998**, *3*, 98.

(13) Seitz, W. R. *CRC Crit. Rev. Anal. Chem.* **1988**, *19*, 135.

(14) Zusman, R.; Rottman, C.; Ottolenghi, M.; Avnir, D. *J. Non-Cryst. Solids* **1990**, *122*, 107.

(15) Safavi, A.; Abdollahi, H. *Anal. Chim. Acta.* **1998**, *367*, 167.

(16) Werner, T.; Wolfbeis, O. S. *Fresenius J. Anal. Chem.* **1993**, *346*, 564.

(17) Courchene, C. E.; Suh, S.; McDonough, T. J. *Tappi. J.* **1994**, *77*, 101.

(18) Allain, L. R. Ph.D Dissertation, "Optical Sensors in Harsh Environments: Determination of Concentrated Strong Acids and Bases for Process Control", University of Tennessee, Knoxville, 1999.

(19) Allain, L. R.; Xue, Z. *Anal. Chem.* **2000**, *72*, 1078.

(20) Cox, R. A.; Yates, K. *Can. J. Chem.* **1983**, *61*, 2225.

(21) Kroschwitz, J. I.; Grant, M. H.; John Wiley & Sons: New York, 1995; Vol. 1, 4, pp 1004-1024, 1302-1003.

(22) Rochester, C. H. *Q. Rev. Chem. Soc.* **1966**, *20*, 511.

(23) Greenwood, N. N.; Earnshaw, A. *Chemistry of the Elements*, 2nd ed.; Pergamon Press: Boston, 1997, pp 89.

(24) Hisham, M. W. M.; Bommaraju, T. V. In *Encyclopedia of Chemical Technology*; 4th, Ed.; John Wiley & Sons: New York, 1995; Vol. 13, pp 894.

(25) Carey, W. P.; Jorgenson, B. *Applied Spectroscopy* **1991**, *45*, 834.

(26) Carey, W. P.; DeGrandpre, M. D.; Jorgenson, B. S. *Anal. Chem.* **1989**, *61*, 1674.

(27) Day, R. S. *Anal. Chem.* **1996**, *2*, 193.

(28) Kuhn, K. J.; Dyke, J. T. *Anal. Chem.* **1996**, *68*, 2890.

(29) Van Staden, J. F. *Fresenius Z. Anal. Chem.* **1987**, *328*, 68.

(30) Allain, L. R.; Sorasaenee, K.; Xue, Z. *Anal. Chem.* **1997**, *69*, 3076.

(31) Allain, L. R.; Canada, T. A.; Xue, Z. *Anal. Chem.* **2001**, *73*, 4592.

(32) Canada, T. A.; Allain, L. R.; Beach, D. B.; Xue, Z. *Anal. Chem.* **2002**, *74*, 2535.

(33) Perrin, C. *J. Am. Chem. Soc.* **1964**, *86*, 256.

(34) Opitz, N.; Leubbers, D. W. *Sens. Actuators* **1983**, *4*, 473.

(35) Wolfbeis, O. S.; Offenbacher, H. *Sens. Actuators* **1986**, *9*, 85.

(36) Lavigne, J. J.; Savoy, S.; Clevenger, M. B.; Ritchie, J. E.; McDoniel, B.; Yoo, S. J.; Anslyn, E. V.; McDevitt, J. T.; Shear, J. B.; Neikirk, D. *J. Am. Chem. Soc.* **1998**, *120*, 6429.

(37) Aussenegg, F. R.; Brunner, H.; Leitner, A.; Lobmaier, C.; Schalkhammer, T.; Pittner, F. *Sens. Actuators B* **1995**, *29*, 204.

(38) Ebelman, M. *Ann. Chimie Phys.* **1846**, *16*, 129.

(39) Brinker, C. J.; Scherer, G. W. *Sol-Gel Science*; Academic Press, Inc.: Boston, 1990, pp 12, 541-546.

(40) Roy, R. *J. Am. Ceram. Soc.* **1969**, *52*, 344.

(41) Hench, L. L.; West, J. K. *Chem. Rev.* **1990**, *90*, 33.

(42) Lin, J.; Brown , C. W. *Anal. Chem.* **1997**, *16*, 200.

(43) Lev, O.; Tsionsky, M.; Rabinovich, L.; Glezer, V.; Sampath, S.; Pankratov, I.; Gun, J. *Anal. Chem.* **1995**, *67*, 22A.

(44) Collinson, M. M. *Crit. Rev. Anal. Chem.* **1999**, *29*, 289.

(45) Lobnik, A.; Oehme, I.; Murkovic, I.; Wolfbeis, O. S. *Analytica. Chimica. Acta.* **1998**, *367*, 159.

(46) Rottman, C.; Ottolenghi, M.; Zusman, R.; Lev, O.; Smith, M. J. H.; Gong, G.; Kagan, M. I.; Avnir, D. *Mat. Lett.* **1992**, *13*, 293.

(47) Xu, H.; Sadik, O. A. *Analyst* **2000**, *125*, 1783.

(48) Jones, T. P.; Coldiron, S. J.; Deninger, W. J.; Porter, M. D. *Appl. Spectrosc.* **1991**, *45*, 1271.

(49) Maher, M. H.; Shahriari, M. R.; Test, J. *J. Test. Eval.* **1993**, *21*, 448.

(50) Dybko, A. A.; Wroblewski, W.; Rozniecka, E.; Pozniakb, K.; Maciejewski, J.; Romaniuk, R.; Brzozka, Z. *Sens. Actuators* **1998**, *B51*, 208.

(51) Im, H.-J.; Yang, Y.; Allain, L. R.; Barnes, C. E.; Dai, S.; Xue, Z. *Environ. Sci. Technol.* **2000**, *34*, 2209.

(52) Yost, T. L.; Fagan, B. C.; Allain, L. R.; Barnes, C. E.; Dai, S.; Sepaniak, M. J.; Xue, Z. *Anal. Chem.* **2000**, *72*, 5516.

(53) Tan, W.; Shi, Z.; Smith, S.; Birnbaum, D.; Kopelman, R. *Science* **1992**, *258*, 778.

(54) Song, A.; Parus, S.; Kopelman, R. *Anal. Chem.* **1997**, *69*, 863.

(55) Clark, H. A.; Hoyer, M.; Phibert, M. A.; Kopelman, R. *Anal. Chem.* **1999**, *71*, 4831.

(56) Bronk, K. S.; Michael, K. L.; Pantano, P.; Walt, D. R. *Anal. Chem.* **1995**, *67*, 2750.

(57) Michael, K. L.; Walt, D. W. *Anal. Biochem.* **1999**, *273*, 168.

(58) Shapiro, B. A. *Respir. Care* **1992**, *37*, 165.

(59) Mignani, A. G.; Baldini, F. *J. Lightwave Technol.* **1995**, *13*, 1396.

(60) Dave, B. C.; Dunn, B.; Valentine, J. S.; Zink, J. I. *Anal. Chem.* **1994**, *66*, 1120A.

(61) Blyth, D. J.; Aylott, J. W.; Richardson, D. J.; Russell, D. A. *Analyst* **1995**, *120*, 2725.

(62) Chung, K. E.; Lan, E. H.; S., D. M.; Dunn, B. S.; Valentine, J. S.; Zink, J. I. *Anal.Chem.* **1995**, *67*, 1505.

(63) Cox, J. A.; Alber, K. S. *J. Electrochem. Soc.* **1996**, *143*, L126.

(64) Reimer, L. *Scanning Electron Microscopy*; Springer-Verlag: New York, 1985.

(65) Watt, I. M. *The Principles and Practice of Electron Microscopy*, 2nd ed.; University Press: Cambridge, 1997.

(66) Brunauer, S.; Emmett, P.; Teller, E. *J. Am. Chem. Soc.* **1938**, *60*, 309.

(67) Dubinin, M. M. *J. Col. Interfac. Sci.* **1967**, *2*, 487.

(68) Brunauer, S.; Deming, L. S.; Deming, W. S.; Teller, E. *J. Am. Chem. Soc.* **1940**, *62*, 1723.

(69) Silverstein, R. M.; Bassler, G. C.; Morrill, T. C. *Spectrometric Identification of Organic Compounds*, 5th ed.; John Wiley & Sons: New York, 1991, pp 91-93.

(70) Ebsworth, E. A. V.; Rankin, D. W. H.; Cradock, S. *Structural Methods in Inorganic Chemistry*, 2nd ed.; CRC Press: Boca Raton, FL, 1991, pp 86-93, 259-263.

(71) Straughan, B. P.; Walker, S. *Spectroscopy*; Chapman and Hall: London, 1976, pp 240-295.

(72) Wagner, C. D.; Riggs, W. M.; Davis, L. E.; Moudler, J. F. *Handbook of X-Ray Photoelectron Spectroscopy*; Perkin-Elmer Corp.: Eden Prairie, MN, 1979.

(73) Edmonds, T. E.; Flatters, N. J.; Jones, C. F.; Miller, J. N. *Talanta* **1988**, *35*, 103.

(74) Zhang, L.; Langmuir, M. E.; Bai, M.; Seitz, W. R. *Talanta* **1997**, *44*, 1691.

(75) McCurley, M. F.; Seitz, W. R. *Anal. Chim. Acta.* **1991**, *249*, 373.

(76) Shamsipur, M.; Azimi, G. *Anal. Lett.* **2001**, *34*, 1603.

(77) Noire, M. H.; Couston, L.; Douarre, E.; Pouyat, D.; Bouzon, C.; Marty, P. *J. Sol. Gel. Sci. Tech.* **2000**, *17*, 131.

(78) Perrin, D. D.; Armarego, W. L. F. *Purification of Laboratory Chemicals*, 3rd ed.; Pergamon Press: Oxford, 1988.

(79) Bowden, K. *Chem. Rev.* **1966**, *66*, 119.

(80) Busing, W. R.; Hornig, D. F. *J. Phys. Chem.* **1961**, *65*, 284.

(81) Ackerman, T. *Z. Physik. Chem. (Frankfort)* **1961**, *27*, 253.

(82) Yagil, G.; Anbar, M. *J. Am. Chem. Soc.* **1963**, *85*, 2376.

(83) Robinson, R. A.; Harned, H. S. *Chem. Rev.* **1941**, *28*, 419.

(84) Schwarzenbach, G.; Sulzberber, R. *Helv. chim. Acta* **1944**, *27*, 348.

(85) Carey, F. A. *Organic Chemistry*, 2nd ed.; McGraw-Hill, Inc.: New York, 1992, pp 323, 324, 937.

(86) McMurry, J. *Organic Chemistry*, 3rd ed.; Wadsworth, Inc.: Belmont, CA., 1992, pp 385, 630.

(87) O'Ferrall, R. A.; Ridd, J. H. *J. Chem. Soc.* **1963**, 5030.

(88) Murray, A. G. *J. Assoc. Official Agr. Chem.* **1929**, *12*, 309.

(89) Peyronel, G. *Gazz. chim. ital.* **1949**, *79*, 792.

(90) Mills, A. L.; Hughes, F. *Chem. & Eng. Data Ser. 2,* **1957**, 35.

(91) Zollinger, H. *Azo and Diazo Chemistry*; Interscience Publishers, Inc.: New York, 1961, pp 347-361.

(92) Woodland, W. C.; Carlin, R. B.; Warner, J. C. *J. Am. Chem. Soc.* **1953**, *75*, 5835.

(93) Aoyagi, T.; Nakamura, A.; Ikeda, H.; Ikeda, T.; Mihara, H.; Ueno, A. *Anal. Chem.* **1997**, *69*, 659.

(94) Rottman, C.; Avnir, D. *J. Am. Chem. Soc.* **2001**, *123*, 5730.

(95) Huheey, J. E.; Keiter, E. A.; Keiter, R. L. *Inorganic Chemistry*, 4 ed.; Harper Collins College Publishers: New York, 1993, pp 320-321.

(96) Blumenthal, W. B. *The Chemical Behavior of Zirconium*; D. Van Nostrand Co., Inc.: Toronto, 1958, pp 201-239.

(97) Klein, C.; Hurlbut Jr., C. S. *Manual of Mineralogy*, 21 ed.; John Wiley & Sons, Inc.: New York, 1977, pp 440-464.

(98) *The Merck Index*, 7 ed.; Merck & Co., Inc.: Rahway, NJ, 1989, pp 10089.

(99) Bragg, W. L. *Atomic Structure of Minerals*; Cornell Univ. Press: Ithaca, NY, 1937, pp 159-162.

(100) Crocombette, J. P. *Phys. Chem. Miner.* **1999**, *27*, 138-143.

(101) Baak, T.; Rapp, C. F.; Hartley, H. T.; Wiens, B. E. *Ceram. Bull.* **1968**, *47*, 727.

(102) Ohta, H.; Suzuki, Y. *Amer. Ceram. Soc. bull.* **1978**, *57*, 602.

(103) Kamiya, K.; Sakka, S.; Tatemichi, Y. *J. Mater. Sci.* **1980**, *15*, 1765.

(104) Das, C. R. *Glass Ceram. Res. Bull.* **1979**, *26*, 11.

(105) Pavlik, R. S.; Klein, L. C.; McCauley, R. A. *J. Non-Cryst. Sol.* **1995**, *78*, 221.

(106) Allain, L. R.; Xue, Z. *Analytica. Chimica. Acta.* **2001**, *433*, 97.

(107) Englehardt, G.; Michel, D. *High-Resolution Solid-State NMR of Silicates and Zeolites*; Wiley: New York, 1987, pp 106-157.

(108) Guittet, M. J.; Crocombette, J. P.; Gautier-Soyer, M. *Phys. Rev. B.* **2001**, *63*, 125117.

(109) Ebbing, D. D. *General Chemistry*, 5 ed.; Houghton Mifflin Company: Boston, 1996, pp 667-695.

(110) Crocombette, J. P.; Ghaleb, D. *J. Nucl. Mater.* **1998**, *257*, 282.

(111) Rayner Jr., G.; Therrien, R.; Lucovsky, G. *Mat. Res. Soc. Symp.* **2000**, *611*, C1.3.1.

(112) Guermeur, C.; Lambard, J.; Gerard, J. F.; Sanchez, C. *J. Mater. Chem.* **1999**, *9*, 769.

(113) Andrianainarivelo, M.; Corriu, R.; Leclercq, D.; Mutin, P. H.; Vioux, A. *J. Mater. Chem.* **1996**, *6*, 1665.

(114) Tarta, P.; Sanz, J.; Serna, C. J.; Ocana, M. *J. Mater. Sci.* **1994**, *29*, 6533.

(115) Gonzalez-Carreno, T.; Tarta, P. J.; Sanz, J.; Serna, C. J.; Ocana, M. *Adv. Sci. Technol.* **1995**, *3B*, 1211.

(116) Hudson, M.; Knowles, J. A. *J. Mater. Chem.* **1996**, *6*, 89.

(117) Drago, R. S.; W. B., *Physical Methods in Chemistry*, Saunders Co.: Philadelphia, 1977, pp 138-139.

(118) Harrison, P. G.; Perry, C. C.; Creaser, D. A.; Li, X. *Eurogel '91 proceedings*, North-Holland, Amsterdam 1992; Elsevier; 175.

(119) Matsuda, A.; Kogure, T.; Matsuno, Y.; Katayama, S.; Tsuno, T.; Tohge, N.; Minami, T. *J. Am. Ceram. Soc.* **1993**, *76*, 2899.

(120) Savado, I. M. M.; Serna, C. J.; Navarro, J. M. F. *J. Non-Cryst. Sol.* **1988**, *100*, 330.

(121) Terry, K. W.; Tilley, D. T. *Chem. Mater.* **1991**, *3*, 1001.

(122) Toba, M.; Mizukami, F.; Niwa, S.; Sano, T.; Maeda, K.; Annila, A.; Komppa, V. *J. Mol. Catal.* **1994**, *94*, 85.

(123) Bhattacharya, A. K.; Hartridge, A.; Mallick, K. K. *J. Mater. Sci.* **1996**, *31*, 5873.

(124) Koone, N.; Shao, Y.; Zerda, T. W. *J. Phys. Chem.* **1995**, *99*, 16976.

(125) Lev, O. *Analusis* **1992**, *20*, 543.

(126) Dunn, B.; Zink, J. I. *Mater. Chem.* **1991**, *1*, 903.

(127) Klein, L. C. *Annu. Rev. Mater. Sci.* **1993**, *23*, 437.

(128) Rivera, D.; Harris, J. M. *Anal. Chem.* **2001**, *73*, 411.

(129) Dozier, W. D.; Drake, J. M.; Klafter, J. *Phys. Rev. Lett.* **1986**, *56*, 197.

(130) Wong, A. L.; Hunnicutt, M. L.; Harris, J. M. *J. Phys. Chem.* **1991**, *95*, 4491.

(131) Zheng, L.; Reid, W. R.; Brennan, J. D. *Anal. Chem.* **1997**, *69*, 3940.

(132) Rilbe, H. *pH and Buffer Theory-A New Approach*; John Wiley & Sons: New York, 1996, pp 135-139.

(133) Alabbas, S. H.; Ashworth, D. C.; Bezzaa, B.; Momin, S. A.; Narayanaswamy, R. *Sens. Actuators A* **1996**, *51*, 129.

(134) Bouse, L.; Hafeman, D.; Tran, N. *Sens. Actuators* **1990**, *81*, 361.

(135) Gopel, W.; Hesse, J.; Zemel, J. N. *in Sensors, a Comprehensive Survey, VHC*; Weiheim, 1989, pp 21.

(136) Dole, M. *J. Am. Chem. Soc.* **1932**, *54*, 3095.

(137) MacInnes, D. A.; Belcher, D. *J. Am. Chem. Soc.* **1931**, *53*, 3315.

(138) Beck, W. H.; Wynne-Jones, W. F. K. *J. Chim. Phys.* **1952**, *49*, C97.

(139) Dai, S.; Shin, Y.; Ju, Y. H.; Burleigh, M. C.; Barnes, C. E.; Xue, Z. *Adv. Mater.* **1999**, *11*, 1226.

(140) Dai, S.; Burleigh, M. C.; Shin, Y.; Morrow, C. C.; Barnes, C. E.; Xue, Z. *Angew. Chem. Int. Ed.* **1999**, *38*, 1235.

(141) Dai, S.; Burleigh, M. C.; Ju, Y. H.; Gao, H. J.; Lin, J. S.; Pennycook, S. J.; Barnes, C. E.; Xue, Z. *J. Am. Chem. Soc.* **2000**, *122*, 992.

(142) Fagan, B. C.; Tipple, C. A.; Xue, Z.; Sepaniak, M. J.; Datskos, P. G. *Talanta* **2000**, *53*, 599.

(143) *The Merck Index of Chemicals and Drugs*; Merch & Co., Inc.: New Jersey, 1960, pp 42, 192, 613, 1603.

(144) Gupta, B. D.; Sharma, S. *Opt. Commun.* **1998**, *154*, 282.

(145) Lin, J.; Liu, D. *Anal. Chim. Acta* **2000**, *408*, 49.

(146) Mohr, G. J.; Wolfbeis, O. S. *Analytica. Chimica. Acta.* **1994**, *292*, 41.

(147) Wolfbeis, O. S.; Marhold, H. *Fresenius J. Anal. Chem.* **1987**, *327*, 347.

(148) Besar, S. S. A.; Kelly, S. W.; Greenhalgh, P. A. *Int. J. Optoelectron.* **1988**, *3*, 318.

(149) Posch, H. E.; Leiner, M. J. P.; Wolfbeis, O. S. *Fresenius J. Anal. Chem.* **1989**, *334*, 162.

(150) Tucker, S.; Robinson, R.; Keane, C.; Boff, M.; Zenko, M.; Batish, S.; Street Jr., K. W. *J. Chem. Ed.* **1989**, *66*, 769.

(151) Barnard, S. M.; Walt, D. R. *Nature* **1991**, *353*, 338.

(152) Bookout, J. T.; Joaquim, T. R.; Magin, K. M.; Rogan, G. J.; Lirette, R. P. *J. Agri. Food Chem.* **2000**, *48*, 5868.

(153) Cruickshank, K. A.; Olvera, J.; Muller, U. R. *J. Chromatography A* **1998**, *817*, 41.

(154) Bronk, K. S.; Walt, D. R. *Anal. Chem.* **1994**, *66*, 3519.

(155) Pantano, P.; Walt, D. R. *Anal. Chem.* **1995**, *67*, 481A.

(156) Bakker, E.; Lerchi, M.; Rosatzin, T.; Rusterholz, B.; Simon, W. *Anal. Chim. Acta* **1993**, *278*, 211.

(157) Bishop, E. *Indicators*; Pergamon Press: Oxford, 1972, pp 104-106, 127, 490-101.

(158) Dean, J. A. E. *Lange's Handbook of Chemistry*, 14th ed.; McGraw-Hill: New York, 1992, pp 8.82, 88.114-115, 119.112-117, 118.116.

(159) Kolthoff, I. M.; Rosenblum, C. *Acid-Base Indicators*; The MacMillan Co.: New York, 1937, pp 72-387.

(160) Casula, R.; Crisponi, G.; Cristiani, F.; Nurchi, V. *Talanta* **1993**, *40*, 1781.

(161) Aragoni, M. C.; Massilmiliano, A.; Guido, C.; Valeria, M. N.; Silvagni, R. *Talanta* **1995**, *42*, 1157.

(162) Gupta, V. D.; Reed, J. B. J. *Pharm. Sci.* **1970**, *59*, 1683.

(163) Paul, M. A.; Long, F. A. *Chem. Rev.* **1957**, *57*, 1.

(164) Hammett, L. P.; Deyrup, A. J. *J. Am. Chem. Soc.* **1932**, *54*, 2721.

(165) Rottman, C.; Grader, G.; De Hazan, Y.; Melchior, S.; Avnir, D. *J. Am. Chem. Soc.* **1999**, *121*, 8533.

(166) Bartels, P. *Z. physik. Chem. (Frankfort, N. F.)* **1956**, *9*, 74.

(167) Dutta, R. K.; Bhat, S. N. *Can. J. Chem.* **1993**, *71*, 1785.

(168) Moulik, S. P.; Paul, B. K.; Mukherjee, D. C. *J. Colloid Interface Sci.* **1993**, *161*, 72.

(169) Singh, M. K.; Pal, H.; Bhasikuttan, A. C.; Sapre, A. V. *Photochem. Photobiol.* **1999**, *69*, 529.

(170) Bisset, A.; Dines, T. J. *J. Raman Spectrosc.* **1991**, *22*, 101.

(171) Meretoga, A. *Suomen Kemistilehti 21* **1948**, *B*, 24.

(172) Holmes, W. C.; Snyder, E. F. *J. Am. Chem. Soc.* **1928**, *50*, 1907.

APPENDICES

Appendix A

I. Matlab™ m files (example using Sensor **TY2**) used in Chapter 2 for the deconvolution of the base and alcohol concentrations based upon a dual-sensor approach.

< tytest.m>

```
%this m file defines both the absorbance vs [base] calibration curve
%and the effect of alcohol (alc) concentration on absorbance for a typical
%sensor,in this example, TY.


function con = test1(x)

%parameters for the calibration curve

a=0.0630193;
b=-0.4260917;
y0=0.487517;

%expression for [OH-] vs Abs

y=y0 + (a*ln(x-b));

%estimated slope (indicator)

b0=8.54350801e-3;
b1=-8.69563547e-4;

slope = b0 + b1*dy;

%adding the absorbance reading

Abs =0.156713;

load xestim.txt;

Aalc = Abs + slope*(x - xestim);
```

```
%expression for the interception of y and Aalc
con= y - Aalc;
```

<tyalc.m>

```
%function Calc = test1(x)

%read x=[NaOH], which is the root from fzero('tytest1')


%parameters for the calibration curve

a=0.0630193;
b=-0.4260917;
y0=0.487517;

%expression for [OH-] vs Abs

y=y0 + (a*ln(x-b));

%estimated slope (indicator)

b0=8.54350801e-3;
b1=-8.69563547e-4;

slope = b0 + b1*dy;

%adding the absorbance reading

Abs =0.156713;


Calc = (Abs - y)/slope
```

<iteration.m>

```
%enter initial guess for NaOH concentration
iniNaOH= 4;
```

```
for i=1:90;

  n=300;  %for the step size

  temp =(iniNaOH -i/n);
  estNaOH(i) =(iniNaOH -i/n);

  save c:\canada\matlab\xestim.txt temp -ascii

  %enter m.file for calculation of interception point
  fzero('tytest', 5);

  x=ans;
  NaOH(i)=ans;

  %enter m.file that estimates [alc]
 tyalc;

  Calc1(i)=Calc;
end

% save estimated data points ([NaOH], Calc) calculated from
% from the differential equations into file "answer.txt"

save c:\canada\matlab\answer.txt estNaOH NaOH Calc1 -ascii -tabs
load answer.txt;
temp1=answer'
save c:\canada\matlab\answer.txt temp1 -ascii -tabs
```

<findvalue.m>

```
%this m file calculates the interception point for the two

%estimated [NaOH] vs Calc curves using two different sensors

j=input('Which set of equations will be used?    ');
i=(j-1)*4;
clear p1 p2 n;
n=input('How many degrees used in the interpolation? [1 to 7]:   ');

p1=polyfit(a(:,i+1),a(:,i+2),n);
```

```
p2=polyfit(a(:,i+3),a(:,i+4),n);

  Csalt=roots(p1 - p2)
  m=input('Which concentration will be used? [1 2 3 4 5]:');
  NaOH=polyval(p1,Calc(m))
  Calc1(j)=Calc(m);
  NaOH1(j)=NaOH;


save c:\canada\matlab\evalconc.txt  Calc1 NaOH1 -ascii –tabs
```

II. UNIX program for importing data

```
#
# make sure there are no files called "wave", "transmit", or "temp"
#
touch wave transmit temp1 temp2
/bin/rm wave transmit temp1 temp2
#
# get wavelengths from first file in "filenames"
#
foreach file ( `head -1 filenames` )
#
# cut first three columns and put it into file "temp1"
#
  cut -c1-3 $file > temp1
#
# end of foreach loop
#
end
#
# loop over file names listed in file "filenames"
#
foreach file ( `cat filenames` )
#
# print current file name to screen
#
  echo $file
#
# cut first three columns and put it into file "wave"
```

```
#
  cut -c1-3 $file > wave
#
# cut columns five to end and put it into file "transmit"
#
  cut -c5- $file > transmit
#
```

Appendix B

An example (Sensor **NR2**) for calculating the C_{HCl} based upon A using Maple™.

```
> a:=0.4534965;

                    a := 0.4534965

> b:=1.7767668;

                    b := 1.7767668

> c:=0.1638536;

                    c :=0.1638536

> d:=4.4745724;

                    d := 4.4745724

> e:=0.506151;

                    e := 0.506151

> (d-(ln((a/(e-c))-1))*b)=x;

                    6.472293765 = x
```

An example (Sensor **NR2**) for calculating $\left(dA/dC_{acid}\right)_{C_{salt}=0}$ based C_{acid} using Maple™.

```
> a:=0.4534965;
                    a := 0.4534965

> b:=1.7767668;

                    b := 1.7767668

> c:=4.4745724;

                    c := 4.4745724

> d:=8.95;

                     d := 8.95

> (a*(exp((c-d)/b)))/(b*(1+(exp((c-d)/b)))^2)=x;

                   .01760862729 = x
```

Appendix C

Matlab™ m files (example using Sensor **NR2**) used in Chapter 4 for the deconvolution of the C_{acid} and C_{salt} based upon a dual-sensor approach.

<nr2test.m>

```
%this m file defines both the absorbance vs [acid] calibration curve
%and the effect of salt concentration on absorbance for a typical
%sensor,in this example, sensor NR2.


function con = test1(x)

%parameters for the calibration curve

a=0.4534965;
b=1.7767668;
x0=4.4745724;
y0=0.1638536;

%expression for [H+] vs Abs

y=y0 + a./(1 + exp((x0 - x)./b));

%calculates the first derivative of calibration curve, if [HCl] is %known returns
predicted slope for ionic strength dependence

dy = (a./b)*(1./(1 + exp(-(x - x0)./b))^2)*exp(-(x - x0)./b);

%estimated slope (indicator)
b0=-0.0115231;
b1=1.5447251;

slope = b0 + b1*dy;

%adding the absorbance reading

Abs =0.5061510;
```

```
load xestim.txt;
Asalt = Abs + slope*(x - xestim);
%expression for the interception of y and Asalt

con= y – Asalt
```

<nr2salt.m>

```
%function Csalt = test1(x)

%read x=[HCl], which is the root from fzero('nr2test')


a=0.4534965;
b=1.7767668;
x0=4.4745724;
y0=0.1638536;

%expression for [H+] vs Abs

y=y0 + a./(1 + exp((x0 - x)./b));

%calculates the first derivative of calibration curve, if [HCl] is known
%returns predicted slope for ionic strength dependence

dy = (a./b)*(1./(1 + exp(-(x - x0)./b))^2)*exp(-(x - x0)./b);

%estimated slope (indicator)

b0=-0.0115231;
b1=1.5447251;

slope = b0 + b1*dy;

%adding the absorbance reading

Abs =0.5061510;


Csalt= (Abs - y)/slope
```

<iteration.m>

```
%enter initial guess for HCl concentration
iniHCl= 6.1;

for i=1:90;

   n=300;  %for the step size

   temp =(iniHCl -i/n);
   estHCl(i) =(iniHCl -i/n);

   save c:\canada\matlab\xestim.txt temp -ascii

   %enter m.file for calculation of interception point
   fzero('nr2test', 5);

   x=ans;
   HCl(i)=ans;

   %enter m.file that estimates [salt]
  nr2salt;

   Csalt1(i)=Csalt;
end

% save estimated data points ([HCl], Csalt) calculated from
% from the differential equations into file "answer.txt"

save c:\canada\matlab\answer.txt estHCl HCl Csalt1 -ascii -tabs
load answer.txt;
temp1=answer'
save c:\canada\matlab\answer.txt temp1 -ascii -tabs
```

<findvalue.m>

```
%this m file calculates the interception point for the two

%estimated [HCl] vs Csalt curves using two different sensors

j=input('Which set of equations will be used?    ');
i=(j-1)*4;
clear p1 p2 n;
```

```
n=input('How many degrees used in the interpolation? [1 to 7]:   ');

p1=polyfit(a(:,i+1),a(:,i+2),n);
p2=polyfit(a(:,i+3),a(:,i+4),n);

   Csalt=roots(p1 - p2)
   m=input('Which concentration will be used? [1 2 3 4 5]:');
   HCl=polyval(p1,Csalt(m))
   Csalt1(j)=Csalt(m);
   HCl1(j)=HCl;


save c:\canada\matlab\evalconc.txt  Csalt1 HCl1 -ascii -tabs
```

Appendix D

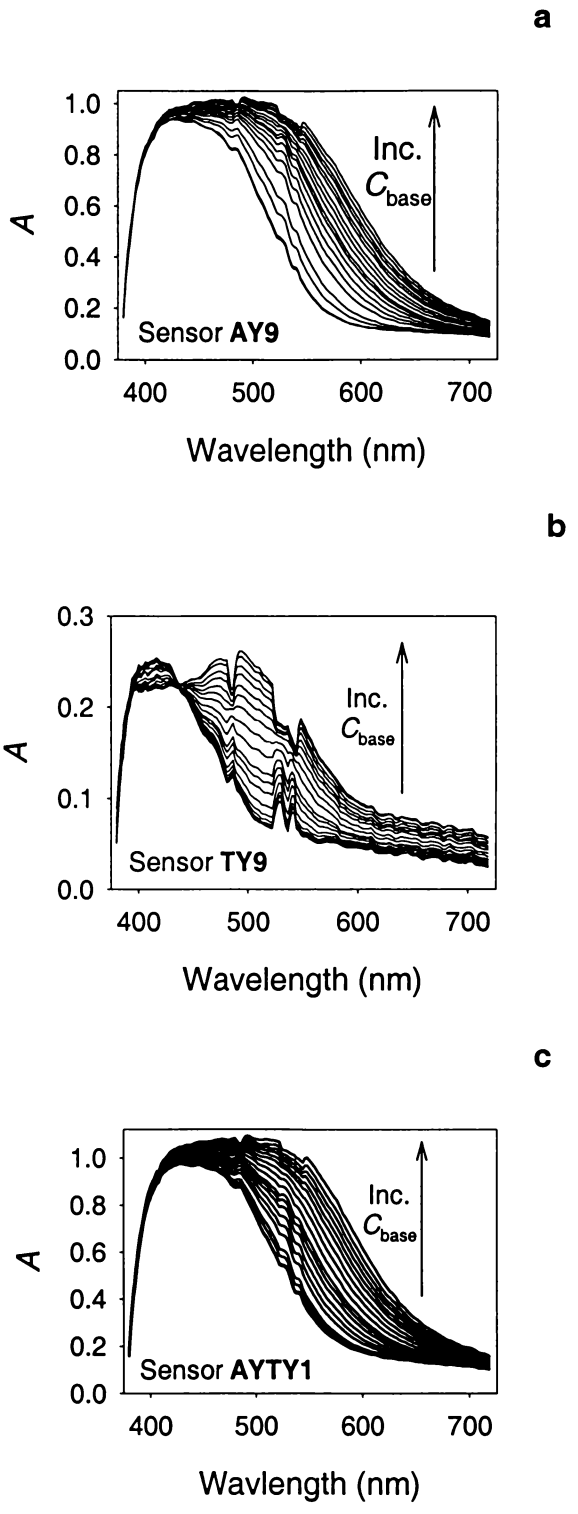

Figure D1. *A* vs λ for Sensors (a) **AY9**, (b) **TY9**, and (c) **AYTY1** in NaOH-H_2O.

VITA

Thomas Andrew Canada was born on September 25, 1974 at St. Anthony's Hospital in Louisville, Kentucky. He graduated with Salutatorian honors (4.0 GPA / 4.0 scale) from Russell County High School in Russell Springs, Kentucky, in 1993. He lettered in basketball and track & field, qualifying for the coveted state meet in the high jump event as a senior. He received several awards while completing his Bachelor of Science degree with a major in chemistry from the University of Kentucky in 1998, including: The Speed Scientific School of Engineering Scholarship, the Salutatorian Commonwealth Scholarship, Commonwealth of Kentucky Scholarship, and the Stephen Harris Cook Undergraduate Fellowship in Chemistry. He graduated with *Cum Laude* honors. It was at the University of Kentucky that he witnessed two national titles in basketball in the course of three straight dominating final four appearances and met his wife, Carrie. He remains a lifelong, avid fan of the Wildcat Dynasty. He later enrolled in graduate school at the University of Tennessee in Knoxville. It was while there that he further developed and characterized optical sol-gel sensors for online monitoring of concentrated strong acids and bases in the presence of organic compounds and salts. He was a general chemistry teaching assistant and research assistant. He received a Research Merit Award and various MCEC presentation and travel awards during his tenure. He presented his research at two ACS National Meetings (219th in San Fransciso, CA., in 2000

and 222nd in Chicago, IL, in 2001) and two Pittcon Meetings (New Orleans, LA 2001 and 2002).